

COMPUTER SIMULATION OF GRAIN BOUNDARY GROOVING BY
ANISOTROPIC SURFACE DRIFT DIFFUSION DUE TO CAPILLARY,
ELECTROMIGRATION AND ELASTOSTATIC FORCES

A THESIS SUBMITTED TO
THE GRADUATE SCHOOL OF NATURAL AND APPLIED SCIENCES
OF
MIDDLE EAST TECHNICAL UNIVERSITY

BY

ÖNCÜ AKYILDIZ

IN PARTIAL FULFILLMENT OF THE REQUIREMENTS
FOR
THE DEGREE OF DOCTOR OF PHILOSOPHY
IN
METALLURGICAL AND MATERIALS ENGINEERING

MAY 2010

Approval of the thesis:

**COMPUTER SIMULATION OF GRAIN BOUNDARY GROOVING BY
ANISOTROPIC SURFACE DRIFT DIFFUSION DUE TO CAPILLARY,
ELECTROMIGRATION AND ELASTOSTATIC FORCES**

submitted by **ÖNCÜ AKYILDIZ** in partial fulfillment of the requirements for the degree of **Doctor of Philosophy in Metallurgical and Materials Engineering Department, Middle East Technical University** by,

Prof. Dr. Canan ÖZGEN _____
Dean, Graduate School of **Natural and Applied Sciences**

Prof. Dr. Tayfur ÖZTÜRK _____
Head of Department, **Metallurgical and Materials Engineering**

Prof. Dr. Tarık Ö. OĞURTANI _____
Supervisor, **Metallurgical and Materials Engineering Dept., METU**

Prof. Dr. M. Kadri AYDINOL _____
Co-Supervisor, **Metallurgical and Materials Engineering Dept., METU**

Examining Committee Members:

Prof. Dr. Salim ÇIRACI _____
Physics Dept., Bilkent University

Prof. Dr. Tarık Ö. OĞURTANI _____
Metallurgical and Materials Engineering Dept., METU

Prof. Dr. Güngör GÜNDÜZ _____
Chemical Engineering Dept., METU

Prof. Dr. Macit ÖZENBAŞ _____
Metallurgical and Materials Engineering Dept., METU

Prof. Dr. Şakir BOR _____
Metallurgical and Materials Engineering Dept., METU

Date: _____ 31 May 2010

I hereby declare that all information in this document has been obtained and presented in accordance with academic rules and ethical conduct. I also declare that, as required by these rules and conduct, I have fully cited and referenced all material and results that are not original to this work.

Name, Last name : Öncü AKYILDIZ

Signature :

ABSTRACT

COMPUTER SIMULATION OF GRAIN BOUNDARY GROOVING BY
ANISOTROPIC SURFACE DRIFT DIFFUSION DUE TO CAPILLARY,
ELECTROMIGRATION AND ELASTOSTATIC FORCES

AKYILDIZ, Öncü

Doctor of Philosophy, Department of Metallurgical and Materials Engineering

Supervisor : Prof. Dr. Tarık Ö. OĞURTANI

Co-Supervisor : Prof. Dr. M. Kadri AYDINOL

May 2010, 242 pages

The aim of this study is to develop a theoretical basis and to perform computational experiments for understanding the grain boundary (GB) grooving in polycrystalline thin film metallic conductors (interconnects) by anisotropic surface diffusion due to capillary, electromigration and elastostatic forces.

To this end, irreversible thermo-kinetics of surfaces and interfaces with triple junction singularities is elaborated, and the resulting well-posed moving boundary value problem is solved using the front-tracking method. To simulate the strain conditions of the interconnects during service, the problem is addressed within the framework of isotropic linear elasticity in two dimensions (plane strain condition). In the formulation of stress induced surface diffusion, not only the contribution due

to elastic strain energy density (ESED) but also that of the elastic dipole tensor interactions (EDTI) between the stress field and the mobile atomic species (monovacancies) is considered. In computation of the elastostatic and electrostatic fields the indirect boundary element method (IBEM) with constant and straight boundary elements is utilized. The resulted non-linear partial differential equation is solved numerically by Euler's method of finite differences.

The dynamic computer simulation experiments identify well known GB groove shapes and shed light on their growing kinetics. They also allow generating some scenarios under several conditions regarding to the applied force fields and/or physicochemical parameters.

The destruction of groove symmetry, termination of the groove penetration with isotropic surface diffusivity, ridge/slit formations with anisotropic diffusivity and the role played by the wetting parameter are all identified for electromigration conditions. The kinetics of accelerated groove deepening with an applied tensile stress is examined in connection with GB cavity growth models in the literature and a diffusive micro-crack formation is reported at the groove tip for high stresses. On the other hand, the use of EDTI provided a means to dynamically simulate GB ridges under compressive stress fields with surface diffusion. An incubation time for hillock growth and a crossover depth over which GB migration becomes energetically favorable is defined and discussed in this context.

Keywords: Thin films, grain boundaries, grooving, surface diffusion, electromigration, film stress, cavity growth, crack, hillock.

ÖZ

KAPİLER, ELEKTROGÖÇ VE ELASTOSTATİK KUVVETLER ETKİSİNDE YÖN BAĞIMLI YÜZEY SÜRÜKLENME DİFÜZYONU İLE TANE SINIRI OLUKLAŞMASININ BİLGİSAYAR BENZETİMİ

AKYILDIZ, Öncü

Doktora, Metalürji ve Malzeme Mühendisliği Bölümü

Tez Yöneticisi : Prof. Dr. Tarık Ö. OĞURTANI

Ortak Tez Yöneticisi : Prof. Dr. M. Kadri AYDINOL

Mayıs 2010, 242 sayfa

Bu çalışmanın amacı, çok kristalli ince film metalik iletkenlerde (ara-bağlantılar) kapiler, elektrogöç ve elastostatik kuvvetler etkisinde yön bağımlı yüzey difüzyonu ile gerçekleşen tane sınırı oluklaşmasını kuramsal yönden ele almak ve meydana gelen olayların anlaşılması için bilgisayar benzetim deneyleri gerçekleştirmektir.

Bu amaçla, üçlü kavşak tekillikleri içeren yüzey ve arayüzeylerin dönüşümsüz termo-kinetiği özenle işlenmiş, ortaya çıkan iyi halli hareketli sınır değer problemi ön takip yöntemi ile çözülmüştür. Ara-bağlantıların çalışma esnasında maruz kaldıkları gerinme şartlarının benzetimi problemi iki boyutlu eşyönlü lineer elastisite kuramı kapsamında ele alınmıştır (düzlemsel gerinim). Gerilme destekli difüzyon probleminde ise elastik gerilme enerjisi yoğunluğunun (EGEY) yanı sıra, hareket halindeki kusurlar (mono-boşluklar) ile gerilme alanı arasındaki elastik

çift–kutuplu tensörel etkileşimler (EÇTE) de hesaba katılmıştır. Elastostatik ve elektrostatik alanlar, sabit ve doğrusal elemanların kullanıldığı, dolaylı sınır eleman yöntemi kullanılarak hesap edilmiştir. Elde edilen doğrusal olmayan kısmi diferansiyel denklem Euler’in sonlu farklar yöntemi kullanılarak çözülmüştür.

Dinamik bilgisayar benzetim deneyleri ile deneysel olarak gözlemlenen belli başlı oluk şekilleri elde edilmiş, bunların büyüme kinetikleri incelenmiştir. Uygulanan kuvvet alanları ve/veya fizikokimyasal etkenlere bağlı birtakım senaryolar da bu sayede incelenebilmiştir.

Elektrogöç şartlarına maruz bırakılan filmlerde oluk simetrisinin bozulması, eşyönlü yüzey difüzyonitesi ile oluk derinliği için bir üst sınırın oluşması, yön bağımlı yüzey difüzyonitesi ile sırt/kesik oluşumları ve tüm bu oluşumlarda ıslanma etkeninin oynadığı rol incelenmiştir. Uygulanan çekme gerilmesi ile hızlanan oluklaşma kinetiği, literatürde yer alan tane sınırı oyuk büyümesi modelleri ile karşılaştırmalı olarak incelenmiş, yüksek gerilmelerde tane sınırında difüzyon mikro–çatlak oluştuğu görülmüştür. Diğer taraftan, gerilme destekli difüzyonun tanımlanmasında EÇTE’nin kullanılmış olması, baskı gerilmesi altında tane sınırlarında sırt oluşumunun yüzey difüzyonu ile açıklanabilmesine ve dinamik bilgisayar benzetimlerinin yapılabilmesine imkân vermiştir. Bu bağlamda, tepecik büyümesi için kuluçka zamanı ve tane sınırı göçünün enerjik olarak elverişli hale geldiği bir geçiş derinliği tanımlanmış ve tartışılmıştır.

Anahtar Sözcükler: İnce filmler, tane sınırı, oluklaşma, yüzey difüzyonu, elektrogöç, film gerilmesi, oyuk büyümesi, çatlak, tepecik.

To My Parents

ACKNOWLEDGEMENTS

I thank to Prof. Dr. Tark  . Oğurtan for his invaluable guidance and endless motivation during the study of this thesis. It has been a great pleasure for me to work under his supervision.

Thanks are due to Profs. G. Gündüz, Ş. Bor, and M. K. Aydınol, M. Özenbaş of Middle East Technical University (METU), S. Çıracı of Bilkent University, E. E. Ören of University of Washington, and M. R. Güngör of University of Massachusetts for their guidance and helpful comments. I also thank to Prof. T. Öztürk on behalf of the Metallurgical and Materials Engineering Department of METU. The help and ease provided by the department is highly acknowledged.

Special thanks to all my friends and to my brother İhsan Önder Akyıldız, for their invaluable helps during the preparation of this thesis.

Finally, I would like to express my deepest gratitude to my mother Gönül Akyıldız, and grandmother Akile Çek for their complimentary love and unshakable faith in me during my life. This thesis is dedicated to the precious memories of my father Bilal Akyıldız and my grandfather İhsan Çek.

This research has been supported by the Scientific and Technological Research Council of Turkey, TUBITAK, trough a research Grant No. 104M399 and 107M011.

TABLE OF CONTENTS

ABSTRACT.....	iv
ÖZ	vi
ACKNOWLEDGEMENTS	ix
TABLE OF CONTENTS.....	x
LIST OF TABLES	xiii
LIST OF FIGURES	xiv
LIST OF SYMBOLS AND ABBREVIATIONS	xxvi
CHAPTERS	
1. LITERATURE SURVEY.....	1
1.1. Introduction	1
1.2. Kinetics of morphological changes by surface diffusion.....	4
1.3. Energetics of morphological changes by surface diffusion	8
1.3.1. Herring's curvature dependent chemical potential.....	8
1.3.2. Chemical potential for stressed solid surfaces	11
1.3.3. Defining a thermodynamic system; Isobaric and isochoric systems	15
1.3.4. Theory of electromigration.....	15
1.4. Mullins' theory of thermal grooving.....	19
1.5. Anisotropic diffusivity	26
1.6. Thermal grooving with surface energy anisotropy	28
1.7. Experimentally observed thermal grooves.....	34

1.8.	Steady state grain boundary diffusion coupled to thermal grooving	37
1.8.1.	Grain boundary diffusive creep cavity/crack or void growth.....	40
1.8.2.	Electromigration induced grain boundary slits or cracks.....	43
1.9.	Surface diffusion under external force fields and non-steady state grain boundary fluxes.....	44
2.	IRREVERSIBLE THERMOKINETIC THEORY OF SURFACES AND INTERFACES WITH TRIPLE JUNCTION SINGULARITIES	57
2.1.	Introduction	57
2.2.	Internal entropy production and rate of entropy flow for discrete microelements	59
2.3.	Internal entropy productions associated with the virtual displacements of the triple junction and the ordinary points	65
2.4.	Global internal entropy production associated with the virtual displacement of an interface interacting with grain boundaries.....	81
3.	MATHEMATICAL MODEL AND NUMERICAL PROCEDURES	89
3.1.	Equations of motion for the ordinary and the triple points	89
3.2.	Normalization and scaling.....	97
3.3.	Physical model; the boundary conditions in normalized and scaled time and space	103
3.4.	Numerical procedures	110
3.5.	Flowchart of the computer code 'GROOVE'	114

4. RESULTS AND DISCUSSIONS	115
4.1. Introduction.....	115
4.2. Thermal grooving revisited: the effect of physicochemical parameters	117
4.3. Thermal grooving with anisotropic surface diffusivity.....	130
4.4. Isotropic electromigration grooving.....	132
4.5. Electromigration grooving with anisotropic surface diffusivity	140
4.5.1. Two fold crystal symmetry, $m = 1$:	142
i. Moderate wetting.....	142
ii. Nearly complete wetting	147
4.5.2. Four fold crystal symmetry, $m = 2$:	149
i. Moderate wetting.....	149
ii. Nearly complete wetting	151
4.5.3. Six fold crystal symmetry, $m = 3$:	153
i. Moderate wetting.....	153
ii. Nearly complete wetting	153
4.6. Effect of elastostatic fields on grooving.....	155
4.6.1. Grain boundary grooving under tensile stresses.....	156
4.6.2. Grain boundary grooving under compressive stresses	174
CONCLUSIONS.....	186
REFERENCES.....	192
APPENDIX A. LIST OF COMPUTER CODE.....	214
CURRICULUM VITAE	240

LIST OF TABLES

TABLES

Table 4.2.1 Selected values of grain boundary energy γ_{gb} and crystal vapor surface energy γ_s for various materials in ergs/cm ² , and corresponding wetting parameters λ and slopes m	121
Table 4.5.1 Summary of the observed film morphologies for {110} planes with 45, 90, 135, 180° tilts. IN=Instable, ST=Stable, R=Ridge, S=Slit.....	141
Table 4.5.2 Summary of the observed film morphologies for {100} planes with 22.5, 45, 67.5, 90° tilts. IN=Instable, ST=Stable, R=Ridge, S=Slit....	142
Table 4.5.3 Summary of the observed film morphologies for {111} planes with 15, 30, 45, 60° tilts. IN=Instable, ST=Stable, R=Ridge, S=Slit.....	142
Table 4.6.1 Physicochemical properties of Al, Cu, Sn, and Pb, Smithells (1967)	155

LIST OF FIGURES

FIGURES

<p>Figure 1.2.1 An arbitrary surface in the x-y plane. \hat{t} is the unit tangent and \hat{n} is the unit normal vector, the subscripts σ, b, v on the fluxes denote the surface, bulk, and void phases respectively. When evaporation condensation mechanism is active, \vec{J}_b and \vec{J}_v entering (leaving) the surface element should also be considered. At a given time any point on the surface may be represented by position vector $\vec{r}(x,y)$</p>	4
<p>Figure 1.3.1.1 The curve $h(x)$ between $x=A$ and B represents a portion of the cross section of a surface between bulk and void phases. $h'(x)$ is the surface perturbed by an infinitesimal amount $\delta h(x)$</p>	9
<p>Figure 1.3.4.1 The diffusion paths of electromigration (Oren, 2003)</p>	18
<p>Figure 1.4.1 Sketch of the curve $h(x,t)$; the surface profile function. d is the groove depth measured from the maxima and w is the separation between the two maxima, namely the groove width. γ_{gb} and γ_s are the grain boundary and surface tensions respectively. $\varphi = \pi - 2\theta$ is the equilibrium dihedral angle, force balance requires: $2\gamma_s \sin\theta = \gamma_{gb}$ at the groove root</p>	22
<p>Figure 1.4.2 Schematic representation of a) continuous array of grains, b) plate like grains that have semicircular ends. Symmetry prevails due to</p>	

assumed isotropic surface properties and solution for the solid lines is enough for interpretation.....	25
Figure 1.5.1 In a) ball model for next neighbor hopping on the (110), (100) and (111) surfaces of a face centered cubic crystal. Arrows mark the possible jumps from an adsorbate at the origin (figure adapted from Barth, 2000), b) analytic function (Eq. 1.5.2) used to represent the orientation dependence: $D_{\sigma}^0 = 1$, $A=1$, $\phi = 0^{\circ}$ (solid red curves) and $\phi = 30^{\circ}$ (dashed blue curves) respectively for $m=1 \rightarrow (110)$, $m=2 \rightarrow (100)$ and $m=3 \rightarrow (111)$ planes.....	27
Figure 1.6.1 Structure of an fcc $(3\bar{2}16)$ surface vicinal to the fcc (001) surface. Figure illustrates zero-temperature steps and kinks that occur on high index (or ‘vicinal’) surfaces (Jeong & Williams, 1999).....	29
Figure 1.6.2 Schematic illustration of equilibrium crystal shapes at finite temperatures, T for a simple cubic model with the nearest neighbor interaction. Equilibrium crystal shapes a) at $T < T_R$: stable (001) facets and b) at $T > T_R$: continuously rounded, have no facet. The regions marked by arrows in a) and b), are vicinal to the low index (001) surface. The difference in mesoscopic structures below and above the roughening temperature is given in c) and d) (Jeong & Williams, 1999).....	30
Figure 1.8.1.1 Grain boundary cavity/slit growth by diffusion across the cavity surface and through the grain boundaries due to a stress gradient, a) array of grain boundary cavities, b) an isolated triple junction cavity.....	41
Figure 2.3.1 Triple junction (TJ) longitudinal displacement along the grain boundary. a) TJ macrostructure, line BB' represents the grain boundary	

and ABC and ADC are the initial and displaced position of the void interfacial layer, respectively. $\Delta\eta$ is the longitudinal virtual displacement of the triple junction along the grain boundary. b) TJ microstructure, h_σ and h_g are the thicknesses of the interfacial and grain boundary layers, respectively. Figure adapted from Oren (2003)..... 65

Figure 2.3.2 Upper left portion of figure 2.3.1. Rotated in clockwise direction and rescaled to show the geometric connections for $\Delta\ell^+ \gg \delta\eta^+$ where the angle $B\hat{D}A' \rightarrow \theta^+$. The right hand side is treated in the same way..... 68

Figure 2.3.3 The curvature relationship given in equation (2.3.7) may be justified by a) considering a circle that pass from three points: $\rho = \kappa^{-1}$, where, ρ is the local radius of curvature. Alternatively, b) shows the unit tangent (\hat{t}) and normal (\hat{n}) vectors at the mid-segments, so as given in c) magnitude of the difference vector $|\hat{t}^- - \hat{t}^+|$ is the base of the isosceles triangle formed by the unit vectors and therefore equal to $2\sin(\pi/2-\theta)$.

Then, curvature may be obtained as: $\kappa = \left| \frac{d\hat{t}}{d\ell} \right| = \left| \lim_{\Delta\ell \rightarrow 0} \frac{\hat{t}(\ell + \Delta\ell) - \hat{t}(\ell)}{\Delta\ell} \right|$

$$= \lim_{\Delta\ell \rightarrow 0} \left| \frac{\hat{t}^- - \hat{t}^+}{\Delta\ell} \right| = \lim_{\Delta\ell \rightarrow 0} \frac{\cos\theta}{\Delta\ell/2} \dots\dots\dots 72$$

Figure 3.2.1 Schematic representation of the two systems subjected to dimensional analysis 97

Figure 3.3.1	Isometric view of a thin metallic bi-crystal thin film with a vertical grain boundary separating it into two grains and in contact with electrode pads.....	103
Figure 3.3.2	The schematic representation of the problem. Sidewalls (blue circles) are subject to Neumann, and the edges (domain boundaries that are perpendicular to the x-axis; red dots) subject to the Dirichlet boundary conditions in considering both elasto and electrostatics problems	104
Figure 3.4.1	Orientation dependence of the normalized surface diffusivities with, $A=1$, $\phi = 0^\circ$ (solid red curves) and $\phi = 30^\circ$ (dashed blue curves) respectively for $m=1 \rightarrow (110)$, $m=2 \rightarrow (100)$ and $m=3 \rightarrow (111)$ planes	111
Figure 3.5.1	Program flowchart.....	114
Figure 4.1.1	Sketch of a grain boundary groove, which evolves on the upper triple junction of figure 3.3.2, illustrating its width, depth, maxima and dihedral angle. Here W and L denote the half film width and length, respectively. The grain boundary extends along the origin	116
Figure 4.2.1	Isotropic thermal grooving for $\lambda=0.5$, $M_L=M_T=0.25$: a) and b) shows the GB profile; c) kinetic data for groove depth, maxima and width; d) TJ velocity and the dihedral angles. The linear correlation factors (R^2) for depth, width, maxima and velocity up to 5 decimals are 1.0, 0.99999, 0.99996 and 0.99974 respectively. Final time for failure is equal to $t_n=27.5$ in normalized scale	118

Figure 4.2.2	a) The relation between depth cofactor ($d/t^{1/4}$) and the slope;	
	b) finite slope ($=\tan(\lambda) = \lambda/\sqrt{1-\lambda^2}$) and the small slope approximation ($=\tan(\lambda)$) as a function of wetting parameter.....	122
Figure 4.2.3	Thermal grooving for different wetting parameters. Simulated profiles are normalized with respect to a) $mt^{0.25}$ and $t^{0.25}$; b) unit depth and unit half width ($w/2$). The $m \rightarrow 0$ curves are plotted using Mullins' profile function. Kinetic data for c) the groove depth and d) the dihedral angles	125
Figure 4.2.4	3D AFM image of a groove developed on the surface of tungsten upon 128 h of annealing in vacuum at 1350 °C taken from Zhang et al. (2002).....	126
Figure 4.2.5	Thermal grooving for $\lambda=0.28$ and $M_L=M_T=0.25$: a) kinetic data for the dihedral angles resulting from present simulation and reported by Zhang et al. (2002) b) kinetic data for the groove depth and the lines obtained from linear regression in the transient and stationary states; the first kinetic equation in the transient regime is $d=0.97t^{0.46}=3.38\tan(\lambda)t^{0.46}=3.33\lambda/\sqrt{1-\lambda^2}t^{0.46}$ and the second one in the stationary regime is $d=0.283t^{0.25}=0.984\tan(\lambda)t^{0.25}=0.97\lambda/\sqrt{1-\lambda^2}t^{0.25}$	127
Figure 4.2.6	Thermal grooving by different TJ mobilities, $M_L=M_T=M$. Kinetic data for a) the groove depth and b) the dihedral angles	128
Figure 4.3.1	Thermal grooving with anisotropic surface diffusivities with $A=10$ a) 2 fold symmetry with 45, 90, 135, and 180° tilt angle, b) 4 fold symmetry with 22.5, 45, 67.5 and 90° tilt angle, c) 6 fold symmetry with	

15, 30, 45, and 60° tilt angle. Experiments were performed for the following physicochemical parameters: $M_L=M_T=0.25$, $\lambda=0.5$	130
Figure 4.3.2 Failure times due to film agglomeration for different tilt angles and fold symmetries.....	131
Figure 4.4.1 Isotropic electromigration grooving for $\lambda=0.5$, $M_L=M_T=0.25$ and $\chi=1.0$: a) and b) shows the GB profile; c) kinetic data for groove depth, maxima and width; d) TJ velocity and the dihedral angles.....	133
Figure 4.4.2 Isotropic electromigration groove with $\chi=3.0$: a) and b) shows the GB profile; c) kinetic data for groove depth, maxima and width; d) TJ velocity and the dihedral angles	136
Figure 4.4.3 TEM micrographs showing the ‘inch worming’ process in a 0.5 μm wide Al film exposed to a current density of $2 \times 10^6 \text{A/cm}^2$ at 350°C. Figures reproduced from Riege et al., 1995 (given as Fig. 3), 1996 (given as Fig. 2); Prybyla et al., 1998 (given as Fig. 1). The dotted lines indicate grain boundaries	137
Figure 4.4.4 Dependence of a) the limiting depth and b) rotation angle to electron wind intensity for different wetting parameters. The equations obtained by linear regression (solid lines) are plotted on the experimental data (triangles).....	138
Figure 4.5.1.1 Electromigration grooves with $\chi=0.5$, on a surface having an anisotropic diffusivity characterized by $A=10$, $m=1$, $\phi=45^\circ$ (first column: a to c) and $\phi=90^\circ$ (second column: d to f). a) and d) shows the GB groove profiles; b) and e) kinetic data for groove depth, maxima and width; c) and f) TJ velocity and the dihedral angles. Ridge formation	

starts with turning over of groove tip trajectory after a certain time, both hillocks on each side of the grain boundary exhibit linear growth while the separation between the two maxima (groove width) decreases linearly for the case $\phi=45^\circ$, but continues to increase in the case of $\phi=90^\circ$ 143

Figure 4.5.1.2 Electromigration groove with $\chi=0.5$ (except part c) and $\chi=5.0$ (c), on a surface having an anisotropic diffusivity characterized by $A=10$, $m=1$, $\phi=135^\circ$. a) and b) shows the GB groove profile; d) kinetic data for groove depth, maxima and width; d) TJ velocity and the dihedral angles for $\chi=0.5$. c) shows the effect of increased electron wind intensity, $\chi=5.0$: a narrow slit, licking up the wind side of the grain boundary evolves and accelerates open circuit failure..... 145

Figure 4.5.1.3 Electromigration groove with $\chi=0.5$ (except parts c, and d), $\chi=1.0$ (c), and $\chi=5.0$ (d), on a surface having an anisotropic diffusivity characterized by $A=10$, $m=1$, $\phi=180^\circ$. a) and b) shows the GB groove profile; e) kinetic data for groove depth, maxima and width; f) TJ velocity and the dihedral angles for $\chi=0.5$. c) and d) shows the effect of increased electron wind intensity, respectively for $\chi=1.0$, and $\chi=5.0$: lateral extension of the blunted region and formation of a channel like groove..... 146

Figure 4.5.1.4 Electromigration groove with $\chi=1.0$ (except part c) and $\chi=5.0$ (c), on a surface having an anisotropic diffusivity characterized by $A=10$, $m=1$, $\phi=135^\circ$. a) and b) shows the GB groove profile; d) kinetic data for groove depth, maxima and width; d) TJ velocity and the dihedral angles for $\chi=1.0$. c) shows the profile evolution for increased electron wind

intensity, $\chi=5.0$: instability in the wind side, secondary oscillations continuously grow out.....	148
Figure 4.5.2.1 Electromigration groove with $\chi=1.0$, on a surface having an anisotropic diffusivity characterized by $A=10$, $m=2$, $\phi=90^\circ$. a) and b) shows the GB profile; c) kinetic data for groove depth, maxima and width; d) TJ velocity and the dihedral angles. Early slit formation at the wind side of the groove root which drags the triple junction and leads open circuitry	150
Figure 4.5.2.2 Electromigration groove with $\chi=10.0$ (except part b) and $\chi=1.0$ (b), on a surface having an anisotropic diffusivity characterized by $A=10$, $m=2$, $\phi=45^\circ$. a) and c) shows the GB groove profile; d) kinetic data for groove depth, maxima and width; d) TJ velocity and the dihedral angles for $\chi=10.0$. b) shows the profile evolution for at a modest EWI, $\chi=1.0$	152
Figure 4.5.3.1 Electromigration grooves with $\chi=1.0$, on a surface having an anisotropic diffusivity characterized by $A=10$, $m=3$, $\phi=30^\circ$ (first column: a to c) and $\phi=60^\circ$ (second column: d to f). a) and d) shows the GB groove profiles; b) and e) kinetic data for groove depth, maxima and width; c) and f) TJ velocity and the dihedral angles. Formation of faceted grain boundary voids of opposite facet orientations	154
Figure 4.6.1.1 Isotropic grain boundary grooving for $\lambda=0.5$, $M_L=M_T=0.25$ and $\Xi=0.1$ which corresponds to 13.25 MPa ($\approx 10^{-4}E$; where E is the elastic modulus) for copper thin film with a length scale $\ell_o=0.1\mu\text{m}$. a) 3D representation of the groove evolution, b) successive 2D profiles;	

curvature and hoop stress distributions corresponding to $t_f=1.1$ (black profile), c) kinetic data for groove depth, maxima, TJ velocity, d) comparison of the stress free and groove under tension profiles given by Genin et al. (1993) with the simulated profile at $t=1.0$; curvature and hoop stress distributions at $t=1.0$, e) kinetic data for groove width and TJ stress, f) energy changes and the kinetic data for the dihedral angle in semi-log scale..... 157

Figure 4.6.1.2 Isotropic grain boundary grooving for $\Xi=1.0$ and $\Xi=5.0$ which correspond to 132.5 and 662.7 MPa for copper thin film with a length scale $\ell_0=0.1\mu\text{m}$. Final time to failure falls $t_n=0.13$ for $\Xi=1.0$ and to $t_n=0.039$ for $\Xi=5.0$ in normalized scale 162

Figure 4.6.1.3 Isotropic grain boundary grooving for $\lambda=0.5$, $M_L=M_T=0.25$ and $\Xi=8.0$ which corresponds to 1.06 GPa for a copper thin film with a length scale $\ell_0=0.1\mu\text{m}$. a) 3D representation of the groove evolution, b) formation and propagation of wedge like groove; curvature and hoop stress distributions corresponding to $t=0.030$ (black profile), c) kinetic data for groove depth, maxima, TJ velocity and the dihedral angle, d) diffusive micro crack formation at the groove root at $t=0.032$ (red profile), e) kinetic data for groove width and TJ stress, f) energy changes in semi-log scale..... 163

Figure 4.6.1.4 a) Groove depth vs. time plot for various EDTI parameters, b) the same plot in zoomed scale; power law region and power law breakdown regions are highlighted. Note that for $\Xi=10.0$ failure takes place before reaching %95 of film thickness by micro crack formation 164

Figure 4.6.1.5 The power law region is expressed as $h(t)=a \times t^b$; in part a) the dependence of coefficient ‘a’, and in b) that of time exponent ‘b’ to EDTI is given. The region where the power law breaks down is modeled by a linear function $h(t)=m \times t+c$; in part c) dependence of the slope ‘m’, and in d) that of intercept ‘c’ to EDTI is given. The resulting functions are labeled as $h^I(\Xi,t)$ and $h^{II}(\Xi,t)$, where superscripts denote the power law and power law break down regions respectively 165

Figure 4.6.1.6 Experimentally obtained groove depth data for $\Xi=0.2$ and 5.0 is presented (open circles) together with the equations 4.6.1.5 and 4.6.1.6 (solid lines)..... 167

Figure 4.6.1.7 In a) the functions used to model the increase in tip stress due to cavity interactions by Pharr and Nix (1979) and the measured tip stresses for different values of EDTI in the present work is compared; and in b) the time evolution of the tip stresses in the present study is given 168

Figure 4.6.1.8 Failure time as a function of EDTI for $\lambda=0.5$, $M_L=M_T=0.25$ 172

Figure 4.6.1.9 Dependence of the rupture time stress exponent on the wetting parameter..... 173

Figure 4.6.2.1 Isotropic grain boundary grooving for $\lambda=0.5$, $M_L=M_T=0.25$ and $\Xi=-0.1$. a) 3D representation of the groove evolution, b) successive 2D profiles; curvature and hoop stress distributions corresponding to $t=3.11$ (black profile), c) kinetic data for groove depth (‘d’), maxima and TJ velocity, d) comparison of the stress free and groove under tension profiles given by Genin et al. (1993) at $t=1.0$; curvature and hoop stress

distributions at $t=1.0$, e) kinetic data for groove depth ('h'), width and TJ stress, f) energy changes and the kinetic data for the dihedral angle in semi-log scale.....	175
Figure 4.6.2.2 Experimentally observed hillocks in a thin aluminum film by Ericson et al. (1991). a) over view showing typical hillock appearances, b) schematic top view of a hillock centered over the grain boundary triple junction, and examples of cross-sectional views, c) and d) TEM cross-sections of different hillocks (compiled from figures 2, 5, 7, 9 of Ericson et al., 1991).....	177
Figure 4.6.2.3 Isotropic grain boundary grooving for $\lambda=0.5$, $M_L=M_T=0.25$ and $\Xi=-1.0$. a) successive 2D profiles; curvature and hoop stress distributions corresponding to $t=0.39$ (black profile), b) kinetic data for groove depth ('d'), maxima and TJ velocity, c) kinetic data for groove width, depth ('h') and TJ stress, d) energy changes and the kinetic data for the dihedral angle in semi-log scale	178
Figure 4.6.2.4 Isotropic grain boundary grooving for $\lambda=0.5$, $M_L=M_T=0.25$ and $\Xi=-3.0$. a) successive 2D profiles; curvature and hoop stress distributions corresponding to $t=0.062$ (black profile), b) kinetic data for groove depth ('d'), maxima and TJ velocity, c) kinetic data for groove width, depth ('h') and TJ stress, d) energy changes and the kinetic data for the dihedral angle in semi-log scale	180
Figure 4.6.2.5 Evolution of the normalized groove tip stress as a function of normalized time for different levels of applied stress in log-log scale	181

Figure 4.6.2.6 The kinetic data for a) groove depth ‘h’, b) groove maxima ‘h_{max}’, and c) groove depth ‘d’ (which is obtained by summing the previous two) for different levels of applied stress:

$\Xi = [0.1, 0.3, 1.0, 2.0, 3.0]$ 182

Figure 4.6.2.7 Analysis of the crossover depth ‘h_c’ and corresponding time data..... 183

LIST OF SYMBOLS AND ABBREVIATIONS

LATIN LETTERS

- A : area
- A_k^j : affinity of the j^{th} chemical reaction taking place in $_k$ phase
- AFM : atomic force microscopy
- BEM : boundary element method
- c : atomic volumetric concentration
- C : similarity constant
- d : groove depth measured from the maxima
- d_a : inter-atomic distance
- \tilde{D}_σ : self diffusivity
- D_σ^0 : minimum surface diffusivity corresponding to a specific surface orientation
- e : unit electronic charge
- E : elastic modulus
- E_∞ : remote applied electric field
- EDTI : elastic dipole tensor interaction
- EM : electromigration
- ESED : elastic strain energy density
- EWI : electron wind intensity

F	: Helmholtz free energy
f	: specific Helmholtz free energy
F_i	: generalized force
FEM	: finite element method
g	: specific Gibbs free energy density
\tilde{g}	: volumetric Gibbs free energy density
g_{vb}	: specific Gibbs free energy of formation
\tilde{g}_{vb}	: volumetric density of Gibbs free energy of formation
GFEDoT	: volumetric density of Gibbs free energy of formation
G^*	: activation energy
GB	: grain boundary
GIEP	: global internal entropy production
h	: groove depth measured from the initial flat surface
h_c	: crossover depth
h_k	: thickness of interfacial layer k
h_{\max}	: maxima depth measured from the initial flat surface
h_s	: limiting groove depth
\hat{I}	: idempotent
IBEM	: indirect boundary element method
IEP	: internal entropy production
J_i	: generalized conjugated flux
k	: Boltzmann constant

ℓ	: curvilinear coordinate along the void surface (arc length)
ℓ_o	: arbitrary scaling length
L	: half film length
LISA	: linear stability analysis
m	: dimensionless parameter that determine the grain symmetry through the number of crystallographic directions corresponding to fast diffusion paths (half fold number)
m	: slope of the tangent line passing through the groove root (or through the surface in general)
n	: number of chemical species
\hat{n}	: surface normal vector
N	: fold number or rotational degree of symmetry
NSTS	: normalized and scaled time and space
\bar{P}	: mean isotropic pressure in the layer
PDE	: partial differential equation
q	: heat received by the system
q^*	: surface effective charge
Q	: deviatoric part of the stress tensor
\vec{r}	: position vector
REF	: rate of entropy flow
S	: entropy
t	: time
t_f	: failure time

t_c	: crossover time
\hat{t}	: surface tangent
T	: temperature
\vec{T}	: traction vector
T_R	: roughening temperature
Tr	: trace operator
TJ	: triple junction
U	: internal energy
u	: displacement normal to the surface
ULSI	: ultra large scale integration
x_i	: atomic fractions
V	: volume
v	: velocity
w	: groove width
W	: film half width
WP	: wetting parameter
Z	: effective electromigration charge

GREEK LETTERS

γ	: surface tension
$\tilde{\gamma}$: surface stiffness
δ	: variational operator
$\delta area$: fractional change in the area
ε	: strain
η	: infinitesimal longitudinal displacement along the grain boundary
θ	: angle formed by the local surface tangent and the abscissa; complementary dihedral angle (at the groove root)
α	: groove depth cofactor
κ	: curvature
λ	: wetting parameter
λ_s	: elastic strain field
μ	: chemical potential
ν	: Poisson's ratio
ρ	: resistivity
ρ	: radius of curvature
σ	: stress
τ_o	: scaling time
ϕ	: the misorientation of the symmetry direction; tilt angle
χ	: electron wind intensity
ω	: reversible work done on the system
A	: surface diffusion anisotropy strength

Γ	: specific mean atomic density
Δ	: space-scaling operator
M	: generalized phenomenological mobility
Ξ	: elastic dipole tensor interaction
P	: power dissipation
Σ	: elastic strain energy density
Φ	: energy received by the system
Ω	: amount of energy transported to the individual phase from the other phases through mass transfer
$\bar{\Omega}$: mean atomic specific volumes

SYMBOLS

$d\xi_{\sigma}^j$: extent of the j^{th} chemical reaction taking place in σ phase
\mathfrak{R}	: phenomenological mobility coefficient
ϑ	: electrostatic potential
φ	: dihedral angle
∇	: del operator
∇^2	: Laplace operator

SUBSCRIPTS

b	: bulk
em	: electromigration
ex	: external
in	: internal
g, gb	: grain boundary
h	: hoop
k	: dummy phase index
L	: longitudinal
ord	: ordinary point
T	: transverse
s	: surroundings
$thrs$: threshold
v	: void
α	: bulk phase
σ	: interfacial layer

SUPERSCRIPTS

- : left hand side of the system
- + : right hand side of the system
- i : dummy index to denote a chemical species
- j : dummy index to denote a chemical reaction
- long* : longitudinal
- trans* : transverse

SIGNS OVER SYMBOLS

- \sim : denotes volumetric quantities
- \wedge : denotes surface densities
- $\hat{}$: denotes normal vectors
- $\vec{}$: denotes vector quantities
- $\bar{}$: denotes normalized quantities

SIGNS UNDER SYMBOLS

- $\underline{}$: denote vectors
- $\underline{\underline{}}$: denote tensors

CHAPTER 1

LITERATURE SURVEY

1.1. Introduction

Polycrystalline materials are composed of tiny perfect crystalline regions (grains) in between internal interfaces called grain boundaries. Grain boundaries and the external free surfaces (which separate the material from the environment) determine the morphology of the material at a major extent.

A material may change its morphology through interface motion if a driving force exists. An important special case, which is the focus of this dissertation, is the grain boundary grooving. Wherever a grain boundary intersects a free surface and whenever the topographic variation associated with the atomic motion is favored by total free energy dissipation, the surface grooves. Grooving can occur via several mass transport mechanisms, such as surface diffusion, bulk diffusion, and evaporation and condensation. Surface diffusion dominates for temperatures far below the melting temperature, and for grooves less than 10 micron in size (Mullins & Shewmon, 1959). If the surface evolution is driven solely by the total excess free energies associated with the interfaces the resulting force for motion is

conventionally called a capillary force, and the new formation is termed as a *thermal groove*. In addition to a capillary force, a force for interface motion is produced whenever motion of the interface allows an applied force to perform work: such a force is an applied force (Balluffi et al., 2005).

This dissertation focuses on grain boundary grooving by anisotropic surface diffusion. Applied electrostatic and elastostatic fields are allowed to perform work on the surfaces of crystals separated by a stationary grain boundary which grooves in the direction normal to the initial flat surface. An irreversible thermo-kinetics formalism which results well posed moving boundary value problem describing the dynamics of curved surfaces and interfaces under external force fields is employed. Then coupled problems of two dimensional linear elasticity and electrostatic potential distribution for each surface configuration are solved by indirect boundary element method. The resulted nonlinear partial differential equation (PDE) for surface drift diffusion is solved numerically by Euler's method of finite differences.

The phenomenon constitutes a problematic basis for silicon based devices. An integrated circuit (IC) contains various interconnected semiconductor components, such as transistors, resistors, capacitors and diodes. Thin films of copper or aluminum/copper alloys (part of the metallization on a device) make electrical contact between these devices on a chip and commonly called as *interconnects*. These lines are exposed to current densities increasing from 10^6 A/m² to 10^{10} A/m², operate at temperatures about one third of their melting point ($T_m=933$ K for Al) and subjected to stresses about 200-800 MPa during production and service

(Ohring, 1971; Jones & Basehore, 1987; Greenebaum et al., 1991; Korhonen et al., 1991). Under these extreme conditions grain boundary grooves may lead to two well known failure mechanism during their evolutionary adventure: 1) film agglomeration (a groove penetrates and finally reaches the substrate); 2) short circuiting (abnormal growth of hillocks on the groove shoulders). Therefore a fundamental understanding of the thermodynamics and evolution kinetics of interconnects is the key to the fabrication and reliable operation of the microelectronic devices.

The literature on morphological evolution of anisotropic surfaces and interfaces mainly rely on classical thermodynamics. The idea is to minimize the free energy of the system by suitable mechanism of mass transport. Considering systems at equilibrium a driving force is determined from the total free energy variation, and a linear kinetic law is used to relate the driving force to the flux. Using this flux, surface shape is updated according to mass conservation. In this chapter a detailed review of these models are given; and the shortcomings due to the assumption of equilibrium is highlighted.

On the other hand the theoretical backbone of this dissertation is the irreversible thermo–kinetics theory of interfaces covering triple junction singularities developed by Ogurtani (2000). In chapter 2, following the fundamental postulate irreversible thermodynamics, conjugate forces and fluxes that derive the shape evolutions through continuity will be derived.

1.2. Kinetics of morphological changes by surface diffusion

It is useful to outline the surface diffusion driven motion of an arbitrary surface before proceeding further into the detailed literature review. The atomic flux (vector field; the bar signs over symbols are to denote vector quantities) on such a solid surface given in figure 1.2.1 may be defined at a per length basis by:

$$\vec{J}_\sigma = \frac{\text{\# of atoms}}{(\text{length})(\text{time})} \quad (\# \text{ m}^{-1} \text{ s}^{-1}) \quad (1.2.1)$$

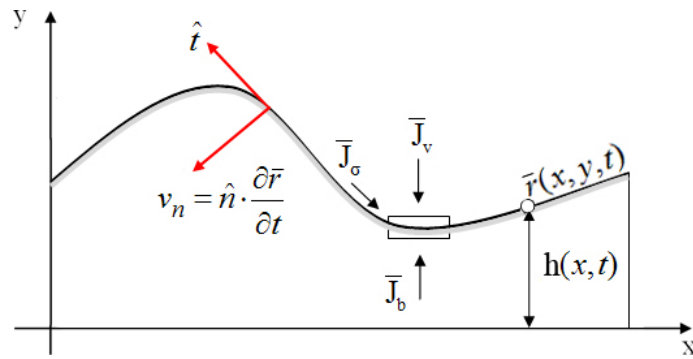


Figure 1.2.1: An arbitrary surface in the x - y plane. \hat{t} is the unit tangent and \hat{n} is the unit normal vector, the subscripts σ , b , v on the fluxes denote the surface, bulk, and void phases respectively. When evaporation condensation mechanism is active, \bar{J}_b and \bar{J}_v entering (leaving) the surface element should also be considered. At a given time any point on the surface may be represented by position vector $\bar{r}(x, y)$.

When a surface element gains atoms, it moves with a velocity v_n (scalar field) in the direction normal to the surface. Defining Ω as the volume per atom in the solid the ratio $\frac{v_n}{\Omega}$ gives the atoms gained per unit area per unit time. This quantity is related to the flux divergence through conservation of mass:

$$\frac{v_n}{\Omega} + \nabla \cdot \vec{J}_\sigma = 0 \quad (\text{the continuity equation}) \quad (\# \text{ m}^{-2} \text{ s}^{-1}) \quad (1.2.2a)$$

$$v_n = -\Omega \nabla \cdot \vec{J}_\sigma \quad (\text{m s}^{-1}) \quad (1.2.2b)$$

Once the diffusion flux is obtained surface can be evolved using the velocity calculated by this equation. The atomic flux on the surface can be related to the driving force for diffusion through atomic mobility M by using a linear kinetic law (Sun & Suo, 1997):

$$\vec{J}_\sigma = M\vec{F} \quad (\# \text{ m}^{-1} \text{ s}^{-1}) \quad (1.2.3)$$

This connection is a typical consequence of linear irreversible thermodynamics as shown in the next chapter and as underlined by Sun and Suo (1997) is incidentally adopted by Herring (1951) and Mullins (1957).

The literature of diffusion controlled surface morphological changes is fulfilled by the following concept: the driving force in Eq. (1.2.3) may be interpreted as a

gradient energy which is everywhere continuous even at the singularities; otherwise the flux might go to infinity. The assumed surface diffusion potential is a scalar field that reflects a change in energy that results from the motion of species; therefore, it includes energy-storage mechanisms and any constraints on motion (Ballufi et al., 2005). Therefore all efforts start with a definition of the term *surface chemical potential*, μ_σ , whose gradients drive the overall processes. On the other hand if one follows the irreversible thermodynamics formalism, the *conjugate forces and fluxes* given in Eq. (1.2.3) may be obtained from the Helmholtz or power dissipation function. Helmholtz function for an isothermal system is the internal entropy production multiplied by the temperature; the topic will be discussed into detail in chapter 2. However by definition, the diffusion fluxes of individual chemical species in entropy production term can't transfer into an operationally definable reference system, such as a solid lattice even for isotropic solids under the mechanical equilibrium condition (de Groot, 1951; Haase, 1969). This argument strictly makes use of the chemical potentials thermodynamically meaningless. The present thesis follows the irreversible formalism developed originally by Ogurtani (2000) for interfaces having singularities in contrast to which may be called Herring formalism that is going to be detailed in this chapter.

Following Herring school, the driving force in Eq. (1.2.3) is a vector on the interface that is derived from gradient of a scalar field which has units of energy per atom. If atoms diffuse from an interfacial element with high potential to another with low potential, then the driving force is the negative gradient of the surface diffusion potential μ_σ :

$$\vec{F} = -\nabla\mu_{\sigma} \quad (\text{N \#}^{-1}) \quad (1.2.4)$$

Substituting Eqs. (1.2.4→3→2) and assuming a position independent atomic mobility one can relate the normal velocity of the free surface to the Laplacian of the surface diffusion potential:

$$v_n = \Omega M \nabla^2 \mu_{\sigma} \quad (\text{m s}^{-1}) \quad (1.2.5)$$

Another common representation of Eq. (1.2.5) may be obtained by the following form of the Nernst – Einstein equation which ties the mobility and surface self diffusivity, D_{σ} :

$$M = \frac{h_{\sigma} D_{\sigma}}{\Omega kT} \quad (1.2.6)$$

Here h_{σ} is the thickness of the surface layer, k is the Boltzmann constant and T is the absolute temperature. Substitution Eq. (1.2.6→5) yields:

$$v_n = \frac{D_{\sigma} h_{\sigma}}{kT} \nabla^2 \mu_{\sigma} \quad (\text{m s}^{-1}) \quad (1.2.7)$$

1.3. Energetics of morphological changes by surface diffusion

If there is no exchange of energy between the solid and its surroundings then the change in free energy for a given change in shape represents the driving force for that shape change (Eq. 1.2.4). So, the next step is to obtain a proper definition for the total free energy that could be used in connection with Eq. (1.2.7). The very first study in this field came from Herring in 1951 which strictly rely on the equilibrium thermodynamics and the Gibbs description of interfaces and surfaces (Gibbs, 1948; Defay et al., 1966). He extends the classical Gibbs-Thomson equation for an orientation dependent surface tension γ_s , as in a crystal.

1.3.1. Herring's equation of curvature dependent chemical potential

The Gibbs-Thomson equation reflects typical consequence of the dependence of equilibrium vapor pressure of a liquid drop on its radius of curvature; i.e. it relates the curvature of a surface to the chemical potential of the surface atoms when surface tension γ_s , is independent of orientation. Herring's theory, in a similar way, assumes that the free energy of the system is the surface energy summed over all surfaces and grain boundaries, and the amount of free energy decrease is associated with per unit volume of matter moving per unit distance on the surface and as a result describes a driving force at every point on the solid surface.

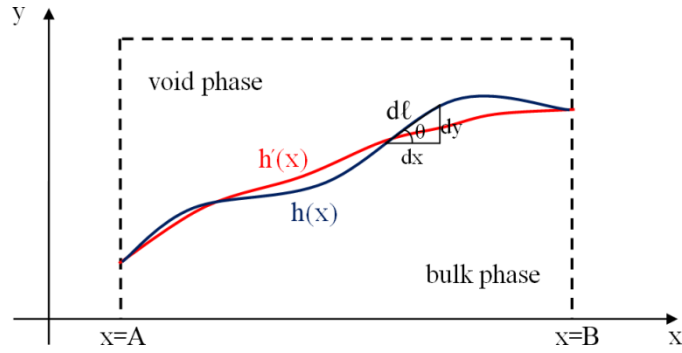


Figure 1.3.1.1: The curve $h(x)$ between $x=A$ and B represents a portion of the cross section of a surface between bulk and void phases. $h'(x)$ is the surface perturbed by an infinitesimal amount $\delta h(x)$.

Mullins (1963) gives a derivation of Herring's equation using calculus of variations in two dimensions by considering a monocomponent system, under no applied pressure. In such a system surface tension γ_s , is equal to the specific surface free energy, f_σ . Then the value of the surface free energy, F associated with the curve in figure 1.3.1.1 from A to B , per unit depth, is given by:

$$F_\sigma = \int_A^B \gamma_s d\ell = \int_A^B \gamma_s (h_x) \sqrt{1+h_x^2} dx = \int_A^B G(h_x) dx \quad (1.3.1.1)$$

Here h_x represents differentiation with respect to x ; simply it is the slope of the curve at any point and used as an argument for γ , since it determines the orientation of the surface element. Then if an infinitesimal rearrangement of material forms the new surface: $h'(x)=h(x)+\delta h(x)$. The corresponding variation in F_σ is obtained by calculus of variations as:

$$\delta F_\sigma = \int_A^B \frac{dG}{dh_x} \delta h_x dx = \int_A^B \frac{dG}{dh_x} \frac{d(\delta h)}{dx} dx = - \int_A^B \frac{d}{dx} \left(\frac{dG}{dh_x} \right) \delta h dx \quad (1.3.1.2)$$

Here for simplicity $\delta h(A) = \delta h(B) = 0$ and $\int_A^B \delta h(x) dx = 0$. Assuming the chemical potential $\mu'_\sigma = \mu_\sigma + \mu_0$ to be uniquely determined at all elements of the surface apart from the constant μ_0 , δF must also be given by the following expression:

$$\delta F_\sigma = \frac{1}{\Omega} \int_A^B (\mu_\sigma + \mu_0) \delta h dx = \frac{1}{\Omega} \int_A^B \mu_\sigma \delta h dx \quad (1.3.1.3)$$

Here, μ_0 is defined as the chemical potential at standard state which can arbitrarily be assigned to the value zero in the reservoir, Ω is the atomic volume and $\delta h dx / \Omega$ gives the number of atoms added to the interval dx . Subtracting Eq. (1.3.1.2→3):

$$0 = \int_A^B \left\{ \frac{d}{dx} \left(\frac{dG}{dh_x} \right) + \frac{\mu_\sigma}{\Omega} \right\} \delta h dx \quad (1.3.1.4)$$

Since δh is arbitrary:

$$\mu_\sigma = -\Omega \frac{d}{dx} \left(\frac{dG}{dh_x} \right) = -\Omega \frac{d}{dx} \left(\frac{d}{dh_x} \left(\gamma_s(h_x) \sqrt{1+h_x^2} \right) \right) \quad (1.3.1.5)$$

Using following equalities in performing differentiations:

$$\theta = \arctan(h_x), \quad \frac{d\gamma_s}{dh_x} = \frac{1}{1+h_x^2} \frac{d\gamma_s}{d\theta}, \quad \frac{d}{dx} = h_{xx} \frac{d}{dh_x}$$

Eq. (1.3.1.5) yields:

$$\mu_\sigma = -\Omega \left(\gamma_s + \frac{d^2\gamma_s}{d\theta^2} \right) \frac{h_{xx}}{(1+h_x^2)^{3/2}} = \Omega \left(\gamma_s + \frac{d^2\gamma_s}{d\theta^2} \right) \kappa \quad (1.3.1.6)$$

Here, $\kappa = -h_{xx} (1+h_x^2)^{-3/2}$ is the curvature at a point on the surface and taken to be positive when the surface is concave towards the bulk. For isotropic γ , as in liquids, Eq. (1.3.1.6) directly reduces to Gibbs-Thomson equation. Substituting Eq. (1.3.1.6) into (1.2.7), one may specify a governing differential equation for capillarity induced evolution of surfaces and interfaces.

1.3.2. Chemical potential for stressed solid surfaces

In the development of the chemical potential for stress assisted morphological changes the following underlying assumptions, which are well summarized by Freund (1998) are considered: a) the time required for a perturbed system to reach mechanical equilibrium is typically very small compared to times characteristic of mass rearrangement mechanisms so the mechanical fields are assumed to be in equilibrium at all times b) no externally applied traction acts on the evolving part of

the interface c) all mass rearrangement is coherent; a well defined stress free reference state always exists d) the thermodynamic system is considered as an isochoric isothermal system and there is no exchange of energy between the system and its surroundings.

Asaro & Tiller (1972) made a first serious attempt to develop an equilibrium thermodynamic model of interfacial morphological evolutions by adding the elastic strain energy density directly to the chemical potential defined on a surface. They have discovered that a flat surface of a solid under an elastic strain is unstable and can undulate by surface diffusion; the instability may cause the surface to nucleate cracks (stress corrosion cracking). In later studies Grinfeld (1986) and Srolovitz (1989) have performed the very same linear stability analysis to show that there is a critical wave length of given perturbation over which a given surface is unstable against undulations. For honoring the authors this phenomenon is usually named as ATGS instability.

The adopted chemical potential by these authors account for strain energy density w given to an isotropic surface layer with the infinitesimal addition of matter, to make it fit coherently:

$$\mu_{\sigma} = \mu_0 + \Omega(w + \gamma_s \kappa) \quad (1.3.2.1a)$$

Here, μ_0 is defined as the chemical potential at standard state which is also defined by Herring as flat surface under zero pressure. In this equation the sign convention

for curvature is due to Herring and taken to be positive when the surface is concave towards the bulk (crest on surface) as in Eq. (1.3.1.6), yet the selection is arbitrary and many authors accept vice versa; a positive curvature for a convex void (trough on surface):

$$\mu_{\circ} = \mu_0 + \Omega(w - \gamma_s \kappa) \quad (1.3.2.1b)$$

Both equations are equivalent as long as sign convention is defined properly; the present work adopts the final convention in deriving related equations in the next chapter likewise Rice and Chuang (1981), Suo et al. (1994), Gungor et al. (1998) and in their many publications.

In an earlier work, Herring (1950) gives the chemical potential along a flat grain boundary μ_{gb} due to a tensile stress acting normal to it as:

$$\mu_{\text{gb}} = \mu_0 - \Omega \sigma \quad (1.3.2.2a)$$

This is justified as follows; the traction felt by the grain boundary is displaced with the addition of an atom as the grain expands by volume Ω ; the displacement contributes to work and reduces the potential energy of the system by a corresponding amount. Later Rice and Chuang (1981) modify Eq. (1.3.2.2) by adding strain energy density term:

$$\mu_{\text{gb}} = \mu_0 + \Omega(w - \sigma) \quad (1.3.2.2b)$$

This addition however makes little sense since the stresses are generally much less than the elastic modulus ($\sigma^2/E \ll \sigma$) and can be neglected when accompanies a stress term. This simple fact was anticipated by Srolovitz (1989) and even by the authors themselves.

More complete models that account anisotropy and the coupling between surface tension and normal surface stress has been developed in studies by Grilhe (1993), and Wu (1996) and Freund (1998). Nevertheless Eqs. (1.3.2.1, 2) are the most commonly accepted chemical potentials and basis of the results reported on diffusive evolutions of stressed solid films or islands. Using the linear kinetic law given in Eq. (1.2.3); Eqs. (1.3.2.1a, 2a)→(1.2.4)→(1.2.3) substitution gives the surface and grain boundary flux of diffusing atoms on a stressed solid:

$$\bar{J}_{\sigma} = -\frac{Dh_{\sigma}}{kT} \left(\frac{1-\nu^2}{2E} \nabla \sigma_h^2 + \gamma_s \nabla \kappa \right) \quad (\# \text{ m}^{-1} \text{ s}^{-1}) \quad (1.3.2.3a)$$

$$\bar{J}_{\text{gb}} = \frac{Dh_{\sigma}}{kT} \nabla \sigma_h \quad (\# \text{ m}^{-1} \text{ s}^{-1}) \quad (1.3.2.3b)$$

Here linear elasticity and plain strain conditions are assumed, σ_h is the tangential stress component along the surface and/or interface layer (hoop stress), ν is the Poisson's ratio, and E is the elastic modulus.

1.3.3. Defining a thermodynamic system: Isobaric and isochoric systems

The role played by the elastic strain energy density and energy momentum tensor on the instability of surface and interface undulations and the growth of epitaxial thin films on substrates with or without the presence of external forces has recently been investigated by Ogurtani (2010). The author states that the role played by the elastic strain energy density in isolated systems that are bounded by the fixed rigid walls and/or the traction free surfaces in the absence of the external body forces (isochoric; internally strained) might be positive (like the case given in Eqs. 1.3.2.1) and the elastic strain energy density becomes a main source for the instability and surface roughness. It follows that, in the presence of applied force fields (isobaric systems), its role changes and it becomes a source for stability similar to the capillary forces for both tensile and compressive stresses. However, there exists confusion in the literature due to ill defined thermodynamic systems and due to referring to Herring's work (1950) for both cases in which the interface displacement process has been treated as an isothermal reversible process by minimizing the total Helmholtz free energy function. As shown by Ogurtani and Oren (2005) this results in an apparent sign conflict between isobaric and isochoric systems.

1.3.4. Theory of electromigration

Electromigration (EM) is the transport of material in a conductor under the influence of an applied electrical potential gradient. It is generally considered to be

the result of momentum transfer from the electrons to the ions which make up the lattice of the interconnect material (Arzt & Nix, 1991).

When electrons are conducted through a metal, they interact with imperfections in the lattice and scatter. Scattering occurs whenever an atom is out of place for any reason. Thermal energy produces scattering by causing atoms to vibrate. This is the source of resistance of metals; the higher the temperature, the more out of place the atom is, the greater the scattering and the greater the resistivity. An applied electrical potential gradient can induce diffusion (electromigration) in metals due to a cross effect between the diffusing species and the flux of conduction electrons that will be present (Ballufi et al., 2005). For EM one needs a lot of electrons, and also one needs electron scattering. EM does not occur in semiconductors, but may in some semiconductor materials if they are so heavily doped that they exhibit metallic conduction.

The force acting on diffusing atoms in a conductor originates from the sum of two contributions: 1) the direct electrostatic force tending to drive ions toward the cathode, and 2) the 'friction force' caused by the momentum exchange between ions and scattered electrons (electromigration) tending to drive ions ionic motion in the opposite direction. The latter, i.e. the electron wind force usually dominates so that atomic drift is towards the anode. Accordingly, to describe the EM process an electrostatic analogue may be used. The driving force for electromigration expressed in this way is:

$$\vec{F} = Z^* e \vec{E} = Z^* e \rho \vec{j} \quad (1.3.4.1)$$

Here, Z^* is the effective valance or effective charge, e is the unit electrostatic charge, E is the electrostatic field, ρ is the resistivity and j is the current density. The value of Z^* has been expressed by Huntington & Grone (1961) by using a semi classical ballistic model as:

$$Z^* = \frac{1}{2} \left(\frac{\rho_d N}{\rho N_d} \right) \frac{m^*}{|m^*|} \quad (1.3.4.2)$$

Here N is the density of conducting electrons, ρ_d is the specific defect resistivity, N_d the defect density, ρ is the metal resistivity, and m^* is the effective mass of the electrons near the Fermi surface taking part in the momentum exchange. The effective charge Z^* characterizes the momentum transfer and can be inferred from experimental data.

Above consideration gives the generally excepted description of electromigration physics in failure modeling of IC conductors and successful in explaining many observed features, yet the existence of direct force is has been a highly controversial issue (Hoekstra et al., 2002) and is of an academic interest. In an alternative derivation of the driving force for electromigration, Lodder (1991) discussed the role of electron – phonon interactions to hinder the electrons in screening the force on the bare ion. He claims that the electron – phonon interactions could dominate

for dilute interstitial alloys at the elevated temperatures where electromigration experiments are commonly done. The reader is referred to Hoekstra et al. (2002) for a nice discussion on the essence of electron – phonon interactions.

In general, one can separate electromigration-driven diffusion into three: surface electromigration, bulk electromigration and grain boundary electromigration. The schematic picture of these diffusion paths can be seen in figure 1.3.4.1.

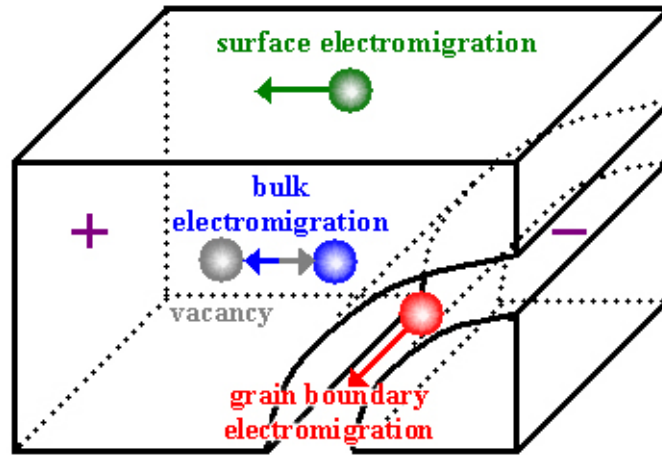


Figure 1.3.4.1: The diffusion paths of electromigration (Oren, 2003).

The surface diffusion is the fastest one and in generally grain boundary diffusion is more rapid than interfacial or bulk diffusion. According to Lloyd (1997), the activation energies, E_a , for the pathways are in general,

$$E_a^{surface} = \frac{3}{2} E_a^{grain\ boundary} = 3E_a^{bulk} \quad (1.3.4.3)$$

Using the linear kinetic law given in Eq. (1.2.3); Eq. (1.3.4.1)→(1.2.3) substitution in connection with Eq. (1.3.1.6) gives the surface flux of atoms due to electron wind force and capillary force:

$$\vec{J}_\sigma = -\frac{Dh_\sigma}{\Omega kT} (eZ^* \vec{E} + \Omega \gamma_s \nabla \kappa) \quad (\# \text{ m}^{-1} \text{ s}^{-1}) \quad (1.3.4.4a)$$

Here the sign convention for curvature is due to Herring and taken to be positive when the surface is concave towards the bulk as is used in Eq. (1.3.1.6) and $\vec{E} = -\nabla \mathcal{G}$ is the electric field vector, where \mathcal{G} is the electrostatic potential. Similarly the grain boundary flux of atoms due to electron wind force along a flat grain boundary ($\kappa = 0$) is:

$$\vec{J}_{gb} = -\frac{Dh_\sigma}{\Omega kT} (eZ^* \vec{E}) \quad (\# \text{ m}^{-1} \text{ s}^{-1}) \quad (1.3.4.4b)$$

1.4. Mullins' theory of thermal grooving

Thermal grooving at grain boundaries is a process of capillary – driven evolution of surface topography in the region where a grain boundary emerges to intersect a free surface of a polycrystalline material. Mullins (1957) derived a general PDE for the rate of change of the profile of a surface for profile changes occurring by surface diffusion mechanism under the following assumptions:

- (1) The system is closed and contains a metal poly-crystal in quasi-equilibrium with its vapor.
- (2) Interface properties are independent of crystallographic orientation.
- (3) All matter transport occurs by surface self diffusion.
- (4) Macroscopic concepts such as surface free energy and curvature are valid.
- (5) There is negligible flow of matter out of the grain boundary; instead, the role of the boundary is to maintain the correct equilibrium angle.
- (6) Absolute value of the profile slope is everywhere small compared to unity; the small slope assumption (SSA).

Under these assumptions he follows the very same procedure described above (Eq. 1.3.1.6→1.2.7) and obtains following equation:

$$v_n = \frac{D_\sigma \gamma_s \Omega^2 v}{kT} \nabla^2 \kappa \quad (\text{m s}^{-1}) \quad (1.4.1)$$

Here, Mullins adopted $v = \frac{h_\sigma}{\Omega}$ as the number of per unit area, instead of using h_σ itself. Owing to isotropy he collects all physical constants into one ($B = D_\sigma \gamma_s \Omega^2 v / kT$) and rewrites Eq. (1.4.1) explicitly in terms of $h(x,t)$:

$$\frac{\partial h}{\partial t} = -B \frac{\partial}{\partial x} \left((1 + h_x^2)^{-1/2} \frac{\partial}{\partial x} \left(h_{xx} (1 + h_x^2)^{-3/2} \right) \right) \quad (1.4.2)$$

This nonlinear PDE is in fourth order in space and hard to solve analytically. Mullins linearized this equation referring to the assumption (6) given above: slope of the surface is everywhere small compared to unity ($h_x \ll 1$; corresponds to a dihedral angle close to 180°):

$$\frac{\partial h}{\partial t} = -Bh_{xxxx} \quad (1.4.3)$$

He considers a symmetrically disposed stationary grain boundary at $x=0$ that is perpendicular to the free surface as in figure 1.4.1. Then he formulates the following initial and boundary conditions:

$$h(x, 0) = 0 \quad (1.4.4a)$$

$$h_x(0, t) = \tan \theta = m \ll 1 \quad (1.4.4b)$$

$$J_{gb}(0, t) = h_{xxx}(0, t) = 0 \quad (1.4.4c)$$

$$h(\pm\infty, t) = h_x(\pm\infty, t) = 0 \quad (1.4.4d)$$

Eq. (1.4.4a) is an initial condition for the problem and assumes an initially flat surface. Eqs. (1.4.4b, c) are the boundary conditions for the triple junction; the first one fixes the dihedral angle ($\varphi = \pi - 2\theta$) at the groove root through mechanical equilibrium ($\sin\theta = \gamma_{gb}/2\gamma_s = \lambda$; where λ may be called as the wetting parameter) and the second sets the flux of atoms out of the boundary to zero. And 1.4.4d assures that flat surface remote from the triple junction at all time.

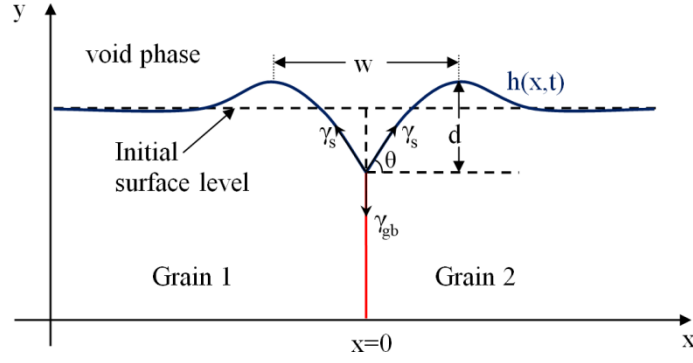


Figure 1.4.1: Sketch of the curve $h(x,t)$; the surface profile function. d is the groove depth measured from the maxima and w is the separation between the two maxima, namely the groove width. γ_{gb} and γ_s are the grain boundary and surface tensions respectively. $\varphi = \pi - 2\theta$ is the equilibrium dihedral angle, force balance requires $2\gamma_s \sin\theta = \gamma_{gb}$ at the groove root.

Mullins obtains an analytic solution of Eq. (1.4.3) subjected initial and boundary conditions defined in Eqs. (1.4.4) as:

$$y(u,t) = m(Bt)^{1/4} Z(u) \quad \text{with: } u = \frac{x}{(Bt)^{1/4}} \quad \text{and} \quad Z(u) = \sum_{n=0}^{\infty} a_n u^n \quad (1.4.5a)$$

$$a_0 = \frac{-1}{\sqrt{2}\Gamma(5/4)}; \quad a_1 = 1; \quad a_2 = \frac{-1}{2\sqrt{2}\Gamma(3/4)}; \quad a_3 = 0; \quad (1.4.5b)$$

$$a_{n+4} = a_n \frac{n-1}{4(n+1)(n+2)(n+3)(n+4)}$$

Here, Γ is the gamma function. It is inferred from Eq. (1.4.5) that the groove shape is dependent upon the material constant $m = \tan\theta$; but is independent of time and the physical parameters comprising B . Mullins (1957) stated that the groove instantly

attains a constant shape whose linear dimensions grow in proportional to $t^{1/4}$, and deduce two technically important equations:

$$d=0.973m(Bt)^{1/4} \quad (1.4.6a)$$

$$w=4.6(Bt)^{1/4} \quad (1.4.6b)$$

The first kinetic equation stands for the steady shape grooves' depth, d and second for its width, w (see Fig. 1.4.1). These two equations give possibility to determine surface diffusion constants experimentally as we will see later in this chapter.

After Mullins' publication in 1957 considerable amount of work had been dedicated by several investigators to obtain a solution that accounts finite slopes at the groove root; some of them will be cited here. Robertson (1971) transforms the nonlinear PDE to an ordinary differential equation of $Z(u)$ by inserting Eq. (1.4.5a) to Eq. (1.4.2) and numerically integrates it to obtain solutions for finite slopes ranging from 0 to 4. He found groove depths lower than estimated by Eq. (1.4.6a) for finite slopes. Zhang & Schneibel (1995) use method of lines approach to solve Eq. (1.4.2); Khenner et al. (2001) categorize the problem as a two dimensional initial boundary value problem of type Hamilton-Jacobi and proposed a numerical solution by using a level set method. Both articles address and discuss several numerical methods to solve the nonlinear PDE. The conclusion shared is that the groove profile stays self similar; the width and height of the groove grow with time t as $t^{1/4}$ as predicted by Mullins' small slope solution.

Several cases regarding to geometry had also been studied in the literature. Mullins theory assumes an isolated groove and it can be inferred from his solution that every film subjected to a long enough annealing time will rupture. Hackney & Ojard (1988) consider an array of equally spaced parallel grain boundaries with the same symmetric contact angle (Fig. 1.4.2a) under SSA. They employ following boundary conditions:

$$h_x(R, t) = h_x(-R, t) = \tan \theta = m \ll 1 \quad (1.4.7a)$$

$$J_{gb}(R, t) = h_{xxx}(R, t) = 0 \quad (1.4.7b)$$

$$h_x(0, t) = 0 \quad (1.4.7c)$$

The third one is the symmetry condition at the center of the grain, whilst the others are self explanatory for a groove root placed to a distance R. They gave an analytic solution for Eq. (1.4.3) that accounts finite grain size 2R. Later Zhang and Schneibel (1995) and Khenner et al. (2001) studied the very same system by solving Eq. (1.4.2) numerically. Both authors observe termination of grooving at long times after formation of identical circular arcs that connect adjacent grain boundaries; a result anticipated long time ago by Srolovitz and Safran (1986) merely from energetic calculations. They show that a groove may go to a finite depth even after an infinite time to anneal and estimate the conditions under which film rupture happens (groove divides the bicrystal into two pieces; and therefore give rise to

island formation on a substrate) as a function of film aspect ratio ($2R/w_0$; see Fig. 1.4.2) and dihedral angle.

Huang et al. (2001) consider a different set of boundary conditions for the end points that are free to move in lateral direction to account finite plate like grains that have semicircular ends (constituting a closed loop, Fig. 1.4.2b). Through large number of finite element analyses they have deduced an empirical formula that relates minimum dihedral angle (below which no splitting occurs) to the film aspect ratio.

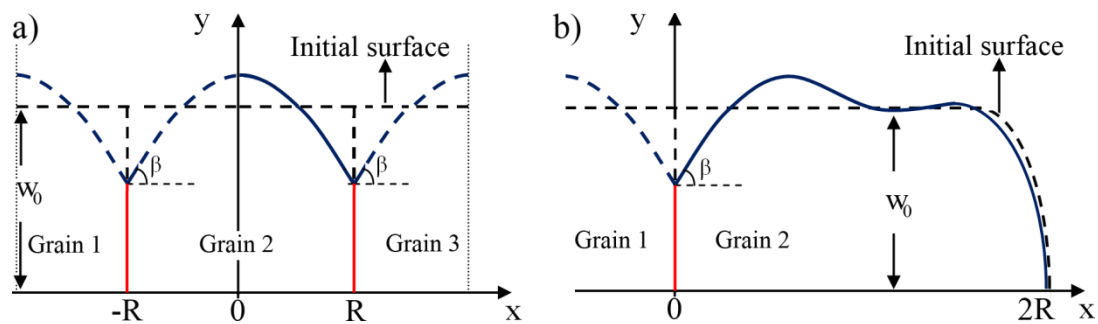


Figure 1.4.2: Schematic representation of a) continuous array of grains, b) plate like grains that have semicircular ends. Symmetry prevails due to assumed isotropic surface properties and solution for the solid lines is enough for interpretation.

Ogurtani and Akyildiz (2005) utilize three different; reflecting, interactive (Fig. 1.4.2a) and free moving (Fig. 1.4.2b) boundary conditions and perform thermal grooving simulations on tilted and normal grain boundaries. Yet, their way of treating the triple junction singularity was completely different from those cited

here and based on a mathematical model which flows only from fundamental postulates of irreversible thermodynamics (see chapter 2). They showed existence of a transient regime and incorporated this regime into their penetration depth formula by stating that the rate of this transient evolution process obeys the first order reaction kinetics. They stated that this regime is totally ignored by researchers employing Mullins' boundary condition at groove root (constant slope).

1.5. Anisotropic diffusivity

The surface diffusivity is known to vary with the crystalline orientation. For an anisotropic surface, equation of motion for thermal grooving, Eq. 1.4.2 should be modified as follows:

$$\frac{\partial h}{\partial t} = -\frac{\Omega^2 \nu}{kT} \frac{\partial}{\partial x} \left\{ \frac{D_\sigma(\theta, \phi)}{(1+h_x^2)^{1/2}} \frac{\partial}{\partial x} \left(\tilde{\gamma}_s(\theta, \phi) \frac{h_{xx}}{(1+h_x^2)^{3/2}} \right) \right\} \quad (1.5.1)$$

Here $D_\sigma(\theta, \phi)$ and $\tilde{\gamma}_s(\theta, \phi)$ are orientation dependent surface diffusivity and surface stiffness ($\tilde{\gamma} = \gamma + \gamma_{\theta\theta}$) respectively. Appropriate analytic functions may be incorporated to reflect the orientation dependence in a specific crystal and specific mechanism.

Figure 1.5.1 shows equivalent surface directions for hopping motion of adatoms on the (110), (100) and (111) surfaces of an fcc crystal, which reflects 2, 4, 6 fold

symmetries respectively. Then the anisotropic diffusivity of surface atoms may be incorporated into a numerical procedure by adapting the following relationship,

$$D_{\sigma}(\theta, \phi) = D_{\sigma}^0 \{1 + A \cos^2 [m(\theta - \phi)]\} \quad (1.5.2)$$

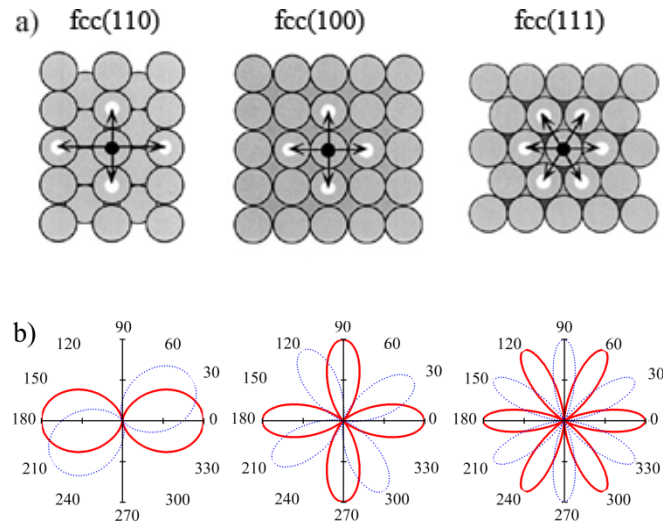


Figure 1.5.1: In a) ball model for next neighbor hopping on the (110), (100) and (111) surfaces of a face centered cubic crystal. Arrows mark the possible jumps from an adsorbate at the origin (figure adapted from Barth, 2000), b) analytic function (Eq. 1.5.2) used to represent the orientation dependence: $D_{\sigma}^0 = 1$, $A = 1$, $\phi = 0^\circ$ (solid red curves) and $\phi = 30^\circ$ (dashed blue curves) respectively for $m = 1 \rightarrow (110)$, $m = 2 \rightarrow (100)$ and $m = 3 \rightarrow (111)$ planes.

In Eq. (1.5.2), D_{σ}^0 is the minimum value of the surface diffusion constant at a specific surface orientation, θ is the complementary dihedral angle. A , m , and ϕ

are dimensionless parameters that determine the strength of the anisotropy, the grain symmetry through the number of crystallographic directions that corresponds to fast diffusion paths, and the misorientation of the symmetry direction with respect to a specified direction say that of the applied electric field E_∞ , respectively. $N = 2m$ corresponds to the rotational degree of symmetry or fold-number.

1.6. Thermal grooving with surface energy anisotropy

Maybe the most serious simplification made in the Mullins model is the assumption of the full isotropy of the surface energy. Obviously, this assumption justifies the use of the continuum approach, with the macroscopic curvature as the only driving force for surface diffusion. However, the importance of the surface free energy anisotropy in determining the dihedral angle of the groove and the groove shape was recognized soon after Mullins' work. Grain boundary grooves can develop facets due to anisotropic surface energy. The presence of facets on surfaces of grooves poses intricate modeling issues since Mullins' theory is inapplicable to deal with the anisotropic surfaces.

The value of surface energy per unit area of a given crystallographic surface orientation is determined by the fine scale structure of that surface. For a high symmetry orientation in a crystal the surface is atomically flat. For other orientations close to this surface, the structure usually consists of flat terraces with well-defined local surface energies, separated by atomic scale ledges or steps as illustrated schematically in figure 1.6.1. The steps alter the macroscopic surface

energy by an amount corresponding to their energy of formation in the configuration relevant to the structure. Below a characteristic roughening transition temperature T_R , “a nominally flat surface of a crystal that is misoriented by a small angle from a high symmetry direction consists of a train of straight parallel steps” (Shenoy & Freund, 2002). At finite temperature, such “vicinal” surfaces can be stable and can appear on rounded edges on the equilibrium crystal shape.

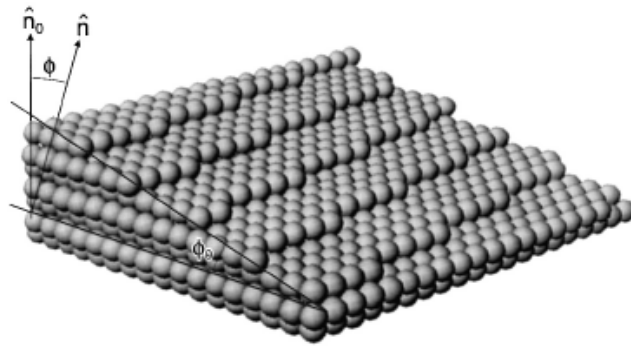


Figure 1.6.1: Structure of an fcc $(3\bar{2}16)$ surface vicinal to the fcc (001) surface. Figure illustrates zero-temperature steps and kinks that occur on high index (or ‘vicinal’) surfaces (Jeong & Williams, 1999).

With increasing temperature, the rounded regions grow at the expense of facets and at T_R (usually below the melting temperature) the surface becomes smoothly rounded as illustrated schematically in figure 1.6.2. Below T_R , “in the Wulff construction of the surface specific Gibbs free energy, the cusp in the γ -plot or the non-analytic term in the surface tension exists as a result of the finite free energy cost per unit length in the formation of a step”. Therefore “the disappearance of

facets is connected to disappearance of cusps in the γ -plot, and implies that the step free energy vanishes and free proliferation of steps is expected for $T > T_R$ " (Jeong & Williams, 1999).

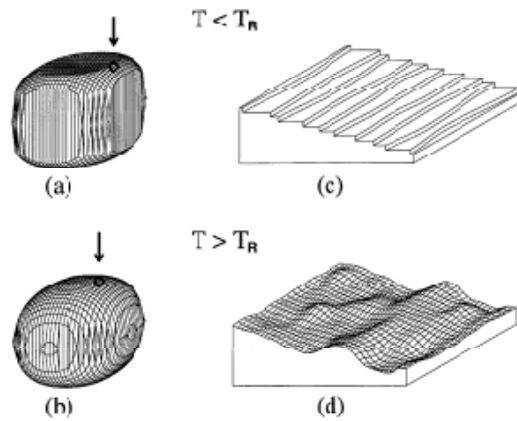


Figure 1.6.2: Schematic illustration of equilibrium crystal shapes at finite temperatures, T for a simple cubic model with the nearest neighbor interaction. Equilibrium crystal shapes a) at $T < T_R$: stable (001) facets and b) at $T > T_R$: continuously rounded, have no facet. The regions marked by arrows in a) and b), are vicinal to the low index (001) surface. The difference in mesoscopic structures below and above the roughening temperature is given in c) and d) (Jeong & Williams, 1999).

Mykura (1961) stated that, in the case of a coherent twin boundary, the surface anisotropy may even cause the formation of a ridge instead of a groove. Bonzel and Mullins (1996) considered the evolution of a pre-perturbed surface topography of the vicinal surface, which is essentially anisotropic. It was found that in the small slope approximation, the flux of the surface atoms is again proportional to the gradient of the surface curvature defined in the proper frame of reference, but should be substituted by a complex expression which depends on the energy of an isolated step, the energy of interaction between steps and the direction of perturbation.

The grain boundary grooving at the singular surfaces were extensively studied by Rabkin et al. (2000), Klinger and Rabkin (2001), Rabkin and Klinger (2001) by explicitly introducing faceted and rough regions, each with different isotropic surface energies. Zhang et al. (2002) derive models describing groove growth while the dihedral angle changes. Inevitably the change in the dihedral angle is assumed to be caused by the change in the surface energy. They express the dihedral angle as a function of time, and after a series of simulations they conclude that changes in the dihedral angle affect the growth exponent for the groove depth much more than the groove width. Growth exponents for depth values as high as 0.4 are possible in this model, whereas Mullins' model predicts an exponent of 0.25 for both the width and depth of the groove. Later, Zhang et al. (2004) study the effect of anisotropic surface free energy on thermal grain boundary grooving using modeling, simulation and experiments on tungsten. Based on Herring's model they show that, for tungsten, when the anisotropy is mild, the groove profiles are self-similar in the

evolution but are often not in proportion to those developed under isotropic material properties. The grooving kinetics again obeys power law with the exponent 0.25. When the anisotropy is critical surface faceting occurs. And, when it is severe the facets coarsen in the evolution. They exhibit the groove profiles in evolution under different degrees of anisotropy.

Wong and coworkers (Xin & Wong, 2001, 2003, 2004; Min & Wong, 2006a, 2006b; Du & Wong, 2006) study orientation dependent surface stiffness instead of the surface free energy explicitly in their treatments. They regularize the surface stiffness by replacing the Dirac delta function by sharply peaked functions while former use an analytic form for the surface free energy which then leads to an analytic surface stiffness and find that faceted grooves still grow with time t with an exponent of 0.25. They stated that, anisotropic groove can be smooth if the groove surface does not cross a facet orientation, moreover the groove has the same shape as the corresponding isotropic groove, but the growth rate is reduced by a factor that depends on the degree of anisotropy. Recently, Ogurtani (2007) has reached exactly the same conclusion for the four fold symmetry by applying special analysis on the surface Gibbs free energy function adapted from Ramasubramaniam and Shenoy (2005). The analytic theory developed in conjunction with the extensive computer simulation experiments irrecoverably proved that the smooth grain boundary groove profiles can be represented by the modified Mullins' function (1957) with great precision for the symmetrically disposed bicrystal, where the Mullins' rate parameter B is modified by an anisotropy constant Ψ as $B \Rightarrow B \times (1 - \Psi)$, and the

isotropic complementary dihedral angle in the slope parameter is replaced by its counterpart in anisotropic case.

Ramasubramaniam and Shenoy (2005) made a very serious and successful attempt to obtain a weak solution of the evolution kinetics of faceted grain boundary grooves. They produced proper connections for the TJ displacement velocity that resulted realistic groove root profiles for the symmetrically disposed grain boundary and intersecting surface configurations that are initially flat and infinite in extent. Inspiring from this article, Ogurtani (2007) made a unique and transparent treatment of the grain boundary triple junction singularity by the weak solution of the extremum problem imposed by the mathematically more sound Dirichlet boundary conditions to reveal the fine topographic details of the groove root-profiles caused by the non-analyticity of the surface stiffness. In a previous work, Ogurtani (2006a) elaborates Hermite orthonormal functions manifold by showing that at the asymptotic limit the discrete monolayer representation of the interfaces and surfaces in more realistic Verschaffelt (1936) and Guggenheim (1959) model may be converged smoothly into the Gibbs abstract model by keeping the intensive variables (specific surface densities) of the interfaces and surfaces invariant and taking the layer thicknesses equal to zero at the limit and extensive variables (contents) infinite. That asymptotic approach, at the expense of the fine features of the grain boundary groove root profiles (rough and faceted regions), was successful not only in eliminating the discontinuity in the particle flux density at the grain boundary triple junction (which results Dirac delta function singularity in the gradient) but also produced most wanted continuity in the derivative of the particle

flux density as speculated by Ramasubramaniam and Shenoy (2005) to surmount the analytical difficulties. Ogurtani et al. (2008) extend this approach to simulate tilted grain boundary grooves in thin metallic films showing four and six fold anisotropy. Later Ogurtani (2009a) studied the very same problem by employing the modified cycloid-curtate function (MCC) as a basis (generator) for the Dirac delta distribution function on the Wulff construction. This new representation gives more flexibility on the shape of the surface profiles even its temperature dependence by considering not only the intensity but also the topography of the surface Gibbs free energy anisotropy. The utilization of the MCC function also furnished a way for the smooth passage from the soft to sharp faceting morphology by fine tuning the Wulff roughness parameter (anisotropy constant) while keeping topography index invariant.

1.7. Experimentally observed thermal grooves

Since its introduction in 1957, Mullins' theory is used extensively in determination of the surface diffusion coefficients (D_s). Once the active mass transport mechanism is confirmed (for evaporation condensation, surface and volume diffusion groove growth obeys $t^{1/2}$, $t^{1/4}$ and $t^{1/3}$ time laws respectively), the ratio of the groove depth (or width) measurements taken at different times yield the B parameter of Eq. (1.4.2). As stated before, B is a collection of physical constants: $B=D_s\gamma_s\Omega^2v/kT$; providing surface energy γ_s is known, constant temperature experimentation gives the surface diffusivity. Grain boundary grooves are also monitored to measure the dihedral angles and therefore to obtain ratio of surface to grain boundary energies.

Classically, measurements were carried out by electron microscopy or by optical profilometry techniques such as vertical scanning interferometry, phase shifting interferometry, etc. After their invention in the early 1980s, scanning probe microscopies (SPMs) open up new possibilities for studying the surface topography of thermal GB grooves. These instruments combine the possibility to scan relatively large surface areas with atomic resolution in the vertical direction (atomic force microscopy, AFM) and in the case of scanning tunneling microscopy (STM) lateral atomic resolution can be achieved. This makes SPMs ideally suited for the quantitative characterization of surface topography.

Mulins and Shewmon (1959) studied grooving kinetics of tilt boundaries in copper by interferometric analysis to show the advantages of the theory in determining D_s . They showed that the dominant process is surface diffusion, and found D_s values in agreement with the ones determined by tracer diffusion studies. A good agreement was also found by Sharma and Spitz (1981) for thermal grooves on thin films of silver from a transmission electron microscopy (TEM) study. Tsoga and Nikolopoulos (1994) studied grain boundary grooving on polished surfaces of polycrystalline alumina after annealing, in air, under vacuum, and in argon atmospheres in the temperature range 1273 to 1736 K. The groove angles, measured by optical interferometry, showed no significant change with experimental conditions. It was determined that surface diffusion was the dominant mechanism for the mass transport and the calculated D_s values in agreement with the literature. Tritscher and Broadbridge (1995) gave a review of experiments (for diverse

materials) where surface diffusion was found to be the dominant mass transfer mechanism.

In recent years, several researchers performed AFM studies of thermal grooving. Schöllhammer et al. (1999) found excellent agreement between measured and predicted groove shapes for symmetrical tilt grain boundaries in copper. Shin et al. (1998) and Lee and Case (1999) analyze surfaces of 99.9% alumina samples and report highly asymmetric GB grooves. Rabkin et al. (2000) attributed the asymmetry they found for GB grooves in NiAl surfaces to the presence of a vicinal surface on one side of a groove and modified Mullins' (1957) linearized equation for thermal GB grooving to take the negligible mass transport on the vicinal surface into account. Qualitative agreement between experimentally observed and calculated groove profiles was found. Rabkin et al. (2006) studied the morphologies of GB grooves formed after annealing of molybdenum bicrystals at the temperature close to the melting point with the aid of scanning force microscopy (SFM). Three typical groove morphologies were observed: (i) Mullins-like, albeit asymmetrical grooves with the sharp root; (ii) grooves with the blunted root, and (iii) grooves with the blunted root with the secondary sub-groove with the sharp root in the region of a primary groove. Sachenko et al. (2000, 2002, 2004) and Zhang et al. (2002, 2004) studied GB grooving on the surfaces of polycrystalline tungsten sheets. They found that unfaceted grooves were in qualitative agreement with the predictions of Mullins' theory of grooving by surface diffusion mass transport. They also observed asymmetric grooves between faceted and unfaceted grains showing unusual growth kinetics. Citing these works on tungsten and that of Munoz

et al. (2003) on alumina, Ogurtani et al. (2008) designed special computer simulations and produced surface morphologies at the stationary state which are in excellent agreement with groove profiles measured by AFM and calculated D_s values which are in agreement with the literature.

1.8. Steady state grain boundary diffusion coupled to thermal grooving

If the grain boundaries, which intersect the free surface, do not transport matter as imposed by Mullins' assumption (5) the corresponding profile evolves via surface diffusion under well-known conditions of scale as completely discussed above. In this approach the only role of the triple junction present in the system is to maintain the equilibrium angle. However, the presence of grain boundary fluxes may change the surface morphology drastically. The problem is studied by considering two coupled processes, namely the surface diffusion taking place on the interface between the bulk and the void phases, and the grain boundary diffusion due to a constant atomic flux along the boundary. Triple junction, a geometric singularity, appears to be the place where these two processes are coupled. The boundary conditions at the triple junction are assumed to be the continuity of the chemical potential (Eq. 1.8.1a), the continuity of mass flux (Eq. 1.8.1b), and the equilibrium capillarity configuration (Eq. 1.8.1c) for geometry; assuming the groove root is at $x=0$ as in figure 1.4.1:

$$\mu_b(0,t) = \mu_\sigma(0,t) \quad (1.8.1a)$$

$$J_b(0,t) = \sum J_\sigma(0,t) \quad (1.8.1b)$$

$$h_x(0, t) = \tan \theta \quad (1.8.1c)$$

In Eq. (1.8.1b) summation extends over the two surface branches. These boundary conditions strictly rely on the validity of Herring's relationship between chemical potential and the curvature is mutually incompatible for the triple junction (see chapter 2). At the triple junction there is no way of defining single curvature because of the large discontinuity due to the finite dihedral angle. Therefore Herring's relationship, which is valid for only smoothly varying surfaces, is not suitable for the triple junctions. Furthermore, the continuity of chemical potential implicitly assumes that there is no local equilibrium, which violates the possibility of internal entropy production. However the triple junction motion is completely natural (irreversible) process. Nevertheless these boundary conditions are employed by the following authors cited below.

Regarding to its physical origin several researchers use the chemical potentials and fluxes for grain boundaries given in section 1.3 in investigating effects of steady state grain boundary fluxes, yet the mathematical treatment is similar. Klinger et al. (1995) bear in mind this similarity and examine the case under isotropic conditions for the intersection of a periodic array of grain boundaries with an external surface for arbitrary grain boundary fluxes. According to their analysis two modes of surface evolution can occur: 1) for moderate magnitudes of J_{gb} the entire surface advances or recedes as material is supplied or removed by the intersecting grain boundaries, 2) for sufficiently large magnitudes of J_{gb} , the grain boundary roots break away from the remaining surface to form rapidly growing ridges or slits. The

transition from the first to the second mode occurs at limiting values of J_{gb} which depend on geometry and material parameters.

They also state that the use of small slope assumption hinders the transition between these two modes; that a global steady state is always possible from the solution of linearized equation. Under this assumption Rosenberg and Ohring (1971) and Genin et al. (1993) treated the isolated groove development with constant grain boundary flux respectively due to EM forces and normal stress gradients acting on the boundary. This was done by superimposing a solution corresponding to the steady state grain boundary diffusion to that of Mullins' thermal grooving. The latter case is repeated for a periodic array of grain boundaries (with a similar configuration given in Fig. 1.4.1a) by Thouless (1993) and more recently by Anderson et al. (2005). For isolated grooves, time law for groove width is found as $t^{1/4}$ whereas groove depth is found to be proportional with $t^{1/4}$ in early stages but replaced eventually by $t^{3/4}$. A tensile stress induced grain boundary flux cause the groove to deepen more rapidly than it does without stress; whereas for compressive stresses it results in a retardation of groove formation. In the case of periodic array of grains the initial dependence of the width on time is again identical to that of the Mullins solution for a surface-diffusion controlled process, i.e. $t^{1/4}$. With the time at which features of the profile interact with those from neighboring boundaries groove width attains a constant value. Groove depth on the other hand, initially accepts $t^{3/4}$, and in later stages becomes linear in t .

Mode 2 type behavior is extensively studied in the literature because of its resemblance to another popular problem of mechanical metallurgy, namely the diffusive creep cavity growth.

1.8.1. Grain boundary diffusive creep cavity/crack or void growth

It is well known that high temperature intergranular fracture of polycrystalline solids invariably occurs by nucleation, diffusive growth and coalescence of grain boundary voids or cavities (Hirth & Nix, 1985). The process sometimes termed as creep cavity growth owing to its low temperature counterpart (creep rupture) where a cavity growth is accepted to occur by plastic deformation. Experimental findings indicate that a concentrated void population generally forms on grain boundaries oriented in a direction perpendicular to the applied tensile loads (Garofalo, 1965). It had been proposed that the growth results from atomic transport of material away from the cavity by surface self diffusion due to capillarity and through the adjoining grain boundary due to fluxes driven by gradients in the normal tractions and controlled by grain boundary self diffusion. Therefore when the thermal groove root break away from the remaining surface due to a sufficiently large grain boundary flux and form a rapidly growing slit (depicted above as mode 2), the problem becomes identical to the one described as diffusive creep cavity growth (see figure 1.8.1.1).

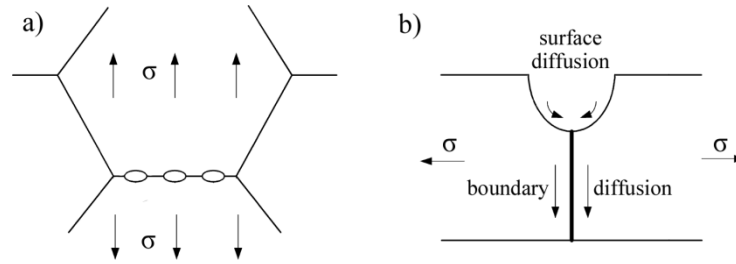


Figure 1.8.1.1: Grain boundary cavity/slit growth by diffusion across the cavity surface and through the grain boundaries due to a stress gradient, a) array of grain boundary cavities, b) an isolated triple junction cavity.

The first model of cavity growth by diffusion was proposed by Hull and Rimmer (1959), based on the assumption that surface diffusion is faster than grain boundary diffusion. In this case, any differences in curvature on the void surface that develop during growth are eliminated quickly by surface diffusion, so that the void has a rounded, equilibrium shape during growth. It was found that the void growth rate increases linearly with increasing applied stress, assuming that the grains on both sides of the boundary are rigid. A correction to the model was made by Weertman (1973), who considered the appropriate boundary condition to be one of zero vacancy flux on the grain boundary at the midpoint between the voids. Raj and Ashby (1975) considered a network of lenticular cavities and obtained a similar conclusion. Raj (1978) examined Cu bicrystals and found the rupture time inversely proportional to stress, consistent with the Hull-Rimmer unconstrained diffusional cavity growth model presented here.

However Yamazaki (1968) and Dobes (1973) work on ellipsoids indicated that the effect of limited surface diffusion is to elongate the cavity surfaces in the direction normal to the applied stress. Such cavities were observed experimentally in tungsten by Stiegler et al. (1967) and in α -iron by Wingrove and Taplin (1969). Chuang and Rice (1973) analyzed crack-like cavity located on a planar grain boundary and moving with a uniform velocity. This time, it was found that the cavity growth rate is proportional to the surface diffusivity and to the third power of the applied stress for $\theta \rightarrow 0$. Later Pharr and Nix (1979) and Martinez and Nix (1982) using finite difference schemes to solve the diffusion equation showed that, under action of both surface and grain boundary diffusion, noses develop at the tip of an equilibrium shaped cavity in the early stages of growth and that, once formed, these noses behave like Chuang – Rice steady state crack. Similarly Chuang et al. (1979) showed under sufficiently high stresses, a void on a grain boundary will form a crack-like slit and propagate rapidly along the grain boundary. Igit and Mawby (1999) model failure of aluminium interconnect line under similar conditions by starting with a thermal groove as an initial condition. They employ different ratios of grain boundary/surface diffusivities each greater than one (surface control; i.e. Chuang – Rice model given above). Huang et al. (2000) used steady state traction distribution obtained by Martinez and Nix (1982) on the grain boundary in simulating growth of grain boundary voids under external tension by a robust finite element method. They confirm formation of a long crack-like configuration by faster movement of atoms near the void tip than those at the void top (elongation of the void in the direction of the grain boundary) when surface diffusion is the rate controlling mechanism. They also state that the rupture time, at which the

neighboring voids link, decreases with increasing diffusivity ratio of the grain boundary and surface and applied external stress for a given initial void spacing.

Needless to say all these studies employ Mullins' boundary conditions for the triple junction. Finally it should be noted here that in all of the cited works in this subsection the elastic effects in grains were neglected, i.e. grains are assumed to be rigid. Attempts to model the combined effects of elastic deformation and diffusion on crack growth had been made by Vitek (1978), Speight et al. (1978), Chuang (1982). A good review of different aspects of diffusive creep cavitations in metals may be found in works of Delph (2002) and Kassner and Hayes (2003).

1.8.2. Electromigration induced grain boundary slits or cracks

Klinger et al. (1996) studied a slit propagating with a constant velocity in an infinite isotropic conductor with an electric field E_∞ applied parallel to the slit by considering EM along both the grain boundary and the slit surface. They specified certain conditions depending upon material constants under which steady state solutions exist and found that for those width and velocity of the slits scale as $E_\infty^{-1/2}$ and $E_\infty^{3/2}$. The steady state growth of grain boundary cracks in interconnects with electric field is considered for an inclined grain boundary by Liu et al. (2001) and Wang et al. (2002). They found exactly the same behavior for the width and velocity and note that the life-time of interconnect under these conditions is then proportional to $E_\infty^{-3/2}$. In these studies, a steady state shape evolution with an equilibrium angle at the crack apex is proposed and it is argued that the crack apex

is not a source of entropy production, which is, in contrary, the most delicate part of the irreversible thermo kinetics theory of the processes associated with the evolution dynamics of closed curved interfaces having singularities.

The most difficult cases to treat arise from the breakdown of the steady-state GB diffusion assumption, as during the transient period or because the applied stress changes appreciably during relaxation (Genin et al., 1993). One must then solve an elastic and/or electrostatic boundary value problem at each time step, using as input the displacements arising from the GB flux divergence in order to obtain the new electrostatic potentials and/or stress and flux.

1.9. Surface diffusion under external force fields and non-steady state grain boundary fluxes

The generalized problem of surface diffusion on a crystalline surface, whether it contains grain boundaries or not, requires solution of elastic and/or electrostatic boundary value problems and postponed till mid 90's due to its computational complexity. The very first study comes from Yang and Srolovitz (1993) on ATGS instability and formation of surface crack. Using the continuum elastic theory they derive a set of equations for the stress state within a uniaxially stressed semi infinite solid bounded by a surface of arbitrary shape. A boundary integral method was used to solve these equations and the strain energy density field, which was used to describe the chemical potential, was obtained. The resultant evolution equation was

solved using a Galerkin finite element method (FEM). They demonstrate formation of deep crack like groove from an initially sinusoidal surface. Chiu and Gao (1993) were able to solve for the stress field analytically when the surface of the solid is of cycloid type. They showed that a cusped cycloid surface is energetically favorable when the surface wavelength exceeds a critical value and is stable once it develops. Kassner and Misbah (1994) numerically analyzed the nonlinear evolution of a uniaxially stressed solid. If the film is thin, its surface approaches the film–substrate interface before the formation of cusps, then different stress fields and the different surface energies of the film and the substrate affect the surface morphology and the film–substrate interface will be prevented from being exposed when the wetting criterion is satisfied. Stranski–Krastanow wetting islands will form in this case. The steady states of island shapes were studied by Spencer and Tersoff, (1996, 1997), Kukta and Freund (1997) and Spencer (1999) and his co-workers (Rudin & Spencer, 1999; Shanahan & Spencer, 1999), and many other researchers. Gao and Nix (1999) gave a review on the theoretical and experimental studies of the surface morphological instability in heteroepitaxial films. The nonlinear evolution of the surface of thin films and the formation of islands were studied by Chiu and Gao (1995), Zhang and Bower (1999a, 1999b) and by Xiang and E (2002). At later stage of the nonlinear evolution of the surface, dislocations will be created for further relaxation near the cusp tips where the stress concentrates.

Gao et al. (1999) developed a model of coupling surface diffusion and a constrained grain-boundary diffusion accounting for the transient behavior of grain-boundary diffusion and the nonsliding condition at the film-substrate interface. Authors state,

previous works of Thouless (1993, 1995), Vinci et al. (1995) and Genin (1995a, 1995b) assume that the film is allowed to slide freely on the substrate with the requirement of the diffusional flux in the grain boundary is taken to be linear function of position along the boundary which in turn leads to a constant flux divergence over the boundary and a uniform rate of separation of the adjoining crystals. They highlight that most metal films of technological interest is bonded to their substrates so that sliding at the film/substrate interface may be severely inhibited. To model such an effect the grain-boundary diffusion is taken to be equivalent to moving an array of climb-edge dislocations into the boundary, i.e. the diffusion wedge was modeled as a continuous array of climb-edge dislocations. They used Eshelby's (1979) solution to elasticity problem of edge dislocations near a free surface as a Green's function for diffusion wedge problem. An exact mathematical formulation was presented and the solution that explicitly considers the transient behavior of the grain boundary diffusion was calculated using numerical methods. Later Zhang and Gao (2002) extend the theory further by coupling with grain boundary grooving by surface diffusion under the assumption of small slope. Buehler et al. (2005) discuss several aspects of the model in connection with atomistic computer simulations and recent experimental findings. Klinger and Rabkin (2007) used the stress distribution along the GB obtained by Gao et al. (1999) to model chemical interdiffusion along the GB in a semi-infinite bicrystal subjected to external stress normal to the boundary plane. They found a diffusion wedge formed at the grain boundary that exhibits a time independent shape, with all its linear dimensions growing with annealing time t , according to the $t^{1/3}$ law. Another model that is used to model the stress distribution along the GB is

the linear spring model proposed by Chason et al. (2002) and Guduru et al. (2003). The latter authors compared the model with the dislocation model by Gao et al. (1999) and found that the two models are in good agreement despite the simplicity of the spring model. Huang et al. (2005) used a similar model to predict the transient behavior of isothermal stress relaxation in copper thin films.

Suo and Wang (1994) performed analytical as well as numerical studies on the morphological evolution (bifurcation) of cylindrical voids in an infinite crystal under biaxial stresses by using some ad hoc concepts borrowed from bulk nonequilibrium thermodynamics (Nicolis & Prigogine, 1989) and supplemented by a variational formulation of the extremum problem. Xia et al. (1997) introduced a two dimensional FEM for computing the motion and evolution of voids by surface diffusion in an elastic, electrically conductive solid. They presented various case studies including the evolution of a void towards a circular shape due to diffusion driven by surface energy, the migration and evolution of a void in a conducting strip due to electromigration induced surface diffusion, and the evolution of a void in an elastic solid due to strain energy driven surface diffusion. Zhang et al. (1998) performed three dimensional finite element modeling to study the motion and evolution of cylindrical voids under electromigration and strain induced surface diffusion in a hypothetical interconnect line. The spatial finite element formulation was further exploited by Zhang and Bower (1999a, 1999b) to study the conditions for formation of islands in a thin film of semiconductor material. Fridline and Bower (1999) applied a FEM model to predict the evolution of the void after an electric field was applied to the strip. The model was extended further (Fridline &

Bower, 2002) to account several kinetic processes involved in interconnect failures, including surface diffusion, interface and grain boundary diffusion, and sliding on grain boundaries and at the interface between line and elastic passivation.

Mahadevan et al. (1999) and Mahadevan and Bradley (1999) studied edge instability in single crystal metal lines, applying a numerical phase field technique. The authors defined the critical value of the applied current when the edge perturbation grows to become a slit shaped void that spans the wire and leads to electrical failure, reducing the circuit lifetime to an unacceptable level. Nathan et al. (2000) and Averbuch et al. (2001) and Khenner et al. (2001) applied the level set approach to study the EM drift and transient electromigration grooving in metallic interconnects. The phase field principle, with an order parameter characterizing the damaged state of the interconnect was further used by Bhate et al. (2000, 2002) for simulating EM and stress induced void evolution. The evolution of the order parameter was governed by a fourth order parabolic PDE, related to the Cahn–Hilliard equation (Cahn & Hilliard, 1958). They solved the PDE by an implicit finite element scheme together with the accompanying mechanical (elastic) and electrical problems.

Gray et al. (1998, 1999) develop and use an approximate Green’s function method to solve the Laplace equation for the electric potential by the boundary element method (BEM), in order to model the void dynamics under electromigration conditions in metallic thin film interconnects. Gungor and Maroudas (1998, 1999a, 1999b) computed the distribution of electric field on the void surface by BEM, with

the use of the Galerkin scheme and linear constant trial functions. They simulated the formation of various morphological features: void faceting, formation of wedge-shaped voids, propagation of slit-like and soliton-like features, and open-circuit failures. Gungor and Maroudas (1999a) also performed theoretical analysis and numerical simulations of the effects of residual stress on the failure mechanisms of passivated metallic thin films and observed that two modes of failure occur concurrently during void morphological evolution; 1) EM-induced formation of faceted slits, and 2) stress-induced formation of fine-scale crack-like features on the void surface. The most interesting finding in their studies is the apparent retardation effect of the applied anisotropic stress system on the void drift motion under the EM forces when there is a very strong anisotropy constant (≤ 1000) in the surface diffusivity combined with a high electron wind intensity ($\leq 10^{10}$ A/m²). They also employed a relatively large and asymmetric remote biaxial stress (≤ 300 - 400 MPa) system having 50% reduction in intensity along the transverse axis compared to the longitudinal axis of the interconnect line. In later studies, Fridline & Bower (1999), Schimschak and Krug (2000), Gungor and Maroudas (2001) put more emphasis on the crucial role of surface diffusion anisotropy. A boundary element approach was applied by Averbuch et al. (2003a, 2003b) for numerical studies of the electromigration in thin film metallizations with a polycrystalline structure, with the external electric field parallel to the grain boundary. Later Nathan et al. (2004) use the same approach to simulate the evolution of a surface intersected by transgranular and intergranular edge voids under isotropic surface diffusion and electric field effects under both mass-conserving and non-mass-conserving boundary conditions. A similarity was found in the surface topology of

transgranular voids between their non-mass-conserving model and Schimschak and Krug's (2000) mass-conserving model. The electric field was found to slow the development of an intergranular groove along a positively tilted grain boundary, and to cause thinning or thickening of grains under non-mass-conserving conditions.

Ogurtani's irreversible thermodynamic treatment (Ogurtani, 2000, 2006b; Ogurtani & Oren, 2005) of morphological evolution of curved void surface layers with or without triple junction singularities at the presence of capillary, electromigration and the strain field interactions for multi-components systems results a well-posed moving free-boundary value problem which is applied to the transgranular (Ogurtani & Oren, 2001; Oren & Ogurtani, 2001) and the intergranular (Oren & Ogurtani, 2002; Ogurtani & Oren, 2004, 2005) void dynamics very successfully. The intergranular dynamics involving void and grain boundary mutual interactions was examined carefully and the very complicated asymmetric disposition of the adjacent grains (duplex texture) is fully accounted for by the internal entropy production (IEP) due to the transversal virtual displacement of the triple junction. Furthermore, the effects of void growth processes (evaporation and condensation) on the morphological evolution of transgranular voids, which caused eventual catastrophic failure of the interconnect line, was considered. Their treatment (Ogurtani & Oren, 2005) involves a governing equation obtained rigorously from the irreversible thermodynamic theory, instead of assuming the self-similar enlargement (which keeps the void shape invariant during growth) of a void with a constant rate of growth, as employed by Kraft et al. (1995). The theory

is then applied to the problem of GB grooving and cathode voiding under the capillary and EM forces by Ogurtani and Akyildiz (2005, 2006). It was shown that the nonequilibrium treatment of the triple junctions having asymmetry is extremely important in the electromigration dominating regime in order to predict the dynamical behavior of the system, where the basic assumptions made on the triple junctions by the equilibrium or ad hoc theories are completely violated. Authors found GB grooving can be completely arrested by the applied current density above a well defined threshold level, just opposite to the assumption of Mullins (1957) and his followers. More recently Bower and Shankar (2007) use a simplified version of Ogurtani's nonequilibrium treatment of the triple junctions in their comprehensive FEM model which includes the effects grain boundary sliding, grain boundary diffusion, grain boundary migration and surface diffusion, as well as elastic deformation and electric current flow within the grains themselves. Ogurtani and Celik (2006) and Ogurtani et al. (2007) performed extensive computer simulations on finite size single crystal films which have Gaussian shaped edge voids/hillocks on their sidewalls. These simulation experiments have proved that even in the presence of strong diffusional anisotropy, the solitary waves (kinks or solitons and even a train of sawtooth waves) can be generated in the EM-dominating regime, if one of the principal axes of the diffusivity dyadic has a special and irreducible orientation with respect to the applied electric field intensity vector. These surface topologies may even result in the EM-induced internal voids, which eventually cause the fatal breakdown in the electrical connection by either hitting the opposite sidewall (breaching) or accumulating at the cathode edge and resulting detrimental voiding at the contact area. Later, kinetics of cathode edge shrinkage and

displacement (drift) coupled strongly with the GB grooving were investigated by Ogurtani and Akyildiz (2008a). It was found that cathode drift velocity and the cathode failure time show the existence of two distinct phases, depending upon the normalized electron wind intensity parameter; the capillary and the EM dominating regimes having current exponents equal to 0 and 1, respectively. Analysis of various experimental data on the cathode drift velocity results a consistent value for the surface drift-diffusion coefficient for copper interconnects exposed to some contaminations during the processing and testing stages. The complete cathode failure time (CCFT) due to the cathode area shrinkage by voiding was also formulated and used to predict very accurate CCFT for metallic lines with bamboo-like, near-bamboo, and even with polycrystalline structures by proper calculation of the cathode-edge path length parameter, in terms of the actual line width, the thickness and the grain size.

A recent computer simulation study was performed by Tan et al. (2006) using FEM (ANSYSTM). Simulation experiments were specially designed to investigate the effects of temperature and stress gradients on the accelerated EM test for Cu narrow interconnects. They used a similar program in their previous studies on the current crowding effects on Cu dual damascene via bottom failure for ULSI applications Tan et al. (2005). The mathematical treatment and the implementation for the atomic flux divergences due to electron-wind force, stress-induced migration and thermally induced migration (Soret effect) have been adopted from the Dalleau et al. (2001). Tan et al. (2005) in one of their studies were interested to simulate the growth behavior of a preexistent void on top of the interconnect line, where they

modified the void simulation algorithm proposed by Dalleau et al. (2001) to include the surface drift diffusion into the scenario. In that study, they employed directly the software available in ANSYSTM to calculate the thermal-electrical and thermal-mechanical coupled-field analyses, which resulted in proper evaluation of the various fluxes, and flux divergences to be used in the void surface displacement velocity calculations. The proper treatment of the thermal stress gradient (TSG) induced by an inhomogeneous temperature field is a rather complicated problem in the mathematical theory of thermoelasticity. It is a close analog of the back-stress (Blech effect) induced by EM in metallic interconnects in ULSI, which is treated very thoroughly by Sukharev et al. (2007), in connection with EM induced degradation in dual-inlaid copper interconnects, using a commercial FEM tool COMSOL MULTIPHYSICSTM. Recently Ogurtani and Akyildiz (2008b, 2008c, 2008d) presented a rigorous formulation of the problem using nonequilibrium mesoscopic thermodynamics. In order to calculate the temperature gradients (and in turn thermal stresses) they develop a methodology in which the void center of mass (centroid) taken as a reference frame for the dynamic localization of the interior points. This unique approach enables the internal nodes to be also mobile and self-adapting, i.e. they are tracking the temporal topography of the mobile intragranular void surface contour. Then the scalar fields are calculated along the surfaces of the sidewalls (including the intragranular void) using a combination of particular and complementary functions (analogous to the theory of ordinary differential equations) similar to the Treffz method. The particular solutions were evaluated on the temporal positions of the specimen and void surfaces without paying any attention to the physical BCs (i.e., Neumann and/or Dirichlet BC). The

complimentary solution uses the fundamental solutions (Greens functions; i.e., point, dipole, and quadruple etc.) of the Laplace equation to handle the problem at the prescribed BCs for the temporal position of the void surface layer, plus the sidewall surfaces and the cathode/anode edges (in the case of finite geometry). For the complementary part an implementation of the indirect boundary element method (IBEM) was preferred (rather than the more sophisticated direct method that is developed and used successfully by Gray et al. (1998, 1999) and Gungor et al. (1998) in connection with the Galerkin boundary integral technique). The computer simulation experiments they performed clearly indicate the vital importance of the TSG as an agent compared to the uniform thermal stress bias fields on the formation of microcracks during the dynamical evolution of intragranular voids with and without the existence of the heat flux crowding regime under the steady-state heat flow. A more revealing physical outcome of these experiments is the predominant role of the elastic dipole tensor interaction (EDTI) associated with the mobile lattice defects compared to the elastic strain energy density (ESED) contribution to the generalized driving force for the surface drift diffusion, in materials exposed to the inhomogeneous thermal-stress fields. This negative situation does not show much improvement on behalf of the ESED, which has been considered in the literature as an indispensable agent in the formulation of the surface drift diffusion taking place in a uniform applied stress fields in tensorial character including the thermal biasing. One has one or two orders of magnitude differences in the intensities associated with EDTI and ESED in the temperature ranges mostly encountered in practice. Ogurtani and Akyildiz (2008b) paid a special attention to the role played by the properly formulated growth term on the morphological evolution kinetics of

pre-existing voids; which seems to be an indispensable factor for the true understanding of the failure mechanisms of flip-chip solder joints. It seems that it is also the primary term in their governing equation, which causes the speedy lateral extension or spreading of the damage region, along the contact area of the flip-chip solder joint by consuming EM induced supersaturated athermal vacancies in the presence of the combined effects of the heat and current crowding, which are enhanced drastically by the proximity of the void to the hot zone.

Ogurtani (2006c) developed a first-order unified linear instability analysis (LISA) of the governing equation for the evolution of surfaces and interfaces under capillary, EM, and elastostatic forces. That analysis showed conclusively that under certain favorable orientations of the anisotropic single-crystal with respect to direction of the electric current, one can establish stability (healing effects) by the application of the electrostatic field on those samples, which are subjected to the compressive stress systems that are primary source for the instability and the crack formations. Otherwise one may have extreme instabilities induced by the electromigration forces on the surface morphology rather than healing effects. This current induced stabilization of stressed solid surfaces (healing phenomenon) had been first reported very recently by Tomar et al. (2008a, 2008b) who also produced very interesting linear instability analysis, in conjunction with the dynamical simulation studies, which reveals improved surface morphological stability over a range of misorientation angles between the electric field and easy direction of surface drift diffusion. More recently Ogurtani (2009b) discuss the phenomena in detail, and underline the predominant role of the EDTI associated

with the mobile lattice defects compared to the ESED contribution to the generalized driving force for the surface drift diffusion, in those materials exposed to the surface tractions and body forces. In fact, this healing effect of EM on the grain boundary grooving first noticed by Averbuch et al. (2003b) as slowing down in the displacement kinetics in their rather early terminated numerical experiments. Later an extensive computer study undertaken by Ogurtani and Akyildiz (2004, 2005) in metallic thin film interconnect lines for the long run times, exclusively prove that this is a genuine effect, and it completely hinders the groove depth displacement in the electromigration dominating regime even though one deals with the isotropic surface diffusivity.

CHAPTER 2

IRREVERSIBLE THERMOKINETIC THEORY OF SURFACES AND INTERFACES WITH TRIPLE JUNCTION SINGULARITIES

2.1. Introduction

As entirely discussed, all those theoretical studies related to the interfaces and surfaces which were reported and cited in chapter 1, are strictly rely on the classical thermodynamics in macroscopic description of physicochemical processes with some obscure modifications in the concept and usage of chemical potentials, and the free energies especially in the presence of externally imposed force fields (electrical, magnetic, etc.) without considering their original mathematical definitions given by Gibbs (1948). All these methods are based on reversible processes and true equilibrium states.

Relying only on the fundamental postulates of linear irreversible thermodynamics, as advocated by Prigogine (1961) for the bulk phases, and utilizing the Verschaffelt (1936) and Guggenheim's (1959) monolayer interface/surface model Ogurtani (2000) has obtained an analytical theory for network of interfaces that are

interconnected by triple junctions and embedded in bulk phases. Later, parts of the theory were published by Ogurtani and Oren (2005) and Ogurtani (2006b).

Here in this chapter we present the necessary and essential parts of the theory mainly by following the work of Ogurtani and Oren (2005). The linear thermodynamics of irreversible processes is introduced for surfaces as well as for bulk phases using the conventional macro-formulation for homogeneous and isotropic close systems. Then, the singular point associated with a triple junction is first treated by using micro-discrete (straight) interfacial elements and then a continuum representation is obtained by taking legitimate limits. The generalized forces and conjugate fluxes associated with the triple junction motion are obtained in terms of the asymmetric dihedral angles and the specific Gibbs free energies of the void surface layer and the grain boundary which are in turn used to obtain the longitudinal and transverse velocities of the triple junction. Ordinary points on surfaces and/or interfaces are also handled within this context as a special or degenerate case of singular point treatment.

2.2. Internal entropy production for discrete microelements

The term microscopic region refers to any small two or three-dimensional region containing a number of molecules sufficiently large not only for microscopic fluctuations to be negligible but also all of the intensive properties are homogeneous in space. The composite system, considered here, has at least two physico-chemically distinct domains separated by thin layers of interphases, which are not only mutually interacting by the exchange of matter and energy but also completely open to the surroundings through the moving or immobile boundaries. For the present specific case of triple junction, the system is an open composite system, which is composed of two bulk phases, namely the interconnect material and the embedded void, and two surface phases, namely the interfacial layer between the void and the bulk region and the grain boundary separating two different grains of the interconnect.

In this theory, the interface is accepted as an autonomous, finite but a thin layer across which the physical properties and/or the structures vary continuously from those of the interior of one phase to those of the interior of the other in accordance with the general view points of Guggenheim (1959), van der Waals and Bakker (1928). Since the interfacial layer is a material system with well-defined volume and material content, its thermodynamic properties do not require any special definition. One may speak of its temperature, entropy, free energy, and composition and so on just as for homogeneous bulk phases. The only functions that call for special comment are the pressure and the interfacial (surface) tension denoted by P

and γ respectively. The certain shortcomings of the monolayer model in equilibrium and non-equilibrium cases are fully discussed by Defay and Prigogine (1966) while they were trying to formulate the thermodynamics of the multi-layer model of surfaces.

In the absence of long range forces, *the total reversible work* done on a flat surface phase (denoted by the subscript σ) with micro-extent, indicated in terms of Δ space-scaling operator, by variations of its volume $d\Delta V_\sigma$, and area $d\Delta A_\sigma$ (keeping its material content unaltered, but stretching) is given as:

$$\delta\Delta w = -\bar{P}d\Delta V_\sigma + \gamma d\Delta A_\sigma \quad (2.2.1)$$

Here \bar{P} is the mean isotropic pressure in the layer, and γ is the surface tension whose value and the location of the surface in which it acts can be uniquely determined by the knowledge of the transverse component of the stress tensor (Laplace, 1806; Buff, 1955; Ono & Kondo, 1960). Its value may be given as:

$$\gamma = \int_0^{h_\sigma} Q dz \quad (2.2.2)$$

where, Q is the deviatoric part of the stress tensor and h_σ is the thickness of the surface layer and also the integration is performed along the surface normal. The above given expression for the reversible work becomes $-Pd\Delta V_b$ for a

homogeneous bulk phase (denoted by the subscript b) in the formulation of the first law of thermodynamics. The local anisotropic properties of the medium are now automatically embedded in the intensive variables, which are characterized by second order tensors or dyadics.

The differential form of the Helmholtz free energy in equilibrium thermodynamics has the same validity for irreversible changes, then for an open surface phase of a micro-extent embedded in an isotropic media it may be written as,

$$d\Delta F_{\sigma} = -\Delta S_{\sigma}dT_{\sigma} - P_{\sigma}d\Delta V_{\sigma} + \gamma d\Delta A_{\sigma} + \sum_i \mu_{\sigma}^i d\Delta n_{\sigma}^i - \sum_j \Delta A_{\sigma}^j d\xi_{\sigma}^j \quad (2.2.3)$$

where, ΔS_{σ} , μ_{σ}^i , Δn_{σ}^i denote the entropy, the chemical potential and the number of i^{th} chemical species in the micro-element, respectively. $d\xi_{\sigma}^j$ and ΔA_{σ}^j are the extent and the affinity of the homogeneous j^{th} chemical reaction taking place in the phase under consideration, the latter is related to the chemical potentials and the stoichiometric numbers as defined by Th. De Donder and Rysselberghe (1936).

In above relationship, it is assumed that, in a single phase only the homogeneous chemical reactions take place and the phase transitions occurring at the mobile boundaries are not considered in the last term. The Helmholtz free energy change due to the passage of the substance i from the phase to the surroundings is accounted by the fourth term in above expression (frozen chemical reactions). Therefore, in the case of a close system, one should subtract only the term given by

$\sum_i \mu_\sigma^i d\Delta n_\sigma^i$, which is closely related to the direct exchange of matter with the surroundings.

Similarly, the Helmholtz free energy change for a bulk phase of a micro-system may be written as,

$$d\Delta F_b = -\Delta S_b dT_b - P_b d\Delta V_b + \sum_i \mu_b^i d\Delta n_b^i - \sum_j \Delta A_b^j d\xi_b^j \quad (2.2.4)$$

The entropy of any system whether it is close or open can change in two distinct ways, namely by the flow of entropy due to the external interactions, $d\Delta S_{ex}$, and by the internal entropy production (IEP) due to the changes inside the system, $d\Delta S_{in}$. Then, the total entropy change can be interpreted as: $d\Delta S = d\Delta S_{in} + d\Delta S_{ex}$. The entropy increase $d\Delta S_{in}$ due to changes taking place inside the system is positive for all natural or irreversible changes, is zero for all reversible changes and is never negative.

Generalization of the first law of thermodynamics for any infinitesimal change associated with an open system, in which not only the energy but also the matter exchange takes place between the system and its surroundings, results:

$$\delta\Delta\Phi = d\Delta U - \delta\Delta w = d(\Delta F + T\Delta S) - \delta\Delta w \quad (2.2.5)$$

where $\delta\Delta\Phi$ is the energy received by the system, in terms of heat and matter transfer processes from the surroundings, $d\Delta U$ is internal energy change, and $\delta\Delta w$ is the reversible work done on the system by external agents, and this work is equal to $-Pd\Delta V$ or $-(Pd\Delta V - \gamma d\Delta A)$ depending upon whether one deals with the bulk phase or the surface phase, respectively.

For a global composite system having discontinuous phases, the total IEP due to the irreversible processes should include the entropy contributions due to transport of heat and chemical species among various phases of the system. Considering the additive property of the entropy changes, and using the splitting procedure as applied by Prigogine (1961), from Eqs. (2.2.3), (2.2.4) and (2.2.5) one may obtain:

$$\frac{d\Delta S_{in}}{\delta t} = -\sum_{i,k} \frac{\mu_k^i}{T_k} \frac{d\Delta n_k^i}{\delta t} + \sum_k \frac{1}{T_k} \frac{\delta\Delta\Omega_k}{\delta t} + \sum_{j,k} \frac{\Delta A_k^j}{T_k} \frac{d\xi_k^j}{\delta t} \quad (2.2.6)$$

The expression given by Eq. (2.2.6) considers the existence of the various homogeneous chemical reactions occurring in different phases of a global system. Double summations with respect to k and i or j indicate summation over various phases (bulk or surface), and over different chemical species or reactions taking place simultaneously in the same phase, respectively. $\delta\Delta\Omega_k$ is the amount of energy transported to the individual phase from the other phases present in the global system due to heat or mass transfer, which also employed by Prigogine (1961) in the treatment of lump and close composite systems. The first term in Eq. (2.2.6) represents an additional contribution to the IEP in the composite system due

to internal entropy flow associated with the transfer of chemical species from one sub domain to another sub domain. The second term in Eq. (2.2.6) drops out for those sub domains having identical temperatures.

For a thermodynamic system composed of interacting open sub systems, IEP is not an additive property unless the whole system is in the state of complete physico-chemical equilibrium. Therefore, in order to calculate global IEP for the whole system, the rate of entropy flow (REF) should also be formulated. One may write the REF from the surrounding to an open composite system as,

$$\frac{d\Delta S_{ex}}{\delta t} = -\sum_{i,k} \frac{\mu_k^i}{T_k} \frac{d\Delta n_{k\leftrightarrow s}^i}{\delta t} + \sum_k \frac{1}{T_k} \frac{\delta\Delta\Omega_{k\leftrightarrow s}}{\delta t} \quad (2.2.7)$$

where the subscript $k\leftrightarrow s$ indicates that the matter and energy exchange takes place between the phases of the system, k , and the surrounding, s . Here, $\delta\Delta\Omega_{k\leftrightarrow s} / \delta t$ and $d\Delta n_{k\leftrightarrow s}^i / \delta t = J_{k,s}^i$ are, the rate flow of energy and the flux of chemical species i to the domain k of the composite open micro-system from its surrounding denoted by s through the heat and matter exchange processes respectively.

2.3. Internal entropy productions associated with the virtual displacements of the triple junction and the ordinary points

Concerning the kinetic behavior of the triple junction, it is assumed that the whole system is in thermal equilibrium and no in situ chemical reaction is taking place other than the phase transformation occurring between the void interfacial layer and the grain boundary region. The sampling domain, which is illustrated in figure 2.3.1, is a very small composite and discrete open micro system, localized into a point of singularity situated in the immediate neighborhood of the junction. This selected composite micro-system is also connected to the neighboring micro-discrete elements by nodes where the exchange or the flow of matter only contributes to the REF but nothing to do with the IEP.

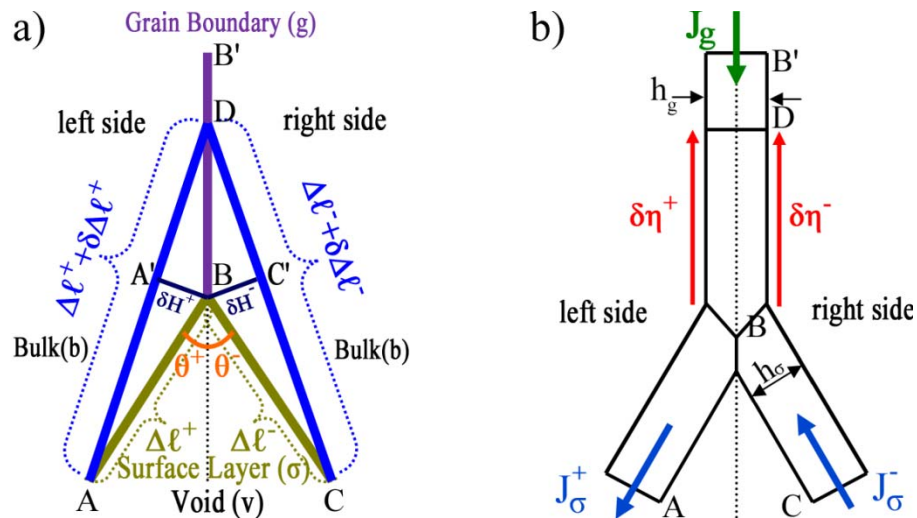


Figure 2.3.1: Triple junction (TJ) longitudinal displacement along the grain boundary. a) TJ macrostructure, line BB' represents the grain boundary and ABC

and ADC are the initial and displaced position of the void interfacial layer, respectively. $\Delta\eta$ is the longitudinal virtual displacement of the triple junction along the grain boundary. b) TJ microstructure, h_σ and h_g are the thicknesses of the interfacial and grain boundary layers, respectively. Figure adapted from Oren (2003).

The individual IEP due to small but finite virtual advancement of a triple junction along the grain boundary can be separately and independently calculated for the symmetric left and right hand side sub-domains of the sampling region, due to the lateral constrain on the grain boundary motion. Then, internal entropy variation for the left hand side sub-system, when the triple junction moves along the grain boundary with a distance $\delta\eta^+$, can be calculated by using following geometric relationships deduced from figure 2.3.1 by assuming: $\Delta\ell^+ \gg \delta\eta^+$ (see also figure 2.3.2):

$$\delta\Delta\ell^+ = \cos\theta^+ \delta\eta^+, \quad \delta H^+ = \sin\theta^+ \delta\eta^+ \quad (2.3.1a)$$

$$\delta\Delta n_b^+ = -\frac{1}{2\Omega_b} \Delta\ell^+ \sin\theta^+ \delta\eta^+, \quad \delta\Delta n_v^+ = \frac{1}{2\Omega_v} \Delta\ell^+ \sin\theta^+ \delta\eta^+ \quad (2.3.1b)$$

$$\delta\Delta n_\sigma^+ = \frac{h_\sigma}{\Omega_\sigma} \cos\theta^+ \delta\eta^+, \quad \delta\Delta n_g^+ = -\frac{h_g}{2\Omega_g} \delta\eta^+ \quad (2.3.1c)$$

In Eqs. (2.3.1), Ω_σ , Ω_g , Ω_b and Ω_v are the mean atomic specific volumes, respectively, associated with void surface layer, grain boundary, bulk and void phases. $\Delta\ell^+$ denote segment length of the void surface layer just next to the triple junction left hand side. h_σ and h_g are the thickness of the surface layer and the grain boundary region and assumed to be invariant. $\delta\Delta n_v^+$ and $\delta\Delta n_b^+$ are the number of atoms gained in the reaction zones associated with the void/interfacial layer, and the bulk/interfacial layer, respectively, while the transformation processes are taking place there during the virtual displacement of the interfacial layer. $\delta\Delta n_g^+$ is the total number of atoms misplaced by the half of the grain boundary during triple junction motion. Similarly, $\delta\Delta n_\sigma^+$ is identically equal to the net atomic gain by the interfacial layer denoted by σ due to enlargement (extension without stretching) of that layer during the displacement operation. δ and Δ are variational and micro-discretization operators, respectively. Exactly similar expressions may be obtained for the other side of the triple junction, which is denoted by negative sign superscript. The specific mean atomic densities associated with the void surface layer and grain boundary can be defined as: $\Gamma_\sigma = h_\sigma / \Omega_\sigma$ and $\Gamma_g = h_g / \Omega_g$, respectively.

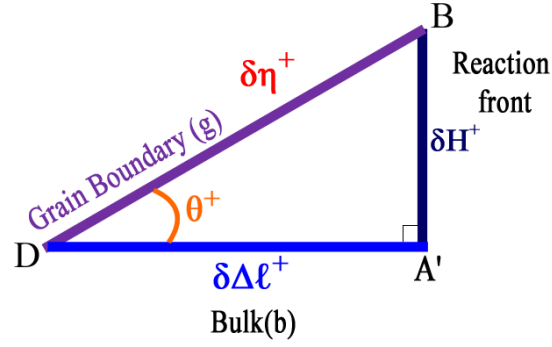


Figure 2.3.2: Upper left portion of figure 2.3.1. Rotated in clockwise direction and rescaled to show the geometric connections for $\Delta\ell^+ \gg \delta\eta^+$ where the angle $B\hat{D}A' \rightarrow \theta^+$. The right hand side is treated in the same way.

In the case of multi-component system, the variations in the number of atomic species could be obtained simply by multiplying the total atomic number variations with respective atomic fractions denoted by x_j^i . Then, the number of chemical species involved in the left hand side phases due to the virtual displacement may be given as:

$$\delta\Delta n_b^{i+} = x_b^i \delta\Delta n_b^+ = \frac{-x_b^i}{2\Omega_b} \Delta\ell^+ \sin \theta^+ \delta\eta^+ \quad (2.3.2a)$$

$$\delta\Delta n_v^{i+} = x_v^i \delta\Delta n_v^+ = \frac{x_v^i}{2\Omega_v} \Delta\ell^+ \sin \theta^+ \delta\eta^+ \quad (2.3.2b)$$

$$\delta\Delta n_\sigma^{i+} = x_\sigma^i \delta\Delta n_\sigma^+ = \frac{x_\sigma^i h_\sigma}{\Omega_\sigma} \cos \theta^+ \delta\eta^+ \quad (2.3.2c)$$

$$\delta\Delta n_g^{i+} = x_g^i \delta\Delta n_g^+ = \frac{-x_g^i h_g}{2\Omega_g} \delta\eta^+ \quad (2.3.2d)$$

Then, the rate of internal entropy production due to triple junction virtual displacement may be written using Eqs. (2.2.6, and 2.3.1-2). In the case of left hand side substitution gives following formula:

$$\frac{\delta \Delta S_{in}^+}{\delta t} = \frac{1}{T} \left\{ \begin{array}{l} \sum_i \left(\frac{x_b^{i+}}{\Omega_b} \mu_b^{i+} - \frac{x_v^{i+}}{\Omega_v} \mu_v^{i+} \right) \frac{1}{2} \Delta \ell^+ \sin \theta^+ \\ + \frac{\Gamma_g}{2} \sum_i x_g^i \mu_g^i - \Gamma_\sigma \cos \theta^+ \sum_i x_\sigma^{i+} \mu_\sigma^{i+} \end{array} \right\} \frac{\delta \eta^+}{\delta t} \quad (2.3.3)$$

In above relationship, the superscript $^+$, on the atomic fractions and the chemical potentials indicate explicitly that those quantities may depend upon the orientation of the local surface normal. For the multi-component surface phases, $g_\sigma = \sum \Gamma_\sigma^i \mu_\sigma^i$, and $g_g = \sum \Gamma_g^i \mu_g^i$ are equal to the specific Gibbs free energy densities associated with the void surface layer, and the grain boundary, respectively. Here, $\Gamma_\sigma^i = \Gamma_\sigma x_\sigma^i$, and $\Gamma_g^i = \Gamma_g x_g^i$ are defined as the specific surface concentration of chemical species in surface layer, and the grain boundary, respectively.

The terms appearing in the first group on the right side of Eq. (2.3.3) such as, $\check{g}_b = \sum x_b^i \mu_b^i / \Omega_b$ and $\check{g}_v = \sum x_v^i \mu_v^i / \Omega_v$ are the volumetric Gibbs free energy densities associated with the bulk and void phases which have their own instantaneous compositions just next to the hypothetical geometric boundaries of the interfacial layer (reaction fronts or zones). Furthermore, these quantities are related to the specific Gibbs free energy densities by the relationship: $g_\sigma = h_\sigma \check{g}_\sigma$.

Dividing both side of Eq. (2.3.3) by δt , and taking following limits: $\delta t \rightarrow 0$, $\Delta \ell \rightarrow 0$, one may immediately obtain the following differential equations representing IEP associated with the virtual displacement of the left and right sides of the triple junction singularity,

$$\lim_{\substack{\delta t \rightarrow 0 \\ \Delta \ell \rightarrow 0}} \frac{\delta \Delta S_{in}^+}{\delta t} = \frac{d \Delta \hat{S}_{in}^+}{dt} = \frac{1}{T} \left(\frac{1}{2} g_g - g_\sigma^+ \cos \theta^+ \right) \frac{d \eta^+}{dt} \quad (\text{J K}^{-1} \text{ m}^{-1} \text{ s}^{-1}) \quad (2.3.4a)$$

$$\lim_{\substack{\delta t \rightarrow 0 \\ \Delta \ell \rightarrow 0}} \frac{\delta \Delta S_{in}^-}{\delta t} = \frac{d \Delta \hat{S}_{in}^-}{dt} = \frac{1}{T} \left(\frac{1}{2} g_g - g_\sigma^- \cos \theta^- \right) \frac{d \eta^-}{dt} \quad (\text{J K}^{-1} \text{ m}^{-1} \text{ s}^{-1}) \quad (2.3.4b)$$

In these expressions the symbol $\hat{}$, emphasize that those IEP terms are line sources in three dimensional space.

Then, the entropy production for the combined system (composed of right and left sides) may be obtained as:

$$\begin{aligned} \frac{\delta \Delta S_{in}^{g\sigma}}{\delta t} &= \frac{\delta \Delta S_{in}^-}{\delta t} + \frac{\delta \Delta S_{in}^+}{\delta t} \\ &= \frac{1}{T} \left\{ -\frac{1}{2} \left(\tilde{g}_{vb}^+ \Delta \ell^+ \sin \theta^+ + \tilde{g}_{vb}^- \Delta \ell^- \sin \theta^- \right) \right\} \frac{\delta \eta_g}{\delta t} \geq 0 \end{aligned} \quad (2.3.5)$$

which yields IEP due to longitudinal displacement of the triple junction along the grain boundary. Applying the consecutive limiting procedures, as described previously, gives:

$$\frac{d\hat{S}_{in}^{g\sigma}}{dt} = \frac{1}{T} \left[g_g - \left(g_{\sigma}^+ \cos \theta^+ + g_{\sigma}^- \cos \theta^- \right) \right] \frac{d\eta_g}{dt} \geq 0 \quad (\text{J K}^{-1} \text{m}^{-1} \text{s}^{-1}) \quad (2.3.6)$$

In Eq. (2.3.5) $\check{g}_{vb} = (\check{g}_v - \check{g}_b)$ corresponds to the volumetric Gibbs free energy density of transformation (GFEDoT) (negative of the affinity of an interfacial reaction such as for condensation or adsorption: $g_{vb} > 0$; and for evaporation or desorption: $g_{vb} < 0$) associated with the transformation of the bulk phase into the *realistic void* phase which contains chemical species even though they are present in a trace amount. In the case of thermostatic equilibrium between a void phase and an adjacent bulk phase, GFEDoT equals to zero if the reaction front is flat. Similarly, the specific Gibbs free energy of transformation between the parent and void phases may be given by $g_{vb} = \check{g}_{vb} h_{\sigma}$.

The IEP density associated with the virtual displacement of an ordinary point along the normal direction of void surface can be also deduced from Eq. (2.3.5). This can be done first by deleting the grain boundary terms, and recognizing that the displacement motion of the curved interface takes place along the local surface normal vector. Since the right and the left hand segments around the selected ordinary point can be chosen arbitrarily, we may take them equal in length that automatically results identical take off angles between the surface normal and the

right and the left segments. Now if one applies the limiting procedure such as; $\Delta\ell \rightarrow 0$ and $\delta t \rightarrow 0$, then the following rigorous continuum relationship may be obtained, by recalling that curvature gives a measure of the rate of change of direction of the tangent with respect to arc length (see figure 2.3.3):

$$\kappa = \lim_{\Delta\ell \rightarrow 0} \frac{\cos\theta}{\Delta\ell/2} \quad (\text{m}^{-1}) \quad (2.3.7)$$

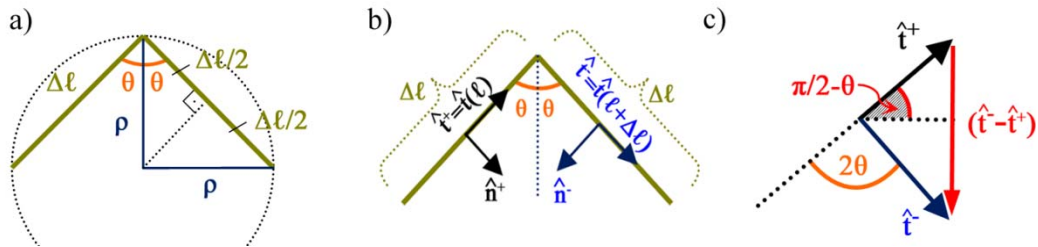


Figure 2.3.3: The curvature relationship given in equation (2.3.7) may be justified by a) considering the circle that pass from three points: $\rho = \kappa^{-1}$, where ρ is the local radius of curvature. Alternatively, b) shows the unit tangent (\hat{t}) and normal (\hat{n}) vectors at the mid-segments, so as given in c) magnitude of the difference vector $|\hat{t}^- - \hat{t}^+|$ is the base of the isosceles triangle formed by the unit vectors and therefore equal to $2\sin(\pi/2-\theta)$. Then, curvature may be obtained as:

$$\kappa = \left| \frac{d\hat{t}}{d\ell} \right| = \left| \lim_{\Delta\ell \rightarrow 0} \frac{\hat{t}(\ell + \Delta\ell) - \hat{t}(\ell)}{\Delta\ell} \right| = \lim_{\Delta\ell \rightarrow 0} \left| \frac{\hat{t}^- - \hat{t}^+}{\Delta\ell} \right| = \lim_{\Delta\ell \rightarrow 0} \frac{\cos\theta}{\Delta\ell/2}.$$

Similarly $\lim_{\Delta\ell \rightarrow 0}$ results $\theta = \pi/2$. Hence, using above described limiting quantities

in Eq. (2.3.5), one may deduce the following expression for the internal entropy production density (the entropy source term) associated with ordinary points:

$$\frac{d\hat{S}_{in}}{dt} = -\frac{1}{T}(\tilde{g}_{vb} + g_{\sigma\kappa})\frac{d\eta}{dt} \geq 0 \quad (\text{J K}^{-1} \text{ m}^{-2} \text{ s}^{-1}) \quad (2.3.8)$$

There is a certain freedom exists in the choice of fluxes and forces, because the entropy production can be split in several ways into fluxes and forces as clearly demonstrated by De Groot (1951). Since it has been assumed on the onset that there is a thermal equilibrium in the system, we may rather use a direct and more plausible approach for the triple junction singularity, namely the concept of power dissipation in the close sense of classical mechanics, and sometimes it is called Helmholtz dissipation function (Haase, 1969). This concept is also advocated and extensively used by Ogurtani and Seeger (1983) in the general formulation of internal friction and dislocation damping phenomenon associated with atomic hopping motions in discrete body centered cubic lattice that is exposed to the interaction fields which are inhomogeneous in space and fluctuating in time. The power dissipation function for an isothermal system is simply given by IEP multiplied by the temperature, and for the present case it is identically equal to the product of the driving force and the velocity:

$$T \frac{d\hat{S}_{in}^{\pm}}{dt} = \hat{F}^{\pm} \frac{d\eta^{\pm}}{dt} \geq 0 \quad (\text{J m}^{-1} \text{ s}^{-1}) \quad (2.3.9)$$

Comparing Eq. (2.3.9) with Eq. (2.3.4), one can immediately deduce the generalized force for the right and left sides as;

$$\hat{F}^+ = \left(\frac{g_g}{2} - g_\sigma^+ \cos \theta^+ \right) \quad (\text{N m}^{-1}) \quad (2.3.10a)$$

$$\hat{F}^- = \left(\frac{g_g}{2} - g_\sigma^- \cos \theta^- \right) \quad (\text{N m}^{-1}) \quad (2.3.10b)$$

These generalized forces are associated with the net material flow, during the triple junction longitudinal displacement along the grain boundary, without making any distinction between intrinsic fluxes related to the individual chemical species. They are also given in per length basis consistent with the IEP formulation which was carried out for a sample of unit length in thickness, and the void surface was assumed to be an arbitrary cylindrical in shape. In the phenomenological relationship between velocity and force, one may prefer to use the force acting on a single atomic particle. Therefore above expressions for generalized forces should be multiplied by an atomic length, d_a , which may be taken as equal to the interatomic distance along the sample thickness. Accordingly, the connection between the triple junction velocity and the atomic generalized force may be written by introducing the phenomenological mobility coefficient \mathfrak{R}^{long} / kT ,

$$\frac{d\eta_g^+}{dt} = \frac{\mathfrak{R}^{long} d_a}{kT} \left(\frac{g_g}{2} - g_\sigma^+ \cos \theta^+ \right) \quad (\text{m s}^{-1}) \quad (2.3.11a)$$

$$\frac{d\eta_g^-}{dt} = \frac{\mathfrak{R}^{long} d_a}{kT} \left(\frac{g_g}{2} - g_\sigma^- \cos \theta^- \right) \quad (\text{m s}^{-1}) \quad (2.3.11b)$$

where, the same mobilities for both sides are employed. One can now immediately formulate the atomic fluxes coming from the triple junction towards the both sides of the void surface layer. These are simply given by the number of atoms present in a volume swept by the triple junction motion along the grain boundary per unit time, and plus the incoming grain boundary atomic flux \hat{J}_g ($\# \text{ m}^{-1} \text{ s}^{-1}$) associated with the long-range drift-diffusion. Since, the velocity of the triple junction is proportional with the net flux accumulated or depleted at the junction, one can write the following expressions;

$$\frac{d\eta_g^+}{dt} = \frac{2}{\Gamma_g} (\hat{J}_\sigma^+ - \hat{J}_g / 2) \quad (\text{m s}^{-1}) \quad (2.3.12a)$$

$$\frac{d\eta_g^-}{dt} = -\frac{2}{\Gamma_g} (\hat{J}_\sigma^- + \hat{J}_g / 2) \quad (\text{m s}^{-1}) \quad (2.3.12b)$$

Combining these expressions with Eqs. (2.3.11) for the triple junction velocities, one gets immediately the following generalized conjugate fluxes:

$$\hat{J}_\sigma^+ = \Gamma_g \frac{\mathfrak{R}^{long} d_a}{2kT} g_\sigma^+ (\lambda^+ - \cos \theta^+) + \hat{J}_g / 2 \quad (\# \text{ m}^{-1} \text{ s}^{-1}) \quad (2.3.13a)$$

$$\hat{J}_\sigma^- = -\Gamma_g \frac{\mathfrak{R}^{long} d_a}{2kT} g_\sigma^- (\lambda^- - \cos \theta^-) - \hat{J}_g / 2 \quad (\# \text{ m}^{-1} \text{ s}^{-1}) \quad (2.3.13b)$$

where the right and left sub-domains are considered separately by splitting the grain boundary diffusion flux equally. At this stage one can immediately write down the expression for the velocity of the triple junction either directly from Eq. (2.3.6), or applying the law of conservation of species to the displacement motion of triple junction, and utilizing Eqs. (2.3.13) for the out-going fluxes from the transformation front:

$$v_g^{long} = \frac{d\eta_g}{dt} = (\hat{J}^+ - \hat{J}^- - \hat{J}_g) \frac{1}{\Gamma_g} = \frac{\mathfrak{R}^{long} d_a}{2kT} \left[g_g - (g_\sigma^+ \cos \theta^+ + g_\sigma^- \cos \theta^-) \right] \quad (2.3.14)$$

In Eqs. (2.3.13), λ^- and λ^+ may be called as the wetting parameters and are given by the following expressions: $\lambda^- = g_g / 2g_\sigma^-$ and $\lambda^+ = g_g / 2g_\sigma^+$. The specific Gibbs free energy of the void surface layer may depend on the orientation of the local surface normal due to the anisotropic behavior of the surface tension γ and/or the specific Helmholtz free energy itself in crystalline solids (Defay & Prigogine, 1966).

The phenomenological mobility coefficient denoted by \mathfrak{R}^{long} , which may also be called as the reaction rate constant associated with the phase transformation. The transformation takes place continuously and reciprocally between two surface phases: 1) the interfacial void surface layer and 2) the grain boundary region just at the triple junction and may be denoted symbolically as: $\sigma \Leftrightarrow gb$. This phenomenological mobility does not make any distinction between individual chemical species and their rate of transfer over the activation energy barrier. Its temperature dependence may be given according to activated complex rate theory of chemical reactions (Yeremin, 1979) as follows:

$$\mathfrak{R}^{long} = \left(\frac{kT}{h} \right) \exp \left(- \frac{\Delta G_{\sigma,g}^*}{kT} \right) \quad (2.3.15)$$

In above expression $\Delta G_{\sigma,g}^*$ is the Gibbs free energy of activation for the transformation of surface phase into the grain boundary phase or vice versa. Eq. (2.3.14) clearly shows that in the case of thermostatic equilibrium at the triple

junction, the displacement velocity becomes identically equal to zero regardless the magnitude of the grain boundary flux. Thermostatic equilibrium establishes when the dihedral angles have reached those values, which make generalized forces given in Eqs. (2.3.10) identically equal to zero, under the assumed constrain on the triple junction, namely no lateral motion is possible. Similarly in above equation, the fluxes associated with the void surface diffusion, they may go through certain modifications in the case of anisotropic behavior of the void surface layer. For isotropic specific Gibbs free energies, $g_{\sigma}^{+} = g_{\sigma}^{-} = g_{\sigma}$, Eq. (2.3.14) takes the following form by utilizing the dimensionless wetting parameter λ , which is given by $\lambda = g_g / (2g_{\sigma})$.

$$v_g^{long} = \frac{\mathfrak{R}^{long} d_a g_{\sigma}}{2kT} \left[2\lambda - (\cos \theta^{+} + \cos \theta^{-}) \right] \quad (\text{m s}^{-1}) \quad (2.3.16)$$

One can easily show, using the technique developed in this section that IEP associated with the transverse virtual displacement of the triple junction, i.e. the motion perpendicular to the grain boundary, may be given by the following rigorous relationship;

$$\frac{\delta \Delta S_{in}^{trans}}{\delta t} = -\frac{1}{T} \left\{ \begin{array}{l} \frac{1}{2} (\tilde{g}_{vb}^{+} \Delta \ell^{+} \cos \theta^{+} - \tilde{g}_{vb}^{-} \Delta \ell^{-} \cos \theta^{-}) \\ + g_{\sigma}^{+} \sin \theta^{+} - g_{\sigma}^{-} \sin \theta^{-} \end{array} \right\} \frac{\delta \eta^{trans}}{\delta t} \geq 0 \quad (2.3.17)$$

Taking successive limits as $\Delta t \rightarrow 0$ and $\Delta \ell^\pm \rightarrow 0$, the IEP for the transverse motion of the triple junction along the designated positive direction becomes;

$$\frac{d\hat{S}_{in}^{trans}}{dt} = -\frac{1}{T} \left(g_{\sigma}^+ \sin \theta^+ - g_{\sigma}^- \sin \theta^- \right) \frac{d\eta^{trans}}{dt} \geq 0 \quad (\text{J K}^{-1} \text{ m}^{-1} \text{ s}^{-1}) \quad (2.3.18)$$

Recalling the assumption of thermal equilibrium, the projection of the dissipative force acting along the direction perpendicular to the grain boundary may be deduced from Eq. (2.3.18) as:

$$F^{trans} = g_{\sigma}^- \sin \theta^- - g_{\sigma}^+ \sin \theta^+ \quad (\text{N m}^{-1}) \quad (2.3.19)$$

This relationship together with Eq. (2.3.14) clearly shows that the triple junction (without constraint) can be in complete physico-chemical equilibrium configuration if and only if the specific interfacial Gibbs free energies associated with the grain boundary and both sides of the void surface layer satisfy the following *vectorial summation rule*: $\bar{g}_g + \bar{g}_{\sigma}^+ + \bar{g}_{\sigma}^- = 0$. The Young formula (Young, 1805) is a similar vectorial relationship between the surface tensions γ associated with the intersecting interfaces in order that mechanical equilibrium exists at the triple junction.

These findings related to the transverse virtual motion of the triple junction is important if the grain boundary migration occurs as a result of some thermally activated processes. In such a situation, the transverse component of the triple junction velocity can be obtained from Eq. (2.3.19):

$$v_g^{trans} = \frac{\mathfrak{R}_g^{trans}}{kT} d_a \left(g_{\sigma}^- \sin \theta^- - g_{\sigma}^+ \sin \theta^+ \right) \quad (\text{m s}^{-1}) \quad (2.3.20)$$

where d_a is the atomic distance and $\mathfrak{R}_g^{trans} / kT$ is the triple junction transverse mobility; a phenomenological coefficient depends on the temperature of the system through an activation energy barrier.

In the case of lateral constraint on the grain boundary motion, the generalized lateral force now generates a particle flow at and through the triple junction along the void interfacial layer to establish thermostatic equilibrium configuration there by adjusting orientations of the neighboring left and right micro-elements. The conjugate particle flux (transverse flow) associated with this force is:

$$\hat{j}_{\sigma}^{trans} = -\text{Sign}(\psi) \Gamma_g \frac{\mathfrak{R}_g^{trans}}{kT} d_a \left(g_{\sigma}^- \sin \theta^- - g_{\sigma}^+ \sin \theta^+ \right) \quad (\# \text{ m}^{-1} \text{ s}^{-1}) \quad (2.3.21)$$

In above expression the angle ψ denotes the amount of rotation of the microelements adjoint to the triple junction in the anti-clockwise direction, and *Sign* is the usual sign function. A close inspection of above flux expression reveals that it tries to eliminate any deviation from the thermostatic equilibrium at the triple junction through the dihedral angle readjustment by transferring mass from one side to another.

2.4. Global internal entropy production associated with the virtual displacement of an interface interacting with grain boundaries

The global IEP (GIEP) associated with the arbitrary virtual displacement, $d\eta/dt$, of an interfacial loop of a finite thickness separating a second phase particle v (realistic void) from the bulk multi-component matrix. In deriving the GIEP, the rate of local entropy density change along the curved interphase boundary must be integrated in order to obtain the desired relationship between generalized forces and conjugate fluxes. The rate of local entropy density change is the only extensive, integrable quantity. Therefore, not only the local internal entropy production (source term) given by Eq. (2.3.8), but also the external entropy flow term needs to be evaluated for the virtual displacement of an interface. For isothermal processes the linear combination of these two terms is given by

$$\frac{\partial \hat{S}}{\partial t} = -\frac{1}{T} \left\{ (\check{g}_{vb} + g_{\sigma\kappa}) \frac{d\eta}{dt} + \Omega_{\sigma} \left[\frac{\partial}{\partial \ell} (\check{g}_{\sigma} J_{\sigma}) + \check{g}_{\sigma} (\hat{J}_b + \hat{J}_v) \right] \right\} \quad (2.4.1)$$

where the last term represents the REF, which can be immediately obtained from Eq. (2.2.7). \hat{J}_v and \hat{J}_b are the total atomic drift diffusion fluxes at the reaction fronts separating the void and the interfacial layer and the bulk and the interfacial layer, in orientations perpendicular to and normal to the interfacial layer respectively.

The first group of terms in Eq. (2.4.1) represents the IEP. The second group of terms similarly represents, respectively, the divergence of the surface entropy flow and the possible contribution due to lateral flow of entropy due to exchange of chemical species between bulk phase and interface and/or void phase and the interface (evaporation and condensation). The interfacial layer including the void side is a completely open system (realistic void), and the displacement process is assumed isothermal. In order to calculate the global rate of entropy change along the whole curved interfacial layer, let us first take the line integral of Eq. (2.4.1) along the entire closed curved interface. Any possible singularity such as a triple junction that may be situated at a point denoted by the open interval $(-\varepsilon, \varepsilon)$ when $\varepsilon \rightarrow 0$ is excluded:

$$\int_{+\varepsilon}^{-\varepsilon} d\ell \frac{\partial \hat{S}}{\partial t} = \lim_{\varepsilon \rightarrow 0} \oint_{\varepsilon} d\ell \frac{\partial \hat{S}}{\partial t} \quad (2.4.2)$$

$$= -\frac{1}{T} \lim_{\varepsilon \rightarrow 0} \left\{ \oint_{\varepsilon} d\ell \left[(\check{g}_{vb} + g_{\sigma} \kappa) \frac{d\vec{\eta}}{dt} + \Omega_{\sigma} \left(\frac{\partial}{\partial \ell} (\check{g}_{\sigma} J_{\sigma}) + \check{g}_{\sigma} \hat{J}_{vb} \right) \right] \right\}$$

In the absence of the particle source or sink terms, the atomic flux divergence is proportional to amount of mass accumulated or depleted on a interface location, which causes the interface to move in a local normal direction. However, here we are considering more general situation namely, the additional entropy source terms associated with the normal components of the atomic flows coming from the bulk phase, and the void region due to condensation or evaporation processes which may be summarized by $\hat{J}_{vb} = \hat{J}_v + \hat{J}_b$. Hence the following rigorous expression applies

for the conservation of atomic species during the virtual displacement of curved interphases having neither variation due to stretching nor in thickness:

$$\left[(c_b - c_v) - h_\sigma \bar{\kappa} c_\sigma \right] \frac{d\eta}{dt} = \sum_i \frac{\partial J_\sigma^i}{\partial \ell} - \sum_i (\hat{J}_b^i + \hat{J}_v^i) = \frac{\partial J_\sigma}{\partial \ell} - \hat{J}_{bv} \quad (2.4.3)$$

c_b , c_v and c_σ are the atomic volumetric concentrations associated with the bulk, void and surface phases, respectively. Assuming that a realistic void is a polyatomic dilute gas in which $c_v = 0$, and $\bar{\kappa} h_\sigma = 0$ the following result is obtained:

$$\frac{d\eta}{dt} = \hat{n} \cdot \frac{\partial \vec{r}}{\partial t} = \Omega_b \left(\frac{\partial J_\sigma}{\partial \ell} - \hat{J}_{vb} \right) \quad (2.4.4)$$

where, $\Omega_b = c_b^{-1}$ is adapted from the literature (Guggenheim, 1959; Ogurtani & Oren, 2001; Wang & Suo, 1996). \hat{n} and \vec{r} are the surface normal and the position vectors, respectively.

Substituting Eq. (2.4.4) into the integrated entropy expression Eq. (2.4.2) gives:

$$\int_{+\varepsilon}^{-\varepsilon} d\ell \frac{\partial \hat{S}}{\partial t} = -\frac{\Omega_\sigma}{T} \lim_{\varepsilon \rightarrow 0} \left\{ \begin{array}{l} \int_{+\varepsilon}^{-\varepsilon} d\ell \left[(\check{g}_{vb} + g_\sigma \kappa) \frac{\partial J_\sigma}{\partial \ell} \right] - \int_{+\varepsilon}^{-\varepsilon} d\ell \left[(\check{g}_{vb} + g_\sigma \kappa) \hat{J}_{vb} \right] \\ + \int_{+\varepsilon}^{-\varepsilon} d\ell \frac{\partial}{\partial \ell} (\check{g}_\sigma J_\sigma) + \int_{+\varepsilon}^{-\varepsilon} d\ell (\check{g}_\sigma \hat{J}_{vb}) \end{array} \right\} \quad (2.4.5)$$

The first and the third group of terms on the right side of above relationship can be integrated by parts. Subsequently the rate of global entropy is split into the global IEP and the REF by carefully inspecting the individual contributions of each term (Ogurtani & Oren, 2001). The global IEP term is identified as:

$$\frac{d}{dt} S_{IEP} = \frac{\Omega_\sigma}{T} \lim_{\varepsilon \rightarrow 0} \left\{ \int_{+\varepsilon}^{-\varepsilon} d\ell \left[J_\sigma \frac{\partial}{\partial \ell} (\check{g}_{vb} + g_\sigma \kappa) \right] + \int_{+\varepsilon}^{-\varepsilon} d\ell \left[(\check{g}_{vb} + g_\sigma \kappa) \hat{J}_{vb} \right] \right\} - \left[(\check{g}_{vb} + g_\sigma \kappa) J_\sigma \right]_{-\varepsilon} + \left[(\check{g}_{vb} + g_\sigma \kappa) J_\sigma \right]_{+\varepsilon} \quad (2.4.6)$$

Similarly, we can collect those terms in Eq. (2.4.6), which are clearly related to the rate of entropy flow or in another word the external entropy contribution associated with the void surface phase excluding the triple junction as a singularity. Hence, one may write:

$$\frac{d}{dt} S_{REF} = \frac{\Omega_\sigma}{T} \lim_{\varepsilon \rightarrow 0} \left\{ - \int_{+\varepsilon}^{-\varepsilon} d\ell (\check{g}_\sigma \hat{J}_{vb}) - \left[\check{g}_\sigma J_\sigma \right]_{-\varepsilon} + \left[\check{g}_\sigma J_\sigma \right]_{+\varepsilon} \right\} \quad (2.4.7)$$

In these expressions $\check{}$ denotes volumetric densities and $\hat{}$ denotes the bulk flux intensities ($\# \text{ m}^{-2} \text{ s}^{-1}$). Here, $J_\sigma = \sum_i J_\sigma^i$ denotes the sumover surface atomic drift-diffusion (convective) fluxes ($\# \text{ m}^{-1} \text{ s}^{-1}$) in the interfacial layer. Similarly, $\hat{J}_b = \sum_i \hat{J}_b^i$ and $\hat{J}_v = \sum_i \hat{J}_v^i$ are the total atomic drift-diffusion flux densities (convective) normal to the interface, and they are coming from the adjacent bulk and void phases, respectively. In this formulation, the total convective fluxes as

well as the drift-diffusion fluxes associated with the individual chemical species are referred to the laboratory reference frame. Because, the whole interconnect material shows constant drift in the direction of the electron wind under the action of the externally applied electromigration forces having free boundary conditions at the cathode and the anode edges. Hence, neither the barycentric velocity complications of Prigogine (1961) entropy source term nor ‘the simple isotropic elastic solid crystal’ reference system (Haase, 1969) enters into the problem. However, in the total atomic drift-flux calculations, relevant summation operations do not include vacancies. Instead the rigorous identities $\hat{J}_b^V = -\hat{J}_b$ and $J_\sigma^V = -J_\sigma$ are valid. The superscript, V , denotes the vacancy drift-diffusion flux density in the relevant phase assuming that it has a crystalline structure. Without crystal structure such connection has no meaning.

In the absence of any possible singularity, the last two terms in Eqs. (2.4.6) and (2.4.7) vanish. It follows from the integrated internal entropy production, given by Eq. (2.4.6),

$$F_\sigma = \Omega_\sigma \left\{ \frac{\partial}{\partial \ell} \left[\frac{1}{T} (\tilde{g}_{vb} + g_\sigma \kappa) \right] + \vec{t} \cdot \vec{F}_{ext} \right\} \quad (2.4.8a)$$

$$F_{vb} = \Omega_\sigma \left\{ \left[\frac{1}{T} (\tilde{g}_{vb} + g_\sigma \kappa) \right] + \vec{n} \cdot \vec{F}_{ext} \right\} \quad (\text{valid for ordinary points}) \quad (2.4.8b)$$

F_σ and F_{vb} denote longitudinal and transverse generalized forces that are acting on the interfacial layer respectively. \vec{t} and \vec{n} denote unit tangent and normal vectors at the void surface, respectively. The last contribution in Eq. (2.4.8b) becomes identically zero since the normal component of the force field intensities (i.e. normal component of the electric field intensity and/or the traction) are all vanish at the void surface. The conjugate fluxes associated with the above forces are identified by using the conventional approach of linear irreversible thermodynamics for isothermal processes in the presence of conservative external force fields. The surface flux is,

$$J_\sigma = \frac{M_\sigma}{kT} \Omega_\sigma \left\{ \frac{\partial}{\partial \ell} (\tilde{g}_{vb} + g_\sigma \kappa) + \vec{t} \cdot \vec{F}_{ext} \right\} \quad (\text{surface flux}) \quad (2.4.9)$$

and the net lateral flux density responsible for the growth process is,

$$\hat{J}_{vb} = \frac{M_{vb}}{kT} \Omega_\sigma (\tilde{g}_{vb} + g_\sigma \kappa) \quad (\text{incoming net flux density}) \quad (2.4.10)$$

Cross-coupling terms between the generalized forces and fluxes has been neglected.

M_σ/k and M_{vb}/k are generalized phenomenological mobilities associated with the respective conjugated forces and fluxes, and k is Boltzmann's constant.

For multi-component systems, where we are interested only in the net atomic (mass) transport regardless to the contributions of individual chemical species, the first generalized-mobility given above may not be easily connected to any combination of the intrinsic surface diffusivities of individual chemical species in the interfacial layer or in the bulk phase. However, for one component system having minor amount of doping elements or impurities, the situation is rather simple where one can easily identify the existence of the following relationship between generalized mobility and the surface self-diffusivity of host matter denoted by \tilde{D}_σ ,

$$\hat{M}_\sigma = \frac{M_\sigma}{kT} = \frac{\tilde{D}_\sigma}{kT} \frac{h_\sigma}{\Omega_\sigma} = \frac{\tilde{D}_\sigma}{kT} \Gamma_\sigma, \quad (2.4.11)$$

\hat{M}_σ may be called surface atomic mobility, and it has the dimension given by ($J^{-1} s^{-1}$). The generalized mobility M_{vb} ($m^2 s^{-1}$) associated with the incoming bulk diffusion flux is related to the transformation rate of chemical species from bulk phase to the interfacial layer or vice versa over the activation energy barrier denoted by ΔG_{vb}^* . Hence, it can be defined according to the transition rate theory of chemical kinetics advocated by Yereimin (1979), as:

$$M_{vb} = \left(\frac{kT}{h} \right) \exp \left(- \frac{\Delta G_{vb}^*}{kT} \right) \quad (2.4.13)$$

Here, h is the Planck's constant. The mobility given in Eq. (2.4.13) may also be used in the following normalized form:

$$\hat{M}_{vb} = \frac{M_{vb}}{kT} \quad (\text{m}^2 \text{ J}^{-1} \text{ s}^{-1}) \quad (2.3.20)$$

CHAPTER 3

MATHEMATICAL MODEL AND NUMERICAL PROCEDURES

3.1. Equations of motion for the ordinary and the triple points

The general form of conservation law in physics is employed to obtain the normal displacement velocity of an *ordinary* point, v_{σ}^{ord} on a surface;

$$\frac{v_{\sigma}^{ord}}{\Omega_{\sigma}} = \hat{n} \cdot \frac{\partial \vec{r}}{\partial t} = \nabla \cdot J_{\sigma} - \hat{J}_{vb} \quad (3.1.1)$$

Eq. (3.1.1) simply states that the rate of change of the position of a particle in a direction of normal to the surface is due to the sources (sinks) of that particle (\hat{J}_{vb} ; # m⁻² s⁻¹) and due to the divergence of the flux of that particle (J_{σ} ; # m⁻¹ s⁻¹).

Here, as can be understood from the context, \hat{n} and \vec{r} are the surface normal and the position vectors, respectively (see figure 1.2.1). Ω_{σ} is defined as the mean atomic volume of chemical species at the surface.

The conservation law given above is not very meaningful as long as we do not provide expressions for the source and flux. The notations \hat{J}_{vb} and J_σ are due to chapter 2, in which relevant equations were derived by a rigorous linear irreversible treatment of surfaces and interfaces with triple junction singularities. The normal displacement velocity for the ordinary points can be obtained by substituting the surface flux, given by Eq. (2.4.9), and the incoming net lateral flux density, given by Eq. (2.4.10), to Eq. (3.1.1):

$$v_\sigma^{ord} = \frac{\Omega_\sigma^2}{kT} \frac{\partial}{\partial \ell} \left[M_\sigma \left\{ \frac{\partial}{\partial \ell} (\check{g}_{vb} + g_\sigma \kappa) + \vec{t} \cdot \vec{F}_{Ext} \right\} \right] - M_{vb} (\check{g}_{vb} + g_\sigma \kappa) \quad (3.1.2)$$

Here ℓ represents the curvilinear coordinate along the surface (arc length). Eq. (3.1.2) is the most general form of the equation of motion for ordinary points. Considering only the diffusion of chemical species (ignoring the growth term) and by using the Nernst-Einstein relation between the atomic mobility and the surface self-diffusivity of host matter, given by Eq. (2.4.11), we obtain the following evolution equation or the equation of motion for an ordinary point on the surface in its simplest form used in the current work:

$$v_\sigma^{ord} = \frac{\Omega_\sigma h_\sigma}{kT} \frac{\partial}{\partial \ell} \left(D''(\phi, \theta) \frac{\partial}{\partial \ell} \left(\frac{1}{2} \underline{\underline{\sigma}} : \underline{\underline{\varepsilon}} + g_\sigma \kappa \right) + \vec{t} \cdot \vec{F}_{ext} \right) \quad (\text{m s}^{-1}) \quad (3.1.3)$$

where, the angular dependent post factor $D''(\phi, \theta)$ denotes that the surface drift-diffusion is anisotropic. Here, $\underline{\underline{\sigma}}$, and $\underline{\underline{\varepsilon}}$ are the stress and strain tensors; the double

bar signs under the symbols is to designate tensorial quantities and double dot defines double scalar product of the two tensors. In Eq. (3.1.3) only the stress dependent parts of the specific Gibbs free energy density of bulk phase evaluated adjacent to the interfacial layer (the reaction zone) has been incorporated (Ogurtani & Oren, 2005).

On the other hand, the triple junction velocity in the direction along the grain boundary was readily given in chapter 2 by Eq. (2.3.16):

$$v_g^{long} = \frac{\mathfrak{R}^{long} d_a g_\sigma}{2kT} \left[2\lambda - (\cos \theta^+ + \cos \theta^-) \right] \quad (\text{m s}^{-1}) \quad (3.1.4)$$

Finally, the following boundary conditions for the triple junction in terms of the right and the left side fluxes can be deduced from Eqs. (2.3.13) and (2.3.21):

$$\begin{aligned} \hat{J}_o^\pm = \pm \Gamma_g \frac{\mathfrak{R}^{long} d_a}{2kT} g_\sigma (\lambda - \cos \theta^\pm) \pm \hat{J}_g / 2 + \hat{J}_g \\ - \Gamma_g \frac{\mathfrak{R}_g^{trans} d_a}{kT} g_\sigma (\sin \theta^- - \sin \theta^+) \end{aligned} \quad (\# \text{ m}^{-1} \text{ s}^{-1}) \quad (3.1.5)$$

where \hat{J}_g and \hat{J}_g denote the normalized atomic fluxes associated with grain boundary flow, and the drift-diffusion due to external force fields.

In the formulation of the stress induced driving force for the atomic migration, there is a wide spread confusion, as detailed in chapter 1, whether to use elastic strain

energy density function or the strain field interaction potential as suggested by Kröner (1958) and extensively used by Ogurtani and Seeger (1984). Similarly, the basic concept of chemical potential is highly distorted, and the historical warnings of Gibbs and later by Guggenheim against the splitting of μ_i into parts have been completely ignored or forgotten. Below, an irreversible thermodynamic formulation of external driving forces on the flow of matter is presented using the lattice as a reference frame, which is more suitable here rather than the center of mass as employed by Prigogine in his monumental work (Prigogine, 1961) for the treatment of continuum media without structure.

The external conservative generalized forces (per particle) associated with the electromigration and the strain field interactions for chemical species ‘i’ in a phase denoted by α subscript may be presented by the following relationships, respectively (Ogurtani & Oren, 2001):

$$\vec{F}_g^i = -\frac{eZ^i}{T} \nabla \vartheta \quad (\text{N \#}^{-1}) \quad (3.1.6a)$$

$$\vec{F}_\varepsilon^i = \frac{\Omega_\alpha}{T} \nabla (\underline{\lambda}_s^i : \underline{\underline{\sigma}}) \quad (\text{N \#}^{-1}) \quad (3.1.6b)$$

Here, ϑ is the electrostatic potential. Similarly, the generalized external total force density (per unit volume) associated with these electromigration and the strain energy interactions and acting on particles may have the following form for a multi-

component system assuming that $\underline{\lambda}_s^i$ is homogeneous function of space, $\nabla \underline{\lambda}_s^i \cong 0$, whether it is a bulk phase or an interfacial layer:

$$\vec{F}_{ext} = -\frac{1}{T\Omega_\alpha} \left(\sum_i x_\alpha^i \cdot eZ_\alpha^i \right) \cdot \nabla \mathcal{G} + \frac{1}{T} \left(\sum_i x_\alpha^i \cdot \underline{\lambda}_s^i \right) : \nabla \underline{\underline{\sigma}} \quad (\text{N m}^{-3}) \quad (3.1.7)$$

where, x^i denote the atomic fractions. According to the Onsager theory, the total conjugate flux intensity becomes:

$$\vec{J}_{ext}^\alpha = -\frac{M_\alpha}{kT\Omega_\alpha} \left[\left(\sum_i x_\alpha^i \cdot eZ_\alpha^i \right) \cdot \nabla \mathcal{G} - \Omega_\alpha \left(\sum_i x_\alpha^i \cdot \underline{\lambda}_s^i \right) : \nabla \underline{\underline{\sigma}} \right] \quad (\# \text{ m}^{-2} \text{ s}^{-1}) \quad (3.1.8)$$

which is valid for any three or two dimensional phases with lattice structures. Here Ω_α is the mean atomic volume of species in alpha phase and M_α is the phenomenological mobility associated with the net flow of particles (where M_α / k is the cross coupling coefficient). In above expressions, $Z_\alpha^i \leq 0$ and $\underline{\lambda}_s^i$ are effective electromigration charge and the elastic dipole tensor of the individual chemical species denoted by 'i' in a given phase, which may be bulk phase or an interphase. Eqn. (3.1.8) indicates that the multi-component systems exposed to electrostatic as well as elastostatic stress fields can easily be treated by utilizing average values of the effective charge and the elastic dipole tensor, which may be denoted by Z and $\underline{\lambda}_s$. One can easily conjecture that this means elastic dipole tensor is identically equal (with a sign inversion) to the elastic dipole tensor of vacancies responsible for

the hopping motion of individual chemical species. In case of self-interstitial diffusion, the situation becomes more complicated.

Using Eq. (3.1.8), the differential expression related to the ordinary points can be put into the following format:

$$v_{\sigma}^{ord} = \frac{\Omega_{\sigma} h_{\sigma}}{kT} \frac{\partial}{\partial \ell} \left(D^n \frac{\partial}{\partial \ell} \left(g_{\sigma} \kappa + \frac{1}{2} \underline{\underline{\sigma}} : \underline{\underline{\varepsilon}} + \underline{\underline{\lambda}}_s : \underline{\underline{\sigma}} + q^* \frac{g}{\Omega_{\sigma}} \right) \right) \quad (\text{m s}^{-1}) \quad (3.1.9)$$

Here, the second term in the innermost parenthesis is the elastic strain energy density (ESED) contribution, and the third term designates the elastic dipole tensor interactions (EDTI) which measure the intensity of the elastic interaction between the elastic strain field tensor, $\underline{\underline{\lambda}}_s$, associated with the mobile chemical species (i.e., adatom or the mobile atom mono-vacancy pair) at the surface layer and the surface (hoop) stress system generated by applied surface tractions and/or body forces on the bulk medium. The last term in Eq. (3.1.9) is due to electromigration (EM) forces where $q^* = e|Z|$ called the surface effective charge.

In stress calculations we assume plain strain condition for a thin film which is characterized by an invariant loading along z -direction. Then the displacement field takes the form: $u(x, y)$, $v(x, y)$, $w = 0$. From the strain displacement relations, we find that only the three in-plane strains are nonzero: $\varepsilon_{xx}(x,y)$, $\varepsilon_{yy}(x,y)$, $\varepsilon_{xy}(x,y)$, and three out-of-plane strains vanish: $\varepsilon_{zz} = \varepsilon_{xz} = \varepsilon_{yz} = 0$. Further we assume that the shear components are also equal to zero: $\varepsilon_{xy}(x,y) = 0$.

The state of stress and strain is then:

$$\varepsilon = \begin{pmatrix} \varepsilon_{xx} & 0 & 0 \\ 0 & \varepsilon_{yy} & 0 \\ 0 & 0 & 0 \end{pmatrix} \quad \sigma = \begin{pmatrix} \sigma_{xx} & 0 & 0 \\ 0 & \sigma_{yy} & 0 \\ 0 & 0 & \sigma_{zz} \end{pmatrix} \quad (3.1.10)$$

From the generalized Hook's law:

$$\varepsilon_{zz} = \frac{1}{E} (\sigma_{zz} - \nu\sigma_{xx} - \nu\sigma_{yy}) = 0 \quad (3.1.11)$$

$$\Rightarrow \sigma_{zz} = \nu(\sigma_{xx} + \sigma_{yy})$$

Substituting Eq. (3.1.11) in (3.1.10), the trace of the Cartesian stress tensor is obtained as follows:

$$Tr(\underline{\underline{\sigma}}) = (1 + \nu)(\sigma_{xx} + \sigma_{yy}) \quad (3.1.12)$$

The hoop stress in local coordinates is defined by $\sigma_h = \hat{t} \cdot \underline{\underline{\sigma}} \cdot \hat{t}$, where \hat{t} is the unit surface tangent vector. Then, in plane strain condition, for traction free surface above equation is represented by:

$$Tr(\sigma) = (1 + \nu)\sigma_h \quad (3.1.13)$$

Here ν is the Poisons' ratio, E is the elastic modulus and subscript h stands for the *hoop*. Similarly, the stress – strain connection takes the following form:

$$\begin{aligned}\varepsilon_{xx} &= \frac{1}{E} \left(\sigma_{xx} - \nu \sigma_{yy} - \nu \sigma_{zz} \right) \\ \Rightarrow \varepsilon_{xx} &= \frac{1}{E} \left(\sigma_{xx} - \nu \sigma_{yy} - \nu^2 (\sigma_{xx} + \sigma_{yy}) \right) \\ \Rightarrow \varepsilon_{xx} &= \frac{1-\nu^2}{E} \left(\sigma_{xx} - \frac{\nu}{1-\nu} \sigma_{yy} \right)\end{aligned}\tag{3.1.14}$$

And, for traction free surface in local coordinates:

$$\varepsilon_h = \frac{1-\nu^2}{E} \sigma_h\tag{3.1.15}$$

On the other hand, in the case of isotropic mobile defects which have vanishing deviatoric part, the elastic strain field tensor associated with the mobile chemical species at the surface layer can be put into following form using the hydrostatic part:

$$\underline{\underline{\lambda}}_s \equiv \left(1/3 Tr \underline{\underline{\lambda}}_s \right) \hat{\underline{\underline{I}}}\tag{3.1.16}$$

where $\hat{\underline{\underline{I}}}$ is the idempotent tensor.

Then, by performing the double scalar products in Eq. (3.1.9) yields the evolution equation for ordinary points in real time and space as:

$$v_{\sigma}^{ord} = \frac{\Omega_{\sigma} h_{\sigma}}{kT} \frac{\partial}{\partial \ell} \left(D'' \frac{\partial}{\partial \ell} \left(g_{\sigma} \kappa + \frac{1}{2} \sigma_h^2 \frac{(1-\nu^2)}{E} + \frac{Tr(\lambda_s)}{3} (1+\nu) \sigma_h + q^* \frac{\rho}{\Omega_{\sigma}} \right) \right) \quad (3.1.17)$$

Eqs. (3.1.4, 5) and (3.1.17) are the necessary equations to govern the profile evolution of surfaces with triple junction singularities which are exposed to capillary, electromigration and elastostatic forces on a physical domain, whose specification is left to section 3.3.

3.2. Normalization and scaling

The evolution equations given by Eqs. (3.1.4, 5) and (3.1.17) will be normalized and scaled in the following manner. First of all we will look to a similarity criterion for the two systems given in figure 3.2.1.

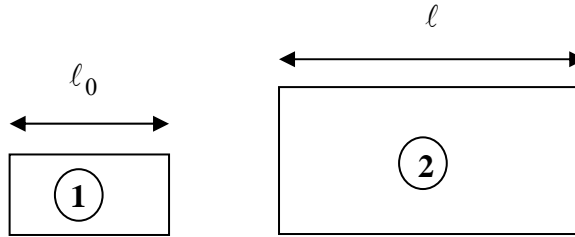


Figure 3.2.1: Schematic representation of the two systems subjected to dimensional analysis.

In this section the subscripts, σ , which was used to denote that a property is associated with the interfacial or surface layer, is dropped out in order to ease the

presentation. With the very same purpose the symbol δ is used to denote the interface thickness, and symbol λ for elastic strain field tensor instead of using h_σ and $\underline{\lambda}_s$. In looking at Eq. (3.1.17) we require similarity in:

$$\text{Geometry: } \ell = C_L \ell_0 \quad (3.2.1a)$$

$$\text{Time: } t = C_t t_0 \quad (3.2.1b)$$

$$\text{Displacement normal to the surface: } u = C_u u_0 \quad (3.2.1c)$$

$$\text{Curvature: } \kappa = C_\kappa \kappa_0 \quad (3.2.1d)$$

$$\text{Surface Gibbs free energy: } g = C_g g_0 \quad (3.2.1e)$$

$$\text{Surface effective charge: } q^* = C_{q^*} q_0^* \quad (3.2.1f)$$

$$\text{Electrostatic potential: } \vartheta = C_\vartheta \vartheta_0 \quad (3.2.1g)$$

$$\text{Stress: } \sigma = C_\sigma \sigma_0 \quad (3.2.1h)$$

$$\text{Elastic strain field tensor: } \lambda = C_\lambda \lambda_0 \quad (3.2.1i)$$

$$\text{Elastic modulus: } E = C_E E_0 \quad (3.2.1j)$$

$$\text{Surface diffusivity: } D = C_D D_0 \quad (3.2.1k)$$

$$\text{Interface thickness: } \delta = C_\delta \delta_0 \quad (3.2.1l)$$

$$\text{Mean atomic volumes of chemical species at the surface: } \Omega = C_\Omega \Omega_0 \quad (3.2.1m)$$

Here C 's are the similarity constants. Writing Eq. (3.1.17) for 1 of figure 3.2.1 for the case of isotropic diffusivity yields:

$$\frac{\partial u_o}{\partial t_o} = \frac{D_o \delta_o}{kT} \frac{\partial^2}{\partial \ell_o^2} (\Omega_o g_o \kappa_o + \frac{\Omega_o (1-\nu^2)}{2E_o} \sigma_o^2 + \Omega_o \frac{|Tr(\lambda_o)|(1+\nu)}{3} \sigma_o + q_o^* g_o) \quad (3.2.2)$$

Similarly, for 2 of figure 3.2.1:

$$\frac{\partial u}{\partial t} = \frac{D\delta}{kT} \frac{\partial^2}{\partial \ell^2} (\Omega g \kappa + \frac{\Omega (1-\nu^2)}{2E} \sigma^2 + \Omega \frac{|Tr(\lambda)|(1+\nu)}{3} \sigma + q^* g) \quad (3.2.3)$$

Substituting Eqs (3.2.1) to (3.2.3) yields:

$$\begin{aligned} \frac{C_u}{C_t} \frac{\partial u_o}{\partial t_o} &= \frac{C_D C_\delta D_o \delta_o}{kT} \frac{1}{C_L^2} \frac{\partial^2}{\partial \ell_o^2} (C_\Omega C_g C_\kappa \Omega_o g_o \kappa_o + \frac{C_\Omega C_\sigma^2 \Omega_o (1-\nu^2)}{2E} \sigma_o^2 \\ &\quad + C_\Omega C_\lambda C_\sigma \Omega_o \frac{|Tr(\lambda_o)|(1+\nu)}{3} \sigma_o + C_{q^*} C_g q_o^* g_o) \end{aligned} \quad (3.2.4)$$

Now, comparing Eqs (3.2.2) and (3.2.4) reads:

$$\begin{aligned} \frac{C_u}{C_t} &\equiv \frac{C_D C_\delta}{kT} \frac{1}{C_L^2} C_\Omega C_g C_\kappa \equiv \frac{C_D C_\delta}{kT} \frac{1}{C_L^2} \frac{C_\Omega C_\sigma^2}{C_E} \equiv \frac{C_D C_\delta}{kT} \frac{1}{C_L^2} C_\Omega C_\lambda C_\sigma \\ &\equiv \frac{C_D C_\delta}{kT} \frac{1}{C_L^2} C_{q^*} C_g \end{aligned} \quad (3.2.5)$$

Then, following identities may be written:

$$\frac{C_\sigma^2}{C_E C_g C_\kappa} = 1, \quad \frac{C_\lambda C_\sigma}{C_g C_\kappa} = 1, \quad \frac{C_{q^*} C_g}{C_\Omega C_g C_\kappa} = 1 \quad (3.2.6)$$

Substituting Eqs (3.2.1) into (3.2.6) and using the basic relations for curvature ($\kappa_0 = 1/\ell_0$) and electrostatic potential ($\mathcal{G}_0 = E_\infty \ell_0$) yields:

$$\Sigma = \frac{1}{2} \frac{\sigma^2 \ell (1-\nu^2)}{Eg} = \frac{1}{2} \frac{\sigma_o^2 \ell_o (1-\nu^2)}{E_o g_o} \quad (3.2.7a)$$

$$\Xi = \frac{1}{3} \frac{|tr(\lambda)|(1+\nu)\sigma \ell}{g} = \frac{1}{3} \frac{|tr(\lambda_o)|(1+\nu)\sigma_o \ell_o}{g_o} \quad (3.2.7b)$$

$$\chi = \frac{q^* E_\infty \ell^2}{\Omega g} = \frac{q_o^* E_\infty \ell_o^2}{\Omega_o g_o} \quad (3.2.7c)$$

These dimensionless parameters may be called as the elastic strain energy density parameter (Σ ; ESED), the elastic dipole tensor interaction parameter (Ξ ; EDTI) and the electronwind intensity parameter (χ ; EWI) and all describe the relative strengths of applied forces with respect to the capillarity.

Now, knowing that similarity requires Eqs. (3.2.7) we can rewrite Eq. (3.1.17) as:

$$\frac{\ell_o \partial \frac{u}{\ell_o}}{\Omega g \partial t} = \frac{D_o}{kT} \frac{D}{D_o} \delta \frac{\partial^2}{\ell_o^2 \partial \left(\frac{\ell}{\ell_o}\right)^2} \left(\begin{array}{l} \kappa \frac{\ell_o}{\ell_o} + \frac{\Omega}{2E} \frac{(1-\nu^2)}{\Omega g} \frac{\ell_o}{\ell_o} \sigma_o^2 \frac{\sigma^2}{\sigma_o^2} \\ + \Omega \frac{|tr(\lambda)|}{3} \frac{(1+\nu)}{\Omega g} \frac{\ell_o}{\ell_o} \sigma_o \frac{\sigma}{\sigma_o} + \frac{q^*}{\Omega g} \frac{\ell_o}{\ell_o} E_\infty \ell_o \frac{\mathcal{G}}{E_\infty \ell_o} \end{array} \right)$$

$$\Rightarrow \frac{\ell_o^4 kT}{\Omega g D_o \delta} \frac{\partial \bar{u}}{\partial t} = \bar{D} \frac{\partial^2}{\partial \bar{\ell}^2} (\bar{\kappa} + \Sigma \bar{\sigma}^2 + \Xi \bar{\sigma} + \chi \bar{\vartheta}) \quad (3.2.8)$$

From this context one may specify a time scale, τ_o , as:

$$\tau_o = \frac{\ell_o^4 kT}{\Omega g D_o \delta} \quad (3.2.9)$$

Then, the evolution equation for ordinary points in normalized and scaled time and space (NSTS) is:

$$\frac{\partial \bar{u}}{\partial \bar{t}} = \bar{v}_\sigma^{ord} = \frac{\partial}{\partial \bar{\ell}} \left(\bar{D} \frac{\partial}{\partial \bar{\ell}} (\bar{\kappa} + \Sigma \bar{\sigma}^2 + \Xi \bar{\sigma} + \chi \bar{\vartheta}) \right) \quad (3.2.10)$$

In which, following normalizations have been used:

$$\bar{\ell} = \ell / \ell_o, \quad \bar{u} = u / \ell_o, \quad \bar{\kappa} = \kappa \ell_o, \quad \bar{D} = D / D_o, \quad (3.2.11a)$$

$$\bar{t} = t / \tau_o, \quad \bar{\sigma} = \sigma / \sigma_o, \quad \bar{\vartheta} = \vartheta / E_\infty \ell_o \quad (3.2.11b)$$

Here σ_o is the nominal uniaxial stress applied at the edges of the specimen.

Eqs. (3.1.4, 5) could also be transformed into NSTS in a similar way. In doing so,

\hat{M}^{long} and \hat{M}^{trans} which correspond to the longitudinal and transverse triple

junction mobilities, can be normalized with respect to the mobility of the surface diffusion denoted by \hat{M}_σ :

$$\bar{M}^{long} = \frac{\hat{M}^{long}}{\hat{M}_\sigma}, \quad \bar{M}^{trans} = \frac{\hat{M}^{trans}}{\hat{M}_\sigma} \quad (3.2.12)$$

where,

$$\hat{M}^{long} = \frac{\mathfrak{R}^{long}}{kT} \frac{h_g}{\Omega_g}, \quad \hat{M}^{trans} = \frac{\mathfrak{R}^{trans}}{kT} \frac{h_\sigma}{\Omega_\sigma}, \quad \hat{M}_\sigma = \frac{D_\sigma^0}{kT} \frac{h_\sigma}{\Omega_\sigma} \quad (3.2.13)$$

Then, equations governing the triple junction motion in NSTS are given as follows:

$$\bar{v}_g^{long} = \bar{M}^{long} \frac{\bar{\Omega}_g \bar{d}_a}{2\bar{\Omega}_\sigma^2 \bar{h}_g} \left[2\lambda - (\cos \theta^+ + \cos \theta^-) \right] \quad (3.2.14)$$

$$\bar{J}_o^\pm = \pm \bar{M}^{long} \frac{\bar{d}_a}{2\bar{\Omega}_\sigma^2} (\lambda - \cos \theta^+) \pm \frac{\bar{J}_g}{2} + \bar{J}_g - \bar{M}^{trans} \frac{\bar{d}_a}{2\bar{\Omega}_\sigma^2} (\sin \theta^- - \sin \theta^+) \quad (3.2.15)$$

3.3. Physical model; the boundary conditions in normalized and scaled time and space

On a silicon chip interconnects are made of several levels of Al or Cu lines. Silicon dioxide fills the space in between to provide insulation. The whole structure is a metal network embedded in an oxide matrix. The tungsten studs serves as vias to link interconnect lines between different levels. TiAl₃, TiN coatings shunt the electric current where voids deplete the metallic Al or Cu (Z. Suo, 1998).

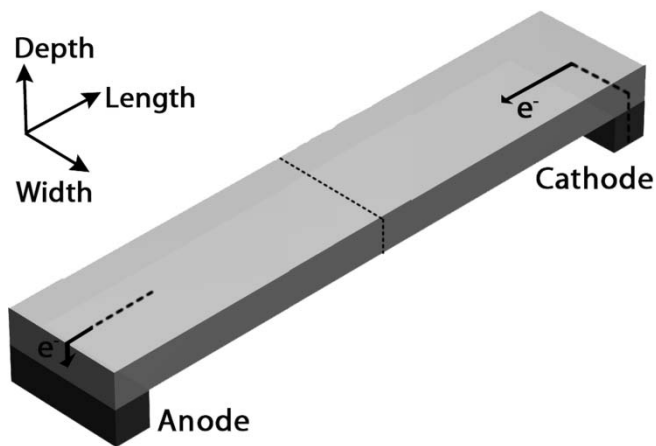


Figure 3.3.1: Isometric view of a thin metallic bi-crystal thin film with a vertical grain boundary separating it into two grains and in contact with electrode pads.

In the present case, we model a thin interconnect film with a with a vertical grain boundary separating it into two grains as sketched in figure 3.3.1. It is assumed that the sample sandwiched with a top and bottom high resistance (TiAl₃, TiN etc)

coatings, which together with the substrate constitute diffusion barrier layers. It is also assumed that the film bonds weakly to these coatings, and only the sidewalls and the edges of the interconnect lines are subjected to the surface drift-diffusion, which are exposed to environment (air) whose conductivity is neglected in this study.

Such a film is assumed to be exposed to an electric field applied far away from its edges and subject to a stress system resembling to residual stress state after its thermal processing and during operational conditions.

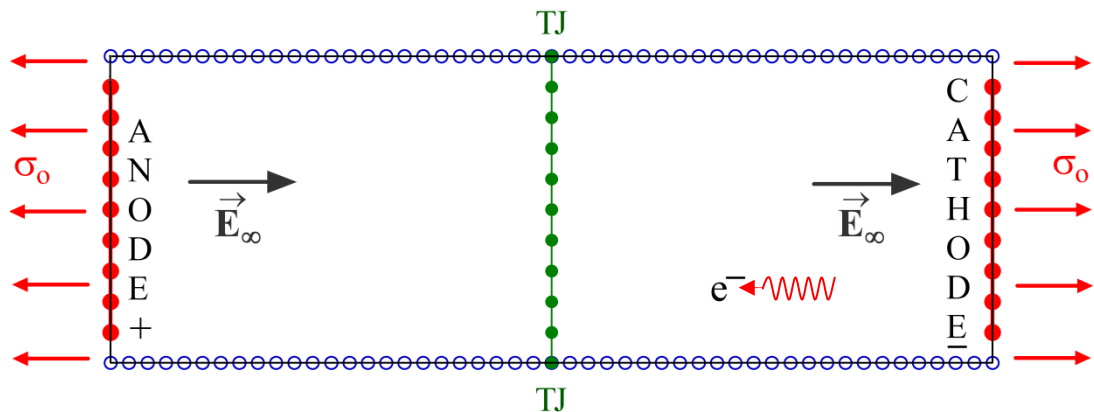


Figure 3.3.2: The schematic representation of the problem. Sidewalls (blue circles) are subject to Neumann, and the edges (domain boundaries that are perpendicular to the x-axis; red dots) subject to the Dirichlet boundary conditions in considering both elasto and electrostatics problems.

The physical model discussed in this section is two-dimensional. In most applications, such an assumption is physically valid since the thickness of metallization lines are usually small ($\approx 2000 - 5000 \text{ \AA}$) compared with the line width. The only reason to make such an approximation is to simplify the mathematical analysis and also to reduce the computation time.

In considering Eq. (3.2.10) note that both electrostatic potential and stress fields (scalar) should be calculated. These are handled in discretized space by solving the electro-elastostatic problem at each time step by using the indirect boundary element method (IBEM). As an initial condition, a flat surface and a freshly formed grain boundary, which cuts the crystal straight into two segments (bi-crystal) is selected as in figure 3.3.2. Therefore, the initial configuration of the system, which may be exposed to the uniform external electro-elastostatic fields, is far from the thermostatic equilibrium state that is mostly assumed as granted by investigators in the literature.

In the computation of the electrostatic potential at the free surface layer, which is exposed to air, we will set the electromigration boundary conditions such that the normal component of the electric field intensity vector is identically equal to zero. At the cathode and anode pads, we will assume that an adaptive external potential difference is applied in order to maintain a constant current flow during the evolution period, regardless the variation of the electrode contact areas there. In this problem, one is seeking the solution of the Laplace equation in a two dimensional domain that is given by the following equation:

$$\nabla^2 \mathcal{G} = 0 \quad (3.3.1a)$$

with the following Neumann boundary conditions at the sidewalls of figure 3.3.2:

$$\hat{n} \cdot \nabla \mathcal{G} = 0 \quad (3.3.1b)$$

Finally with the Dirichlet boundary conditions at the vertical ends of the film, where the electrodes are attached,

$$\mathcal{G} = \pm \mathcal{G}_0 \quad (3.3.1c)$$

Eqs. (3.3.1) describe a distribution of voltage inside a homogenous medium of constant resistance. Here the scalar function \mathcal{G} is the electrostatic potential at the boundaries.

For an isotropic linear elastic material at rest in its strained condition in the absence of body forces, we have the following system of equations,

$$\nabla \cdot \underline{\underline{\sigma}} = 0 \quad (\text{Force equilibrium equations}) \quad (3.3.2a)$$

$$\underline{\underline{\sigma}} = \lambda \hat{I} \text{Tr} \underline{\underline{\epsilon}} + 2\mu \underline{\underline{\epsilon}} \quad (\text{Stress – strain connections, i.e. Hooke's law}) \quad (3.3.2b)$$

$$\underline{\underline{\varepsilon}} = \frac{1}{2}(\nabla \underline{u} + \underline{u} \nabla) \quad (\text{Strain – displacement relations}) \quad (3.3.2c)$$

Here once again the double bars under any symbol indicates dyadic (the second-order tensor or matrix), and single bars indicates vector quantity. $\underline{\underline{\varepsilon}}$ is the elastic (pure) strain field given in terms of displacement vectors \underline{u} , which should satisfy the compatibility conditions presented by (Weatherburn, 1954; Fung, 1965):

$$\nabla \times \underline{\underline{\varepsilon}} \times \nabla = 0 \quad (\text{Compatibility requirements}) \quad (3.3.2d)$$

This equation gives six identical relationships between the components of strain in 3D space. For the plain strain case the six compatibility equations may be reduced with a reasonable accuracy to a single equation (Mase, 1970):

$$\varepsilon_{xx,yy} + \varepsilon_{yy,xx} = 2\varepsilon_{xy,xy} \quad (\text{Compatibility requirement for plane strain}) \quad (3.3.2e)$$

If we substitute Eqs. (3.3.2b, c) into the stress equilibrium equation represented by Eq. (3.3.2a), we obtained the following generalized Navier's equation in the dyadic format, where λ and μ are the Lamé's elastic constants for isotropic materials:

$$(\lambda + \mu)\nabla \nabla \cdot \underline{u} + \mu \nabla^2 \underline{u} = 0 \quad (\text{Navier's equation}) \quad (3.3.3a)$$

Here, one may recall the following useful identities: $Tr \underline{\underline{\varepsilon}} = \nabla \cdot \underline{u}$, $\nabla \cdot \nabla \underline{u} = \nabla^2 \underline{u}$, $\nabla \cdot \underline{u} \nabla = \nabla^2 \underline{u}$, and $\nabla \cdot \underline{\hat{I}} = \underline{\hat{I}} \cdot \nabla = \nabla$, where $\underline{\hat{I}}$ is idempotent tensor, and the explicit definition of ∇ , the delta vector operator in the Cartesian coordinate system may be given by: $\nabla \equiv \hat{i}_k \frac{\partial}{\partial x_k}$, using the Einstein summation rule.

Eq. (3.3.3a) subject to Dirichlet type boundary conditions with prescribed (fixed) displacements at the vertical ends of the film:

$$\underline{u} = 0 \quad (3.3.3b)$$

And the sidewall surfaces are assumed to be traction free, i.e. subject to Neumann boundary conditions:

$$\underline{T} = \hat{n} \cdot \underline{\underline{\sigma}} = 0 \quad (3.3.3c)$$

Once the solutions to both Eqs. (3.3.2) and (3.3.3) are obtained by the use of the indirect boundary element method (IBEM) at each time step, film profile is updated by surface diffusion using Eqs. (3.2.4, 5) and (3.2.10). For a disconnected interfacial layer (finite or infinite) such as one or two-grain sector of interconnect, the additional boundary conditions should be set at the end points of the metallic line for the surface diffusion problem, where the direct contact with electrodes through an interface does exist or not.

Depending upon the experimental conditions in the laboratory testing and the interaction of the test piece with its immediate surroundings one can identify three types of boundary conditions excluding the periodic boundary condition which we have employed in the current study; the reflecting, interactive-barrier and the free moving boundary conditions (Ogurtani & Akyildiz, 2005).

The reflecting boundary condition is also known as insulating BC, does not allow any material flow or leakage due to drift-diffusion caused by chemical, capillary and electromigration forces at the anode and/or cathode edges.

The interactive-barrier BC on the other hand should be taken into account where the capillary reaction (wetting) is taking place at the contact layer between electrode and the interconnect material. This boundary condition is very similar to the grain boundary surface interaction problem (one-sided GB) with one modification, namely the interfacial layer between electrode pad and the edge of the interconnect line stays rigid and impermeable to drift-diffusion flux. However, the contact area will diminish or increase due time. This boundary condition is especially very suitable for the anode side of the interconnect structures, which results a hillock formation at that edge with proper topology, rather than the ordinary up-hill mass accumulation resulted from the application of the reflection BC. It can be also used for the cathode edge, up to the point where the detachment of the interconnect from the electrode pad occurs, which normally indicates catastrophic cathode failure.

Finally, the free-moving BC assumes that there is no direct contact with electrode pads at the cathode and/or anode edges. All these boundary conditions were employed in our previous studies (Akyildiz, 2004; Ogurtani & Akyildiz, 2005, 2008a) and the computer code given in Appendix B is capable of employing them.

3.4. Numerical procedures

We consider an interconnect system composed of two grains and naturally having two triple junctions associated with a grain boundary as illustrated in figure 3.3.2. The interconnect system is considered to be groove free at the beginning and appeared as a collection of nodes as a result of discretization, forming predetermined segment lengths.

Although the model is two dimensional; however, node positions are stored in 3x1 matrices in order to make use of vector algebra. Once node, node centroid positions and segment lengths are introduced, turning angles (or angle between two successive segments), local boundary normal vectors and the node curvatures (in connection with the fundamental definition of radius of curvature), are calculated by using discrete geometric relationships.

As stated before in the evaluation of the electrostatic potential as well as the hoop stress along the perturbed sidewalls of the thin metallic film the indirect boundary element method (IBEM) that employs the straight constant line elements have been utilized (Beer & Watson, 1992; Brebbia & Dominguez, 1992; Beer et al., 2008).

Comparing with finite element method (FEM), IBEM requires less number of nodes, less computing time, and storage but offers higher accuracy and efficiency in analysis, especially in analysis of thin structures (Beer & Watson, 1992). For the solution of the resulted system of linear equations LU factorization with partial pivoting has been employed (Mathews, 1992).

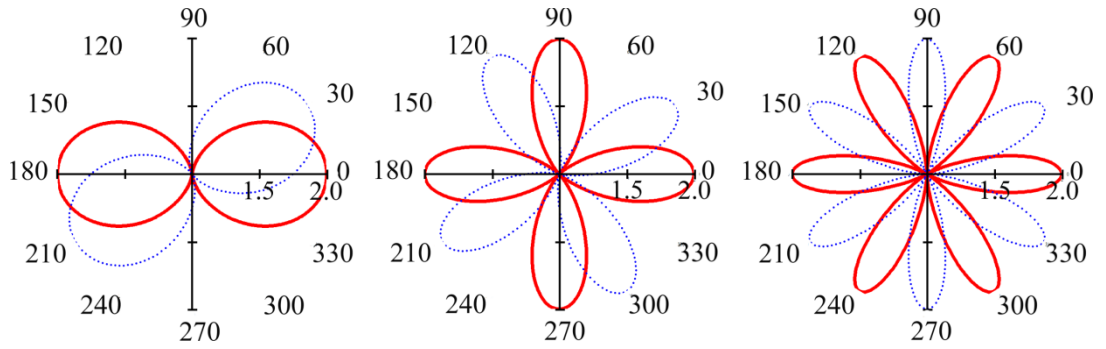


Figure 3.4.1: Orientation dependence of the normalized surface diffusivities with, $A=1$, $\phi = 0^\circ$ (solid red curves) and $\phi = 30^\circ$ (dashed blue curves) respectively for $m=1 \rightarrow (110)$, $m=2 \rightarrow (100)$ and $m=3 \rightarrow (111)$ planes.

The anisotropic diffusivity of surface atoms is incorporated into the numerical procedure by adapting the following relationship,

$$\bar{D}^n(\theta, \phi; m) = \frac{\tilde{D}_\sigma}{D_\sigma^0} = 1 + A \cos^2 [m(\theta - \phi)] \quad (3.4.1)$$

where D_{σ}^0 is the minimum surface diffusivity corresponding to a specific surface orientation, θ is the angle formed by the local tangent to the surface and the direction of the applied electric field. A , m , and ϕ are dimensionless parameters that determine the strength of the anisotropy, the grain symmetry through the number of crystallographic directions that corresponds to fast diffusion paths (half-fold number), and the misorientation of the symmetry direction with respect to the direction of the applied electric field E_{∞} , respectively.

The explicit Adams-Bashford formula of second order (Gear, 1971) is used to perform the time integration of the evolution equations with a time step determined from the maximum surface velocity such that the displacement increment is kept constant for all time step increments. This so-called adapted time step auto-control mechanism combined with the self-recovery effect associated with the capillary term guarantees the long time numerical stability and the accuracy of the explicit algorithm even after performing several hundred to several millions steps.

Accuracy and efficiency of the numerical methods require a strict control of number and position of system nodes. For an accurate and efficient study a remeshing technique that guarantees keeping the distance between two successive nodes, i.e. the segment lengths below a critical value in order to keep the accuracy in an acceptable level, and inhibits formation of useless nodes causing loss of efficiency should be employed. A shape preserving parametric cubic spline interpolation which keeps concavity of the data is employed to reset the node positions after each calculation step, so that a constant segment size is forced.

All these methods are implemented in the FORTRAN code named '*GROOVE*' whose flowchart is given the next section. The code itself is also given in Appendix.

3.5. Flowchart of the computer code ‘GROOVE’

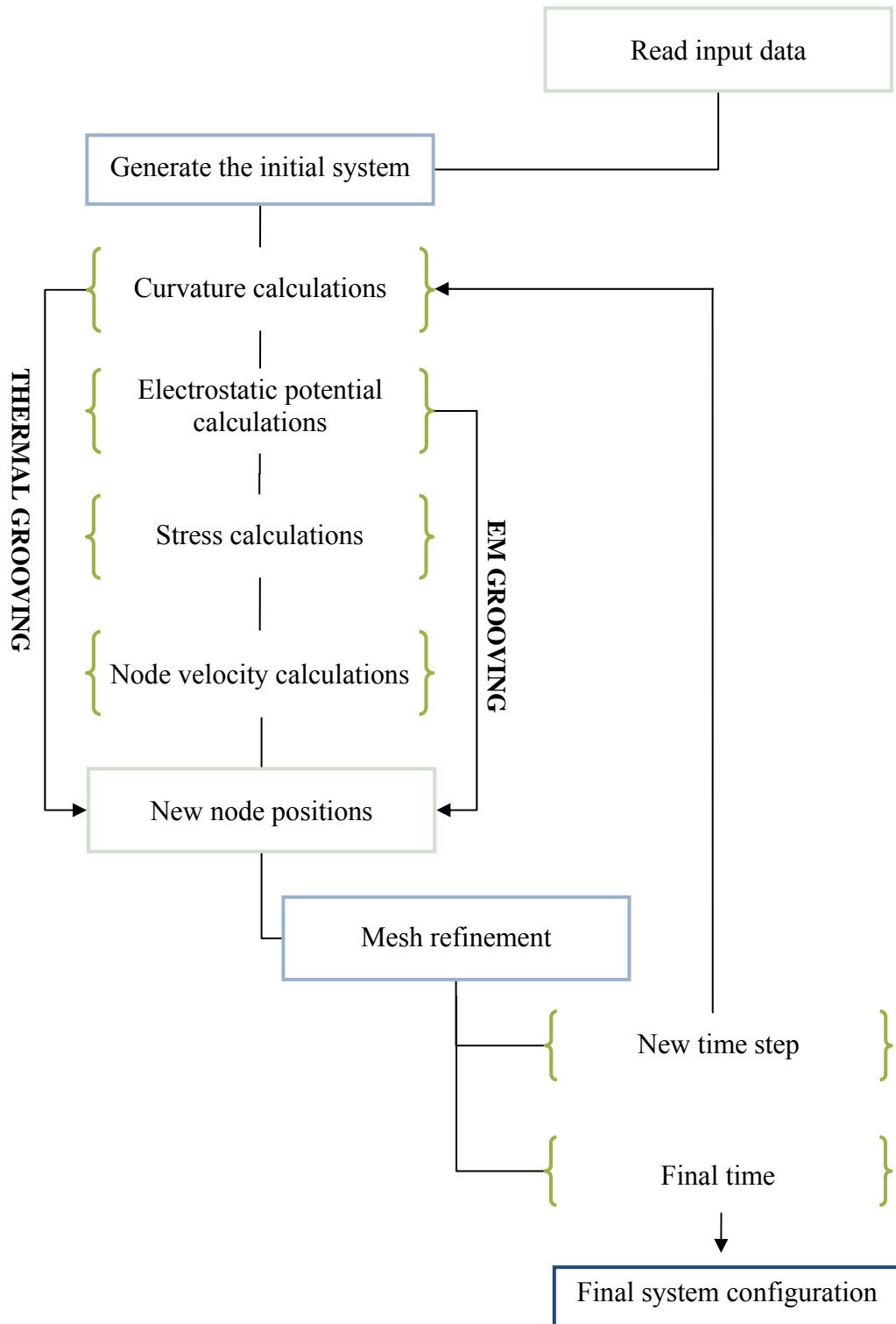


Figure 3.5.1: Program flowchart.

CHAPTER 4

RESULTS AND DISCUSSIONS

4.1. Introduction

Here the results of the computer simulation experiments will be given in a concise way. At first we seek answers to the questions: what kind of groove morphology will form by electromigration, stress and capillarity assisted surface drift diffusion? and how this morphology is affected by a change in applied force intensity? To answer the first question we will compare the general features of the profiles obtained with the ones for a thermal groove, in which only the capillary forces are in action. So, before proceeding further the thermal grooving problem or the classical Mullins' problem (Mullins, 1957) is reexamined in section 4.2. Then, in following sections, we will investigate effects of applied force fields and surface diffusion anisotropy on the evolution of bi-crystal thin films under specified conditions in a non-dimensional space. Finally reverting back to real time and space by renormalizations enables us to analyze and compare the computer simulation experiments with the laboratory experiments published in the literature.

The dimensional analysis of the governing equations presented in chapter 3 provides a parameter space to be explored to understand the effects of applied force fields on the evolution of bi-crystal thin films. Results of the computer simulations performed in this parameter space will only be presented for the upper half of the modeled thin film owing to the symmetry of figure 3.3.2 about x-axis. Accordingly the convention used to describe the groove morphology in these experiments is given in figure 4.1.1.

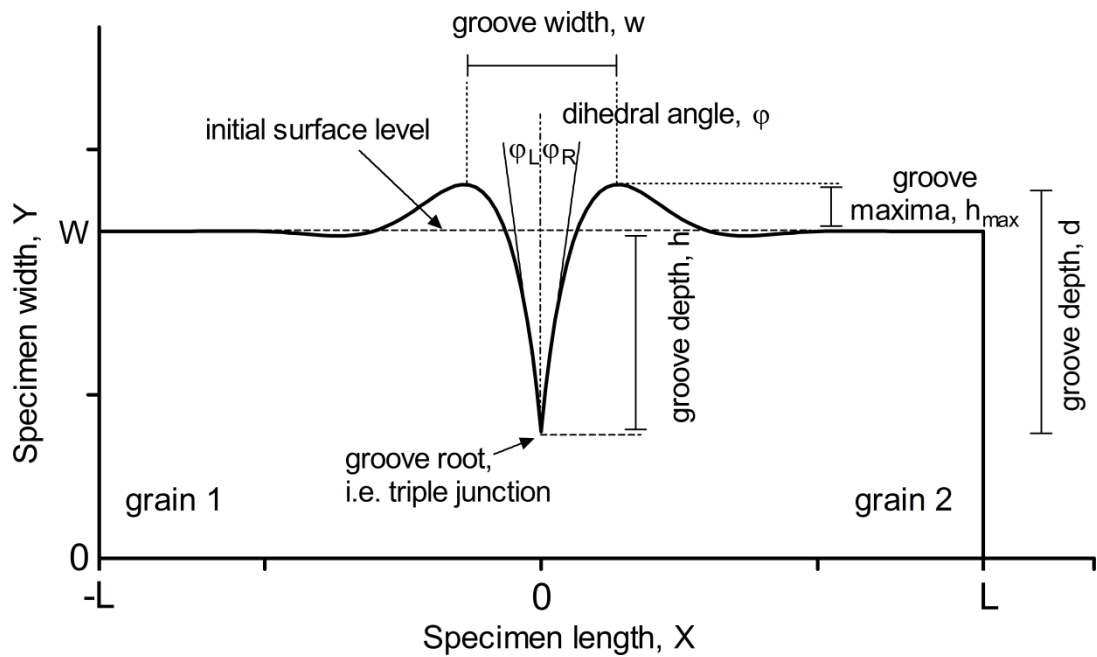


Figure 4.1.1: Sketch of a grain boundary groove, which evolves on the upper triple junction of figure 3.3.2, illustrating its width, depth, maxima and dihedral angle. Here W and L denote the half film width and length, respectively. The grain boundary extends along the origin.

It might be beneficial to get some idea on the magnitude of the tentative time constant, $\tau_o = kT\ell_o^4 / \Omega_\sigma D_\sigma h_\sigma g_\sigma^o$, introduced previously in section 3.2 which will be encountered in the next sections while applying the computer simulation results on the available experimental data in the literature. The following tentative atomistic structural constants for copper might be considered, $\Omega_\sigma = 1.18 \times 10^{-29} \text{ m}^3$ (mean atomic volume), $h_\sigma = 2.56 \times 10^{-10} \text{ m}$ (interface thickness). Similarly, the surface diffusivity and the surface specific Gibbs free energy may be taken as equal to $D_\sigma = 5.85 \times 10^{-5} \exp(-0.95 \text{ eV}/kT) \text{ m}^2/\text{s}$ and $g_\sigma^o = \gamma = 1.725 \text{ J/m}^2$, respectively, for the uncontaminated free surfaces (Ogurtani & Oren, 2004). Then one finds $\tau_o = 5.85 \times [10^2 - 10^6] \text{ s}$ depending upon the selected scale length $\ell_o = [0.1 - 1.0] \mu\text{m}$ in above given range at $T = 573 \text{ K}$, that is standard device accelerated test temperature (Tu, 2003). At the room temperature, $T = 300 \text{ K}$, one obtains about eight orders of magnitudes higher values for the time constant such as $\tau_o = 1.22 \times [10^{10} - 10^{14}] \text{ s}$.

4.2. Thermal grooving revisited: the effect of physicochemical parameters

Figure 4.2.1 shows the evolutionary kinetics of a thermal groove having triple junction (TJ) mobilities equal to $M_L = M_T = 0.25$, and a wetting parameter of $\lambda = 0.5$. The initial configurations of the reported systems are always a flat surface having a freshly formed grain boundary cutting the crystal into two pieces. Accordingly; the groove tip displacement is measured with respect to the original surface and the positive direction is chosen towards the bulk.

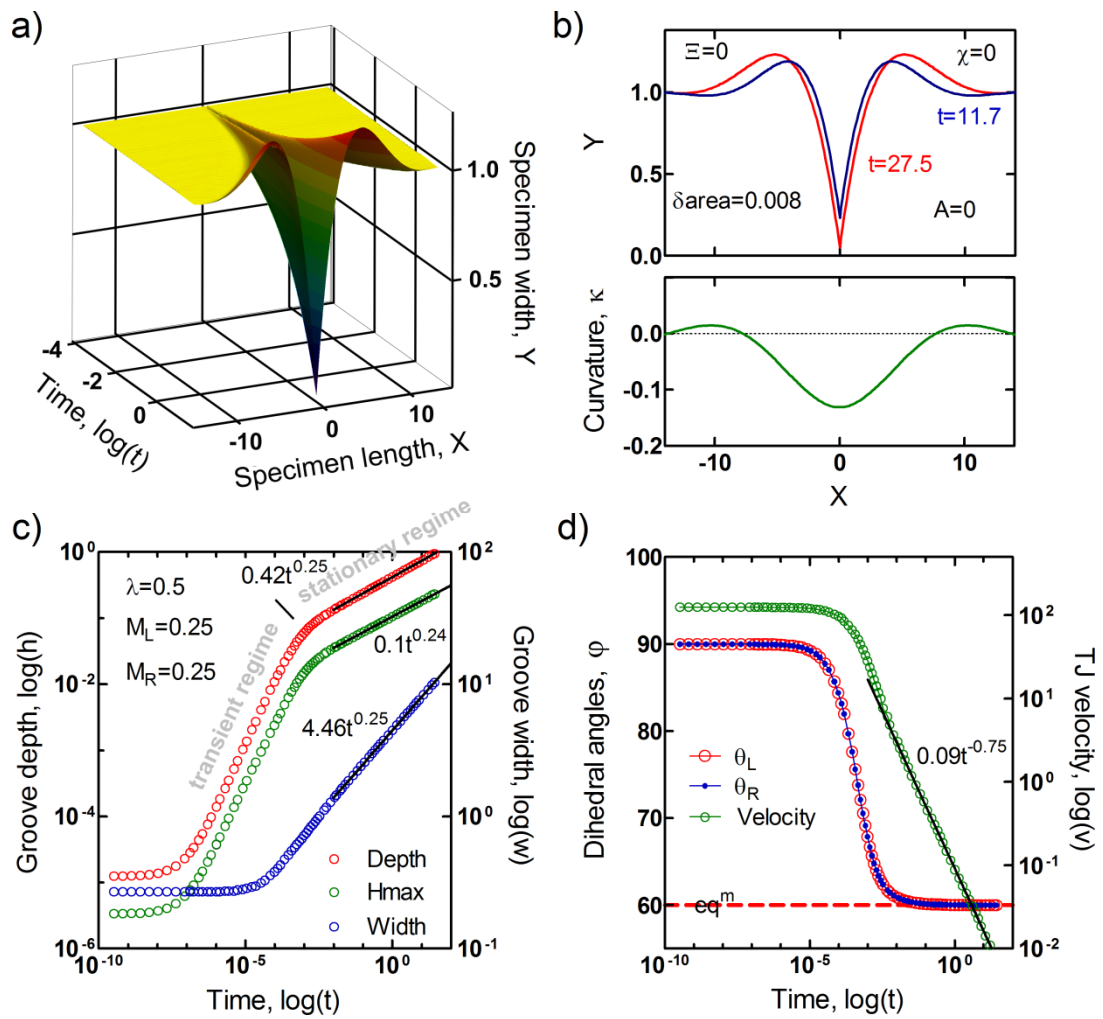


Figure 4.2.1: Isotropic thermal grooving for $\lambda=0.5$, $M_L=M_T=0.25$: a) and b) shows the GB profile; c) kinetic data for groove depth, maxima and width; d) TJ velocity and the dihedral angles. The linear correlation factors (R^2) for depth, width, maxima and velocity up to 5 decimals are 1.0, 0.99999, 0.99996 and 0.99974 respectively. Final time for failure is equal to $t_n=27.5$ in normalized scale.

The curvature plot given in the lower portion of the figure 4.2.1b in fact has a discontinuity at the groove root ($X=0$). However this discontinuity constitutes no

problem in computations hence the longitudinal and transverse motions of the TJs are defined by boundary conditions deduced from the irreversible thermodynamic theory of surfaces and interfaces (Ogurtani, 2000). The figure simply reflects interpolation of the curvature at that point not to disturb the overall plot. $\delta area$ value reported in figure 4.2.1b is the total fractional change in the area (material content) of the specimen due to numerical rounding errors. Otherwise, it should be equal to zero due to the mass conserving boundary conditions imposed on the system.

Analysis of the normalized penetration depth versus time data given in figure 4.2.1c shows that the system reaches a stationary regime roughly around $t=0.01$, and stays there till the end of the experiment with a time exponent $n=0.25$. This regime defines a time independent groove shape having linear dimensions changing with $t^{1/4}$ which agrees the analytic solution for surface diffusion dominant mass transport (Mullins, 1957). The previous stage of the groove trajectory shall be called as transient; this regime is completely ignored in many experimental studies due it covers a short ride in time, and also in many theoretical studies due to improper boundary conditions based on reversible thermodynamics at the groove root. Mullins (1957) gives the equation for depth of the groove which reaches stationary regime as: $h=0.78m(Bt)^{1/4}$; in this notation h is the depth measured from the initial flat surface, m is the slope of the tangent line passing through the groove root $m=tan(\theta)$; here θ is the complementary dihedral angle ($\theta=\pi/2-\phi$) which approximates to ratio $\gamma_{gb}/2\gamma_s$ (what we call the wetting parameter, WP, and designate by λ) for small values (*small slope approximation*; $\theta=asin(\gamma_{gb}/2\gamma_s)\approx \gamma_{gb}/2\gamma_s$). γ_{gb} and γ_s stands for the grain boundary and specific surface free energies

respectively. The parameter B is a collection of physicochemical and kinetic constants. This parameter is embedded to our time scale, which is described in detail in section 3.2. So in order to compare our equation with Mullins' we have to divide our cofactor with the *tangent* of the wetting parameter $\lambda=0.5$, but we never have to worry about the parameter B . The result is $h=0.42t^{0.25}=0.77\tan(\lambda)t^{0.25}$; which is close to the equation given by Mullins. Mullins denote the groove width with s (separation between the two maxima) and gives its equation as: $s=4.6(Bt)^{0.25}$, this is close to $w=4.46t^{0.25}$ which we have obtained. The time law for the two maxima in figure 4.2.1c is $h_{max}=0.18\tan(\lambda)t^{0.24}$ and for the TJ velocity in (d) is $v=0.09t^{-0.75}$ which can simply be regarded as the time derivative of the groove depth. Mullins gives the equation for the depth of the groove measured from the maximum of the surface to the groove root as: $d=0.973m(Bt)^{1/4}$. Needless to say the cofactor in this equation corresponds to the sum of the cofactors of our equations h and h_{max} ; $0.77+0.18=0.95$. The time independent ratio of the groove width and depth was given by Mullins as $s/d=4.73/m$ compared to our $4.69/\tan(\lambda)$. The linear correlation factors (R^2) for depth, width, maxima and velocity up to 5 decimals are 1.0 , 0.99999 , 0.99996 and 0.99974 respectively. These values demonstrate the extreme long range stability in the experiment.

Mullins' theoretical coefficients approximated further as the wetting parameter gets smaller (which is consistent with Mullins's small slope approximation), yet the results presented in above analysis of figure 4.2.1 demonstrate complete accordance of the front tracking method with the analytical Mullins' solution for this relatively large value of the wetting parameter ($\lambda=0.5 \rightarrow m=0.577$). The time exponents and

cofactors obtained in this study are definitely realistic for finite slopes (no small slope assumption) and for finite GB TJ mobilities.

Table 4.2.1: Selected values of grain boundary energy γ_{gb} and crystal vapor surface energy γ_s for various materials in ergs/cm², and corresponding wetting parameters λ and slopes m .

Material	γ_{gb}	γ_s	$\lambda = \gamma_{gb}/2\gamma_s$	m
Ag	790 ^a	1140 ^a	0.346	0.349
	375 ^b	1100 ^b	0.191	0.195
	375 ^c	1136 ^c	0.165	0.167
Al	625 ^a	1140 ^d		
	324 ^b	980 ^b	0.165	0.167
Au	364 ^a	1485 ^a	0.123	0.124
	378 ^{b,c}	1400 ^{b,c}	0.135	0.136
Cu	646 ^a	1725 ^a	0.187	0.190
		1670 ^a		0.160 ^e
	625 ^b	1780 ^b	0.176	0.178
	625 ^c	1736 ^c	0.18	0.183
	654 ^f	1752 ^f	0.187	0.190
Fe	780 ^a	1950 ^a	0.200	0.204
Ni	690 ^a	1725 ^a	0.200	0.204
	565	2280 ^{g, h}	0.124	0.125 ^g
W		2900 ^a		
	1400	2800 ^{h, i}	0.25	0.26 ⁱ
	1080 ^c	2634 ^c	0.205	0.209

REFERENCES:

- a: Hirth and Lothe, 1968
- b: Liu et al., 2001
- c: Murr, 1975
- d: Smith et al., 1991
- e: Mullins, 1957
- f: Chen et al., 2007
- g: Ogurtani, 2009a
- h: Gao, 1991
- i: Bihn et al., 1976

For most of the metals in vacuum or inert atmospheres λ is on the order of $0.125 - 0.25$ (Shewmon, 1966) which yield slopes less than 0.3 (see Table 4.2.1). Thus Mullins' small slope solution yielded satisfactory results. However for some surface active environments such as liquid metals or active gases λ can even be close to unity (Robertson, 1971).

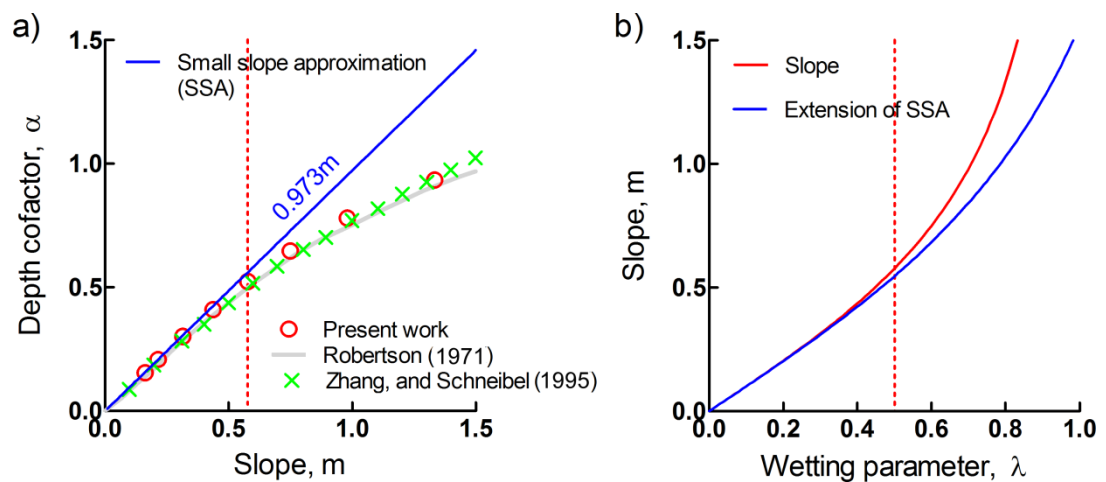


Figure 4.2.2: a) The relation between depth cofactor ($d/t^{1/4}$) and the slope; b) finite slope ($=\tan(\alpha \sin(\lambda)) = \lambda/\sqrt{1-\lambda^2}$) and the small slope approximation ($=\tan(\lambda)$) as a function of wetting parameter.

Numerical solutions of the nonlinear fourth order differential equation describing the phenomena for finite slopes are also obtained by Robertson (1971), and Zhang and Schneibel (1995). Both authors stated that as m grows larger, the depth of the groove profile ($d=\alpha t^{1/4}$) becomes lower than that assumed by Mullins' solution. Relevant figures from those are digitized and given in figure 4.2.2a together with

the values obtained from the present study. Robertson (1971) remarked the dependence of the slope m to the ratio of the grain boundary and surface energies ($\gamma_{gb}/\gamma_s=2\lambda$). In figure 4.2.2b Robertson's figure 6 is redrawn to show the deviation from the small slope approximation. In citing Robertson's work Zhang and Schneibel (1995) said that his results for the groove depth in the case of small dihedral angles, or large slopes, smaller than theirs and thus deviate further from Mullins' result for the linearized surface diffusion equation. We may say the very same thing for Zhang and Schneibel's work (1995) compared to ours by looking at figure 4.2.2a for small slopes. But both studies are in good agreement in general. In figure 4.2.2 the wetting parameter used in the experiment given in figure 4.2.1 ($\lambda=0.5$) and the corresponding slope is shown by red markers to indicate the level of agreement.

Figure 4.2.3 shows systems response at different values of the wetting parameter. Following Robertson (1971), to enable comparison with Mullins (1957), groove profiles are normalized with respect to $mt^{0.25}$ in y-axis and $t^{0.25}$ in x-axis in figure 4.2.3a. On this plot each curve has a unit slope at $X/t^{0.25}=0$, and it compares steady groove shapes for each λ whose dimensions grow in proportion with $t^{0.25}$. In figure 4.2.3b normalization is done with respect to unit depth and unit half width ($W/2$), where Y_0 is the value of Y at $X=0$. The curves labeled as $m \rightarrow 0$ are the curves calculated by Mullins (1957) using small slope approximation. These two figures show, for the stationary grooves, that h_{max} decreases with increasing λ (or m) and the profiles become relatively steeper at the groove root and bends away more sharply with increasing λ (Robertson, 1971). In figure 4.2.3c we see that the transition time

to stationary region (final linear region in the log-log plot) is approximately the same for all experiments. Lowering the wetting parameter prolongs the observation time of steady grooves hence the equilibrium dihedral angle is established at lower groove depths. The $0.973\tan(\lambda)t^{0.25}$ lines shown in the figure reflects the fact that changing λ does not affect the time exponent, which is a function of mass transport mechanism. Experimentally calculated connections may be extracted from figure 4.2.2a by using $d=at^{1/4}$. The equilibrium dihedral angles in figure 4.2.3d can simply be calculated by taking arccosine of λ according to our convention.

Ogurtani and Akyildiz (2005) show the existence of a transient regime and incorporate this regime into their penetration depth formula by stating that the rate of this evolution process in the transient regime obeys the first order reaction kinetics. This regime is totally ignored by researchers employing Mullins' boundary condition at groove root (constant slope). On the other hand Zhang et al. (2002) in their grooving experiments with tungsten at 1350 °C observed grain boundary grooves with dihedral angles decrease continuously. They have found a time exponent of 0.44 for the depth of these grooves. They have assumed that the change of the dihedral angle is stemming from a change in surface free energy during experimentation due to changes in the surface composition by segregation or adsorption. They explain the phenomena at this basis by noting that they are not aware of an article addressing changing dihedral angles in the model.

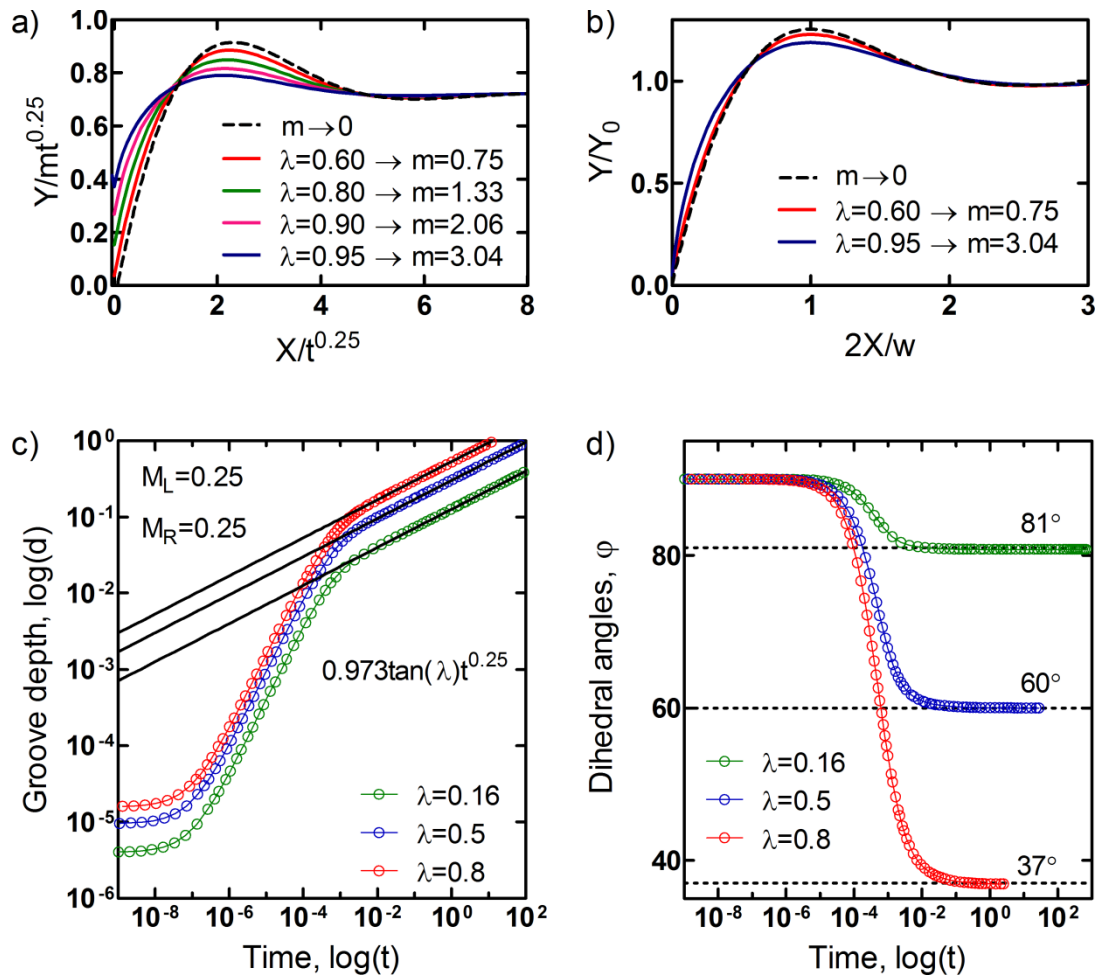


Figure 4.2.3: Thermal grooving for different wetting parameters. Simulated profiles are normalized with respect to a) $mt^{0.25}$ and $t^{0.25}$; b) unit depth and unit half width ($w/2$). The $m \rightarrow 0$ curves are plotted using Mullins' profile function. Kinetic data for c) the groove depth and d) the dihedral angles.

Zhang et al. (2002) report the values of average dihedral angles (2ϕ) for tungsten as 163.3 , 157.4 , 153.6 , 150.1° successively at 16 , 32 , 64 , and 128 hours. They have extracted this data from the 3D atomic force microscopy (AFM) images at each annealing time; one of those images (at 128 h) is given in figure 4.2.4. This ϕ data is plotted in figure 4.2.5a together with the results of the computer simulation

experiment performed for $\lambda=0.28$ and $M_L=M_T=0.25$. In the simulation experiment $\phi=81^\circ$ is observed at $t=10^{-4}$; this determines the scaling factor used in plot 4.2.5a: $10^{-4}/16=2.5 \times 10^{-5}$.

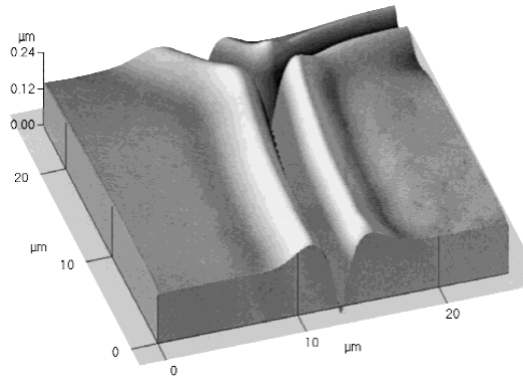


Figure 4.2.4: 3D AFM image of a groove developed on the surface of tungsten upon 128 h of annealing in vacuum at 1350 °C taken from Zhang et al. (2002).

By looking at figure 4.2.5 it could be suggested that the changing dihedral angle phenomena reported by Zhang et al. (2002) is due to observation of non-steady grooves. In this time interval an attempt to determine a kinetic equation by regression analysis yields a time exponent of 0.46 ; close to the reported value 0.44 . Sachenko et al. (2000) state that the vapor pressure of tungsten at 1350 °C is 2×10^{-16} Pa and due to this evaporation condensation mechanism is not likely to operate. They also calculate the characteristic length above which the volume diffusion dominates surface diffusion in the order of 8 m , and after stating the groove widths measured in the experiments are in the order of $1 \text{ } \mu\text{m}$, they conclude

that the dominant mass transport mechanism should be the surface diffusion. However the time exponents observed by Zhang et al. (2002) for the same experimental setup are physically meaningless at this basis and figure 4.2.5b clearly demonstrates the appearance of usual kinetic law for surface diffusion dominated mass transport on later times.

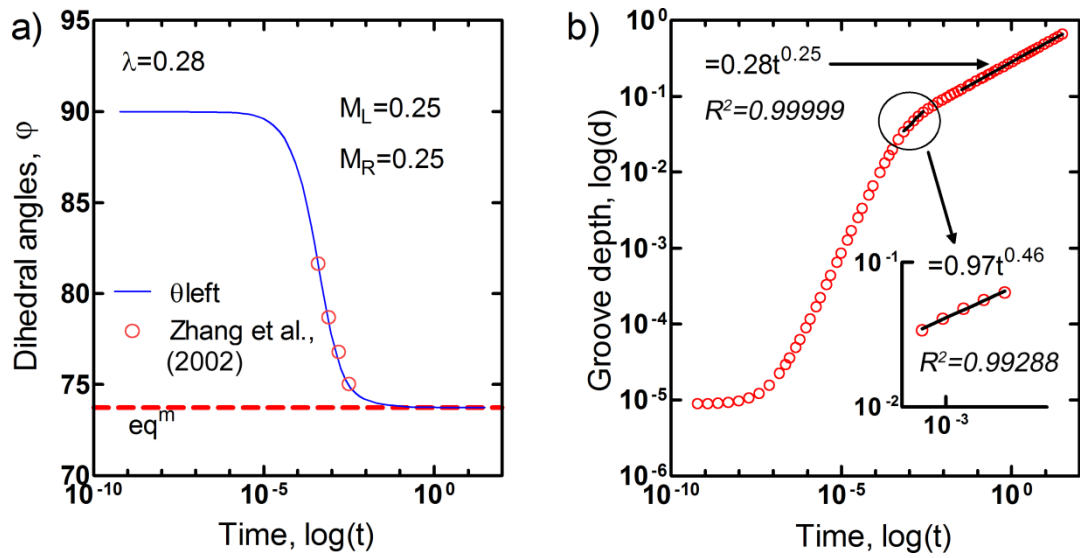


Figure 4.2.5: Thermal grooving for $\lambda=0.28$ and $M_L=M_T=0.25$: a) kinetic data for the dihedral angles resulting from present simulation and reported by Zhang et al. (2002) b) kinetic data for the groove depth and the lines obtained from linear regression in the transient and stationary states; the first kinetic equation in the transient regime is $d=0.97t^{0.46}=3.38\tan(\lambda)t^{0.46}=3.33\lambda/\sqrt{1-\lambda^2}t^{0.46}$ and the second one in the stationary regime is $d=0.283t^{0.25}=0.984\tan(\lambda)t^{0.25}=0.97\lambda/\sqrt{1-\lambda^2}t^{0.25}$.

Figure 4.2.6 outlines the kinetic data for GB grooves having different longitudinal and transverse GB triple junction mobilities, but the same wetting parameter $\lambda=0.8$. It shows that the time spent at the transient regime is increasing by lowering the mobilities, and for low mobilities the equilibrium dihedral angle is hardly reached; one have to wait for extremely long computation times.

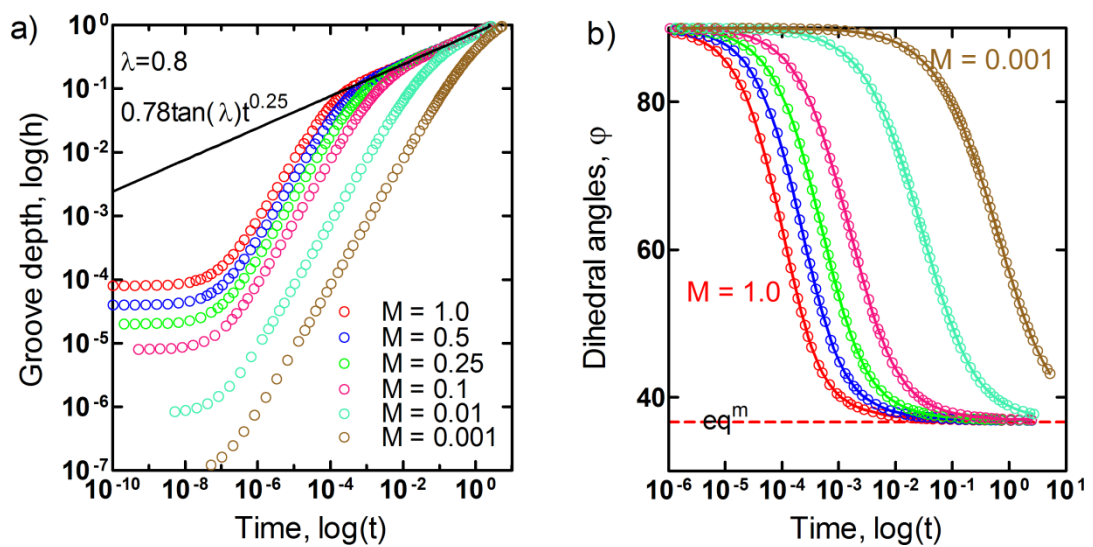


Figure 4.2.6: Thermal grooving by different TJ mobilities, $M_L=M_T=M$. Kinetic data for a) the groove depth and b) the dihedral angles.

The assumption of instantaneous formation of the equilibrium angle at the groove root highly depends on the TJ mobility. Since flux is proportional to mobility, an increase in mobility increases the evolution rate and hence decreases the time to observe stationary state grooves and vice versa.

Unlike the groove depth, no transient regime is observed for the groove width whose time evolution is given in figure 4.2.1c. Robertson (1971) observes a slight decrease in groove width cofactor with increasing slope which does not depart more than 5% from the value 4.6 at $m \rightarrow 0$. We did not observe a change greater than this amount. However precise calculation of the width has a practical importance. Since its introduction in 1957, Mullins' theory is used extensively in determination of the surface diffusion coefficients (D_s). Once the active mass transport mechanism is confirmed (e.g. if surface diffusion, by assuring groove grows in proportion with $t^{0.25}$), the ratio of the groove depth (or width) measurements taken at different times yield the B parameter. As stated before, B is a collection of physical constants: $B = D_s \gamma_s \Omega^2 v / kT$; providing surface energy γ_s is known, constant temperature experimentation gives the surface diffusivity. Here Ω is the atomic volume, v is the surface concentration of diffusing atoms, k is the Boltzmann's constant and T is the absolute temperature. It is experimentally difficult to obtain reproducible measurements for the groove depth (scanning the vertical direction) either by interferometry (due to 'tails' on the fringe pattern at the groove root; Gjostein, 1963) or by scanning probe microscopy (SPMs) techniques (due to non zero tip diameter; see e.g. Sachenko et al., 2002 for a detailed discussion). Because of these inconveniences most of the D_s calculations involve measurements of groove width. Then a value of 5% uncertainty may lead to D_s within an accuracy of about 20% (Robertson, 1971).

4.3. Thermal grooving with anisotropic surface diffusivity

In figure 4.3.1 several grain boundary groove profiles are given for different fold symmetries and tilt angles. A slight modification of the groove width and maxima is observed to take place. These modifications may be introduced to Mullins' solution by the use of two additional parameters (width and height adjustment factors) as it has been suggested by Ogurtani (2007) to govern the anisotropy due to surface free energy. It has also been observed that formation of secondary oscillations is a strong function of anisotropy.

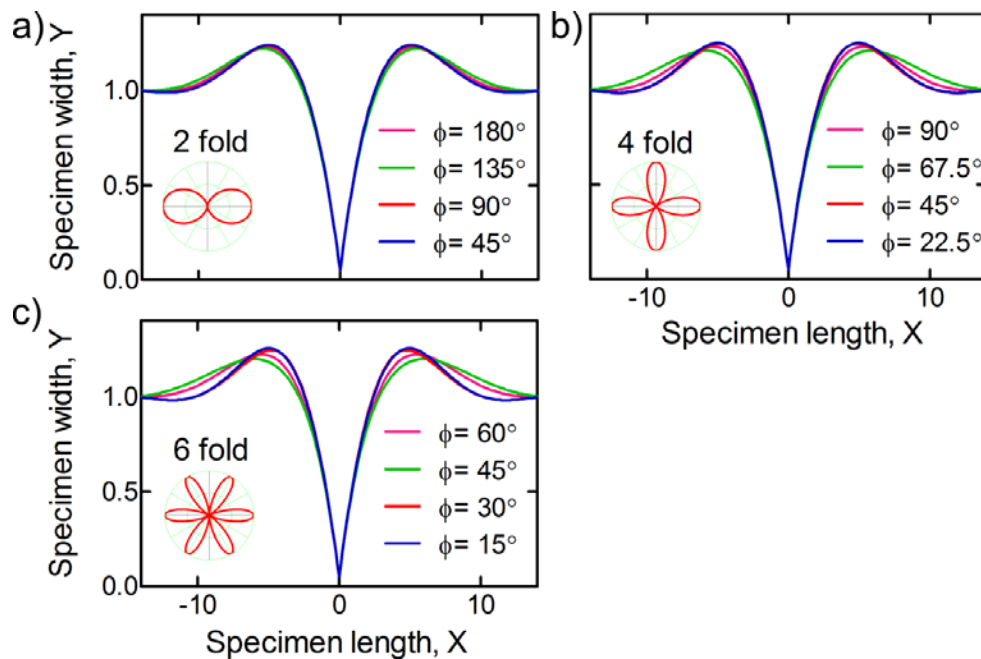


Figure 4.3.1: Thermal grooving with anisotropic surface diffusivities with $A=10$: a) 2 fold symmetry with 45, 90, 135, and 180° tilt angle, b) 4 fold symmetry with 22.5, 45, 67.5 and 90° tilt angle, c) 6 fold symmetry with 15, 30, 45, and 60° tilt angle.

Experiments were performed for the following physicochemical parameters:
 $M_L=M_T=0.25$, $\lambda=0.5$.

In figure 4.3.2 the failure times due to film agglomeration are plotted as a function of the tilt angle for different fold symmetries. The isotropic failure time, $t=27.5$, is also given in the same figure. The longest lifetime is achieved in the case of isotropic surface diffusivity. Lifetime decreases as the degree of folding increases because of the introduction of the fast diffusion paths. For two fold symmetry (which corresponds to $\{110\}$ planes in an fcc crystal) the longest lifetime is at 90° orientation. For four fold it is at 45° , and for six fold at 30° . The other orientations may be grouped as fatal which resulted very short lifetimes.

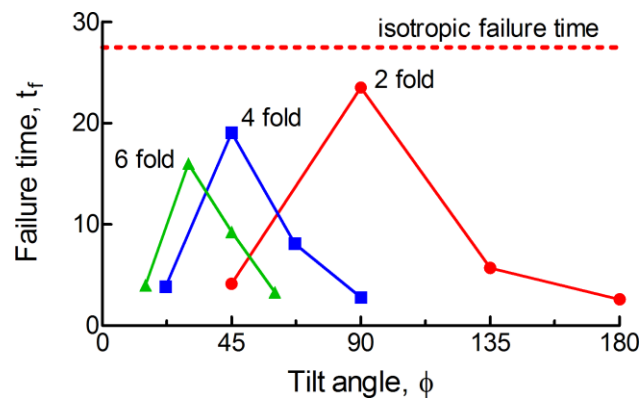


Figure 4.3.2: Failure times due to film agglomeration for different tilt angles and fold symmetries.

4.4. Isotropic grain boundary grooving under the effect of electromigration

In figure 4.4.1, the surface topographical evolution of electromigration (EM) groove for a normal grain boundary under the action of the capillary and electromigration forces is presented. The electric field vector is directed towards to positive x direction (normal to the GB; see figure 3.3.1, 2) which leads to an electron wind in the opposite direction. A nonsymmetrical groove is expected to develop as a result of the bias in mass transport due to the applied current.

The windward side of the GB (cathodic grain) shows an extra mass accumulation compared to the leeward side (anodic grain). Figure 4.4.1b draws attention to two snapshots having same depths at considerably different times. It looks like the groove root is trapped at a certain depth and after then the windward side hillock starts to buckle from its top while the dihedral angle is preserved at the root. This intricate behavior can also be tracked from figure 4.4.1c, in which kinetic data for groove depth, maxima and width is given. All of these parameters remain almost unchanged except the groove width which accepts a steeper slope during the windward side hillock's travel to cathode. In figure 4.4.1d deviation of the left and right angles from the quasi-equilibrium value by rotating towards the windward side is shown. The angular difference is kept constant and the triple junction velocity decreases asymptotically during the travel time.

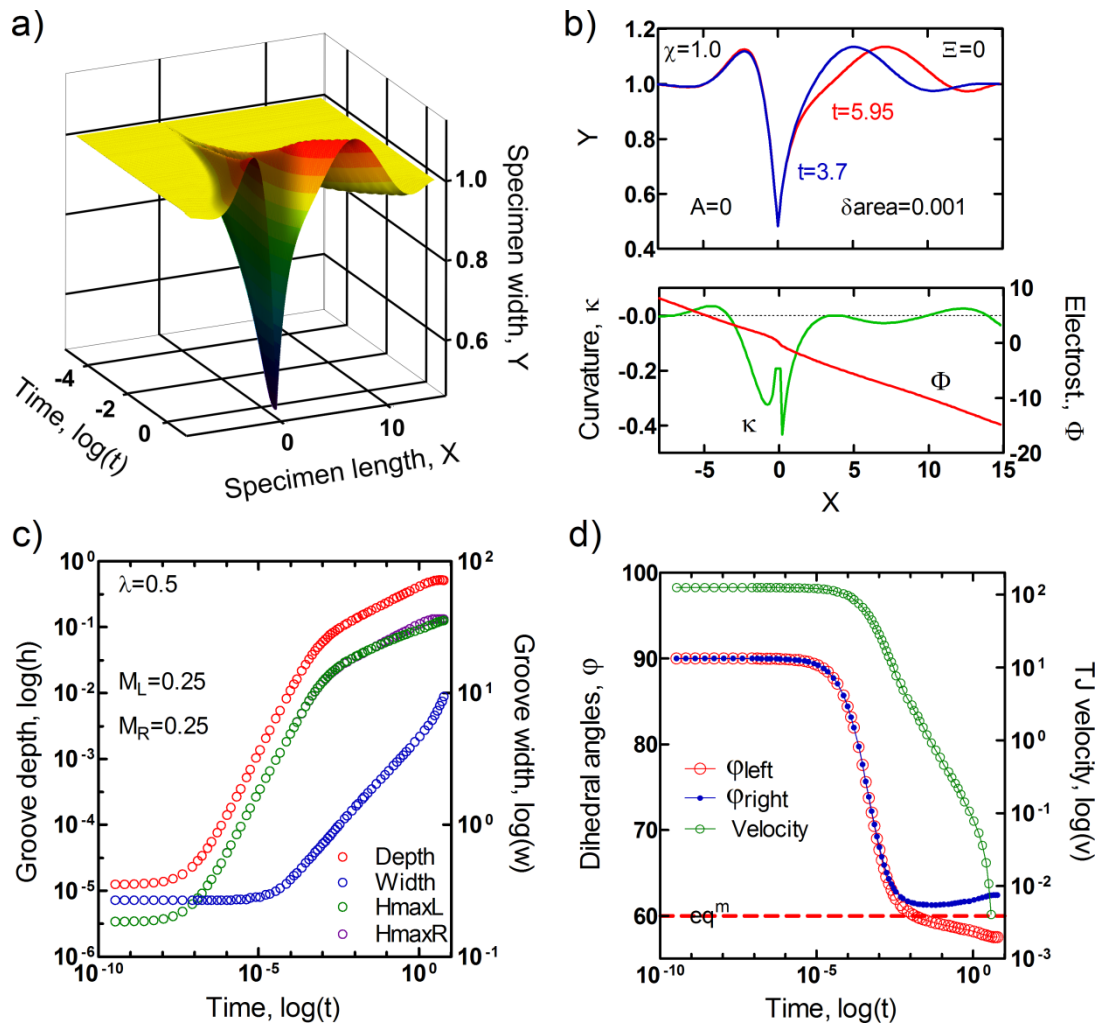


Figure 4.4.1: Isotropic electromigration grooving for $\lambda=0.5$, $M_L=M_T=0.25$ and $\chi=1.0$: a) and b) shows the GB profile; c) kinetic data for groove depth, maxima and width; d) TJ velocity and the dihedral angles.

The deceleration of the grooving kinetics by an applied electric field was also observed by Averbuch et al. (2003b) and Nathan et al. (2004) in their numerical experiments with the mass conserving boundary conditions on the specimen edges.

These boundary conditions let changing anode and cathode areas and simulate a constant voltage (CV) difference between the electrode pads. Yet they have

employed Mullins' boundary condition stemming from the energetic considerations at the groove root (fixed dihedral angle) and unable to reveal the non equilibrium state of the triple junction kinetics given in figure 4.4.1d. Ogurtani and Akyildiz (2005) studied very same problem on a finite sample where they have couple the grooving problem with cathode edge voiding and drifting by utilizing reflecting (mass conserving) and/or free moving boundary conditions on the specimen edges. They have reported groove tip arrestment above threshold electron wind intensity (EWI) level on their constant current (CC) set up and state that the TJ displacement velocity slows down drastically while the system is proceeding towards the asymptotic value of the groove depth which is found to be a monotonically decreasing function of EWI parameter. Here, these observations will be extended by isolating the grooving problem from that of cathode related phenomena.

In figure 4.4.2 effect of increasing EWI can be tracked. Figure 4.4.2b shows that increased EWI takes the groove stop time earlier and lowers the limiting depth. The leeward side hillock (h_{maxL}) is depressed further, the disintegration of the two hillocks is exaggerated (increased width) and a secondary maximum grows out at the windward side so that a wavy look appears. Looks like the traveling surface wave (hillock) on the windward side with slightly growing in amplitude is the only change taking place and a new type of quasi-equilibrium is established at rest of the system.

Here one may question the validity of employing relatively large wetting parameter ($\lambda = 0.5$) to that of common metals (e.g. $\lambda_{Al} \approx 0.16$) but still commenting on these. The main reason of this selection is to reduce the dihedral angles, which allows us to have rather sharp groove profile formation to ease visualization of the process. Similarly, the large WP shortens the life time of the transient regime, and therefore reduces the time for the establishment of the stationary non-equilibrium state, where one observes formation of the equilibrium dihedral angles at the groove tip. Actually, we have studied grain boundary grooving kinetics in a rather large span of wetting parameters: $\lambda = [0.16, \dots, 0.8]$ and always tried to be careful to keep the level of correspondence at each time.

Riege and coworkers (Riege et al., 1995, 1996; Prybyla et al., 1998) performed in situ TEM observations of 4000 Å thick, 250 μm long Al(0.5wt%Cu) interconnects (both unpassivated and passivated, where the passivation consisted of SiO₂ deposited at 350°C to a thickness of 1000 Å) with line widths ranging from 0.2, 0.3, 0.5, 0.8, and 1.0 μm exposed to a current density of $2 \times 10^6 \text{ A/cm}^2$ at temperatures 200 - 370°C. The samples were prepared directly on a thin SiO₂/SiN bilayer deposited on a standard Si(100) wafer. They observe formation of voids along the sidewalls, their growth, migration, pinning, film failure and healing with respect to the detailed local microstructure. One of the most commonly observed process, named as ‘inch-warming’ by the authors, was described as follows: a triangular-shaped void nucleated at the sidewalls, migrated quickly and intersected a grain boundary (or readily formed there), stagnate for long times (see figure 4.4.3a) and transforms into a long narrow void (see figure 4.4.3b).

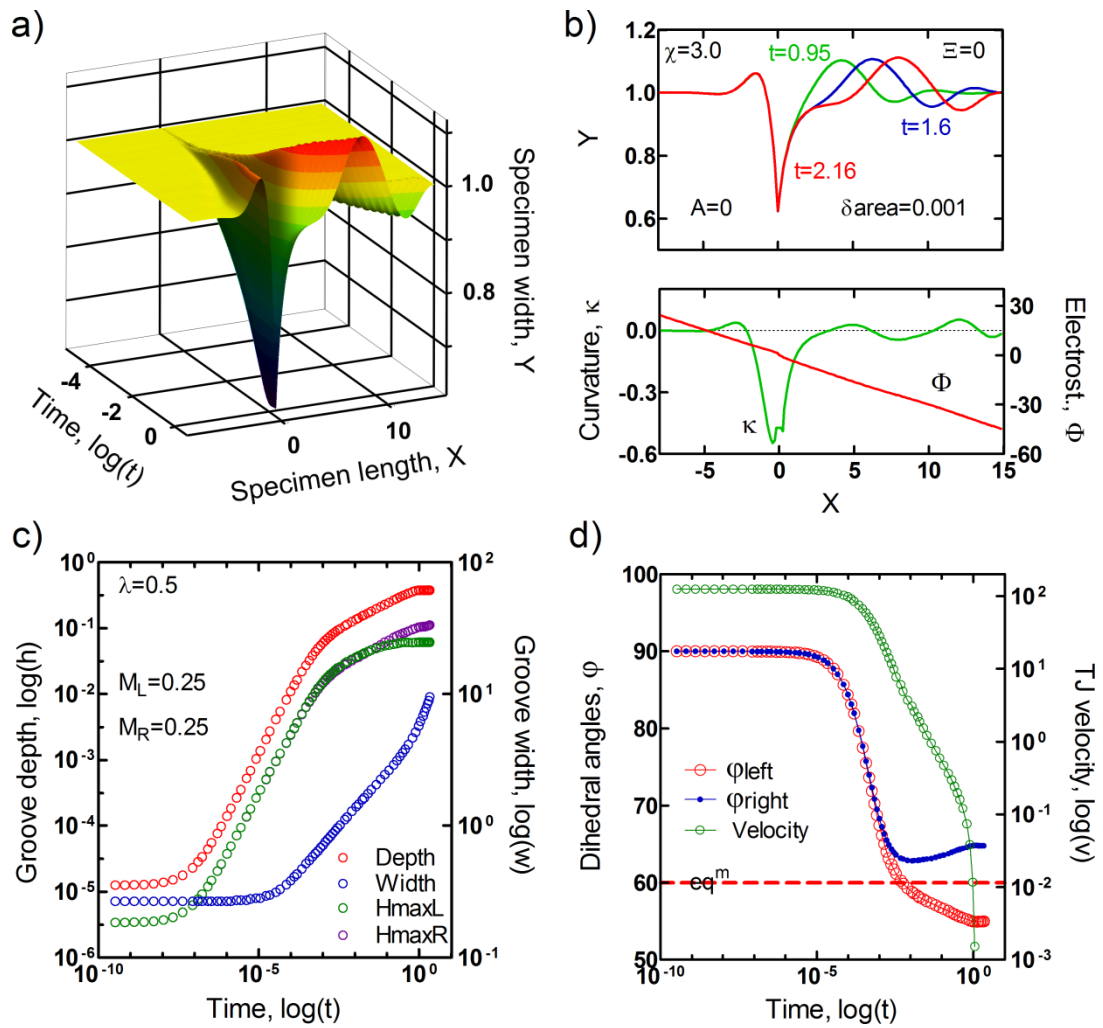


Figure 4.4.2: Isotropic electromigration groove with $\chi=3.0$: a) and b) shows the GB profile; c) kinetic data for groove depth, maxima and width; d) TJ velocity and the dihedral angles.

The tendency of a grain boundary to trap voids was also observed by Ogurtani and Oren (2005). When the profile evolution given in figure 4.4.2b is compared with the TEM snapshots given in figure 4.4.3 one may say, once a migrating surface void is trapped by the grain boundary it may evolve like a grain boundary groove during

the time of stagnation. This may explain the elongation of the windward side (right hand side) of the void during it reside at the triple junction.

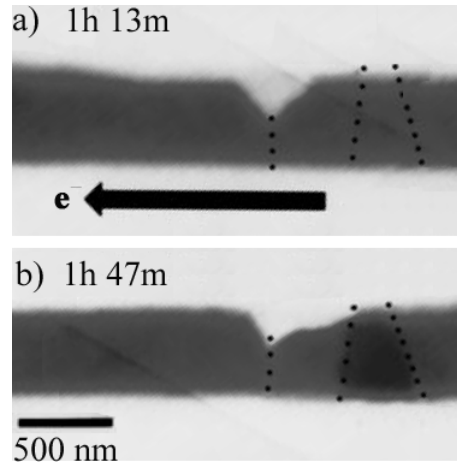


Figure 4.4.3: TEM micrographs showing the ‘inch worming’ process in a 0.5 μm wide Al film exposed to a current density of $2 \times 10^6 \text{ A/cm}^2$ at 350°C . Figures reproduced from Riege et al., 1995 (given as Fig. 3), 1996 (given as Fig. 2); Prybyla et al., 1998 (given as Fig. 1). The dotted lines indicate grain boundaries.

The application of the renormalization procedure using the reported value of film thickness ($0.4 \mu\text{m}$) and the material properties for aluminum (mean atomic volume: $\Omega = 1.66 \times 10^{-29} \text{ m}^3$, specific surface Gibbs free energy: $\gamma = 1.08 \text{ Jm}^{-2}$, surface effective charge: $z^* = 4$, electrical resistance: $\rho = 2.7 \times 10^{-8} \text{ ohm}\cdot\text{m}$), the value of electron wind intensity parameter used in the experiment presented in figure 4.4.2, $\chi = 3.0$, corresponds to a current density of $1.94 \times 10^6 \text{ A/cm}^2$. This matches the experimental conditions of Riege et al (1995, 1996).

The limiting depths and amounts of rotations from the quasi-equilibrium values (towards the windward side) are collected from several experiments for different combinations of EWIs and wetting parameters (WP) are plotted in figure 4.4.5.

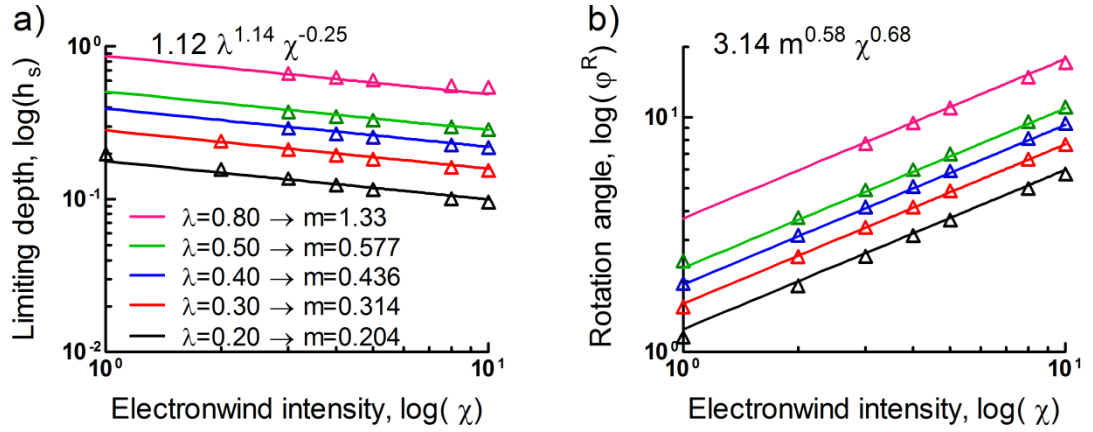


Figure 4.4.4: Dependence of a) the limiting depth and b) rotation angle to electron wind intensity for different wetting parameters. The equations obtained by linear regression (solid lines) are plotted on the experimental data (triangles).

From a large number of simulation experiment results we obtain expressions for limiting depth (h_s) and the degree of rotation (φ^R) as a function of EWI and WP in normalized time and space:

$$h_s(\chi, \lambda) = 1.12 \lambda^{1.14} \chi^{-0.25} \quad (4.4.1)$$

$$\varphi^R(\chi, \lambda) = 3.14 (\tan \lambda)^{0.58} \chi^{0.68} = 3.14 m^{0.58} \chi^{0.68} \quad (4.4.2)$$

Since the depths given in our experiments are normalized to unity, Eq. 4.4.1 can be used to calculate the threshold value for EWI (by setting $h_s=1.0$) above which complete agglomeration of the film could be observed:

$$\chi_{thrs} = 1.574\lambda^{4.56} \quad (4.4.3)$$

In other words there is a well defined regime in which applied current has no freezing (healing) effect on groove penetration. This can be called as capillary dominant regime as was done by Ogurtani and Akyildiz (2005) who found that the total elapsed time for splitting the bicrystal into two pieces in this regime is a monotonic function of EWI. Above the threshold level (electromigration regime) one will observe groove tip arrestment and the upper limit for penetration depth can be calculated by Eq. 4.4.1. Using the value of the WP given by Mullins (1957) for copper, $\lambda=0.16$, the calculated value for χ_{thrs} is 3.695×10^{-4} . This corresponds to 23.75 A/m^2 for a copper film having a thickness of $0.1 \text{ }\mu\text{m}$. In this calculation the specific surface Gibbs free energy, the surface effective charge, electrical resistance and mean atomic volume for copper are taken as: $\gamma_s=1.78 \text{ J/m}^2$, $z^*=12$, $\rho=1.7 \times 10^{-8} \text{ ohm}\cdot\text{m}$, $\Omega=0.0118 \times 10^{-27} \text{ m}^3$, respectively. Typical electromigration tests on thin films of the same order of thickness usually employ an applied electric in the order of $10^4 - 10^{10} \text{ A/m}^2$ (Lloyd et al., 1999). Comparing the two, it is unlikely to observe agglomeration failure at the grain boundaries during electromigration testing of copper. However for a hypothetical material having a WP of $\lambda=0.95$ but all other physical properties same with copper the χ_{thrs} is calculated as $1.245 \rightarrow 8 \times 10^4 \text{ A/m}^2$

which is in range of EM testing. This strong λ dependence should be kept in mind while testing with unconventional materials or testing in surface active environments. Eq. 4.4.2 also predicts a finite amount rotation of the dihedral angle towards the windward side even in the capillary dominant regime, which maybe calculated as 1.708×10^{-3} and 6.742° respectively for of $\lambda=0.16$ and 0.95 .

4.5. Electromigration grooving with anisotropic surface diffusivity

Surface diffusion anisotropy is determined by the variation of surface diffusivity with surface orientation and also depends on the grain orientation for each grain of the polycrystalline metallic thin film. In Eq. (3.4.1), the anisotropy of surface diffusion is quantified through the dimensionless parameters, which are fully discussed in section 3.4.

Grain orientation is expressed by the crystallographic direction normal to the surface of the film and the misorientation of the crystallographic symmetry axis in the grain with respect to the applied electric field (termed as tilt or misorientation angle). The parameter m in Eq. 3.4.1) is an integer that characterizes thin film surface plane which is cut into two by a perpendicular grain boundary. In *fcc* metals, such as aluminum or copper, these symmetry axis correspond to $\langle 110 \rangle$ crystallographic directions. Each of the $\{110\}$ planes contain only one $\langle 110 \rangle$ axis, therefore these planes have $m=1$. In the same way, for $\{100\}$ planes $m=2$, and for $\{111\}$ planes $m=3$. The term '*n-fold*' symmetry is used to denote the number of the

fast diffusion paths on a crystallographic plane. Since each crystallographic axis corresponds to two opposite directions, $n=2m$.

Two experimental setups were studied; firstly by setting up a moderate value for the wetting parameter ($\lambda=0.5$; $M_L=M_T=0.25$) to generate simulations in the limit of the small slope approximation and secondly by setting up a high value for the wetting parameter ($\lambda=0.8$; $M_L=M_T=1.0$) in order to examine nearly complete wetting case. A systematic study will be presented here for each set up and each symmetry plane and selected tilt angles, where the anisotropy constant is taken to be invariant ($A=10$).

We have obtained a rich variety of film morphologies in regard to several grain orientations, therefore it is useful to summarize the computer simulation results before proceeding further (see Tables 4.5). In following subsections we will present these in detail. In following tables we have highlighted the orientations in which we observe a change in grain boundary morphology from ridge to slit (or vice versa) by a change in wetting parameter in comparing two setups.

Table 4.5.1: Summary of the observed film morphologies for $\{110\}$ planes with 45, 90, 135, 180° tilts. IN=Instable, ST=Stable, R=Ridge, S=Slit.

m=1		Lee side		GB		Wind side	
ϕ	λ	$\lambda=0.5$	$\lambda=0.8$	$\lambda=0.5$	$\lambda=0.8$	$\lambda=0.5$	$\lambda=0.8$
45		IN	IN	R	S	ST	ST
90		ST	ST	R	R	IN	IN
135		ST	ST	S	S	IN	IN
180		ST	ST	S	S	ST	ST

Table 4.5.2: Summary of the observed film morphologies for {100} planes with 22.5, 45, 67.5, 90° tilts. IN=Instable, ST=Stable, R=Ridge, S=Slit.

m=2		Lee side		GB		Wind side	
ϕ	λ	$\lambda=0.5$	$\lambda=0.8$	$\lambda=0.5$	$\lambda=0.8$	$\lambda=0.5$	$\lambda=0.8$
22.5		IN	IN	S	S	ST	ST
45		ST	ST	R	S	IN	ST
67.5		ST	ST	R	R	IN	IN
90		ST	ST	S	S	ST	ST

Table 4.5.3: Summary of the observed film morphologies for {111} planes with 15, 30, 45, 60° tilts. IN=Instable, ST=Stable, R=Ridge, S=Slit.

m=3		Lee side		GB		Wind side	
ϕ	λ	$\lambda=0.5$	$\lambda=0.8$	$\lambda=0.5$	$\lambda=0.8$	$\lambda=0.5$	$\lambda=0.8$
15		IN	IN	S	R	ST	IN
30		ST	ST	S	S	ST	ST
45		ST	ST	R	S	IN	IN
60		ST	ST	S	S	ST	IN

4.5.1. Two fold crystal symmetry, m = 1:

i. Moderate wetting, $\lambda=0.5$

A morphology which is called ‘grain boundary ridge growth’ in the literature is observed to form on {110} planes for the tilt angles $\phi=45^\circ$ and $\phi=90^\circ$. Figure 4.5.1.1 shows, mass pile up at the grain boundaries starts after a definite time of groove deepening. After the inversion of the groove tip trajectory, the windward side hillock grows at a faster rate than the leeward side, while a penetrating void formed adjacent to the leeside for $\phi=45^\circ$ case (figure 4.5.1.1ab).

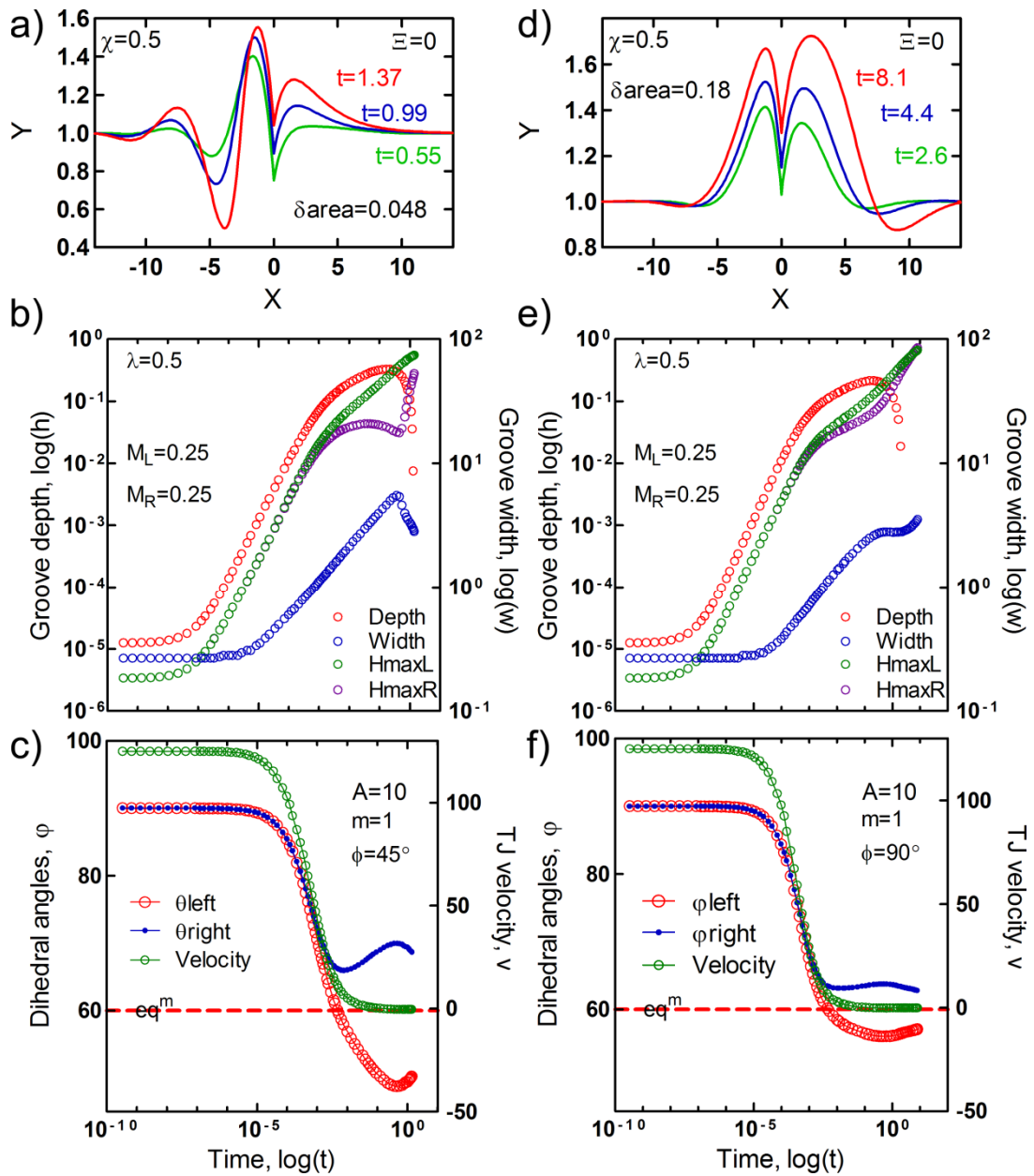


Figure 4.5.1.1: Electromigration grooves with $\chi=0.5$, on a surface having an anisotropic diffusivity characterized by $A=10$, $m=1$, $\phi=45^\circ$ (first column: a to c) and $\phi=90^\circ$ (second column: d to f). a) and d) shows the GB groove profiles; b) and e) kinetic data for groove depth, maxima and width; c) and f) TJ velocity and the dihedral angles. Ridge formation starts with turning over of groove tip trajectory after a certain time, both hillocks on each side of the grain boundary exhibit linear

growth while the separation between the two maxima (groove width) decreases linearly for the case $\phi=45^\circ$, but continues to increase in the case of $\phi=90^\circ$.

For $\phi=90^\circ$ similar phenomena observed, but this time for lee and wind sides. Figures 4.5.1.1cf demonstrate that, these evolutions are towards the quasi-equilibrium dihedral angle dictated by the WP. An increase in electron wind intensity lowers the tip turning depth and time in both cases. Both the extreme hillock growth and deep penetration of the secondary oscillations on the lee or windward sides are problematic.

In figures 4.5.1.2 and 4.5.1.3 slits form near the wind side of the grain boundary with an increase in electron wind intensity.

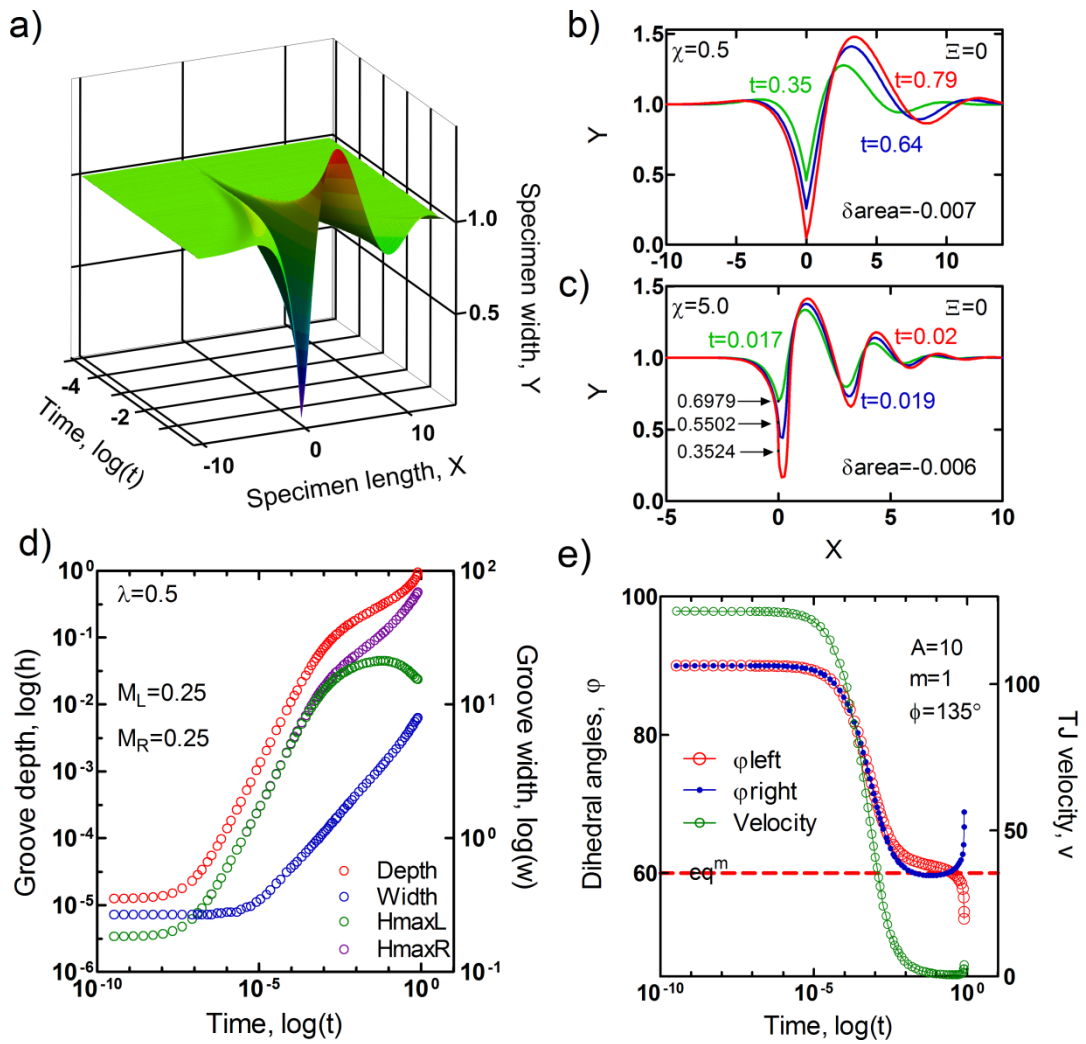


Figure 4.5.1.2: Electromigration groove with $\chi=0.5$ (except part c) and $\chi=5.0$ (c), on a surface having an anisotropic diffusivity characterized by $A=10$, $m=1$, $\phi=135^\circ$. a) and b) shows the GB groove profile; d) kinetic data for groove depth, maxima and width; d) TJ velocity and the dihedral angles for $\chi=0.5$. c) shows the effect of increased electron wind intensity, $\chi=5.0$: a narrow slit, licking up the wind side of the grain boundary evolves and accelerates open circuit failure.

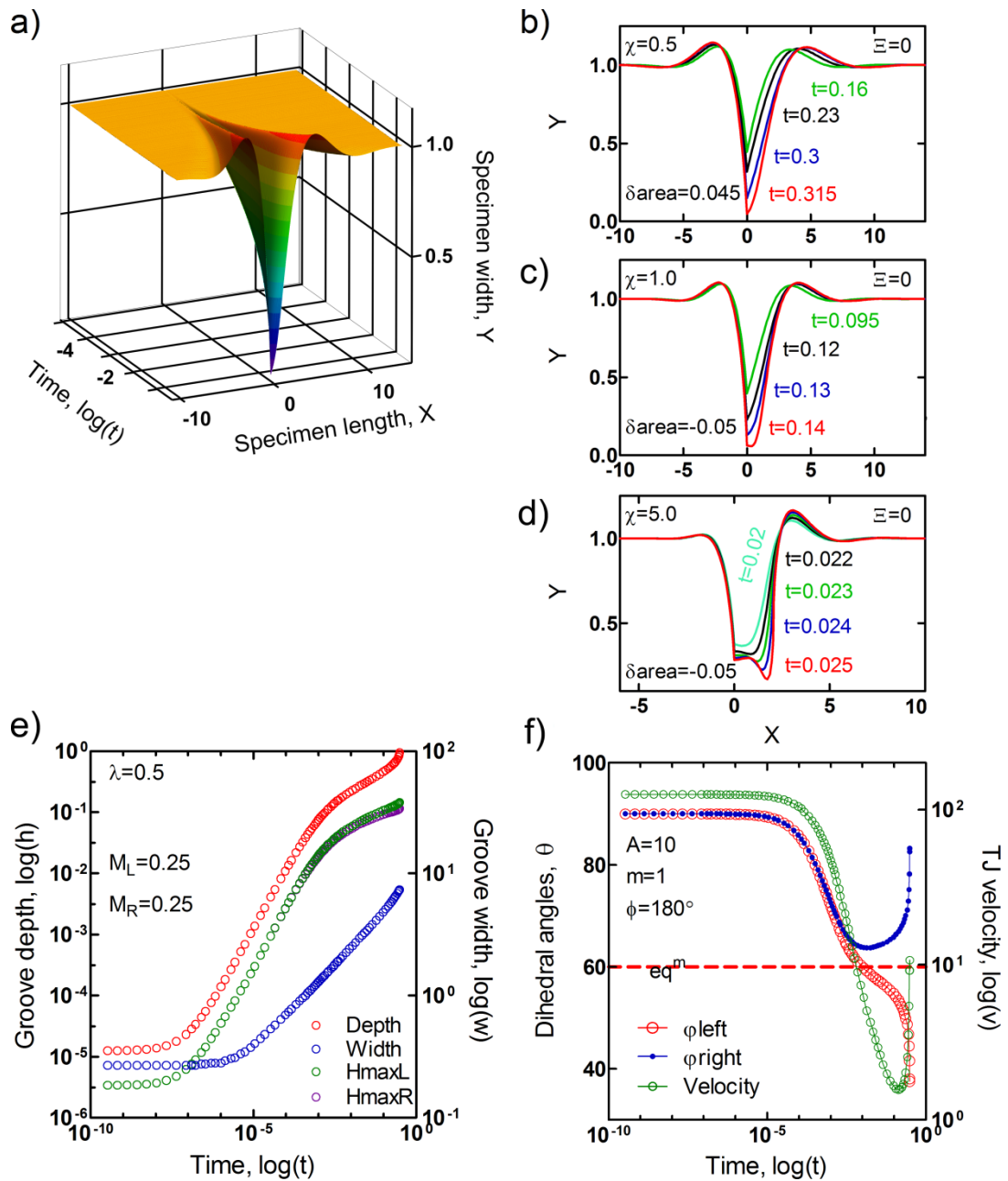


Figure 4.5.1.3: Electromigration groove with $\chi=0.5$ (except parts c, and d), $\chi=1.0$ (c), and $\chi=5.0$ (d), on a surface having an anisotropic diffusivity characterized by $A=10$, $m=1$, $\phi=180^\circ$. a) and b) shows the GB groove profile; e) kinetic data for groove depth, maxima and width; f) TJ velocity and the dihedral angles for $\chi=0.5$. c) and d) shows the effect of increased electron wind intensity, respectively for

$\chi=1.0$, and $\chi=5.0$: lateral extension of the blunted region and formation of a channel like groove.

With the increased EWI, groove root is no longer the minima in these experiments. Groove tips initially get blunted during the slit formation and then the advancing slit accelerates open circuit failure in each case. After slit formation triple junction velocities reported in figures 4.5.1.2e and 4.5.1.3f increase asymptotically, which may be an indication of a drag force exerted by advancing slits on the junctions. Unlike the $\phi=135^\circ$ case, for $\phi=180^\circ$ further increase in EWI leads lateral extension (in x-direction) of the blunted region and leads to a channel like formation. On the other hand the secondary oscillation on the wind side when $\phi=135^\circ$, is not observed for $\phi=180^\circ$.

ii. Nearly complete wetting, $\lambda=0.8$

In this set ($\lambda=0.8$; $M_L=M_T=1.0$) for $\phi=45^\circ$, unlike figure 4.5.1.1ac, no indication of ridge formation is observed. Instead groove tip penetrates deeply, with a rate proportional to the applied EWI. For $\phi=90^\circ$ however, a grain boundary ridge with similar characteristics defined in figure 4.5.1.1df, grows out.

$\lambda=0.8$ counterpart of the $\phi=135^\circ$ experiment presented in figure 4.5.1.2 can be found in figure 4.5.1.4. The response to an increase in EWI is again formation of slit like intrusion. However, now the groove remains sharp but the secondary oscillations in the wind side continuously grow out and the nearest oscillation leads

to open circuit failure. Further increase in EWI multiplies the number of oscillatory waves on the wind side which is an indication of extreme instability in this orientation.

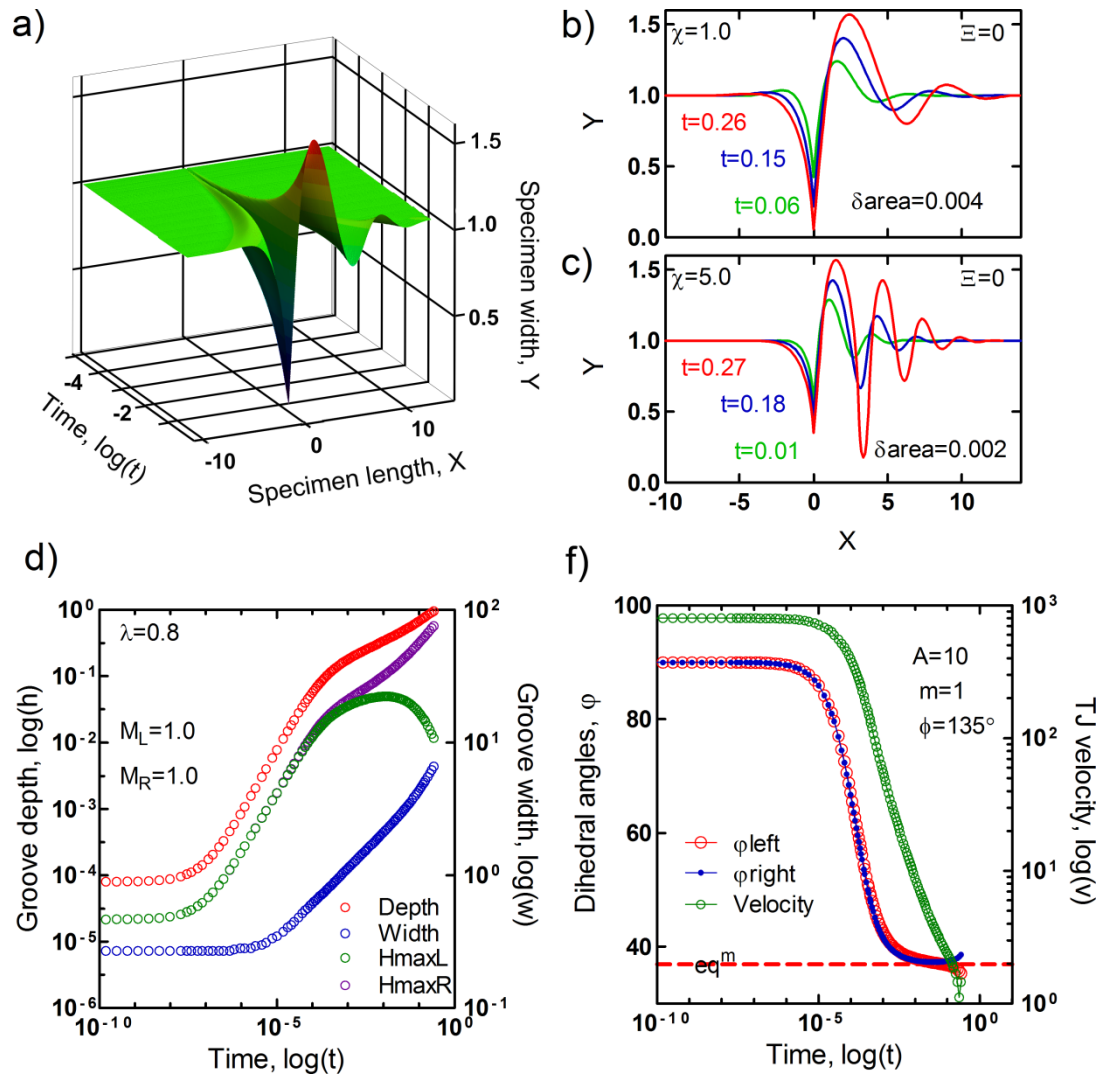


Figure 4.5.1.4: Electromigration groove with $\chi=1.0$ (except part c) and $\chi=5.0$ (c), on a surface having an anisotropic diffusivity characterized by $A=10$, $m=1$, $\phi=135^\circ$. a) and b) shows the GB groove profile; d) kinetic data for groove depth, maxima

and width; d) TJ velocity and the dihedral angles for $\chi=1.0$. c) shows the profile evolution for increased electron wind intensity, $\chi=5.0$: instability in the wind side, secondary oscillations continuously grow out.

For $\phi=180^\circ$ case, we observe similar formation presented in figure 4.5.1.3, with a smaller lateral extension of the blunted region and therefore forming a narrower channel.

4.5.2. Four fold crystal symmetry, $m = 2$:

i. Moderate wetting, $\lambda=0.5$

Morphological evolution on $\{100\}$ planes for the tilt angle $\phi=22.5^\circ$, results strong instability with a slight increase in EWI ($\chi=0.5 \rightarrow 1.0$) by producing regenerative oscillatory waves on the lee side of the triple junction. This instability is associated with a slit licking up the wind side of grain boundary which demonstrates itself with an increase in triple junction velocity. Slit formation is favored by increased EWI. The very same behavior is observed also in the high mobility regime.

In the case of 45° degrees misorientation, a grain boundary ridge with a similar configuration presented in figure 4.5.1.1df ($m=1$, $\phi=90^\circ$) is observed to form. The ridge growth rate is proportional to the applied EWI.

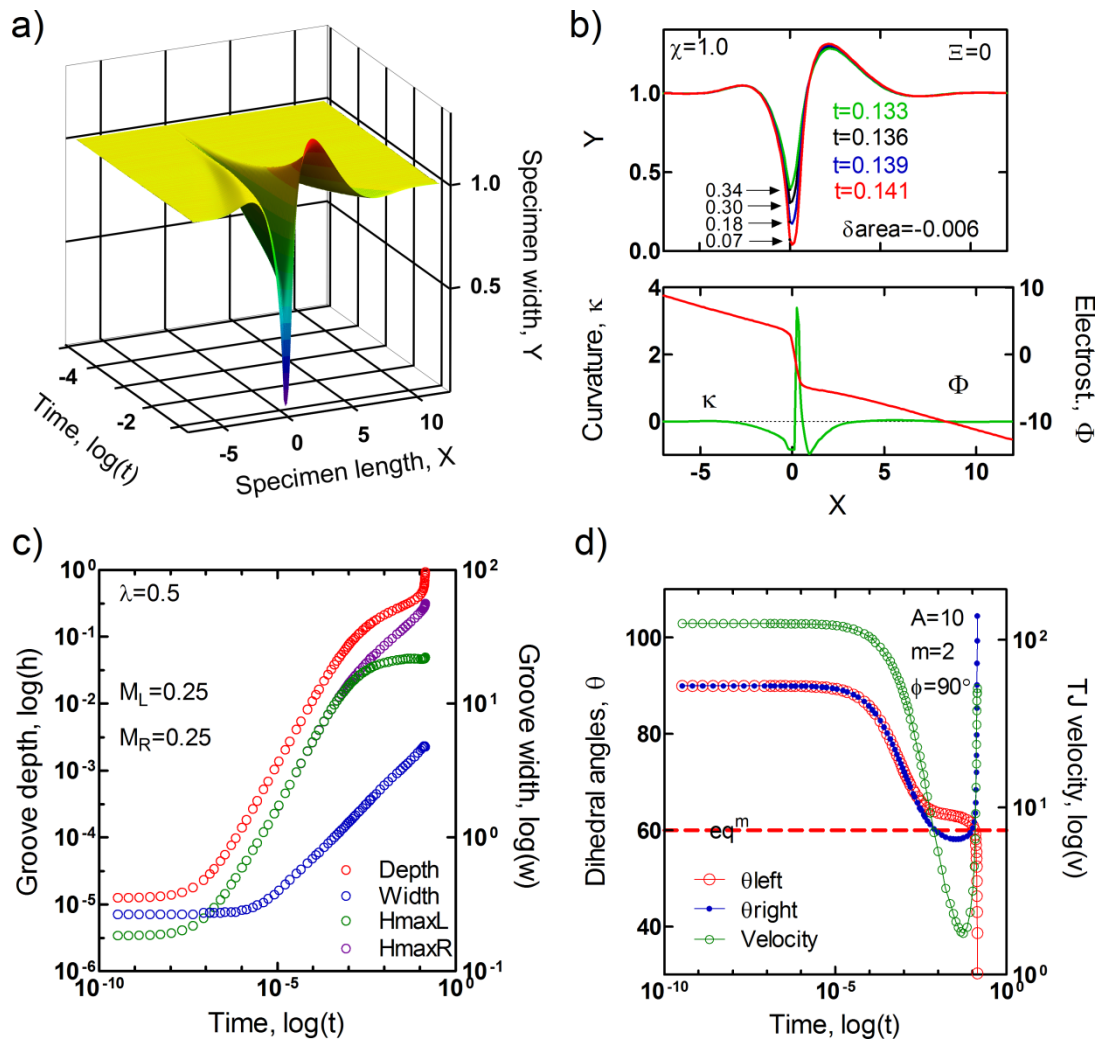


Figure 4.5.2.1: Electromigration groove with $\chi=1.0$, on a surface having an anisotropic diffusivity characterized by $A=10$, $m=2$, $\phi=90^\circ$. a) and b) shows the GB profile; c) kinetic data for groove depth, maxima and width; d) TJ velocity and the dihedral angles. Early slit formation at the wind side of the groove root which drags the triple junction and leads open circuitry.

For 67.5° degrees misorientation, the instability is observed in the windward side (which was observed in the leeward side of $\phi=22.5^\circ$ oriented specimen). In this

respect the $\phi=67.5^\circ$ is like the mirror symmetry of $\phi=22.5^\circ$. However this time, an increase in EWI favors ridge formation with a bigger hillock on oscillating side (windward side). Again, the very same behavior is observed in the high mobility regime.

In figure 4.5.2.1, early slit formation at the wind side of the groove root under a modest EWI ($\chi=1.0$), and triple junction dragging at a misorientation $\phi=90^\circ$ is presented. Here the slit tip advances faster than the groove root just as the case given in figure 4.5.1.2c ($m=1$, $\phi=135^\circ$) under $\chi=5.0$, while there is a little change in the right and left side maximas. Once the slit forms at $t=0.133$, it advances extremely fast and failure takes place at $t=0.141$.

ii. Nearly complete wetting, $\lambda=0.8$

In section i) the morphology observed at 45° misorientation, is referred to figure 4.5.1.1df ($m=1$, $\phi=90^\circ$), which was defined as a typical grain boundary ridge growth. It is interesting to observe a faceted slit extending along the grain boundary in the case of increased WP, whose growth rate is proportional to the applied EWI. As can be seen from figure 4.5.2.2bc, an order of magnitude increase in EWI ($\chi=1.0 \rightarrow 10.0$), leads to a decrease in failure time with same amount ($t_f=0.1 \rightarrow 0.009$).

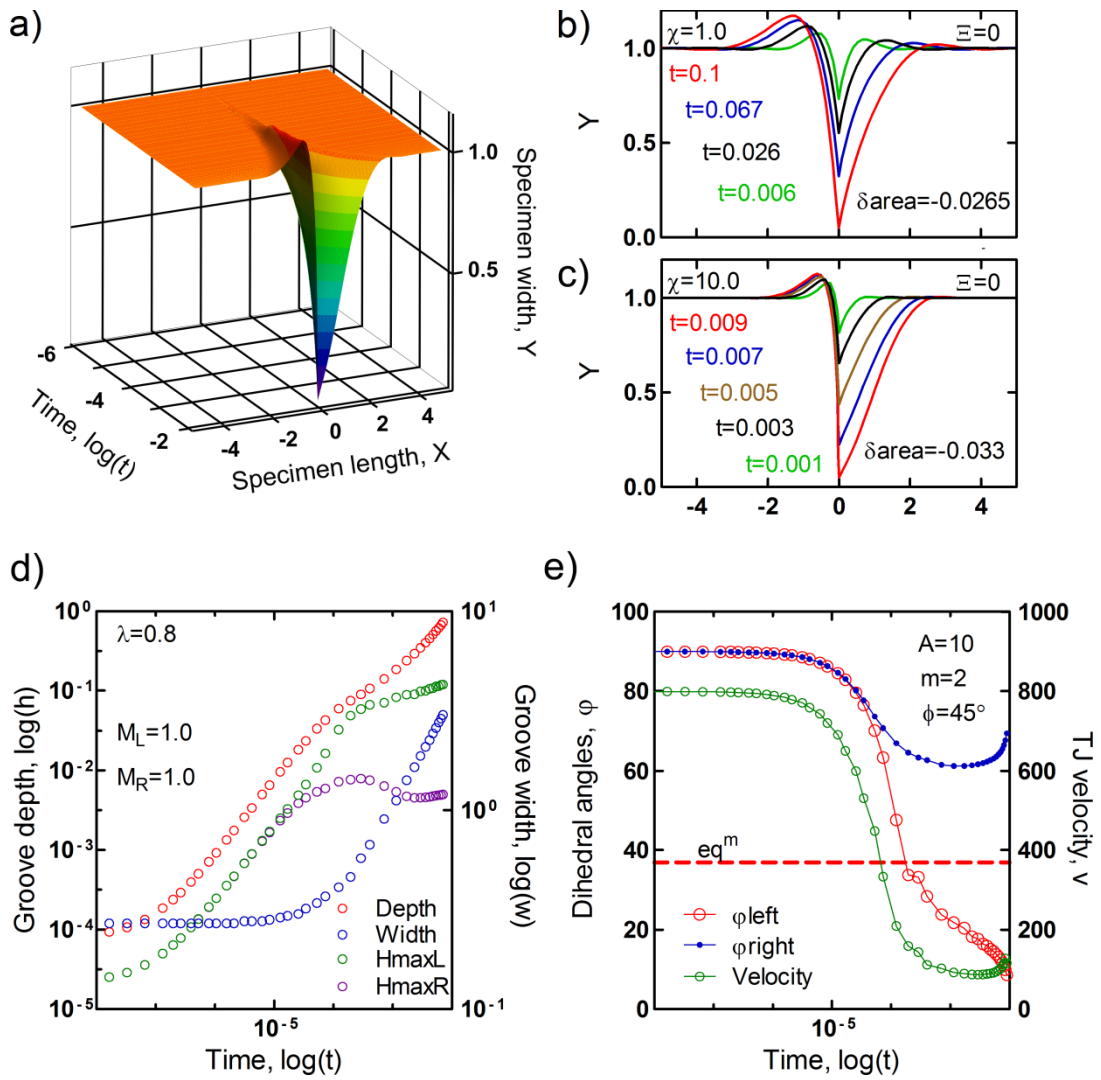


Figure 4.5.2.2: Electromigration groove with $\chi=10.0$ (except part b) and $\chi=1.0$ (b), on a surface having an anisotropic diffusivity characterized by $A=10$, $m=2$, $\phi=45^\circ$. a) and c) shows the GB groove profile; d) kinetic data for groove depth, maxima and width; d) TJ velocity and the dihedral angles for $\chi=10.0$. b) shows the profile evolution for at a modest EWI, $\chi=1.0$.

4.5.3. Six fold crystal symmetry, $m = 3$:

i. Moderate wetting, $\lambda=0.5$

The $\phi=15^\circ$ case of six fold symmetric bicrystal follows a somewhat similar profile evolution with $\phi=22.5^\circ$ case of four fold symmetry; namely a strong instability at the lee side even with the modest values of EWI ($\chi=1.0$) which is associated with a slit licking up the wind side of the grain boundary.

Morphological evolution on $\{111\}$ planes for the tilt angle $\phi=45^\circ$, ended up with a grain boundary ridge formation, showing instability (regenerative oscillatory waves) at the wind side (can be viewed as mirror symmetry of figure 4.4.1.1; $m=1$, $\phi=45^\circ$).

In figure 4.5.3.1 formation of faceted grain boundary voids of opposite facet orientations for $\phi=30^\circ$ and $\phi=60^\circ$ tilt angles are presented. A sharp triangular hillock forms on the leeward side of $\phi=30^\circ$, and on the opposite side of $\phi=60^\circ$.

ii. Nearly complete wetting, $\lambda=0.8$

In this case the slit formation reported in i) section for $\phi=15^\circ$ is replaced by a ridge formation; where the reported ridge formation for $\phi=45^\circ$ is replaced by a slit

formation. However, the strong instabilities reported in both experiments observed to take place as they were.

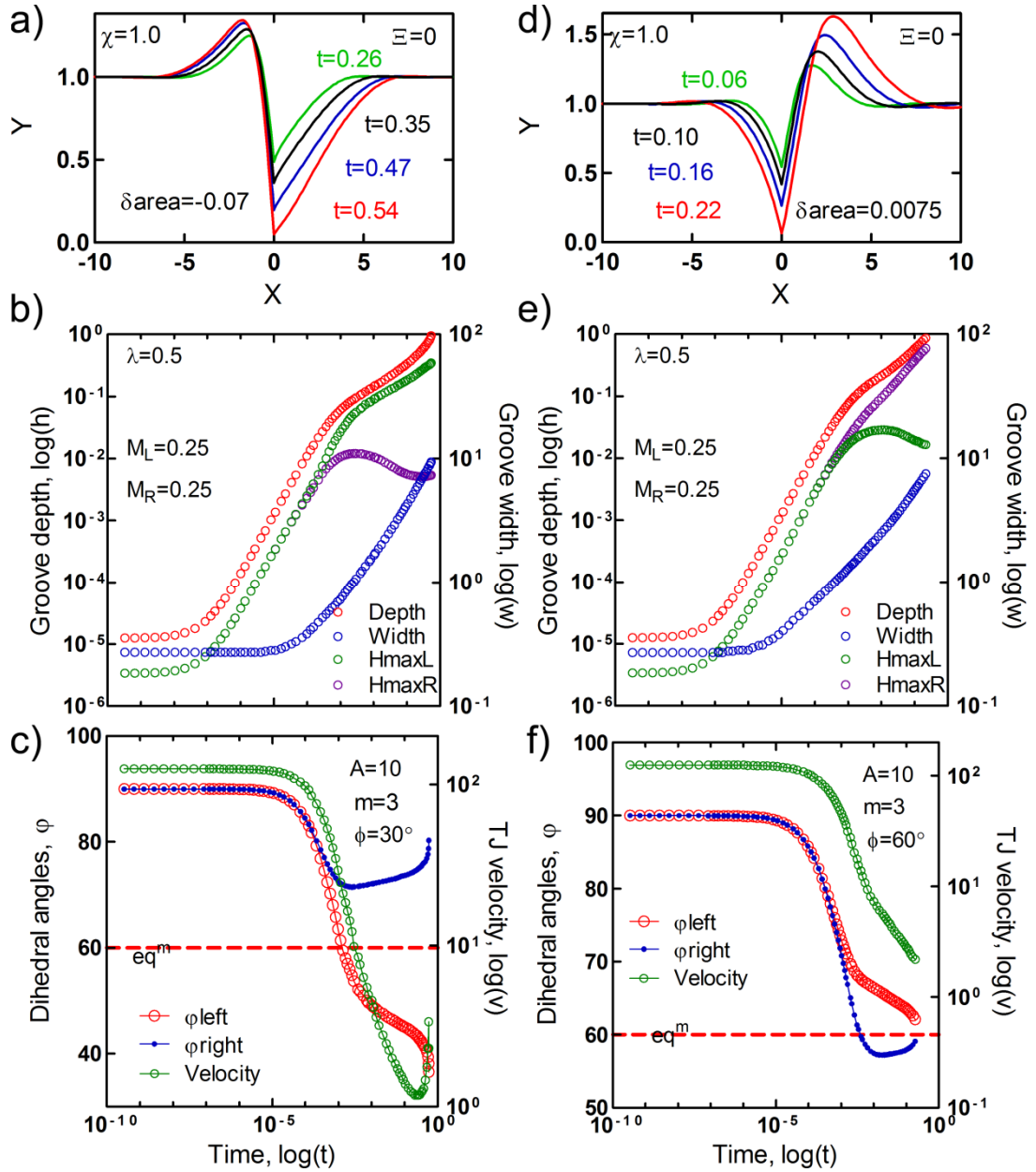


Figure 4.5.3.1: Electromigration grooves with $\chi=1.0$, on a surface having an anisotropic diffusivity characterized by $A=10$, $m=3$, $\phi=30^\circ$ (first column: a to c)

and $\phi=60^\circ$ (second column: d to f). a) and d) shows the GB groove profiles; b) and e) kinetic data for groove depth, maxima and width; c) and f) TJ velocity and the dihedral angles. Formation of faceted grain boundary voids of opposite facet orientations.

On the other hand, the experiments with $\phi=30^\circ$ and $\phi=60^\circ$ tilt angles resulted in very similar morphologies to the ones reported in figure 4.5.3.1 with narrower faceted grain boundary voids and sharper triangular hillocks.

4.6. Effect of an elastostatic field on grooving

The effect of an applied stress field is studied by altering the elastic dipole tensor interaction (EDTI) parameter in a wide range [$\Xi = \pm 0.1, \dots, \pm 10$].

Table 4.6.1: Physicochemical properties of Al, Cu, Sn, and Pb, Smithells (1967).

	Al	Cu	Sn	Pb
Elastic Moduli (GPa)	70.6	129.8	49.9	16.1
Poisson' Ratio	0.345	0.343	0.35	0.44
Surface tension (Nm ⁻¹)	0.915	1.780	0.685	0.480
Electrical Resistivity (Ωm)	2.7×10^{-8}	1.7×10^{-8}	16.8×10^{-8}	27×10^{-8}
Thermal Expansion (K ⁻¹)	2.43×10^{-5}	1.72×10^{-5}	2.38×10^{-5}	3.0×10^{-5}
$ \text{tr}(\underline{\lambda}_s) $	0.69	0.3	0.6	0.6
D_s^o (m ² s ⁻¹)	3×10^{-6}	5.84×10^{-5}	4.9×10^{-4}	-
h_σ (m)	2.86×10^{-10}	2.56×10^{-10}	5×10^{-10}	-

The elastic strain energy density (ESED) contribution on the other hand is ignored with the reasoning that it makes little sense since the applied stresses are much less than the elastic modulus ($\sigma^2/E \ll \sigma$) and can be neglected when accompanies a stress term. Using the values tabulated in Table 4.6.1; for a copper film with a scaling length of $\ell_0=0.1\mu\text{m}$ this interval corresponds to $[\pm 13.25 - \pm 1325]$ MPa (for aluminum: $[\pm 2.96 - \pm 296]$ MPa).

4.6.1. Grain boundary grooving under tensile stresses:

In figure 4.6.1.1 the kinetics of grain boundary grooving under a tensile stress field characterized by $\Xi=0.1$ is given. As can be seen from figure 4.6.1.1b the final time for film agglomeration eventually reduces to $t_f=1.1$ compared to $t_f=27.5$ that of thermal grooving; the applied tensile stress causes the groove to deepen more rapidly and enhances film breakup compared to that produced by capillarity alone. This can also be tracked from the kinetic data given in figure 4.6.1.1c: the penetration depth deviates from the $t^{0.25}$ time law (given by the dashed black lines) at around $t \approx 0.1$ and a simultaneous depression of the ridges (maximas) on both sides take place. During this process no observable deviation from the attained quasi equilibrium dihedral angle (figure 4.6.1.1f) takes place, yet close inspection in zoomed scale show symptoms of positive deviation. In figure 4.6.1.1e the kinetics of the groove width and the value of the hoop stress at the triple junction are given in detail. There observed two linear regimes in width vs. time plot again separated roughly at around $t \approx 0.1$ which also seems to be the onset of the asymptotic increase in triple junction stress.

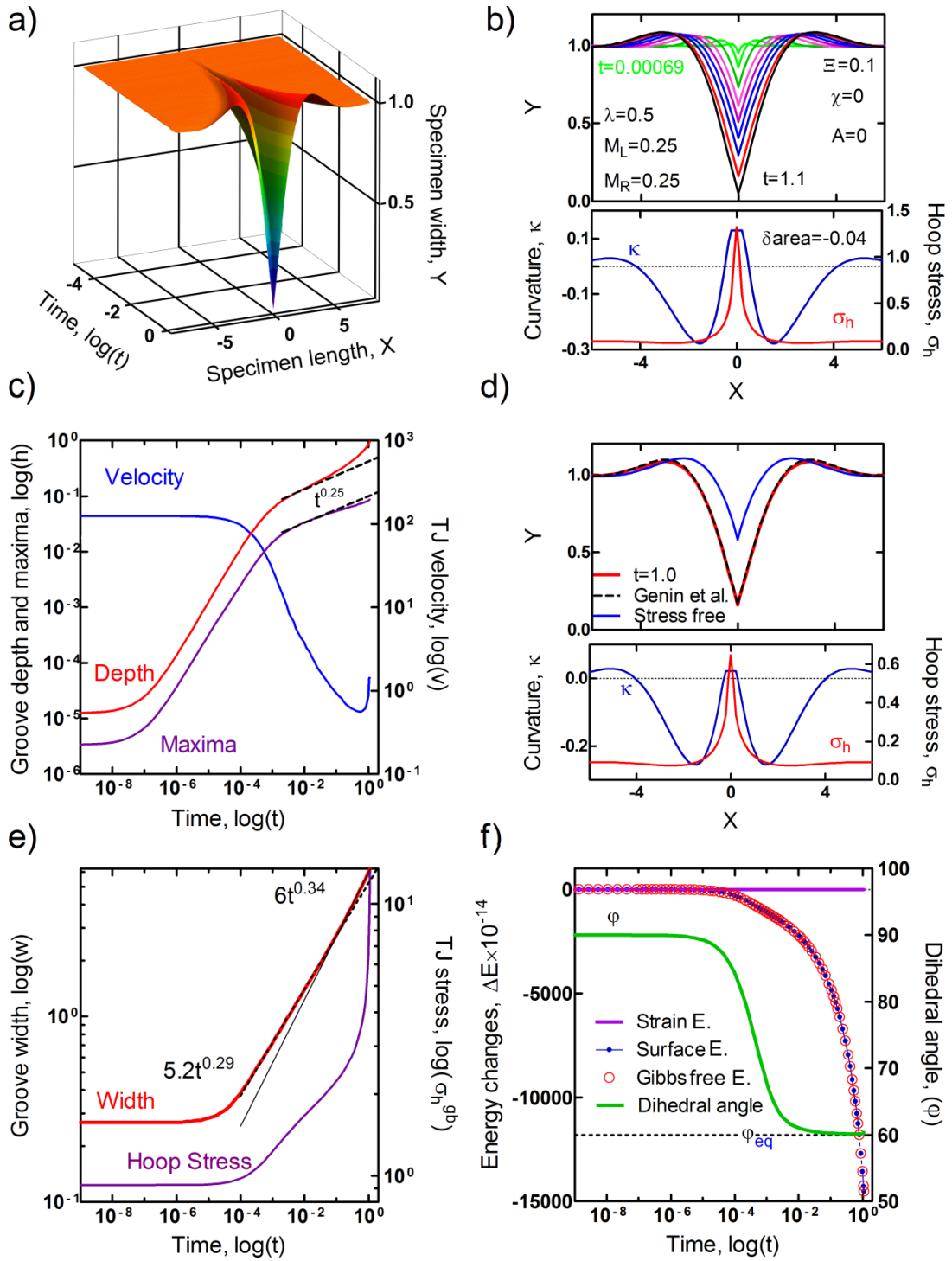


Figure 4.6.1.1: Isotropic grain boundary grooving for $\lambda=0.5$, $M_L=M_T=0.25$ and $\Xi=0.1$ which corresponds to 13.25 MPa ($\approx 10^{-4}E$; where E is the elastic modulus) for copper thin film with a length scale $\ell_0=0.1\mu\text{m}$. a) 3D representation of the

groove evolution, b) successive 2D profiles; curvature and hoop stress distributions corresponding to $t_f=1.1$ (black profile), c) kinetic data for groove depth, maxima, TJ velocity, d) comparison of the stress free and groove under tension profiles given by Genin et al. (1993) with the simulated profile at $t=1.0$; curvature and hoop stress distributions at $t=1.0$, e) kinetic data for groove width and TJ stress, f) energy changes and the kinetic data for the dihedral angle in semi-log scale.

Genin et al. (1993) extended Mullins' small slope solution by considering stress induced GB diffusion using the Herring relation (Herring, 1950, 1951) between chemical potential of atoms in the GB and stress applied normal it. They assume that the GB diffusional flux is a linear function of position along the boundary which in turn leads to a constant flux divergence over the boundary. Then they tried to analyze the effect of stress by superimposing a solution corresponding to the steady state grain boundary diffusion (without a groove) to Mullin's solution of thermal grooving. In figure 5 of their paper, they compare stress free groove with the one under tension with an arbitrary grain boundary flux of $j=0.5$ at the triple junction at a time $t=1.0$. With these values the superposed solution of thermal grooving has a magnitude twice to that of steady state grain boundary diffusion solution at the TJ.

In figure 4.6.1.1d above mentioned profile (Genin et al. 1993; Fig. 5 of p. 3545) is reproduced for $\lambda=0.5$ and given in connection with simulated profiles at $t\approx 1.0$. There exists a qualitative agreement between the two profiles as can be seen from this figure. The key point in this agreement should be the observation of quasi

constant dihedral angle reported in figure 4.6.1.1f; Genin et al. (1993) utilize Mullins' constant dihedral angle boundary condition at the triple junction. We will show even for a slight increase in the assumed stress level, the nonlinear dynamical evolution of the triple junction will not permit a constant dihedral angle to form. On the other hand, the proposed solution by Genin et al. (1993) is limited only to some certain cases which entail some strict assumptions; therefore in their analysis authors define a crossover time (t_c ; over which the two superposed terms make contributions of equal magnitude at the TJ) and show validity of these assumptions below this time. We found no means to match the simulated profiles and solution of Genin et al. (1993) after the simulation time of figure 4.6.1.1d. Even the solution proposed by Genin et al. (1993) holds for long times, a difference in profiles should be expected at longer times due to their consideration of infinitely long grain boundary compared to our bamboo like model (TJ stress given in figure 4.6.1.1e shows an asymptotic increase as the film thickness goes to zero) and also due to the stress induced surface diffusion considered in our work. Furthermore the level of stress assumed by Genin et al. (and in the experiment presented in figure 4.6.1.1) is on the order of *10 MPa*; yet, the thin films of technological importance are known to be exposed to thermal stresses up to 1 GPa (Bower and Shankar, 2007), the assumptions of the analysis presented by Genin et al. at these stress levels will instantaneously be broke down per se.

The energy changes given in figure 4.6.1.1f may be computed by recognition of an isobaric system; a composite system enclosed by external flexible and diathermal boundaries that allow not only to establish the thermal equilibrium in the system,

but also permit to have a direct contact with the external constant body, and the surface traction forces, that means the work done on the system is non-vanishing, $\Delta W \neq 0$ (Ogurtani, 2009b). Then for a discrete free surface contour line, letting n to designate the total number of nodes, one may write down the rate of total strain energy change at a given time step i during the evolution as:

$$P_i = -\frac{(1-\nu^2)}{2E} \mathfrak{T}_i \sum_{j=0}^{n-1} \frac{\bar{\sigma}_{ij}^2}{n} \bar{v}_{ij} \quad (4.6.1.1)$$

Here, $E/(1-\nu^2)$ is the plain strain elastic modulus, \mathfrak{T}_i is the total temporal length of the surface at a given time step i , and with j standing for the nodes of discrete surface, $\bar{\sigma}_{ij}$ and \bar{v}_{ij} are the calculated normalized hoop stresses and velocities at each node. The summation is performed over the free surface contour line exposed to the surface drift diffusion. Then, the change in total elastic strain energy δW during the evolution process (composed of m time steps) may be calculated as a function of discrete normalized time \bar{t}_i by simple integration (*i.e.*, summation) procedure applied to above expression:

$$\delta W_i = \sum_{k=0}^i \frac{P_k}{i} \bar{t}_i < 0 \quad (4.6.1.2)$$

Eq. (4.6.1.2) is used to compute the change in total elastic strain energy given in figure 4.6.1.1f. On the other hand, the film surface free energy (capillary) change including the grain boundary may be computed by the following equation:

$$\delta F_i = g_\sigma^o (\mathfrak{S}_i - 2\lambda \bar{h}_i) \quad (4.6.1.3)$$

Here, \bar{h}_i is the temporal depth measured from the initial flat surface, $\lambda = \frac{g_{gb}^o}{2g_\sigma^o}$ is the wetting parameter, where g_σ^o , g_{gb}^o are the specific surface and grain boundary Gibbs free energies respectively. Then the global Gibbs free energy variation is deducible from these formulas,

$$\delta G_i = \delta F_i - \delta W_i \quad (4.6.1.4)$$

Figure 4.6.1.1f clearly shows that the strain energy release of the film compared to its surface free energy is extremely small at this level of stress. Then the global Gibbs free energy change closely follows the change in surface free energy.

In figure 4.6.1.2 the effect of an increase in stress level on the profile evolution can be followed. It is evident that the groove tip kinetics is accelerated (penetration depth) and the evolution of the groove maximas on both sides are suppressed further with increasing EDTI.

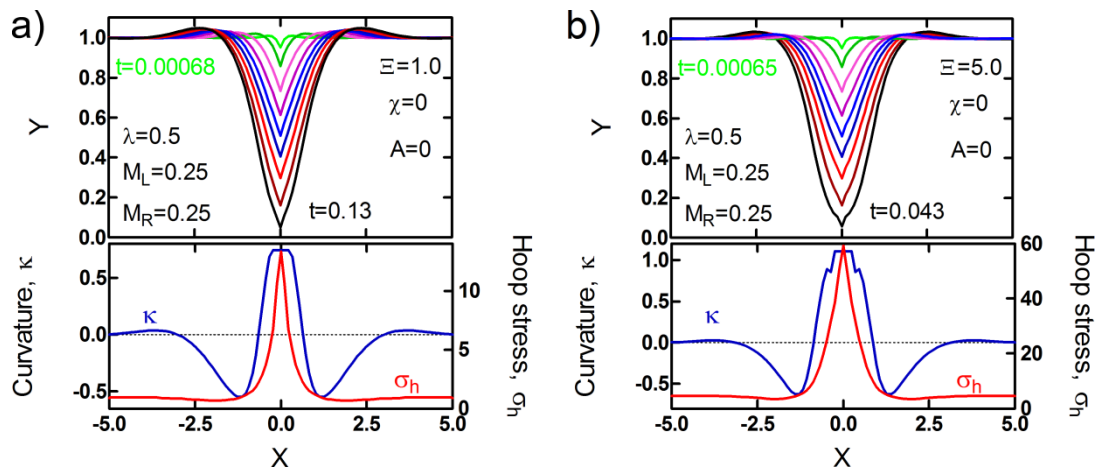


Figure 4.6.1.2: Isotropic grain boundary grooving for $\Xi=1.0$ and $\Xi=5.0$ which correspond to 132.5 and 662.7 MPa for copper thin film with a length scale $\ell_0=0.1\mu\text{m}$. Final time to failure falls $t_n=0.13$ for $\Xi=1.0$ and to $t_n=0.039$ for $\Xi=5.0$ in normalized scale.

Close inspection of $\Xi=1.0$ profile in figure 4.6.1.2a shows the lateral extension tendency of the groove tip vicinity at later times. This observation is supported by the evolution of the dihedral angle; it makes minima (slightly above the equilibrium value) through the way relaxing its quasi equilibrium value and then start to increase. The process becomes more apparent in figure 4.6.1.2b ($\Xi=5.0$) and leaves a sharp crack like feature at the tip of the grain boundary, which also indicates itself on the curvature plot. Further increase in EDTI results in the following scenario given figure 4.6.1.3. It is now possible to trace the formation of a diffusive micro crack at the groove root. With this formation random fluctuations, in the triple junction velocity and the dihedral angles vs. time plots, start to dominate. The curvature plots presented in figure 4.6.1.3bd keep a track of the crack nucleation.

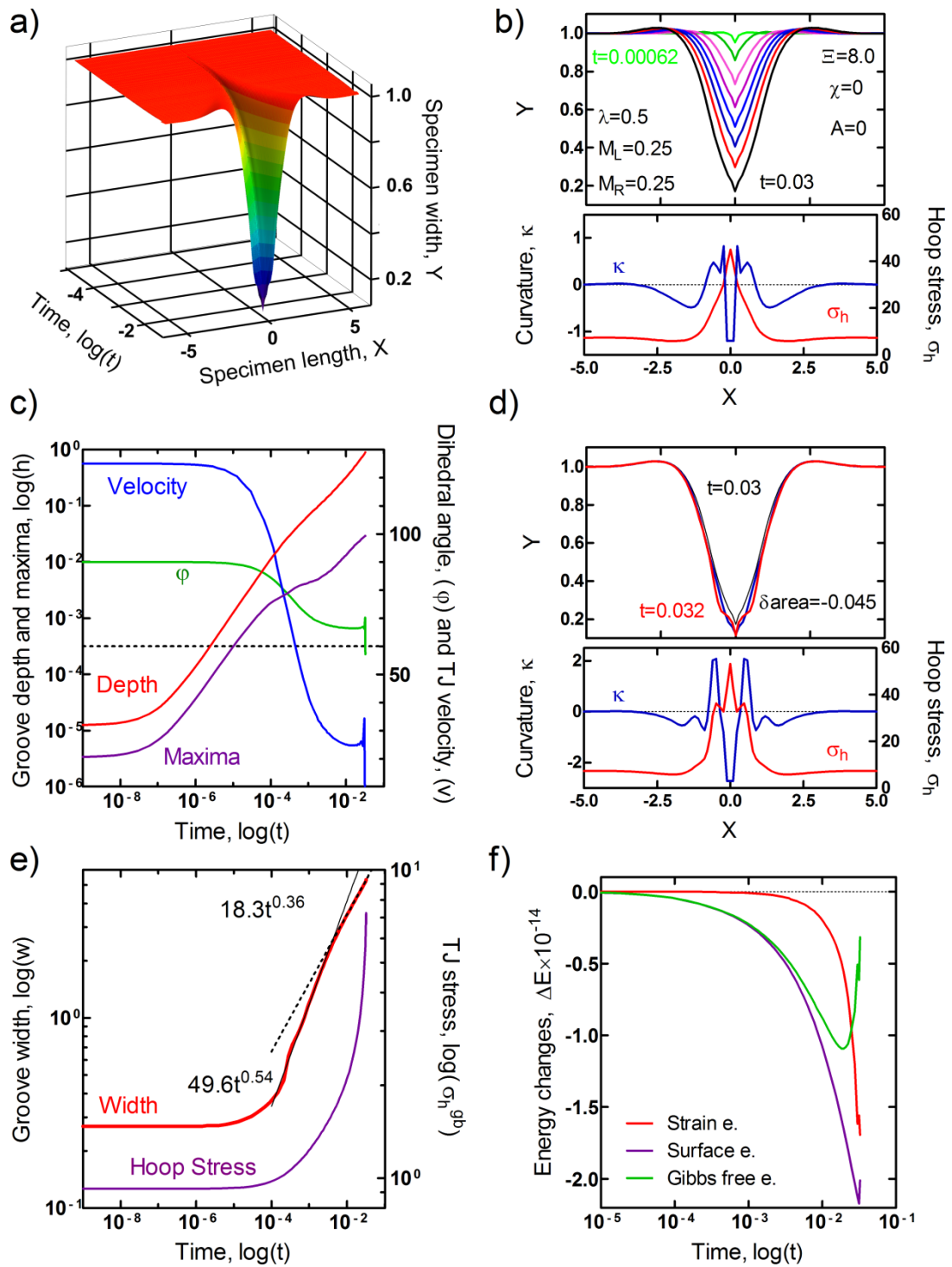


Figure 4.6.1.3: Isotropic grain boundary grooving for $\lambda=0.5$, $M_L=M_T=0.25$ and $\Xi=8.0$ which corresponds to 1.06 GPa for a copper thin film with a length scale $\ell_0=0.1\mu\text{m}$. a) 3D representation of the groove evolution, b) formation and

propagation of wedge like groove; curvature and hoop stress distributions corresponding to $t=0.030$ (black profile), c) kinetic data for groove depth, maxima, TJ velocity and the dihedral angle, d) diffusive micro crack formation at the groove root at $t=0.032$ (red profile), e) kinetic data for groove width and TJ stress, f) energy changes in semi-log scale.

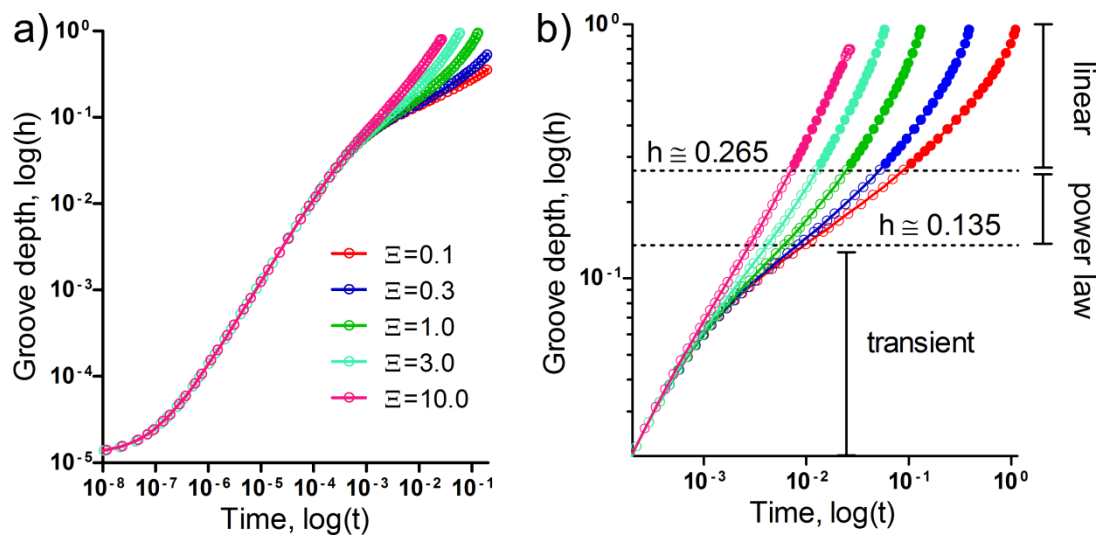


Figure 4.6.1.4: a) Groove depth vs. time plot for various EDTI parameters, b) the same plot in zoomed scale; power law and linear regions are highlighted. Note that for $\Xi=10.0$ failure takes place before reaching %95 of film thickness by micro crack formation.

The groove penetration depth versus time plots presented in c) parts of figures 4.6.1.1-3 seem to have a power law region which is a function of EDTI followed after a transient region which is not affected by a change in EDTI. Unlike the thermal groove counterpart, power law region in this case breaks down after a

certain time and another regime takes place. We have analyze this behavior in an experimentation set which includes 16 experiments of different EDTI values: $\Xi=[0.1, 0.2, 0.3, 0.5, 0.8, 1.0, 1.5, 2.0, 3.0, 4.0, 5.0, 6.0, 7.0, 8.0, 9.0, 10.0]$. In figure 4.6.1.4 five of these are given in order to have a clear presentation: $\Xi=[0.1, 0.3, 1.0, 3.0, 10.0]$.

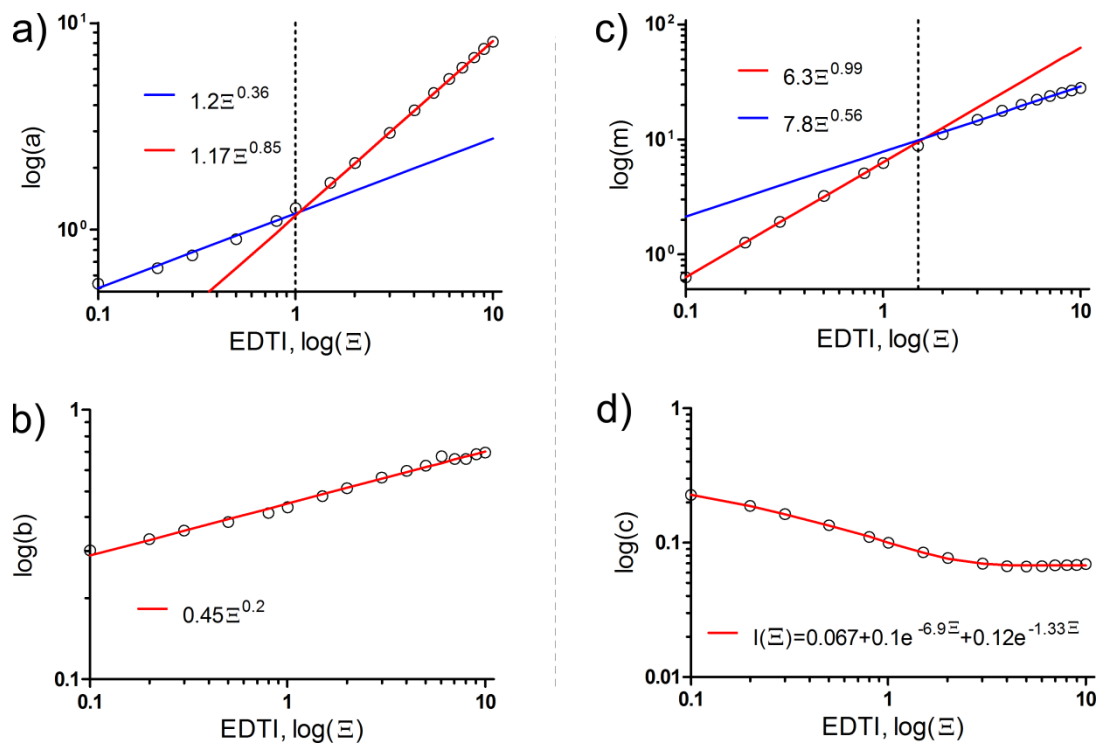


Figure 4.6.1.5: The power law region is expressed as $h(t)=a \times t^b$; in part a) the dependence of coefficient ‘a’, and in b) that of time exponent ‘b’ to EDTI is given. The region where the power law breaks down is modeled by a linear function $h(t)=m \times t+c$; in part c) dependence of the slope ‘m’, and in d) that of intercept ‘c’ to EDTI is given. The resulting functions are labeled as $h^I(\Xi,t)$ and $h^{II}(\Xi,t)$, where superscripts denote the power law and linear regions respectively.

It is found that the power law breakdown region can be modeled by using a linear function. The analyses of both regions are presented in figure 4.6.1.5, which results in the following analytic equations:

$$\bar{h}'(\Xi, \bar{t}) = \begin{cases} 1.2\Xi^{0.36}\bar{t}^{0.45\Xi^{0.2}}; & \Xi \leq 1.0 \\ 1.2\Xi^{0.85}\bar{t}^{0.45\Xi^{0.2}}; & \Xi > 2.0 \end{cases} \quad \text{(power law)} \quad (4.6.1.5)$$

and,

$$\bar{h}''(\Xi, \bar{t}) = \begin{cases} 6.3\Xi^{0.99}\bar{t} + I(\Xi); & \Xi \leq 1.0 \\ 7.8\Xi^{0.56}\bar{t} + I(\Xi); & \Xi > 2.0 \end{cases} \quad \text{(linear)} \quad (4.6.1.6a)$$

where,

$$I(\Xi) = 0.067 + 0.1e^{-6.9\Xi} + 0.12e^{-1.33\Xi} \quad (4.6.1.6b)$$

The result of the regression analysis is presented in figure 4.6.1.6 to show the goodness of fitting, the linear correlation factors (R^2) found during the analysis were over 0.98 in each case.

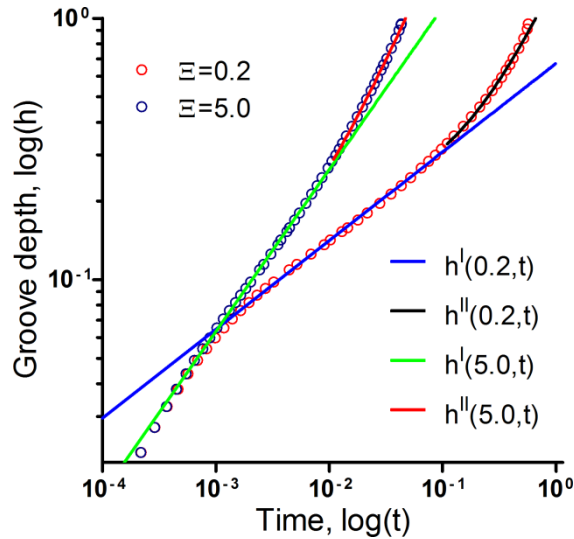


Figure 4.6.1.6: Experimentally obtained groove depth data for $\Xi=0.2$ and 5.0 is presented (open circles) together with the equations 4.6.1.5 and 4.6.1.6 (solid lines).

Although we presented the upper half of the film profiles due to symmetry and for clarity, as described in detail in previous chapter, the model considers a bamboo line in which a grain boundary ends up on the two sidewalls; as the film evolves the upper and lower triple junctions approach each other (or recedes as in the case of ridge growth). Therefore (essentially), the shape of the groove depth vs. time curves resulting from the model presented here is similar to studies of growth of array of grain boundary cavities rather than those of isolated ones. Pharr and Nix (1979) studied grain boundary cavity growth controlled by surface diffusion. They consider array of cavities of known geometry and model the change in the tip stress as the cavity grows in the expense of the grain boundary area by using a function of the form $\sigma_{tip} = \sigma_{app} / (1 - r^n)$ where r represents the time dependent crack length and $n=1, 2$ respectively for two and three dimensional cavities. In figure 4.6.1.7 this functional

forms are compared with our experimentally measured triple junction stresses at each time step. The authors observe, when compared with the isolated cavity, this increase in stress, due to decreased grain boundary length, results in an increase in the tip curvature (in fact curvature at a crack tip is ill defined, but the authors model a round, blunted tip rather than a sharp discontinuity and strictly follow Herring) and in turn leads to a crack becoming sharper as it grows. They state that this phenomenon may give an explanation of the observed macroscopic cracking in metals under creep conditions which imply that a process for crack tip sharpening must operate to counterbalance the blunting effects due to creep deformation. Here we go one step further by introducing surface diffusion mediated micro crack formation at the groove root.

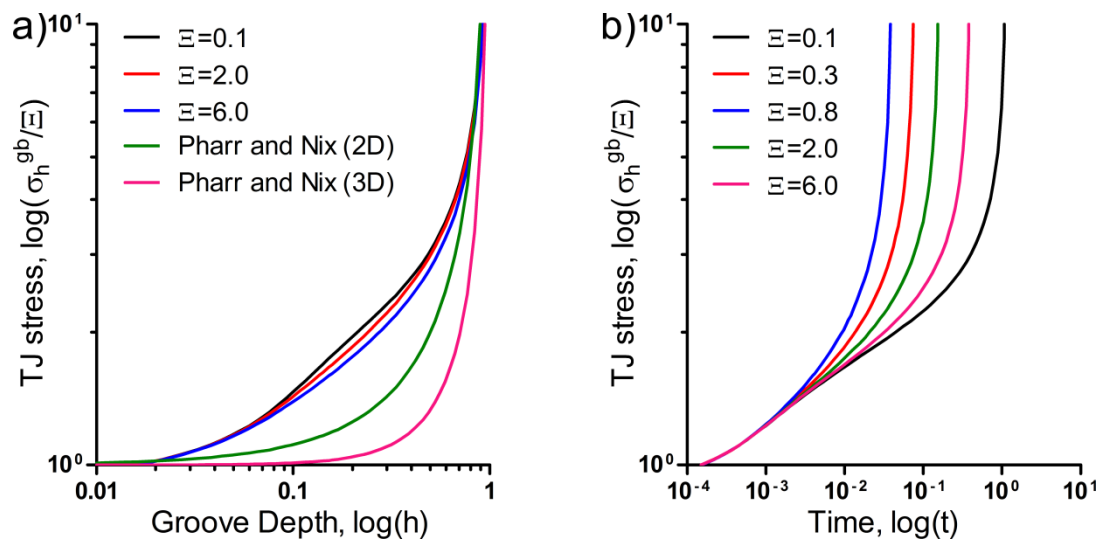


Figure 4.6.1.7: In a) the functions used to model the increase in tip stress due to cavity interactions by Pharr and Nix (1979) and the measured tip stresses for different values of EDTI in the present work is compared; and in b) the time evolution of the tip stresses in the present study is given.

The Hull – Rimmer model of cavity growth assumes that surface diffusion is much faster than the grain boundary diffusion; accordingly the cavity growth rate predicted by this model is linearly proportional to remote or applied normal stress (σ_o) to the boundary (Hull & Rimmer, 1959):

$$\frac{dh}{dt} \cong \frac{D_{gb} h_{gb} \Omega_{gb} \sigma_o}{2kT h a} \quad (\text{Hull – Rimmer}) \quad (4.6.1.7)$$

In Eq. (4.6.1.7) D_{gb} , h_{gb} , Ω_{gb} are the grain boundary diffusivity, interfacial thickness, and the mean atomic volume, respectively. In this model an array of equally spaced circular cavities with cavity spacing of ‘a’ and radius of ‘h’ were considered. Later suggested improved relationships between the cavity growth rate and stress, including modifications to the diffusion lengths (the entire grain boundary is a vacancy source), stress redistribution (the integration of the stress over the entire boundary should equal the applied stress), cavity geometry (cavities are not perfectly spherical) and the “jacking” effect, where atoms deposited on the boundary cause displacement of the grains (Raj & Ashby, 1975; Speight & Beere, 1975; Riedel, 1987) are all in a similar form (Kassner & Hayes, 2003) to that of Eq. (4.6.1.7).

On the other hand, differentiating Eq. (4.6.1.6) with respect to normalized time one may obtain the following equation:

$$\frac{d\bar{h}''}{d\bar{t}} \cong \begin{cases} 6.3\Xi; & \Xi \leq 1.0 \\ 7.8\Xi^{0.5}; & \Xi > 2.0 \end{cases} \quad (4.6.1.8)$$

Reverting back to real time and space above equation yields:

$$\frac{dh''}{dt} \cong \begin{cases} \frac{2D_\sigma h_\sigma |\text{tr}(\underline{\lambda}_s)| (1+\nu) \Omega_\sigma \sigma_o}{kT \ell_o^2}; & \sigma_o \leq \frac{3g_\sigma^o}{|\text{tr}(\underline{\lambda}_s)| (1+\nu) \ell_o} \quad (4.6.1.9a) \\ \frac{4.5D_\sigma h_\sigma \Omega_\sigma}{kT} \left(\frac{|\text{tr}(\underline{\lambda}_s)| g_\sigma^o (1+\nu) \sigma_o}{\ell_o^5} \right)^{1/2}; & \sigma_o > \frac{6g_\sigma^o}{|\text{tr}(\underline{\lambda}_s)| (1+\nu) \ell_o} \quad (4.6.1.9b) \end{cases}$$

Noting Eqs. (3.2.13) and assuming $h_{gb}=h_\sigma$, $\Omega_{gb}=\Omega_\sigma$, Eq. (4.6.1.9) is in accord with the Hull – Rimmer growth rate equation at moderate stress levels, yet it predicts a nonlinear dependence on applied stress above a threshold value which is inversely proportional to the scaling length, say the film thickness. For a 1 μm thick film this stress threshold ($6\gamma^{Cu}/|\text{tr}(\underline{\lambda}_s^{Cu})|(1+\nu)\ell_o$) is calculated as 26.5 MPa with the given material constants for copper.

On the other extreme the Chuang – Rice model of cavity growth assumes that grain boundary diffusion is much faster than the surface diffusion. This time, it was found that the cavity growth rate is proportional to the third power of the applied stress, σ_o^3 , for low stresses and for high stresses the rate varies as $\sigma_o^{3/2}$ (Kassner & Hayes, 2003).

$$\frac{dh}{dt} \cong \frac{D_{\sigma} h_{\sigma} \Omega_{\sigma} \sigma_{\sigma}^3}{2kT\gamma_s^2} \quad (\text{Chuang – Rice}) \quad (4.6.1.10)$$

Aforementioned analysis of Pharr and Nix (1979) predicts somewhat shorter rupture times than those observed experimentally for grain boundary cavities in silver by Goods and Nix (1978a, 1978b), which are consistent with the ones predicted by Chuang and Rice (1973) model after a modification to account cavity interactions by the use of above given functional form of σ_{tip} for the three dimensional case ($n=2$) rather than two dimensions ($n=1$). Igit and Mawby (1999) models failure of aluminum bamboo line of a similar configuration used in the present work. They start with a thermal groove as an initial condition and then activate stress induced grain boundary diffusion and employ different ratios of grain boundary/surface diffusivities each greater than one (surface control; i.e. Chuang – Rice model). Their analysis predicts a rupture time inversely proportional to the 3/2 power of the applied stress (this result obtained by digitizing their Fig. 4 and by excluding the first two data point, then one obtains $t_f \propto 1/\sigma^{1.66}$ with a correlation coefficient $R^2=0.976$).

Corresponding relationships between the rupture time and applied stress may be obtained by integrating Eqs. (4.6.1.7, 10) between the critical radius (below which sintering occurs) and half cavity spacing. Similarly Eq. (4.6.1.8) may be integrated for normalized groove depth between [0, 1] to obtain the rupture times. On the other hand the rupture time data can be collected directly from the simulation experiments; this presents a corrected result hence we have identified different

regions in penetration depth vs. time plots other than the linear region. Yet, both methods produce consistent results as presented in figure 4.6.1.8.

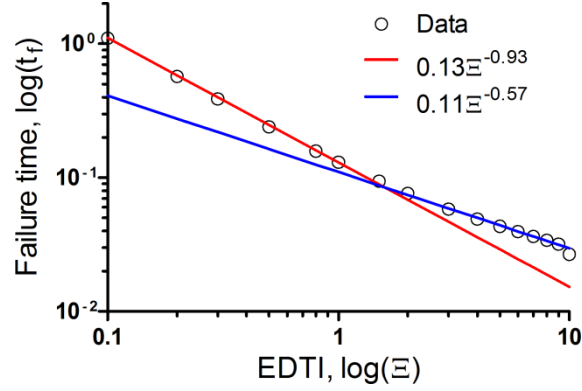


Figure 4.6.1.8: Failure time as a function of EDTI for $\lambda=0.5$, $M_L=M_T=0.25$.

It should be mentioned here that, because of phenomena reported previously in figures (4.6.1.2, 3) for high stress levels, not all the failure takes place when groove penetration reaches to the %95 of the film thickness (i.e. film agglomeration) but also assumed to happen when a sharp crack tip nucleates and random fluctuations start to dominate the system. At this level we assume that sudden rupture takes place by infinitely fast crack propagation. From figure 4.6.1.8 following equations are obtained by linear regression analysis:

$$\bar{t}_f \cong \begin{cases} 0.13\Xi^{-0.93}; & \Xi \leq 1.0 \\ 0.11\Xi^{-0.57}; & \Xi > 2.0 \end{cases} \quad (4.6.1.11)$$

Reverting back to real time and space above equation yields:

$$t_f \cong \begin{cases} \frac{kT \ell_o^3}{2.5 D_\sigma h_\sigma |tr(\underline{\lambda}_s)|(1+\nu)\Omega_\sigma \sigma_o}; & \sigma_o \leq \frac{3g_\sigma^o}{|tr(\underline{\lambda}_s)|(1+\nu)\ell_o} \quad (4.6.1.12a) \\ \frac{kT}{5.2 D_\sigma h_\sigma \Omega_\sigma} \left(\frac{\ell_o^7}{|tr(\underline{\lambda}_s)|g_\sigma^o(1+\nu)\sigma_o} \right)^{1/2}; & \sigma_o > \frac{6g_\sigma^o}{|tr(\underline{\lambda}_s)|(1+\nu)\ell_o} \quad (4.6.1.12b) \end{cases}$$

In order to investigate effect of wetting on the rupture times we have performed extensive simulation experiments for a set of wetting parameters, $\lambda=[0.16, 0.3, 0.5, 0.8, 0.97]$. Result of this analysis is presented in figure 4.6.1.9, accordingly stress dependence of the rupture time takes the form of $\sigma^{[-1.2, \dots, -0.7]}$ for low stresses and $\sigma^{[-0.75, \dots, -0.4]}$ for high stresses as wetting parameter differs in $[0.01, \dots, 1.0]$ range.

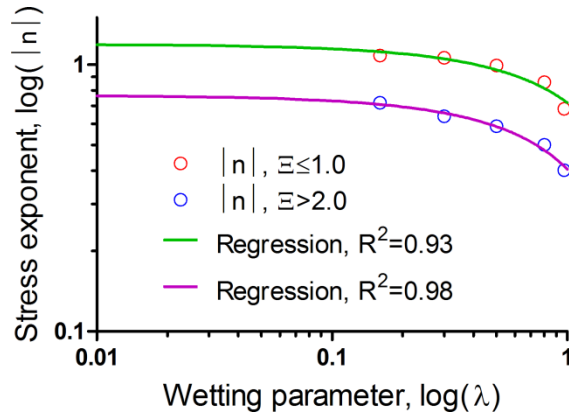


Figure 4.6.1.9: Dependence of the rupture time stress exponent on the wetting parameter.

4.6.2. Grain boundary grooving under compressive stresses:

Successive profiles given in figure 4.6.2.1ab show that the evolution under a compressive stress field ($\Xi=-0.1$) tend to form a ridge at the grain boundary. The groove depth 'h' (depth measured from the initial flat surface towards the bulk) follows a transient followed by a $t^{1/4}$ trajectory to a certain depth which may be called as the crossover depth (h_c) and then turns back by leaving a smooth peak in depth 'd' versus time plot, crosses its initial position at $h=0$ and continues upwards to take negative values. This is presented in figure 4.6.2.1e on a semi log scale. Another characteristic length; the depth measured from the maxima to the root; depth 'd' is given in figure 4.6.2.1c in log-log scale together with the position of the maxima ($d=h+h_{max}$). This plot clearly shows that the distance from the groove root to the maxima is kept constant during the ridge growth in which no observable deviation from the attained quasi equilibrium dihedral angle (figure 4.6.2.1f) takes place, and the triple junction velocity (figure 4.6.2.1c) stays constant without showing gross temporal variations. All these indicate that the ridge translates in a local steady state at a constant velocity. In figure 4.6.2.1e the kinetics of the groove width and the value of the hoop stress at the triple junction are given. The compressive hoop stress value reported in this plot increase in magnitude as the groove deepens to h_c and then decreases as the grain boundary length increases with the ridge formation.

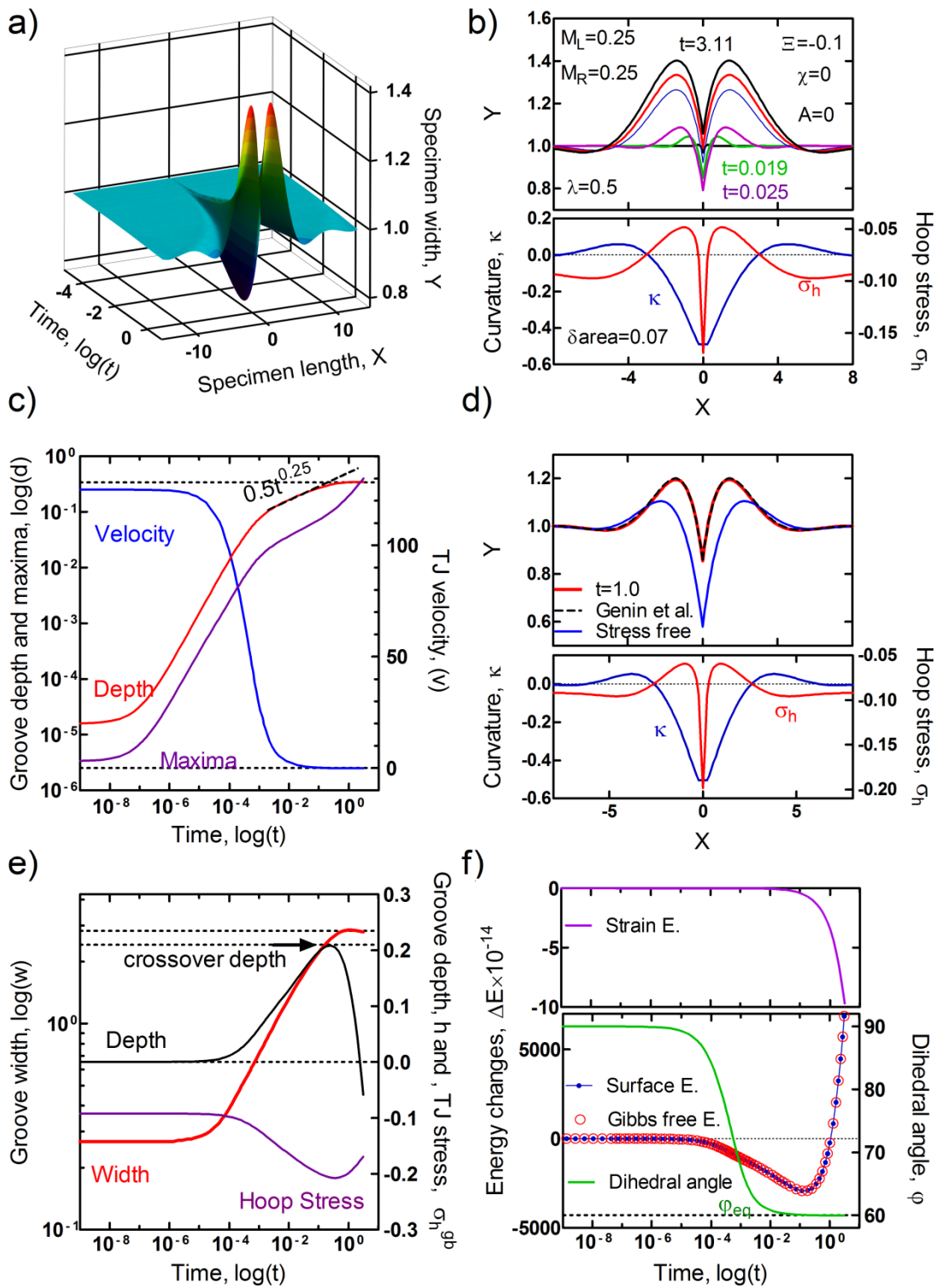


Figure 4.6.2.1: Isotropic grain boundary grooving for $\lambda=0.5$, $M_L=M_T=0.25$ and $\Xi=-0.1$. a) 3D representation of the groove evolution, b) successive 2D profiles;

curvature and hoop stress distributions corresponding to $t=3.11$ (black profile), c) kinetic data for groove depth ('d'), maxima and TJ velocity, d) comparison of the stress free and groove under tension profiles given by Genin et al. (1993) at $t=1.0$; curvature and hoop stress distributions at $t=1.0$, e) kinetic data for groove depth ('h'), width and TJ stress, f) energy changes and the kinetic data for the dihedral angle in semi-log scale.

We have presented the solution proposed by Genin et al. (1993) in figure 4.6.2.1b by reproducing it (using their equations 23-27) for an arbitrary constant grain boundary flux of $j=0.4$, and for $\lambda=0.5$, $B=1.0$, and $t=1.0$. There exists a qualitative agreement with the simulated profile as can be seen from this figure, again we believe that the key point in this agreement should be the observation of quasi constant dihedral angle reported in figure 4.6.1.1f and the satisfaction of the steady state assumption (locally) during the natural evolution of the groove at his moderately low stress value; Genin et al. (1993) utilize Mullins' constant dihedral angle boundary condition at the triple junction.

The energy change plots given in figure 4.6.2.1f indicate that the strain energy decreases as the surface roughness increases, but the change in global Gibbs free energy strictly follows the change in the surface energy (due surface area increase) which makes a minima in negative scale and then monotonically increases to assume positive values. This plot clearly shows that the process is energetically unfavorable, i.e. kinetically driven effects dominate during the process.

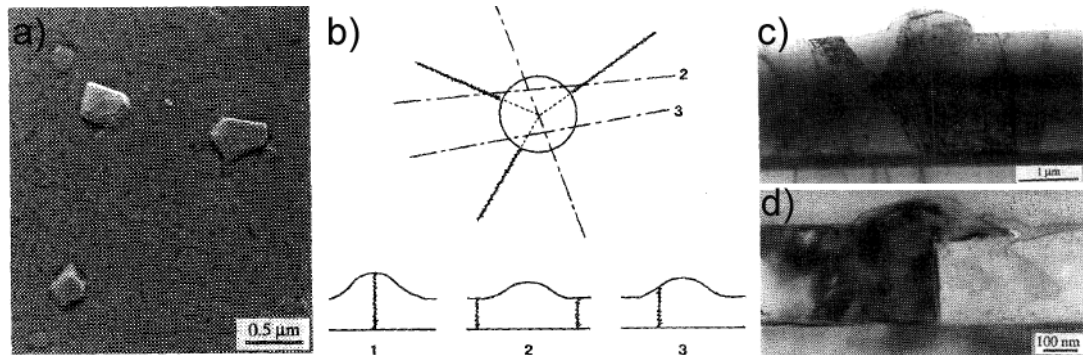


Figure 4.6.2.2: Experimentally observed hillocks in a thin aluminum film by Ericson et al. (1991). a) over view showing typical hillock appearances, b) schematic top view of a hillock centered over the grain boundary triple junction, and examples of cross-sectional views, c) and d) TEM cross-sections of different hillocks (compiled from figures 2, 5, 7, 9 of Ericson et al., 1991).

One of the most commonly observed surface reconstruction phenomena in thin films is the formation of hillocks. In situ observations of thin films show that hillocks generally form in the vicinity of grain boundary triple junctions and it is believed that they are formed under the influence of residual and/or thermo-mechanical compressive stresses induced during deposition and/or thermal cycling, respectively (Philofsky et al., 1973; Chang et al., 1989; Ericson et al., 1991; Genin, 1995a, 1995b, 1996; Kim et al., 2001). However, it is not easy to observe hillocks atop grain boundaries through cross-sectional micrographs; the limitation of planar cuts (cross-sectional views) through three dimensional structures is discussed by Ericson et al. (1991) (see figure 4.6.2.2).

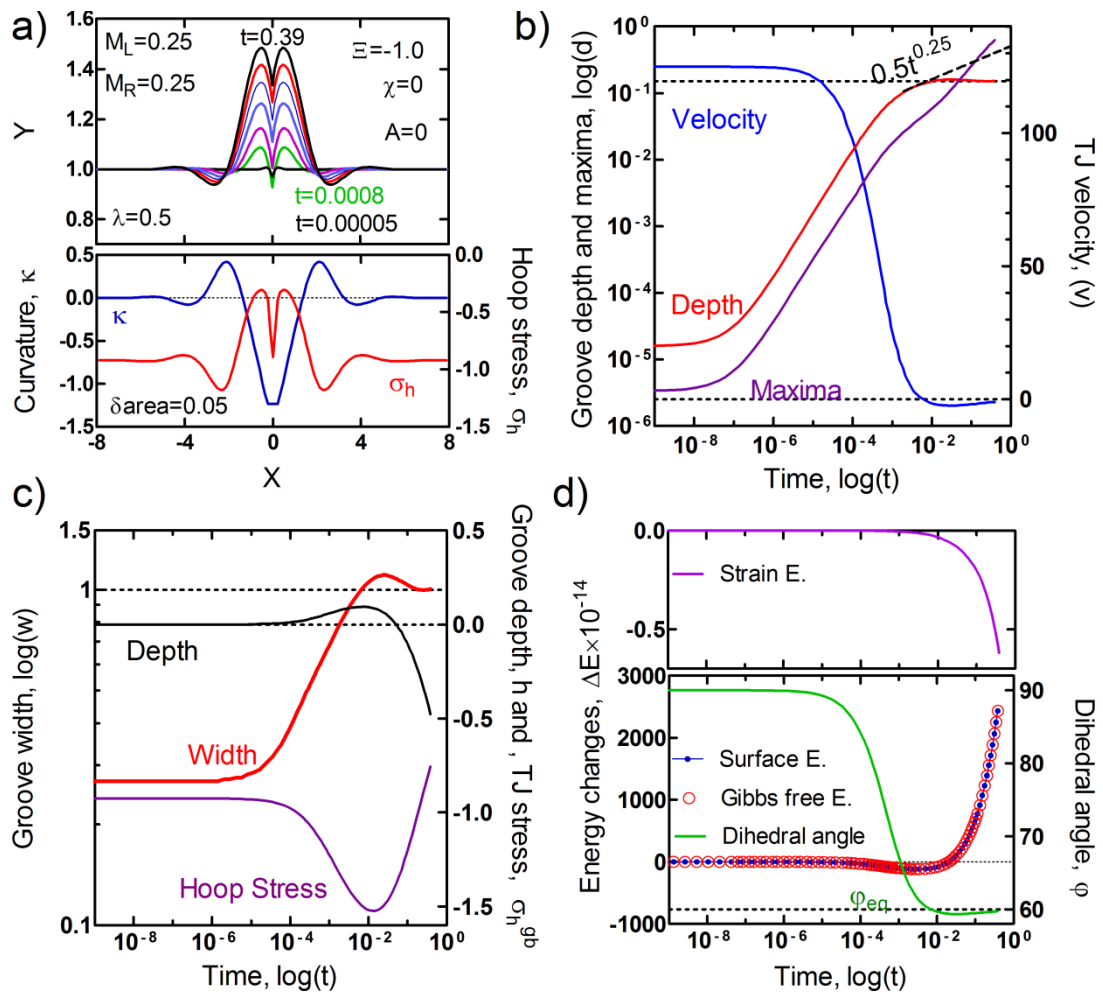


Figure 4.6.2.3: Isotropic grain boundary grooving for $\lambda=0.5$, $M_L=M_T=0.25$ and $\Xi=-1.0$. a) successive 2D profiles; curvature and hoop stress distributions corresponding to $t=0.39$ (black profile), b) kinetic data for groove depth ('d'), maxima and TJ velocity, c) kinetic data for groove width, depth ('h') and TJ stress, d) energy changes and the kinetic data for the dihedral angle in semi-log scale.

Furthermore as argued by Genin (1995b) and as presented by figure 4.6.2.1f the assumption of grain boundaries are immobile is severe in this case hence ridge

growth is energetically unfavorable and places the grain boundary in a metastable condition which forces it to migrate. Genin (1995a, 1996) suggests a model for hillock formation relying on the solution for compressive stress induced ridges provided earlier by Genin et al. (1993) together with grain boundary migration (grain growth). Later, carefully prepared experimental set up by Kim et al. (2001) show the interplay between compressive stress induced ridge formation and grain growth (i.e. grain boundary migration) in hillock formation without question.

In this respect the present model resembles to an earlier work of Genin (1995b) and able to describe the initial stages of hillock formation where the grain boundary motion is hindered. Another limitation of the study of Genin et al. (1993), except from those discussed in section 4.5.2.1, and Genin (1995a, 1995b) was the absence of long range diffusion into hillock from surroundings film area (Kim et al., 2001) as presented in figure 4.6.2.1b. Kim et al. (2001) indicate the essence of long range diffusion citing Chaudhari's hillock model (1974) in which an analysis of lattice diffusion (Nabarro – Herring creep) is presented. Presland et al. (1972) on the other hand provide evidences for surface diffusion controlled mechanism during hillock growth in thin silver films. The authors directly adopt results of the Hull – Rimmer theory by noting the analogy of the problem with that of grain boundary void growth after making suitable arrangements. Therefore, they gave a hillock growth rate that is linearly proportional with the stress. However, to our present knowledge, there exists no gross scale simulation study in the literature that reflects the dominant effect of long range surface drift diffusion. Here, in figures 4.6.2.3, 4 we

have presented the effect of an increase in stress (EDTI) in growth kinetics of a grain boundary groove by surface diffusion under a compressive stress field.

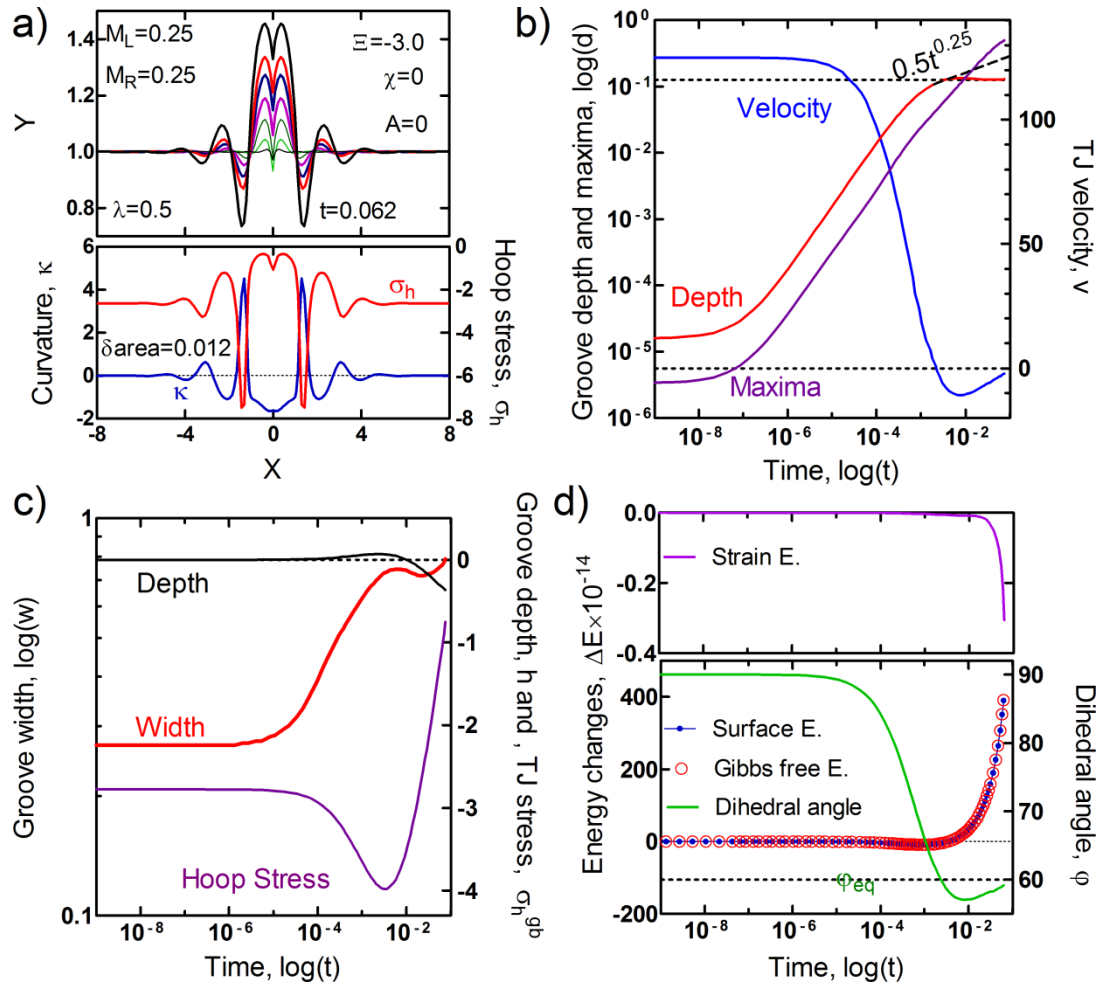


Figure 4.6.2.4: Isotropic grain boundary grooving for $\lambda=0.5$, $M_L=M_T=0.25$ and $\Xi=-3.0$. a) successive 2D profiles; curvature and hoop stress distributions corresponding to $t=0.062$ (black profile), b) kinetic data for groove depth ('d'), maxima and TJ velocity, c) kinetic data for groove width, depth ('h') and TJ stress, d) energy changes and the kinetic data for the dihedral angle in semi-log scale.

In each case distance 'd' reaches a constant value which is inversely proportional to the applied stress and similarly the value of the crossover depth decreases as stress increases. The amplitude of the secondary oscillations on both sides of the groove root rapidly increases with the applied stress during this kinetically driven evolution so that one may speak of extremely high surface instability above certain values.

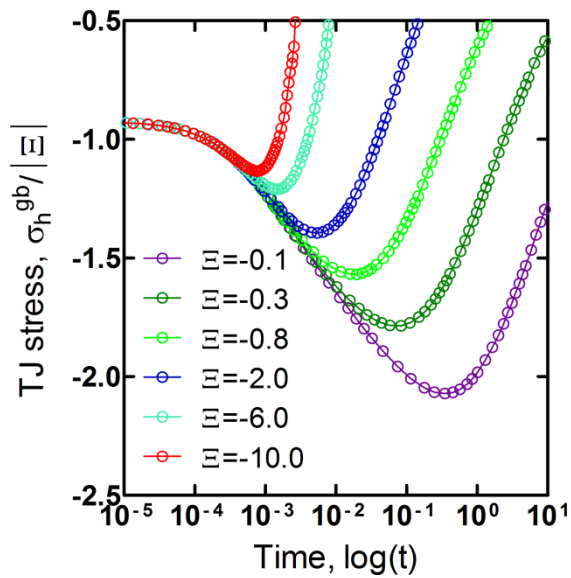


Figure 4.6.2.5: Evolution of the normalized groove tip stress as a function of normalized time for different levels of applied stress in log-log scale.

Figure 4.6.2.5 illustrates the evolution of the normalized groove tip stress as a function of normalized time in log-log scale. The compressive tip stress increases in magnitude as the groove deepens initially, and decreases once the grain boundary

area start to increase due to ridge growth. The rate of this inversion is proportional with the amount of applied stress.

The kinetic data for groove depth 'h', groove maxima, and groove depth 'd' (which is obtained by summing the previous two) for different levels of applied stress is presented in figure 4.6.2.6. An analysis of crossover depths and times collected from this figure may provide an incubation time for hillock formation or may give an estimate of the time and depth where grain boundary migration may start to occur if it is possible, as in the case of Genin's (1995a) model.

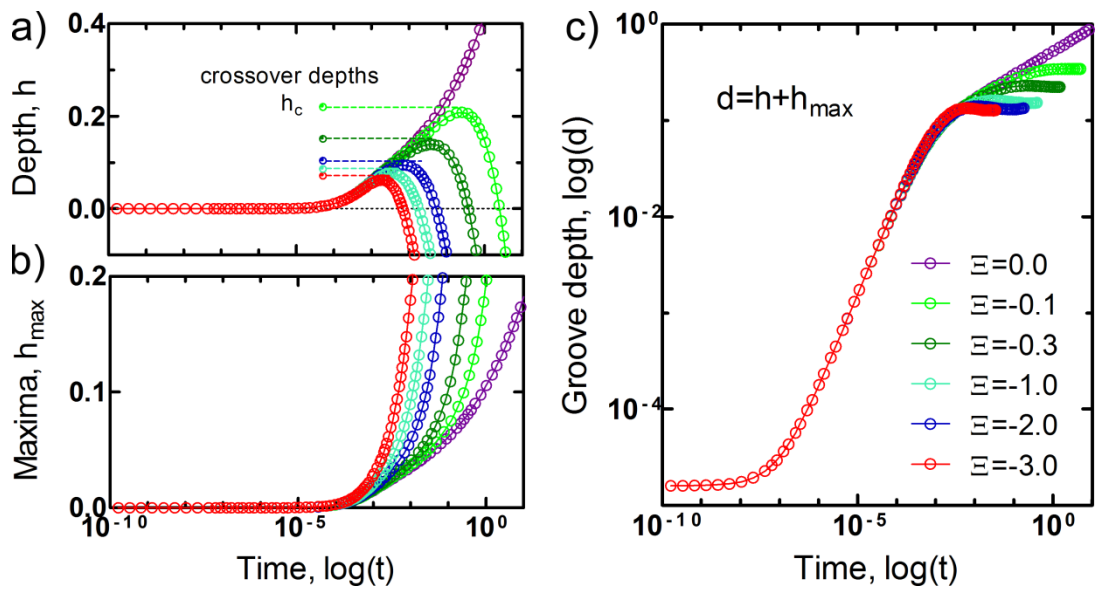


Figure 4.6.2.6: The kinetic data for a) groove depth 'h', b) groove maxima ' h_{\max} ', and c) groove depth 'd' (which is obtained by summing the previous two) for different levels of applied stress; $\Xi=-[0.1, 0.3, 1.0, 2.0, 3.0]$.

Such an analysis is presented in figure 4.6.2.7 and following equations are obtained by linear regression:

$$\bar{h}_c \cong 0.096 |\Xi|^{-0.32} \quad (4.6.2.1)$$

$$\bar{t}_c \cong \begin{cases} 0.0062 |\Xi|^{-1.6}; & \Xi \leq 1.0 \\ 0.0058 |\Xi|^{-0.8}; & \Xi > 2.0 \end{cases} \quad (4.6.2.2)$$

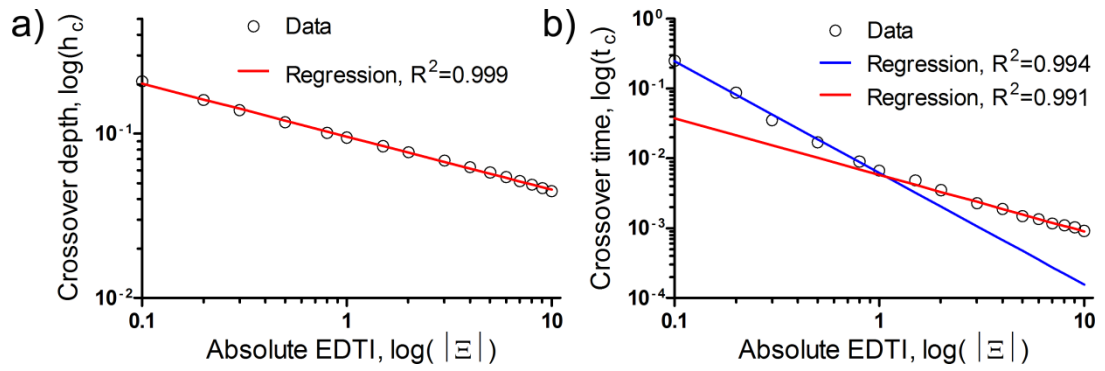


Figure 4.6.2.7: Analysis of the crossover depth ‘ h_c ’ and corresponding time data.

Reverting back to real time and space above equations yield:

$$h_c \cong \left(\frac{0.002 g_\sigma^o \ell_o^2}{|tr(\underline{\lambda}_c)| (1+\nu) \sigma_o} \right)^{0.32} \quad (4.6.2.3)$$

$$t_c \cong \begin{cases} \frac{0.035kT}{D_\sigma h_\sigma \Omega_\sigma} \left(\frac{\ell_o^{1.5} g_\sigma^{0.375}}{|tr(\underline{\lambda}_s)|(1+\nu)\sigma_o} \right)^{1.6}; & \sigma_o \leq \frac{3g_\sigma^o}{|tr(\underline{\lambda}_s)|(1+\nu)\ell_o} \quad (4.6.2.4a) \\ \frac{0.014kT}{D_\sigma h_\sigma \Omega_\sigma} \left(\frac{\ell_o^4 g_\sigma^{o-0.25}}{|tr(\underline{\lambda}_s)|(1+\nu)\sigma_o} \right)^{0.8}; & \sigma_o > \frac{6g_\sigma^o}{|tr(\underline{\lambda}_s)|(1+\nu)\ell_o} \quad (4.6.2.4b) \end{cases}$$

Here, the crucial role of the use of EDTI as driving force for surface diffusion in explaining certain phenomenon in those materials exposed to the surface tractions and body forces (dead loading) is once again shown for case of grain boundary grooving under compressive stresses. The drawback of the use of strain energy as the driving force for surface stability problems was also anticipated by Aziz et al. (1991) and in several cases by Ogurtani and coworkers (Ogurtani & Oren, 2001, 2005; Ogurtani & Akyildiz, 2008b, 2008c, 2008d; Ogurtani, 2009b). The strain energy driven instability is predicted to occur for stresses of either sign, however for a kinetically driven instability if the interface is unstable for a given stress state, then it is necessarily stable for the opposite stress state (Barvosa-Carter, 1998). Lahiri (1970) study hillocks on a Pb film and observe that they grow under a compressive stress and shrink in height with a sign reversal (under tension). Similarly Barvosa-Carter et al. (1998) found that the corrugated Si (001) interface is stable under tension and roughens under compression. The elastic dipole tensor interaction (EDTI) energy may be given by, $u_{EDTI} = -\Omega_\sigma \underline{\lambda}_s : \underline{\sigma}$, as suggested by Kröner (1958) and is extensively used by Ogurtani & Seeger (1984). The concept was effectively used by Sukharev et al. (2007) for simulating the back-stresses (Blech effect) induced by electromigration, and by Ogurtani and Akyildiz (2008b,

2008c, 2008d) for simulating intragranular void evolution and by Ogurtani (2009b) for simulating surface stability of single crystal metallic thin films.

CHAPTER 5

CONCLUSIONS

The dynamic computer simulation experiments presented in chapter 4 identify well known, experimentally observed grain boundary groove shapes and shed light on their growing kinetics. They also allow generating some scenarios under several conditions regarding to the applied force fields and/or physicochemical parameters which are used to explain some related phenomena like grain boundary cavity/crack growth and hillock formation on film surfaces.

Simulations on thermal grooving for finite slopes, in which the only driving force is the capillarity, result in a time independent groove shape having linear dimensions growing with $t^{1/4}$, which agrees with the analytic (small slope) solution obtained by Mullins (1957). This stationary state is attained after a transient, which was found to obey the first order reaction kinetics (Ogurtani & Akyildiz, 2005). The transient regime appears to be important in interpreting experimental findings, especially with low triple junction mobilities where stationary states are hardly reached. This is demonstrated by introducing an analysis of experimental thermal grooving data reported for tungsten in the literature (Zhang et al., 2002), which strictly connects the observed 'changing dihedral angle' phenomena to the transient grooving

behavior. The phenomenon was previously connected tacitly by Zhang et al. (2002) to the changes take place in the surface energy due to changes in surface composition (segregation, adsorption) during experimentation. When anisotropic surface diffusivity is considered, groove penetration rate found to increase as the degree of folding increases, yet the overall morphology is not affected much. It has also been observed that formation of secondary oscillations is a strong function of anisotropy.

An applied electric field generates a bias in mass transport and destroys the groove symmetry; in the case of isotropy, the windward side of the grain boundary (cathodic grain) shows an extra mass accumulation compared to the leeward side (anodic grain). It does not modify the $t^{1/4}$ time law for triple junction penetration but puts an abrupt limit for the penetration depth (healing effect). After the termination of the groove penetration, the windward side hillock observed to buckle and move towards the cathode by leaving an elongated, narrower grooved area (void region) which is in accord with in situ TEM observations made by Riege and coworkers (Riege et al., 1995, 1996; Prybyla et al., 1998). The analysis suggests an inverse relationship between the terminal groove depth and the electronwind intensity (EWI) which is an indication of current crowding effect. Through a large number of simulations, not only the terminal groove depth but also the amount of rotation at the groove root to the windward side to assume a new quasi-equilibrium dihedral angle is determined as a function of EWI and wetting parameter. These connections could be useful in making quantitative comparisons with laboratory experiments. A threshold value for the EWI, below which no freezing effect is observed and

agglomeration failure takes place, is obtained as a function of wetting parameter. The estimated threshold current densities are much below the testing/operating conditions of conventional interconnects. This explains why we do not observe asymmetric-thermal-groove-like regions in postmortem evaluations of split/failed interconnects. Rather, postmortem examinations of failed interconnects, as well as in situ observations using scanning and tunneling electron microscopy, shows that open circuit failures often occur with the formation of crack-like slits oriented along grain boundaries that are perpendicular to the interconnect line (Fridline & Bower, 2002). The present study identifies the effect of the anisotropy in surface diffusion coefficient extensively by considering 96 different combinations surface textures, electron wind intensities, and wetting parameters. In certain textures, fatal slits extending along the grain boundaries are observed and their response to changes in electron wind intensity is reported. These simulations provide a map in selecting the most proper microtexture with respect to the applied current flow to reduce adverse effects of the diffusion anisotropy and to improve interconnect reliability. On the other extreme for the anisotropic surface diffusion, ridge formations at the triple junctions are observed and their response to changes in electron wind intensity is examined. It is also shown that the wetting parameter is highly effective on these morphology determinations.

The effect of an applied stress field is studied by altering the elastic dipole tensor interaction parameter in a wide range [$\Xi = \pm 0.1, \dots, \pm 10$] which correspond to [$\pm 13.25 - \pm 1325$] MPa for copper and [$\pm 2.96 - \pm 296$] MPa for aluminum with scaling length of $\ell_0 = 0.1 \mu\text{m}$. The results of the simulations was first compared with

that of Genin et al. (1993) who analyzed the effect of stress on grooving by superimposing a solution corresponding to the steady state grain boundary diffusion (without a groove) to Mullin's solution of thermal grooving. Accordingly, the applied tensile stress causes the groove to deepen more rapidly and enhances film breakup compared to that produced by capillarity alone as observed by Genin et al. (1993). Furthermore, the kinetics of accelerated groove deepening with an applied tensile stress is examined in connection with grain boundary cavity growth models in the literature. Triple junction displacement kinetics, after the transient, shows two distinct sequential regimes in log – log plot: a) power law and b) linear regimes. In the first regime, kinetics of penetration depth is described with a stress dependent time exponent of the form $0.45\Xi^{0.2}$ (with $\ell_0=1\mu\text{m} \rightarrow 0.16\sigma^{0.2}$ (aluminum) $\rightarrow 0.04\sigma^{0.2}$ (copper)). This power law regime eventually breaks down at a time, which is inversely proportional to the amount of applied stress, and replaced by a regime that is described by a linear kinetic law. This final regime assumes a Hull – Rimmer type growth (growth rate proportional with σ) at low stresses, but shows a nonlinear stress dependence for high stress values (growth rate proportional with $\sigma^{1/2}$). Stress level at the triple junction increases as the grain boundary is consumed during groove penetration (cavity growth). This increase in tip stress is monitored and a diffusive micro-crack formation is reported at the groove tip for high stresses which may constitute a physical basis for the observed microscopic cracking in thin films. Analysis of the failure times for $\lambda=0.5$, in accordance with above growth rates, gives stress exponents of -1 and $-1/2$ respectively at low and high stresses. These exponents approach respectively to -1.2 and $-3/4$ as the wetting parameter gets smaller.

The elastic strain energy density derived surface evolutions have no means to make a distinction between tensile and compressive stresses as the energy is quadratically proportional to stress. On the other hand, the use of elastic dipole tensor interactions between the stress field and the mobile atomic species (monovacancies) as a driving force for surface diffusion in the present model provided direct means to observe effects of compressive stress fields on the evolution of bicrystal film. Accordingly, application of compressive stress slows down the groove penetration and favors development of grain boundary ridge profiles that are in accord with results obtained by Genin et al. (1993). The present theory has great potential to describe the growth kinetics of experimentally observed hillocks in thin films, yet as the grain boundary area increases during ridge growth the process through an immobile boundary (normal to the initial film surface) is energetically unfavorable and a more complete model should account for the grain boundary migration (grain growth). Therefore, incorporation of grain boundary migration (triple junction transverse motion) put forth as a future objective, but an incubation time for hillock growth and a crossover depth, over which grain boundary migration becomes energetically favorable, are defined and discussed within the limits of the present model. For $\lambda=0.5$, crossover depth is found to be proportional with $\sigma^{-0.3}$. It is also found that stress dependence of the incubation time for hillock growth distinguishes between high and low stresses, and is proportional to $\sigma^{-1.6}$ and $\sigma^{-0.8}$ respectively.

The followings are the future recommendations:

In the present model we ignore the direct transfer of chemical species between bulk and void phases through the interface layer (growth) and consider only the drift-diffusion of chemical species along the surface of the film. The growth term in Eq. (3.1.2) could also be taken into account as an active mass transport mechanism which may identify the grooving kinetics under evaporation (i.e. corrosive atmospheres, $\tilde{g}_{vb} < 0$) or condensation.

As discussed in this thesis, specific surface Gibbs free energy enters into the formulation, which is in general not constant, but rather a function of space (i.e. orientation dependent surface stiffness) and time due to any possible compositional variations at the reaction front during the evolution phenomenon. Therefore, the exact solution of the problem involves the complete numerical solution of the time dependent diffusion equation with drift (convective) term by utilizing proper boundary and initial conditions.

As a final point, the combined effects of electromigration and stress migration should also be considered in detail.

REFERENCES

- Akyildiz, O. (2004). Computer simulations of grain boundary grooving and cathode voiding in bamboo interconnects by surface diffusion under capillary and electromigration forces. Unpublished master's thesis, Middle East Technical University, Ankara, TURKEY.
- Anderson, P. M., Wang, J., & Narayanaswamy, S. (2005). Thermal grooving in single versus multilayer thin films. *Materials Research Society Symposium Proceedings*, 854, U7.4.1.
- Arzt, E., & Nix, W. D. (1991). A model for the effect of line width and mechanical strength on electromigration failure of interconnects with “near-bamboo” grain structures. *Journal of Materials Research*, 6(4), 731-736. doi: 10.1557/JMR.1991.0731.
- Asaro, R. J., & Tiller, W. A. (1972). Interface morphology development during stress corrosion cracking: Part I. Via surface diffusion. *Metallurgical Transactions*, 3(7), 1789-1796. doi: 10.1007/BF02642562.
- Averbuch, A., Israeli, M., & Ravve, I. (2003a). Electromigration of intergranular voids in metal films for microelectronic interconnects. *Journal of Computational Physics*, 186(2), 481-502. doi: 10.1016/S0021-9991(03)00070-6.
- Averbuch, A., Israeli, M., Nathan, M., & Ravve, I. (2003b). Surface evolution in bare bamboo-type metal lines under diffusion and electric field effects. *Journal of Computational Physics*, 188(2), 640-677. Elsevier. Retrieved from <http://linkinghub.elsevier.com/retrieve/pii/S0021999103001992>.
- Averbuch, A., Israeli, M., Ravve, I., & Yavneh, I. (2001). Computation for Electromigration in Interconnects of Microelectronic Devices. *Journal of Computational Physics*, 167(2), 316-371. doi: 10.1006/jcph.2000.6677.

- Balluffi, R. W., Allen, S. M., & Carter, W. C. (2005). *Kinetics of Materials*. Hoboken, NJ, USA: John Wiley & Sons, Inc. doi: 10.1002/0471749311.
- Barth, J. V. (2000). Transport of adsorbates at metal surfaces: from thermal migration to hot precursors. *Surface Science Reports*, 40(3-5), 75-149. doi: 10.1016/S0167-5729(00)00002-9.
- Barvosa-Carter, W., Aziz, M. J., Gray, L. J., & Kaplan, T. (1998). Kinetically driven growth instability in stressed solids. *Physical Review Letters*, 81(7), 1445-1448. doi: 10.1103/PhysRevLett.81.1445.
- Beer, G., & Watson, J. O. (1992). *Introduction To Finite And Boundary Element Methods For Engineers* (p. 141). New York, USA: John Wiley & Sons.
- Beer, G., Smith, I., & Duenser, C. (2008). *The Boundary Element Method with Programming For Engineers and Scientists*. New York, USA: SpringerWien.
- Bhate, D. N., Bower, A. F., & Kumar, A. (2002). A phase field model for failure in interconnect lines due to coupled diffusion mechanisms. *Journal of the Mechanics and Physics of Solids*, 50(10), 2057-2083. doi: 10.1016/S0022-5096(02)00019-4.
- Bhate, D. N., Kumar, A., & Bower, A. F. (2000). Diffuse interface model for electromigration and stress voiding. *Journal of Applied Physics*, 87(4), 1712. doi: 10.1063/1.372082.
- Binh, V., Chaudier, M., Couturier, J., Uzan, R., & Drechsler, M. (1976). Grain boundary groove evolutions by surface self-diffusion on a plane and on a wire. *Surface Science*, 57(1), 184-204. doi: 10.1016/0039-6028(76)90176-X.
- Bonzel, H. P., & Mullins, W. W. (1996). Smoothing of perturbed vicinal surfaces. *Surface Science*, 350(1-3), 285-300. doi: 10.1016/0039-6028(95)01111-0.
- Bower, A. F., & Shankar, S. (2007). A finite element model of electromigration induced void nucleation, growth and evolution in interconnects. *Modelling and Simulation in Materials Science and Engineering*, 15(8), 923-940. doi: 10.1088/0965-0393/15/8/008.
- Brebbia, C. A., & Dominguez, J. (1992). *Boundary Elements An Introductory Course* (p. 160). New York, USA: McGraw Hill.

- Buehler, M. J., Balk, T. J., Arzt, E., & Gao, H. (2005). Constrained grain boundary diffusion in thin copper films. *Handbook of Theoretical and Computational Nanotechnology*, X, 1 - 35.
- Buff, F. P. (1955). Spherical interface. II. Molecular theory. *The Journal of Chemical Physics*, 23(3), 419. doi: 10.1063/1.1742005.
- Cahn, J. W., & Hilliard, J. E. (1958). Free energy of a nonuniform system. I. Interfacial free energy. *The Journal of Chemical Physics*, 28(2), 258. doi: 10.1063/1.1744102.
- Chang, C. Y., Vook, R. W., Lee, Y. C., & Hoshi, I. (1989). Isothermal annealing of hillocks in Al-Cu films. *Thin Solid Films*, 181(1-2), 57-63. doi: 10.1016/0040-6090(89)90472-0.
- Chason, E., Sheldon, B. W., Freund, L. B., Floro, J. A., & Hearne, S. J. (2002). Origin of compressive residual stress in polycrystalline thin films. *Physical Review Letters*, 88(15), 1-4. doi: 10.1103/PhysRevLett.88.156103.
- Chaudhari, P. (1974). Hillock growth in thin films. *Journal of Applied Physics*, 45(10), 4339. doi: 10.1063/1.1663054.
- Chen, N., Li, Z., Wang, H., & Sun, J. (2007). Grain boundary void growth in bamboo interconnect under thermal residual stress field. *Journal of Applied Physics*, 101(3), 033535. doi: 10.1063/1.2436833.
- Chiu, C., & Gao, H. (1993). Stress singularities along a cycloid rough surface. *International Journal of Solids and Structures*, 30(21), 2983-3012. doi: 10.1016/0020-7683(93)90208-O.
- Chiu, C., & Gao, H. (1995). A numerical study of stress controlled surface diffusion during epitaxial film growth. *Materials Research Society Symposium Proceedings*, 356, 33.
- Chuang, T. J. (1982). A diffusive crack-growth model for creep fracture. *Journal of the American Ceramic Society*, 65(2), 93-103. doi: 10.1111/j.1151-2916.1982.tb10365.x.
- Chuang, T. J., & Rice, J. R. (1973). The shape of intergranular creep cracks growing by surface diffusion. *Acta Metallurgica*, 21(12), 1625-1628. doi: 10.1016/0001-6160(73)90105-3.

- Chuang, T. J., Kagawa, K., Rice, J. R., & Sills, L. (1979). Overview no. 2 Non-equilibrium models for diffusive cavitation of grain interfaces. *Acta Metallurgica*, 27(3), 265-284. doi: 10.1016/0001-6160(79)90021-X.
- Dalleau, D., & Weidezaage, K. (2001). Three-dimensional voids simulation in chip metallization structures: a contribution to reliability evaluation. *Microelectronics Reliability*, 41(9-10), 1625-1630. doi: 10.1016/S0026-2714(01)00151-2.
- De Groot, S. R. (1951). *Thermodynamics of Irreversible Processes* (p. 98). Amsterdam, Holland: North-Holland Pub. Co.
- Defay, R., & Prigogine, I. (1966). *Surface tension and adsorption*. (A. Bellemans). New York, USA: John Wiley & Sons.
- Delph, T. J. (2002). Some selected topics in creep cavitation. *Metallurgical and Materials Transactions A*, 33(2), 383-390. doi: 10.1007/s11661-002-0099-0.
- Dobes, F. (1973). The influence of surface diffusion on the growth of grain boundary voids in creep. *Scripta Metallurgica*, 7(12), 1231-1234. doi: 10.1016/0036-9748(73)90068-9.
- Donder, T. D., & Rysselberghe, P. V. (1936). *Affinity*. Menlo Park, USA: Stanford University Press.
- Du, P., & Wong, H. (2006). A delta-function model for axially symmetric crystals. *Scripta Materialia*, 55(12), 1171-1174. doi: 10.1016/j.scriptamat.2006.07.042.
- Ericson, F., Kristensen, N., Schweitz, J., & Smith, U. (1991). A transmission electron microscopy study of hillocks in thin aluminum films. *Journal of Vacuum Science & Technology B: Microelectronics and Nanometer Structures*, 9(1), 58. doi: 10.1116/1.585790.
- Eshelby, J. D. (1979). Boundary problems \for dislocations\. In F. R. Nabarro, *Dislocations in Solids. Vol 1. The Elastic Theory* (pp. 167-221). New York, USA: North-Holland Pub. Co.
- Freund, L. B. (1998). A surface chemical potential for elastic solids. *Journal of the Mechanics and Physics of Solids*, 46(10), 1835-1844. doi: 10.1016/S0022-5096(98)00019-2.

- Fridline, D., & Bower, A. F. (1999). Influence of anisotropic surface diffusivity on electromigration induced void migration and evolution. *Journal of Applied Physics*, 85(6), 3168. doi: 10.1063/1.369656.
- Fridline, D., & Bower, A. F. (2002). Numerical simulations of stress induced void evolution and growth in interconnects. *Journal of Applied Physics*, 91(4), 2380. doi: 10.1063/1.1428097.
- Fung, Y. C. (1965). *Foundation of solid mechanics* (p. 385). New Jersey: Prentice-Hall Inc.
- Gao, H. (1991). A boundary perturbation analysis for elastic inclusions and interfaces. *International Journal of Solids and Structures*, 28(6), 703-725. doi: 10.1016/0020-7683(91)90151-5.
- Gao, H. (1999). Crack-like grain-boundary diffusion wedges in thin metal films. *Acta Materialia*, 47(10), 2865-2878. doi: 10.1016/S1359-6454(99)00178-0.
- Gao, H., & Nix, W. D. (1999). Surface roughening of heteroepitaxial thin films. *Annual Review of Materials Science*, 29(1), 173-209. doi: 10.1146/annurev.matsci.29.1.173.
- Garofalo, F. (1965). *Fundamentals of creep and creep-rupture in metals*. New York, USA: The Macmillan Company.
- Gear, C. W. (1971). *Numerical initial value problems in ordinary differential equations*. Englewood Cliffs, N. J.: Prentice-Hall.
- Genin, F. Y. (1995a). Effect of stress on grain boundary motion in thin films. *Journal of Applied Physics*, 77(10), 5130. doi: 10.1063/1.359324.
- Genin, F. Y. (1995b). The initial stages of the formation of holes and hillocks in thin films under equal biaxial stress. *Acta Metallurgica et Materialia*, 43(12), 4289-4300. doi: 10.1016/0956-7151(95)00132-F.
- Genin, F. Y., & Siekhaus, W. J. (1996). Experimental study to validate a model of hillock's formation in aluminum thin films. *Journal of Applied Physics*, 79(7), 3560. doi: 10.1063/1.361408.
- Genin, F. Y., Mullins, W. W., & Wynblatt, P. (1993). The effect of stress on grain boundary grooving. *Acta Metallurgica et Materialia*, 41(12), 3541-3547. doi: 10.1016/0956-7151(93)90234-J.

- Gibbs, W. (1948). *The Collected Works of J. Willard Gibbs, Vol. I Thermodynamics*. New Haven: Yale University Press.
- Gjostein, N. A. (1963). Surface self-diffusion. In W. D. Robertson & N. A. Gjostein, *Metal Surfaces: Structure, Energetics and Kinetics*. Metals Park, Ohio: American Society for Metals.
- Goods, S., & Nix, W. D. (1978). The coalescence of large grain boundary cavities in silver during tension creep. *Acta Metallurgica*, 26(5), 753-758. doi: 10.1016/0001-6160(78)90025-1.
- Goods, S., & Nix, W. D. (1978). The kinetics of cavity growth and creep fracture in silver containing implanted grain boundary cavities. *Acta Metallurgica*, 26(5), 739-752. doi: 10.1016/0001-6160(78)90024-X.
- Gray, L. J., Maroudas, D., & Enmark, M. N. (1998). Galerkin boundary integral method for evaluating surface derivatives. *Computational Mechanics*, 22(2), 187-193. doi: 10.1007/s004660050352.
- Gray, L. J., Maroudas, D., & Enmark, M. N. (1999). Approximate Green's functions in boundary integral analysis. *Engineering Analysis with Boundary Elements*, 23(3), 267-274. doi: 10.1016/S0955-7997(98)00076-9.
- Greenebaum, B., Sauter, A. I., Flinn, P. A., & Nix, W. D. (1991). Stress in metal lines under passivation; comparison of experiment with finite element calculations. *Applied Physics Letters*, 58(17), 1845. doi: 10.1063/1.105075.
- Grilhe, J. (1993). Study of roughness formation induced by homogeneous stress at the free surfaces of solids. *Acta Metallurgica et Materialia*, 41(3), 909-913. doi: 10.1016/0956-7151(93)90024-M.
- Grinfel'D, M. A. (1986). Instability of the separation boundary between a nonhydrostatically stressed elastic body and a melt. *Soviet Physics Doklady*, 31, 831.
- Guduru, P. R., Chason, E., & Freund, L. B. (2003). Mechanics of compressive stress evolution during thin film growth. *Journal of the Mechanics and Physics of Solids*, 51(11-12), 2127-2148. doi: 10.1016/j.jmps.2003.09.013.
- Guggenheim, E. A. (1959). *Thermodynamics* (3 ed., p. 46). Amsterdam, Holland: North-Holland.

- Gungor, M. R., & Maroudas, D. (1998). Electromigration-induced failure of metallic thin films due to transgranular void propagation. *Applied Physics Letters*, 72(26), 3452-3454. doi:10.1063/1.121663
- Gungor, M. R., & Maroudas, D. (1999a). Nonhydrostatic stress effects on failure of passivated metallic thin films due to void surface electromigration. *Surface Science*, 432(3), L604-L610. doi: 10.1016/S0039-6028(99)00655-X.
- Gungor, M. R., & Maroudas, D. (1999b). Theoretical analysis of electromigration-induced failure of metallic thin films due to transgranular void propagation. *Journal of Applied Physics*, 85(4), 2233. doi: 10.1063/1.369532.
- Gungor, M. R., & Maroudas, D. (2001). Modeling of electromechanically-induced failure of passivated metallic thin films used in device interconnections. *International Journal of Fracture*, 109, 47-68. doi: 10.1023/A:1011054731371.
- Gungor, M. R., Maroudas, D., & Gray, L. J. (1998). Effects of mechanical stress on electromigration-driven transgranular void dynamics in passivated metallic thin films. *Applied Physics Letters*, 73(26), 3848-3850. doi: 10.1063/1.122913
- Haase, R. (1969). *Thermodynamics of Irreversible Processes* (p. 245). Massachusetts, USA: Addison-Wesley.
- Hackney, S. A., & Ojard, G. (1988). Grain boundary grooving at finite grain size. *Scripta Metallurgica*, 22(11), 1731-1735. doi: 10.1016/S0036-9748(88)80274-6.
- Herring, C. (1950). Diffusional viscosity of a polycrystalline solid. *Journal of Applied Physics*, 21(5), 437. doi: 10.1063/1.1699681.
- Herring, C. (1951). *The physics of powder metallurgy*. (W. E. Kinston) (p. 143). New York, USA: McGraw-Hill.
- Hirth, J. P., & Lothe, J. (1968). *Theory of Dislocations* (p. 458, 764). New York, USA: McGraw-Hill.

- Hirth, J. P., & Nix, W. D. (1985). Analysis of cavity nucleation in solids subjected to external and internal stresses. *Acta Metallurgica*, 33(3), 359-368. doi: 10.1016/0001-6160(85)90078-1.
- Huang, P., Li, Z., & Sun, J. (2000). Finite-element simulation of the diffusive growth of grain boundary voids. *Modelling and Simulation in Materials Science and Engineering*, 8, 843. doi: 10.1088/0965-0393/8/6/306.
- Huang, P., Li, Z., & Sun, J. (2001). Finite element analysis for surface diffusion-controlled shape instabilities of plate-like grains. *Computational Materials Science*, 20(1), 66-76. doi: 10.1016/S0927-0256(00)00126-9.
- Huang, R., Gan, D., & Ho, P. S. (2005). Isothermal stress relaxation in electroplated Cu films. II. Kinetic modeling. *Journal of Applied Physics*, 97(10), 103532. doi: 10.1063/1.1904721.
- Hull, D., & Rimmer, D. E. (1959). The growth of grain-boundary voids under stress. *Philosophical Magazine*, 4(42), 673-687. doi: 10.1080/14786435908243264.
- Huntington, H., & Grone, A. (1961). Current-induced marker motion in gold wires☆. *Journal of Physics and Chemistry of Solids*, 20(1-2), 76-87. doi: 10.1016/0022-3697(61)90138-X.
- Igic, P., & Mawby, P. A. (1999). Numerical modelling of stress-induced failure in sub-micron aluminium interconnects in VLSI systems. *Solid-State Electronics*, 43(2), 255-261. doi: 10.1016/S0038-1101(98)00252-4.
- Jeong, H., & Williams, E. D. (1999). Steps on surfaces: experiment and theory. *Surface Science Reports*, 34(6-8), 171-294. doi: 10.1016/S0167-5729(98)00010-7.
- Jones, R. E., & Basehore, M. L. (1987). Stress analysis of encapsulated fine-line aluminum interconnect. *Applied Physics Letters*, 50(12), 725. doi: 10.1063/1.98263.
- Kassner, K., & Misbah, C. (1994). Non-linear evolution of a uniaxially stressed solid: a route to fracture? *Europhysics Letters (EPL)*, 28(4), 245-250. doi: 10.1209/0295-5075/28/4/005.

- Kassner, M. E., & Hayes, T. A. (2003). Creep cavitation in metals. *International Journal of Plasticity*, 19(10), 1715-1748. doi: 10.1016/S0749-6419(02)00111-0.
- Khenner, M. (2001). Numerical simulation of grain-boundary grooving by level set method. *Journal of Computational Physics*, 170(2), 764-784. doi: 10.1006/jcph.2001.6760.
- Khenner, M., Averbuch, A., Israeli, M., Nathan, M., & Glickman, E. E. (2001). Level set modeling of transient electromigration grooving. *Computational Materials Science*, 20(2), 235-250. doi: 10.1016/S0927-0256(00)00179-8.
- Kim, D., Nix, W. D., Vinci, R. P., Deal, M. D., & Plummer, J. D. (2001). Study of the effect of grain boundary migration on hillock formation in Al thin films. *Journal of Applied Physics*, 90(2), 781. doi: 10.1063/1.1381045.
- Klinger, L. M., & Rabkin, E. (2007). The effect of stress on grain boundary interdiffusion in a semi-infinite bicrystal. *Acta Materialia*, 55(14), 4689-4698. doi: 10.1016/j.actamat.2007.04.039.
- Klinger, L. M., Chu, X., Mullins, W. W., & Bauer, C. L. (1996). Grain-boundary slit propagation in an electric field. *Journal of Applied Physics*, 80(12), 6670-6676.
- Klinger, L. M., Glickman, E. E., Fradkov, V. E., Mullins, W. W., & Bauer, C. L. (1995). Extensions of thermal grooving for arbitrary grain-boundary flux. *Journal of Applied Physics*, 78(6), 3833.
- Klinger, L., & Rabkin, E. (2001). Effects of surface anisotropy on grain boundary grooving. *Interface Science*, 9, 55-63. doi: 10.1023/A:1011270830969.
- Korhonen, M. A., Paszkiet, C. A., & Li, C. (1991). Mechanisms of thermal stress relaxation and stress-induced voiding in narrow aluminum-based metallizations. *Journal of Applied Physics*, 69(12), 8083. doi: 10.1063/1.347457.
- Kraft, O., Möckl, U. E., & Arzt, E. (1995). Shape changes of voids in bamboo lines: A new electromigration failure mechanism. *Quality and Reliability Engineering International*, 11(4), 279-283. doi: 10.1002/qre.4680110412.
- Kröner, E. (1958). *Kontinuums theorie der Versetzungen und Eigenspannungen*. Berlin: Springer.

- Kukta, R. V., & Freund, L. B. (1997). Minimum energy configuration of epitaxial material clusters on a lattice-mismatched substrate. *Journal of the Mechanics and Physics of Solids*, 45(11-12), 1835-1860. doi: 10.1016/S0022-5096(97)00031-8.
- Lahiri, S. K. (1970). Stress relief and hillock formation in thin lead films. *Journal of Applied Physics*, 41(7), 3172. doi: 10.1063/1.1659383.
- Laplace, P. S. (1806). *Mechanique Celeste, Vol 10*. (I. I. suppl. Au X Livre) (p. 147).
- Lee, K. Y., & Case, E. D. (1999). A comparison of theoretical and experimental profiles for thermally-induced grain-boundary grooving. *The European Physical Journal Applied Physics*, 8(3), 197-214. doi: 10.1051/epjap:1999247.
- Liu, C., Lee, S., & Chuang, T. J. (2001). Grain boundary crack growth. *Materials Science and Engineering B*, 86(2), 101-108. doi: 10.1016/S0921-5107(00)00804-7.
- Lloyd, J. R. (1997). Electromigration in thin film conductors. *Defect and Diffusion Forum*, 143-147, 1661-1672. doi: 10.4028/www.scientific.net/DDF.143-147.1661.
- Mahadevan, M., & Bradley, R. (1999). Simulations and theory of electromigration-induced slit formation in unpassivated single-crystal metal lines. *Physical Review B*, 59(16), 11037-11046. doi: 10.1103/PhysRevB.59.11037.
- Mahadevan, M., Bradley, R. M., & Debierre, J. (1999). Simulations of an electromigration-induced edge instability in single-crystal metal lines. *Europhysics Letters (EPL)*, 45(6), 680-685. doi: 10.1209/epl/i1999-00221-7.
- Martinez, L., & Nix, W. D. (1982). A numerical study of cavity growth controlled by coupled surface and grain boundary diffusion. *Metallurgical Transactions A*, 13(3), 427-437. doi: 10.1007/BF02643351.
- Mase, G. E. (1970). *Theory and Problems of Continuum Mechanics, Schaum's Outline Series* (p. 146). New York: McGraw-Hill.

- Mathews, J. H. (1992). *Numerical Methods for Mathematics, Science and Engineering* (p. 148, 175). New Jersey, USA: Prentice-Hall International Edition.
- Min, D., & Wong, H. (2006a). Grain-boundary grooving by surface diffusion with asymmetric and strongly anisotropic surface energies. *Journal of Applied Physics*, 99(2), 023515. doi: 10.1063/1.2159082.
- Min, D., & Wong, H. (2006b). The effect of strong surface energy anisotropy on migrating grain-boundary grooves. *Journal of Applied Physics*, 100(5), 053523. doi: 10.1063/1.2336980.
- Mullins, W. W. (1957). Theory of thermal grooving. *Journal of Applied Physics*, 28(3), 333. doi: 10.1063/1.1722742.
- Mullins, W. W. (1963). Solid surface morphologies governed by capillarity. In *Metal Surfaces: Structure, Energetics and Kinetics* (p. 17). Cleveland Ohio: ASM.
- Mullins, W. W., & Shewmon, P. G. (1959). The kinetics of grain boundary grooving in copper. *Acta Metallurgica*, 7(3), 163-170. doi: 10.1016/0001-6160(59)90069-0.
- Munoz, N. E., Gilliss, S. R., & Carter, C. B. (2003). The monitoring of grain-boundary grooves in alumina. *Philosophical Magazine Letters*, 84(1), 21-26. doi: 10.1080/09500830310001614487.
- Murr, L. E. (1975). *Interfacial Phenomena in Metals and Alloys* (p. 10). Massachusetts: Addison-Wesley.
- Mykura, H. (1961). The variation of the surface tension of nickel with crystallographic orientation. *Acta Metallurgica*, 9(6), 570-576. doi: 10.1016/0001-6160(61)90160-2.
- Nathan, M., Averbuch, A., & Israeli, M. (2004). Electromigration-induced surface evolution in bamboo lines with transgranular and intergranular edge voids. *Thin Solid Films*, 466(1-2), 347-350. doi: 10.1016/j.tsf.2004.03.019.
- Nathan, M., Glickman, E. E., Khenner, M., Averbuch, A., & Israeli, M. (2000). Electromigration drift velocity in Cu interconnects modeled with the level set method. *Applied Physics Letters*, 77(21), 3355-3357. doi: 10.1063/1.1327274.

- Nicolis, G., & Prigogine, I. (1989). *Exploring Complexity: An Introduction* (1 ed.). New York, USA: W.H. Freeman & Company.
- Ogurtani, T. O. (2000). Irreversible thermokinetics theory of surfaces and interfaces with a special reference to triple junctions. *unpublished*.
- Ogurtani, T. O. (2006a). Variational formulation of irreversible thermodynamics of surfaces and interfaces with grain-boundary triple-junction singularities under the capillary and electromigration forces in anisotropic two-dimensional space. *Physical Review B*, 73(23), 1-17. doi: 10.1103/PhysRevB.73.235408.
- Ogurtani, T. O. (2006b). Mesoscopic nonequilibrium thermodynamics of solid surfaces and interfaces with triple junction singularities under the capillary and electromigration forces in anisotropic three-dimensional space. *The Journal of chemical physics*, 124(14), 144706. doi: 10.1063/1.2185625.
- Ogurtani, T. O. (2006c). Unified theory of linear instability of anisotropic surfaces and interfaces under capillary, electrostatic, and elastostatic forces: The regrowth of epitaxial amorphous silicon. *Physical Review B*, 74(15), 1-25. doi: 10.1103/PhysRevB.74.155422.
- Ogurtani, T. O. (2007). Dirichlet extremum problem associated with the asymmetric grain-boundary thermal grooving under the Dirac δ -type anisotropic surface stiffness in bicrystal thin solid films. *Journal of Applied Physics*, 102(6), 063517. doi: 10.1063/1.2781574.
- Ogurtani, T. O. (2009a). Thermal grain-boundary grooving in bicrystal thin solid films having strong anisotropic surface Gibbs free energy represented by the modified cycloid-curtate function. *Journal of Crystal Growth*, 311(6), 1584-1593. doi: 10.1016/j.jcrysgro.2009.01.084.
- Ogurtani, T. O. (2009b). The orientation dependent electromigration induced healing on the surface cracks and roughness caused by the uniaxial compressive stresses in single crystal metallic thin films. *Journal of Applied Physics*, 106(5), 053503. doi: 10.1063/1.3211855.
- Ogurtani, T. O. (2010). Non-equilibrium thermodynamics of spontaneous versus forced morphological evolutions of strained thin solid films on deformable substrates: Theory and Application. *submitted*.
- Ogurtani, T. O., & Akyildiz, O. (2005). Grain boundary grooving and cathode voiding in bamboo-like metallic interconnects by surface drift diffusion under

the capillary and electromigration forces. *Journal of Applied Physics*, 97(9), 093520. doi: 10.1063/1.1883305.

Ogurtani, T. O., & Akyildiz, O. (2006). Computer simulations on the grain boundary grooving and cathode edge displacement in bamboo-like metallic interconnects. *Materials Research Society Symposium Proceedings*, 914, 0914-F09-22.

Ogurtani, T. O., & Akyildiz, O. (2008a). Cathode edge displacement by voiding coupled with grain boundary grooving in bamboo like metallic interconnects by surface drift-diffusion under the capillary and electromigration forces. *International Journal of Solids and Structures*, 45(3-4), 921-942. doi: 10.1016/j.ijsolstr.2007.09.007.

Ogurtani, T. O., & Akyildiz, O. (2008b). Morphological evolution of voids by surface drift diffusion driven by capillary, electromigration, and thermal-stress gradients induced by steady-state heat flow in passivated metallic thin films and flip chip solder joints. I. Theory. *Journal of Applied Physics*, 104(2), 023521. doi: 10.1063/1.2958088.

Ogurtani, T. O., & Akyildiz, O. (2008c). Morphological evolution of voids by surface drift diffusion driven by the capillary, electromigration, and thermal-stress gradient induced by the steady state heat flow in passivated metallic thin films and flip-chip solder joints. II. Applications. *Journal of Applied Physics*, 104(2), 023522. doi: 10.1063/1.2958303.

Ogurtani, T. O., & Akyildiz, O. (2008d). Morphological evolution of intragranular void under the thermal-stress gradient generated by the steady state heat flow in encapsulated metallic films: special reference to flip chip solder joints. *Solid State Phenomena*, 139, 151-156. doi: 10.4028/www.scientific.net/SSP.139.151.

Ogurtani, T. O., & Celik, A. (2006). Surface morphological evolution on single crystal films by strong anisotropic drift diffusion under capillary and electromigration forces. *Journal of Applied Physics*, 100(4), 043504. doi: 10.1063/1.2234800.

Ogurtani, T. O., & Oren, E. E. (2001). Computer simulation of void growth dynamics under the action of electromigration and capillary forces in narrow thin interconnects. *Journal of Applied Physics*, 90(3), 1564. doi: 10.1063/1.1382835.

- Ogurtani, T. O., & Oren, E. E. (2004). Electromigration-induced void grain-boundary interactions: The mean time to failure for copper interconnects with bamboo and near-bamboo structures. *Journal of Applied Physics*, 96(12), 7246. doi: 10.1063/1.1815389.
- Ogurtani, T. O., & Oren, E. E. (2005). Irreversible thermodynamics of triple junctions during the intergranular void motion under the electromigration forces. *International Journal of Solids and Structures*, 42(13), 3918-3952. doi: 10.1016/j.ijsolstr.2004.11.013.
- Ogurtani, T. O., & Seeger, A. K. (1983). The kinetics of hopping motion of interstitials with chemical reactions in arbitrary time dependent inhomogeneous interactive fields. *The Journal of Chemical Physics*, 79(10), 5041. doi: 10.1063/1.445599.
- Ogurtani, T. O., & Seeger, A. K. (1984). Internal friction and viscosity associated with mobile interstitials in the presence of a kink harmonically or uniformly moving in anisotropic body-centered cubic metals. *Journal of Applied Physics*, 55(8), 2857. doi: 10.1063/1.333317.
- Ogurtani, T. O., Akyildiz, O., & Oren, E. E. (2008). Morphological evolution of tilted grain-boundary thermal grooving by surface diffusion in bicrystal thin solid films having strong anisotropic surface Gibbs free energies. *Journal of Applied Physics*, 104(1), 013518. doi: 10.1063/1.2952520.
- Ogurtani, T. O., Celik, A., & Oren, E. E. (2007). Morphological evolution of edge-hillocks on single-crystal films having anisotropic drift-diffusion under the capillary and electromigration forces. *Thin Solid Films*, 515(5), 2974-2983. doi: 10.1016/j.tsf.2006.08.020.
- Ohring, M. (1971). Electromigration Damage in Thin Films due to Grain Boundary Grooving Processes. *Journal of Applied Physics*, 42(7), 2653. doi: 10.1063/1.1660603.
- Ono, S., & Kondo, S. (1960). Molecular theory of surface tension in liquids. In E. Flügge, *Handbuch der physik*, Vol.X (p. 159). Berlin, Germany: Springer-Verlag.
- Oren, E. E. (2003). Computer simulation of electromigration induced void – grain boundary interactions with a special reference to the prediction of cathode failure times in bamboo structures. Unpublished doctoral dissertation, Middle East Technical University, Ankara, TURKEY.

- Oren, E. E., & Ogurtani, T. O. (2001). The effect of initial void configuration on the morphological evolution under the action of normalized electron wind forces. *Materials Research Society Symposium Proceedings*, 714, 1-6.
- Oren, E. E., & Ogurtani, T. O. (2002). Void intergranular motion under the action of electromigration forces in thin film interconnects with bamboo structure. *Materials Research Society Symposium Proceedings*, 695, 1-7.
- Pharr, G., & Nix, W. D. (1979). A numerical study of cavity growth controlled by surface diffusion. *Acta Metallurgica*, 27(10), 1615-1631.
doi: 10.1016/0001-6160(79)90044-0.
- Philofsky, E., Ravi, K., Hall, E., & Black, J. (1971). *Surface reconstruction of aluminum metallization -- a new potential wearout mechanism. 9th Reliability Physics Symposium* (pp. 120-128). IEEE. doi: 10.1109/IRPS.1971.362503.
- Presland, A. E., Price, G. L., & Trimm, D. L. (1972). Hillock formation by surface diffusion on thin silver films. *Surface Science*, 29(2), 424-434.
doi: 10.1016/0039-6028(72)90229-4.
- Prigogine, I. (1961). *Introduction to Thermodynamics of Irreversible Processes. Interscience* (p. 29). New York, USA: Interscience Publishers.
- Prybyla, J. A., Riege, S. P., Grabowski, S. P., & Hunt, A. W. (1998). Temperature dependence of electromigration dynamics in Al interconnects by real-time microscopy. *Applied Physics Letters*, 73(8), 1083. Retrieved from <http://link.aip.org/link/?APPLAB/73/1083/1>.
- Rabkin, E., & Klinger, L. (2001). The fascination of grain boundary grooves. *Advanced Engineering Materials*, 3(5), 277-282.
doi: 10.1002/1527-2648(200105)3:53.0.CO;2-G.
- Rabkin, E., Gabelev, A., Klinger, L., Semenov, V. N., & Bozhko, S. I. (2006). Grain boundary grooving in molybdenum bicrystals. *Journal of Materials Science*, 41(16), 5151-5160. doi: 10.1007/s10853-006-0438-4.
- Rabkin, E., Klinger, L., & Semenov, V. N. (2000). Grain boundary grooving at the singular surfaces. *Acta Materialia*, 48(7), 1533-1540.
doi: 10.1016/S1359-6454(99)00432-2.

- Raj, R. (1978). Intergranular fracture in bicrystals. *Acta Metallurgica*, 26(2), 341-349. doi: 10.1016/0001-6160(78)90133-5.
- Raj, R., & Ashby, M. (1975). Intergranular fracture at elevated temperature. *Scripta Metallurgica*, 9(4), xv-xv. doi: 10.1016/0036-9748(75)90189-1.
- Ramasubramaniam, A., & Shenoy, V. B. (2005). On the evolution of faceted grain-boundary grooves by surface diffusion. *Acta Materialia*, 53, 2943-2956. doi: 10.1016/j.actamat.2005.03.013.
- Rice, J. R., & Chuang, T. J. (1981). Energy variations in diffusive cavity growth. *Journal of the American Ceramic Society*, 64(1), 46-53. doi: 10.1111/j.1151-2916.1981.tb09557.x.
- Riedel, H. (1987). *Fracture at High Temperatures*. Berlin: Springer-Verlag.
- Riege, S. P., Hunt, A. W., & Prybyla, J. A. (1995). Real-time tem studies of electromigration in submicron aluminum runners. *Materials Research Society Symposium Proceedings*, 391, 249.
- Riege, S. P., Prybyla, J. A., & Hunt, A. W. (1996). Influence of microstructure on electromigration dynamics in submicron Al interconnects: Real-time imaging. *Applied Physics Letters*, 69(16), 2367. doi: 10.1063/1.117527.
- Robertson, W. M. (1971). Grain-boundary grooving by surface diffusion for finite surface slopes. *Journal of Applied Physics*, 42(1), 463. doi: 10.1063/1.1659625.
- Rosenberg, R., & Ohring, M. (1971). Void formation and growth during electromigration in thin films. *Journal of Applied Physics*, 42(13), 5671. doi: 10.1063/1.1659998.
- Rudin, C. D., & Spencer, B. J. (1999). Equilibrium island ridge arrays in strained solid films. *Journal of Applied Physics*, 86(10), 5530. doi: 10.1063/1.371556.
- Sachenko, P. P., Schneibel, J. H., & Zhang, W. (2002). Effect of faceting on the thermal grain-boundary grooving of tungsten. *Philosophical Magazine A*, 82(4), 815-829. doi: 10.1080/01418610208243204.
- Sachenko, P. P., Schneibel, J. H., & Zhang, W. (2004). Observations of secondary oscillations in thermal grain boundary grooves. *Scripta Materialia*, 50(9), 1253-1257. doi: 10.1016/j.scriptamat.2004.01.030.

- Sachenko, P. P., Schneibel, J. H., Swadener, J. G., & Zhang, W. (2000). Experimental and simulated grain boundary groove profiles in tungsten. *Philosophical Magazine Letters*, *80*(9), 627-631. doi: 10.1080/09500830050134345.
- Schimschak, M., & Krug, J. (2000). Electromigration-driven shape evolution of two-dimensional voids. *Journal of Applied Physics*, *87*(2), 695. doi: 10.1063/1.371928.
- Schöllhammer, J., Chang, L., Rabkin, E., Baretzky, B., Gust, W., Mittemeijer, E., et al. (1999). Measurement of the profile and the dihedral angle of grain boundary grooves by atomic force microscopy. *Zeitschrift für Metallkunde*, *90*, 687-690.
- Shanahan, L. L., & Spencer, B. J. (2002). A codimension-two free boundary problem for the equilibrium shapes of a small three-dimensional island in an epitaxially strained solid film. *Interfaces and Free Boundaries*, *4*(1).
- Sharma, S. K., & Spitz, J. (1981). Thermal grooving in thin silver films. *Journal of Materials Science*, *16*(2), 535-536. doi: 10.1007/BF00738649.
- Shenoy, V. B., & Freund, L. B. (2002). A continuum description of the energetics and evolution of stepped surfaces in strained nanostructures. *Journal of the Mechanics and Physics of Solids*, *50*(9), 1817-1841. doi: 10.1016/S0022-5096(02)00015-7.
- Shewmon, P. G. (1966). Energy and structure of grain boundaries. In *Recrystallization, Grain Growth and Textures* (p. 165). Metals Park, Ohio: ASM.
- Shin, W., Seo, W., & Koumoto, K. (1998). Grain-boundary grooves and surface diffusion in polycrystalline alumina measured by atomic force microscope. *Journal of the European Ceramic Society*, *18*(6), 595-600. doi: 10.1016/S0955-2219(97)00207-0.
- Smithells, C. J. (1967), *Metals Reference Book, Vol. 3* (p. 686-708). London: Butterworths.
- Smith, U., Kristensen, N., Ericson, F., & Schweitz, J. (1991). Local stress relaxation phenomena in thin aluminum films. *Journal of Vacuum Science & Technology A: Vacuum, Surfaces, and Films*, *9*(4), 2527. doi: 10.1116/1.577268.

- Speight, M. V., & Beere, W. (1975). Vacancy potential and void growth on grain boundaries. *Metal Science*, 9(1), 190–191.
doi: 10.1179/030634575790445161.
- Speight, M., Beere, W., & Roberts, G. (1978). Growth of intergranular cracks by diffusion. *Materials Science and Engineering*, 36(2), 155-163.
doi: 10.1016/0025-5416(78)90067-8.
- Spencer, B. J. (1999). Asymptotic derivation of the glued-wetting-layer model and contact-angle condition for Stranski-Krastanow islands. *Physical Review B*, 59(3), 2011-2017. doi: 10.1103/PhysRevB.59.2011.
- Spencer, B. J., & Tersoff, J. (1996). Equilibrium shapes of small strained islands. *Materials Research Society Symposium Proceedings*, 399, 283-288.
- Spencer, B. J., & Tersoff, J. (1997). Equilibrium shapes and properties of epitaxially strained islands. *Physical Review Letters*, 79(24), 4858-4861.
doi: 10.1103/PhysRevLett.79.4858.
- Srolovitz, D. J. (1989). On the stability of surfaces of stressed solids. *Acta Metallurgica*, 37(2), 621-625. doi: 10.1016/0001-6160(89)90246-0.
- Srolovitz, D. J., & Safran, S. A. (1986). Capillary instabilities in thin films. I. Energetics. *Journal of Applied Physics*, 60(1), 247. doi: 10.1063/1.337689.
- Stiegler, J., Farrell, K., Loh, B. T., & McCoy, H. (1967). Nature of creep cavities in tungsten. *ASM Trans. Quart.*, 60, 494.
- Sukharev, V., Nix, W. D., & Zschech, E. (2007). A model for electromigration-induced degradation mechanisms in dual-inlaid copper interconnects: Effect of microstructure. *Journal of Applied Physics*, 102(5), 053505.
doi: 10.1063/1.2775538.
- Sun, B., & Suo, Z. (1997). A finite element method for simulating interface motion—II. Large shape change due to surface diffusion. *Acta Materialia*, 45(12), 4953-4962. doi: 10.1016/S1359-6454(97)00197-3.
- Sun, B., Suo, Z., & Yang, W. (1997). A finite element method for simulating interface motion—I. Migration of phase and grain boundaries. *Acta Materialia*, 45(5), 1907-1915. doi: 10.1016/S1359-6454(96)00323-0.

- Suo, Z. (1997). Motions of microsoipc surfaces in materials. In *Advances in Applied Mechanics Volume 33, Advances in Applied Mechanics (Vol. 33)*. Elsevier. doi: 10.1016/S0065-2156(08)70387-9.
- Suo, Z. (1998). Stable state of interconnect under temperature change and electric current. *Acta Materialia*, 46(11), 3725-3732. doi: 10.1016/S1359-6454(98)00098-6.
- Suo, Z., & Wang, W. (1994). Diffusive void bifurcation in stressed solid. *Journal of Applied Physics*, 76(6), 3410. doi: 10.1063/1.357471.
- Suo, Z., Wang, W., & Yang, M. (1994). Electromigration instability: Transgranular slits in interconnects. *Applied Physics Letters*, 64(15), 1944. doi: 10.1063/1.111750.
- Tan, C. M., & Roy, A. (2006). Investigation of the effect of temperature and stress gradients on accelerated EM test for Cu narrow interconnects. *Thin Solid Films*, 504(1-2), 288-293. doi: 10.1016/j.tsf.2005.09.101.
- Tan, C. M., Roy, A., Vairagar, A. V., Krishnamoorthy, A., & Mhaisalkar, S. G. (2005). Current crowding effect on copper dual damascene via bottom failure for ulsi applications. *IEEE Transactions On Device And Materials Reliability*, 5(2), 198-205.
- Thouless, M. D. (1993). Effect of surface diffusion on the creep of thin films a n d sintered arrays of particles. *Acta Metallurgica et Materialia*, 41(4), 1057-1064. doi: 10.1016/0956-7151(93)90155-L
- Thouless, M. D. (1995). Modeling the development and relaxation of stresses in films. *Annual Review of Materials Science*, 25(1), 69-96. doi: 10.1146/annurev.ms.25.080195.000441.
- Tomar, V., Gungor, M. R., & Maroudas, D. (2008a). Current-induced stabilization of surface morphology in stressed solids. *Physical Review Letters*, 100(3), 1-4. doi: 10.1103/PhysRevLett.100.036106.
- Tomar, V., Gungor, M. R., & Maroudas, D. (2008b). Theoretical analysis of texture effects on the surface morphological stability of metallic thin films. *Applied Physics Letters*, 92(18), 181905. doi: 10.1063/1.2912037.

- Tritscher, P., & Broadbridge, P. (1995). Grain boundary grooving by surface diffusion: an analytic nonlinear model for a symmetric groove. *Proceedings of the Royal Society: Mathematical and Physical Sciences (1990-1995)*, 450(1940), 569-587. doi: 10.1098/rspa.1995.0101.
- Tsoga, A., & Nikolopoulos, P. (1994). Groove angles and surface mass transport in polycrystalline alumina. *Journal of the American Ceramic Society*, 77(4), 954-960. doi: 10.1111/j.1151-2916.1994.tb07252.x
- Tu, K. N. (2003). Recent advances on electromigration in very-large-scale-integration of interconnects. *Journal of Applied Physics*, 94(9), 5451. doi: 10.1063/1.1611263.
- Van Der Waals, J. D., & Bakker, G. (1928). *Handbook Experimental Physik, Vol.6.* (W. Wien & F. Harms) *Handbook Experimental Physik*. Leipzig, Germany: Akademische Verlagsgesellschaft.
- Verschaffelt, J. E. (1936). The thermomechanics of the superficial layer. I. Generalities; pure substances. *Bulletins de l'Academie Royale des Sciences, des Lettres et des Beaux Arts de Belgique*, 22, 373.
- Vinci, R. P., Zielinski, E., & Bravman, J. (1995). Thermal strain and stress in copper thin films. *Thin Solid Films*, 262, 142-153. doi: 10.1016/0040-6090(95)05834-6
- Vitek, V. (1978). A theory of diffusion controlled intergranular creep crack growth. *Acta Metallurgica*, 26(9), 1345-1356. doi: 10.1016/0001-6160(78)90150-5.
- Wang, W. L., Lee, S., & Chuang, T. J. (2002). Steady-state crack growth along a grain boundary in interconnects with a high electric field intensity. *Philosophical Magazine A*, 82(5), 955-970. doi: 10.1080/01418610110095193.
- Wang, W., & Suo, Z. (1996). A simulation of electromigration-induced transgranular slits. *Journal of Applied Physics*, 79(5), 2394. doi: 10.1063/1.361166.
- Weatherburn, C. E. (1954). *Advanced vector analysis* (p. 140). London: G. Bell and Sons LTD.

- Weertman, J. (1973). Hull-Rimmer grain boundary void growth theory - a correction☆. *Scripta Metallurgica*, 7(10), 1129-1130.
doi: 10.1016/0036-9748(73)90027-6.
- Wingrove, A. L., & Taplin, D. M. (1969). The morphology and growth of creep cavities in alpha-iron. *Journal of Materials Science*, 4(9), 789-796.
doi: 10.1007/BF00551074.
- Wu, C. (1996). The chemical potential for stress-driven surface diffusion. *Journal of the Mechanics and Physics of Solids*, 44(12), 2059-2077.
doi: 10.1016/S0022-5096(96)00059-2.
- Xia, L., Bower, A. F., Suo, Z., & Shih, C. F. (1997). A finite element analysis of the motion and evolution of voids due to strain and electromigration induced surface diffusion. *Journal of the Mechanics and Physics of Solids*, 45(9), 1473-1493. doi: 10.1016/S0022-5096(97)00013-6.
- Xiang, Y., & E, W. (2002). Nonlinear evolution equation for the stress-driven morphological instability. *Journal of Applied Physics*, 91(11), 9414.
doi: 10.1063/1.1477259.
- Xin, T., & Wong, H. (2001). A δ -function model of facets. *Surface Science*, 487(1-3), L529-L533. doi: 10.1016/S0039-6028(01)01158-X.
- Xin, T., & Wong, H. (2003). Grain-boundary grooving by surface diffusion with strong surface energy anisotropy. *Acta Materialia*, 51(8), 2305-2317.
doi: 10.1016/S1359-6454(03)00039-9.
- Xin, T., & Wong, H. (2004). A spike-function model of facets. *Materials Science and Engineering A*, 364(1-2), 287-295. doi: 10.1016/j.msea.2003.08.042.
- Yamazaki, M. (1968). The growth of intergranular cracks at high temperatures. *Journal of the Japan Institute of Metals*, 32, 403.
- Yang, W., & Srolovitz, D. J. (1993). Cracklike surface instabilities in stressed solids. *Physical Review Letters*, 71(10), 1593-1596.
doi: 10.1103/PhysRevLett.71.1593.
- Yeremin, E. N. (1979). *The Foundations of Chemical Kinetics* (p. 215). Moscow, Russia: MIR Publishers.

- Young, T. (1805). An Essay on the Cohesion of Fluids. *Philosophical Transactions of the Royal Society of London (1776-1886)*, 95(-1), 65-87. doi: 10.1098/rstl.1805.0005.
- Zhang, L., & Gao, H. (2002). Coupled grain boundary and surface diffusion in a polycrystalline thin film constrained by substrate. *Zeitschrift für Metallkunde*, 93, 417.
- Zhang, W., & Schneibel, J. H. (1995). Numerical simulation of grain-boundary grooving by surface diffusion. *Computational Materials Science*, 3(3), 347-358. doi: 10.1016/0927-0256(94)00073-L.
- Zhang, W., Sachenko, P. P., & Gladwell, I. (2004). Thermal grain boundary grooving with anisotropic surface free energies. *Acta Materialia*, 52(1), 107-116. doi: 10.1016/j.actamat.2003.08.033.
- Zhang, W., Sachenko, P. P., & Schneibel, J. H. (2002). Kinetics of thermal grain boundary grooving for changing dihedral angles. *Journal of Materials Research*, 17(6), 1495-1501. doi: 10.1557/JMR.2002.0222.
- Zhang, Y. W., & Bower, A. F. (1999a). Numerical simulations of island formation in a coherent strained epitaxial thin film system. *Journal of the Mechanics and Physics of Solids*, 47(11), 2273-2297. doi: 10.1016/S0022-5096(99)00026-5.
- Zhang, Y. W., & Bower, A. F. (1999b). Three dimensional simulations of island formation in a coherent strained epitaxial film. *Thin Solid Films*, 357(1), 8-12. doi: 10.1016/S0040-6090(99)00465-4.
- Zhang, Y. W., Bower, A. F., Xia, L., & Shih, C. F. (1998). Three dimensional finite element analysis of the evolution of voids and thin films by strain and electromigration induced surface diffusion. *Journal of the Mechanics and Physics of Solids*, 47(1), 173-199. doi: 10.1016/S0022-5096(98)00079-9.

APPENDIX A

LIST OF COMPUTER CODE

```
! variable declations
module global_variables

    implicit none
    ! IMSL* Fortran Numerical Library Version 6.0.0
    include 'link_fnl_static.h'

    type vec
        real(8) x,y,z
    end type

    type arr
        real(8) x(2,2)
    end type

    type arr1
        real(8) x(3,2)
    end type

    real(8)      :: pi = 3.141592653589793d0
    integer     :: mdiv,mc,MODE,mmL,mmR,gb1,gb2,BC,nloop,t,H,nu,nr,nd,nl,
    nt,mint,gnew,cont,ipiv(10000),info,nt_1,nt_2,NDATA
    real(8)     :: AAL,AAR,BBL,BBR,phiL,phiR,tet,alfa,JTU,Vu,JLu, JRu, JTD,
    Vd,JLd, JRd, Jgu, Jgd, lamda,rmax,rmin,lamda_A,lamda_C,sl,sw,ro,betta,MG
    ,MT,MGB,MTA,MTC,delta,omega,deltat,eptime,timet,dmean,vmax,chi,C0,C1
    ,C2,C3,C4,e_s,nu_s,r_s,sigx,xi,siglam,ta,ta_o,td
    type (vec)  :: RT(10000),DR(10000),LLN(10000),ANTI(3),NC(10000),RC
    (10000),RM(10000),DDR(10000),DS(10000),TETA(10000),KAPPA(10000),K
    (10000),P(10000),DTETA(10000),zeta(10000),DD(10000),SS(10000),V
    (10000),V1(10000),QSS(3),EF_1(10000),EF_2(10000),EF_TC(10000),EF_TN
    (10000),TN(10000),UB(10000),US(10000),strain(10000),ux(10000),uy
    (10000),hoopstress(10000)

    type (vec),dimension(:),allocatable      :: RC_MU,RC_FS,TR_FS
    real(8),dimension(:,:),allocatable     :: TT,UU,FT,UT,GT,CSCOEFX,
    CSCOEFY
    real(8),dimension(:),allocatable       :: CC,TR,XDATA,YDATA,SDATA,
    BREAK

end module

! operator overloadings for several operations
module vector_operator

    use global_variables
    implicit none
    ! overload operator * for cross product
    interface operator (*)
        module procedure cross
    end interface

```

```

! overload operator * for cross product
interface operator (*)
    module procedure cross
end interface
!
! overload operator * for double vector multiplication
interface operator (*)
    module procedure double_vector_multiplication
end interface
!
! overload operator * for double arr multiplication
interface operator (*)
    module procedure double_arr_multiplication
end interface
!
! overload operator * for double arr1 multiplication
interface operator (*)
    module procedure double_arr1_multiplication
end interface
!
! overload operator * for integer vector multiplication
interface operator (*)
    module procedure integer_vector_multiplication
end interface
!
! overload operator / for vector double division
interface operator (/)
    module procedure double_vector_division
end interface
!
! overload operator / for vector integer division
interface operator (/)
    module procedure integer_vector_division
end interface
!
! overload operator + for vector vector summation
interface operator (+)
    module procedure summation
end interface
!
! overload operator + for arr arr summation
interface operator (+)
    module procedure summation_arr
end interface
!
! overload operator + for arr1 arr1 summation
interface operator (+)
    module procedure summation_arr1
end interface
!
! overload operator - for vector vector subtraction
interface operator (-)
    module procedure subtraction
end interface
!
! overload operator = for vec assign vec
interface assignment (=)
    module procedure vec_eq_vec
end interface
!
! overload operator = for arr assign arr
interface assignment (=)
    module procedure arr_eq_arr
end interface
!
! overload operator = for arr1 assign arr1
interface assignment (=)
    module procedure arr1_eq_arr1

```

```

end interface
!
contains

type (vec) function cross(a,b)
  use global_variables
  implicit none
  type (vec), INTENT(IN) :: a,b
  cross%x = a%y*b%z-a%z*b%y
  cross%y = -a%x*b%z+a%z*b%x
  cross%z = a%x*b%y-a%y*b%x
end function cross
!
type (vec) function summation(a,b)
  use global_variables
  implicit none
  type (vec), INTENT(IN) :: a,b
  summation%x = a%x+b%x
  summation%y = a%y+b%y
  summation%z = a%z+b%z
end function summation
!
type (arr) function summation_arr(a,b)
  use global_variables
  implicit none
  type (arr), INTENT(IN) :: a,b
  summation_arr%x(1,1) = a%x(1,1)+b%x(1,1)
  summation_arr%x(1,2) = a%x(1,2)+b%x(1,2)
  summation_arr%x(2,1) = a%x(2,1)+b%x(2,1)
  summation_arr%x(2,2) = a%x(2,2)+b%x(2,2)
end function summation_arr
!
type (arr1) function summation_arr1(a,b)
  use global_variables
  implicit none
  type (arr1), INTENT(IN) :: a,b
  summation_arr1%x(1,1) = a%x(1,1)+b%x(1,1)
  summation_arr1%x(1,2) = a%x(1,2)+b%x(1,2)
  summation_arr1%x(2,1) = a%x(2,1)+b%x(2,1)
  summation_arr1%x(2,2) = a%x(2,2)+b%x(2,2)
  summation_arr1%x(3,1) = a%x(3,1)+b%x(3,1)
  summation_arr1%x(3,2) = a%x(3,2)+b%x(3,2)
end function summation_arr1
!
type (vec) function subtraction(a,b)
  use global_variables
  implicit none
  type (vec), INTENT(IN) :: a,b
  subtraction%x = a%x-b%x
  subtraction%y = a%y-b%y
  subtraction%z = a%z-b%z
end function subtraction
!
type (vec) function double_vector_multiplication(a,b)
  use global_variables
  implicit none
  real(8), INTENT(IN) :: a
  type (vec), INTENT(IN) :: b
  double_vector_multiplication%x = a*b%x
  double_vector_multiplication%y = a*b%y
  double_vector_multiplication%z = a*b%z
end function double_vector_multiplication
!
type (arr) function double_arr_multiplication(a,b)
  use global_variables
  implicit none
  real(8), INTENT(IN) :: a
  type (arr), INTENT(IN) :: b

```

```

        double_arr_multiplication%x(1,1) = a*b%x(1,1)
        double_arr_multiplication%x(1,2) = a*b%x(1,2)
        double_arr_multiplication%x(2,1) = a*b%x(2,1)
        double_arr_multiplication%x(2,2) = a*b%x(2,2)
end function double_arr_multiplication
!
type (arr1) function double_arr1_multiplication(a,b)
    use global_variables
    implicit none
    real(8), INTENT(IN) :: a
    type (arr1), INTENT(IN) :: b
    double_arr1_multiplication%x(1,1) = a*b%x(1,1)
    double_arr1_multiplication%x(1,2) = a*b%x(1,2)
    double_arr1_multiplication%x(2,1) = a*b%x(2,1)
    double_arr1_multiplication%x(2,2) = a*b%x(2,2)
    double_arr1_multiplication%x(3,1) = a*b%x(3,1)
    double_arr1_multiplication%x(3,2) = a*b%x(3,2)
end function double_arr1_multiplication
!
type (vec) function integer_vector_multiplication(a,b)
    use global_variables
    implicit none
    integer, INTENT(IN) :: a
    type (vec), INTENT(IN) :: b
    integer_vector_multiplication%x = a*b%x
    integer_vector_multiplication%y = a*b%y
    integer_vector_multiplication%z = a*b%z
end function integer_vector_multiplication
!
type (vec) function double_vector_division(a,b)
    use global_variables
    implicit none
    type (vec), INTENT(IN) :: a
    real(8), INTENT(IN) :: b
    double_vector_division%x = a%x/b
    double_vector_division%y = a%y/b
    double_vector_division%z = a%z/b
end function double_vector_division
!
type (vec) function integer_vector_division(a,b)
    use global_variables
    implicit none
    type (vec), INTENT(IN) :: a
    integer, INTENT(IN) :: b
    integer_vector_division%x = a%x/b
    integer_vector_division%y = a%y/b
    integer_vector_division%z = a%z/b
end function integer_vector_division
!
subroutine arr_eq1_arr(a,b)
    use global_variables
    implicit none
    type (arr), INTENT(OUT) :: a
    type (arr), INTENT(IN) :: b
    a%x(1,1) = b%x(1,1)
    a%x(1,2) = b%x(1,2)
    a%x(2,1) = b%x(2,1)
    a%x(2,2) = b%x(2,2)
end subroutine
!
subroutine arr1_eq1_arr1(a,b)
    use global_variables
    implicit none
    type (arr1), INTENT(OUT) :: a
    type (arr1), INTENT(IN) :: b
    a%x(1,1) = b%x(1,1)
    a%x(1,2) = b%x(1,2)
    a%x(2,1) = b%x(2,1)

```

```

        a%x(2,2) = b%x(2,2)
        a%x(3,1) = b%x(3,1)
        a%x(3,2) = b%x(3,2)
    end subroutine
    !
    subroutine vec_eql_vec(a,b)
        use global_variables
        implicit none
        type (vec), INTENT(OUT) :: a
        type (vec), INTENT(IN) :: b
        a%x = b%x
        a%y = b%y
        a%z = b%z
    end subroutine

end module vector_operator

! this function calculates the magnitude of a vector
double precision function absvec(a)

    use global_variables
    implicit none

    type (vec) :: a

    absvec = dsqrt(a%x*a%x+a%y*a%y+a%z*a%z)

end

! this function calculates dot product of two vectors
double precision function dot(a,b)

    use global_variables
    implicit none

    type (vec) :: a,b

    dot = a%x*b%x+a%y*b%y+a%z*b%z

end function dot

! this routine assigns an anticlockwise rotation matrix
subroutine ccrot(w)

    use global_variables
    implicit none
    real(8) :: w

    ANTI(1)%x = dcos(w)
    ANTI(1)%y = dsin(w)
    ANTI(1)%z = 0.0d0
    ANTI(2)%x = -dsin(w)
    ANTI(2)%y = dcos(w)
    ANTI(2)%z = 0.0d0
    ANTI(3)%x = 0.0d0
    ANTI(3)%y = 0.0d0
    ANTI(3)%z = 1.0d0

end subroutine ccrot

! this routine reads program inputs
subroutine input

    use global_variables
    implicit none

    character(12) :: dummy

```

```

open(1,file='input.txt')
! betta: film aspect ratio
read(1,'(a62,f24.16)') dummy,betta
! sw: film half width
read(1,'(a62,f24.16)') dummy,sw
! mdiv: number of divisions on sidewalls
read(1,'(a62,i15)') dummy,mdiv
! mc: number of divisions on perpendicular walls
read(1,'(a62,i15)') dummy,mc
! AAL: diffusivity anisotropy intensity of the left side grain
read(1,'(a62,f24.16)') dummy,AAL
! AAR: diffusivity anisotropy intensity of the right side grain
read(1,'(a62,f24.16)') dummy,AAR
! BBL: surface energy anisotropy intensity of the left grain
read(1,'(a62,f24.16)') dummy,BBL
! BBR: surface energy anisotropy intensity of the right grain
read(1,'(a62,f24.16)') dummy,BBR
! mmL: half fold number of the left side grain
read(1,'(a62,i15)') dummy,mmL
! mmR: half fold number of the right side grain
read(1,'(a62,i15)') dummy,mmR
! phiL: tilt angle of the left side grain
read(1,'(a62,f24.16)') dummy,phiL
! phiR: tilt angle of the right side grain
read(1,'(a62,f24.16)') dummy,phiR
! lamda: wetting parameter
read(1,'(a62,f24.16)') dummy,lamda
! gb1: node number of the upper grain boundary
read(1,'(a62,i15)') dummy,gb1
! gb2: node number of the lower grain boundary
read(1,'(a62,i15)') dummy,gb2
! BC: selection of boundary condition for diffusion problem
read(1,'(a62,i15)') dummy,BC
read(1,'(a62)') dummy ! BC = 0 :: Anode = IBC, Cathode = FBC
read(1,'(a62)') dummy ! BC = 1 :: Anode = RBC, Cathode = FBC
read(1,'(a62)') dummy ! BC = 2 :: Anode = IBC, Cathode = IBC
read(1,'(a62)') dummy ! BC = 3 :: Anode = RBC, Cathode = RBC
! MG: grain boundary longitudinal mobility
read(1,'(a62,f24.16)') dummy,MG
! MT: grain boundary transverse mobility
read(1,'(a62,f24.16)') dummy,MT
! MGB: grain boundary drift mobility
read(1,'(a62,f24.16)') dummy,MGB
! delta: grain boundary thickness
read(1,'(a62,f24.16)') dummy,delta
! omega: mean atomic volume
read(1,'(a62,f24.16)') dummy,omega
! deltat: initial time interval
read(1,'(a62,f24.16)') dummy,deltat
! nloop: final loop number
read(1,'(a62,i15)') dummy,nloop
! eptime: time step corrector
read(1,'(a62,f24.16)') dummy,eptime
! mint: integration segment number (must be odd)
read(1,'(a62,i15)') dummy,mint
! e_s: elastic modulus
read(1,'(a62,f24.16)') dummy,e_s
! nu_s: Poisson's ratio
read(1,'(a62,f24.16)') dummy,nu_s
! r_s: ratio of the stress components (sigxx/sigyy)
read(1,'(a62,f24.16)') dummy,r_s
! sigx: remote stress
read(1,'(a62,f24.16)') dummy,sigx
! chi: electronwind intensity
read(1,'(a62,f24.16)') dummy,chi
! xi: elastic dipole tensor interaction intensity
read(1,'(a62,f24.16)') dummy,xi
! siglam: elastic strain energy intensity

```

```

read(1,'(a62,f24.16)') dummy,siglam
! lamda_A: wetting parameter of leftmost_grain-anode junction
read(1,'(a62,f24.16)') dummy,lamda_A
! lamda_C: wetting parameter of rightmost_grain-cathode junction
read(1,'(a62,f24.16)') dummy,lamda_C
! MTA: longitudinal mobility leftmost_grain-anode junction
read(1,'(a62,f24.16)') dummy,MTA
! MTC: longitudinal mobility rightmost_grain-cathode junction
read(1,'(a62,f24.16)') dummy,MTC
! MODE: selection of the surface Gibbs free energy function
read(1,'(a62,i15)') dummy,MODE
read(1,'(a62,f24.16)') dummy,alfa
! MODE = 1 :: OGURTANI's GFE func (Ogurtani, 2006a)
! MODE = 2 :: SHENOY's GFE func (Ramasubramaniam & Shenoy, 2005)
! MODE = 3 :: CURTATE GFE func (Ogurtani, 2009a)
read(1,'(a62,i15)') dummy,cont

nloop = 2*nloop
! ro: scaling factor
ro = 0.5d0/dsqrt((betta*sw)**2+sw**2)
! sl: half film length
sl = betta*ro*sw
! sw: half film width
sw = ro*sw
! C0-4: elastic coefficients for plane strain
C0 = 0.25d0*(1.0d0+nu_s)/(pi*e_s*(1.0d0-nu_s))
C1 = 3.0d0-4.0d0*nu_s
C2 = 0.25d0/(pi*(1.0d0-nu_s))
C3 = 1.0d0-2.0d0*nu_s
C4 = 2.0d0
! gbl,2: grain boundary node positions
gbl = gbl+1
gb2 = gb2+2*mdiv+2*mc+1
! dmean: mean segment length
dmean = sl/mdiv
! phiL,R: tilt angles
phiL = phiL*pi/180
phiR = phiR*pi/180
close (1)

end subroutine

! this routine prints program outputs
subroutine output(counter)

use global_variables
implicit none

integer :: i, counter
character *13 :: filename
real(8) :: aci_1_L,aci_1_R,aci_2_R,aci_2_L
double precision, external :: dot
!
open(1,file='name.txt')
if (counter.LT.10) then
write(1,'(a3,i1,a3,a4)') '000',counter,'csl','.txt'
else if (counter.LT.100) then
write(1,'(a2,i2,a3,a4)') '00',counter,'csl','.txt'
else if (counter.LT.1000) then
write(1,'(a1,i3,a3,a4)') '0',counter,'csl','.txt'
else
write(1,'(i4,a3,a4)') counter,'csl','.txt'
end if
close(1)
!
open(2,file='name.txt')
read(2,'(a11)') filename
close(2)

```

```

!
print*, 'Printing output: ', filename
! compute the instantaneous dihedral angles
aci_1_L = dacos(dot(DR(gb1-1), ta)/DS(gb1-1))
aci_1_R = dacos(dot(DR(gb1), td)/DS(gb1))
aci_2_R = dacos(dot(DR(gb2-1), td)/DS(gb2-1))
aci_2_L = dacos(dot(DR(gb2), ta)/DS(gb2))
!
open(3, file=filename)
write(3, '(20(f30.16),5(i12),(f30.16),4(i10),5(f30.16))') RT(1)%x
,RT(1)%y,V(1),TETA(1),KAPPA(1),DTETA(1),DD(1),SS(1),0.0d0,0.0d0,
EF_TN(1),CC(1),zeta(1),0.0d0,ux(1),uy(1),0.0d0,hoopstress(1),0.0d0,
timet+eptime*dmean/vmax,H,t,nt,gb1,gb2,timet,nu,nr,nd,nl,aci_1_L,
aci_1_R,aci_2_R,aci_2_L
do i = 2, nt
write(3, '(20(f30.16))') RT(i)%x,RT(i)%y,V(i),TETA(i),KAPPA
(i),DTETA(i),DD(i),SS(i),0.0d0,0.0d0,EF_TN(i),CC(i),zeta(i),0.0d0,ux
(i),uy(i),0.0d0,hoopstress(i)
end do
close(3)

end subroutine

! this routine generates initial 2D mesh, position vectors are stored as
3D vectors: r(x,y,0)
subroutine generate

use global_variables
use vector_operator
implicit none

integer :: i
type (vec) :: ta_d
double precision, external :: absvec

nu = 2*mdiv+1
nr = 2*mc-1
nd = 2*mdiv+1
nl = 2*mc-1
nt = nu+nr+nd+nl
! upper part of the strip
do i = 1, 2*mdiv+1
RT(i)%x = (i-mdiv-1)*s1/mdiv
RT(i)%y = sw
RT(i)%z = 0.0d0
end do
! right edge (cathode) of the strip
do i = 2*mdiv+2, 2*mdiv+2*mc
RT(i)%x = s1
RT(i)%y = -(i-2*mdiv-mc-1)*sw/mc
RT(i)%z = 0.0d0
end do
! lower part of the strip
do i = 2*mdiv+2*mc+1, 4*mdiv+2*mc
RT(i)%x = -(i-3*mdiv-2*mc-1)*s1/mdiv
RT(i)%y = -sw
RT(i)%z = 0.0d0
end do
! left edge (anode) side of the strip
do i = 4*mdiv+2*mc+1, nt
RT(i)%x = -s1
RT(i)%y = (i-4*mdiv-3*mc-1)*sw/mc
RT(i)%z = 0.0d0
end do

ta_o%x = 0.0d0
ta_o%y = -1.0d0
ta_o%z = 0.0d0

```

```

    ta_d = RT(gb2)-RT(gb1)
    ta = ta_d/absvec(ta_d)
    td = (-1.0d0)*ta

end subroutine

! this routine calculates difference vectors between successive position
! vectors and their magnitudes
subroutine DELR_F

    use global_variables
    use vector_operator
    implicit none

    integer :: i
    double precision, external :: absvec

    do i = 1, nt-1
        DR(i) = RT(i+1)-RT(i)
        DS(i) = absvec(DR(i))
    end do

    DR(nt) = RT(1)-RT(nt)
    DS(nt) = absvec(DR(nt))

end subroutine

subroutine DELREM(ni,nf)

    use global_variables
    use vector_operator
    implicit none

    integer :: i,ni,nf
    double precision, external :: absvec

    do i = ni, nf-1
        DDR(i) = RT(i+1)-RT(i)
    end do

end subroutine

! this routine calculates the angle between two successive 3D vectors in
! given set of vectors
subroutine PSIR_F

    use global_variables
    use vector_operator
    implicit none

    integer :: i
    type (vec) :: kk
    double precision, external :: dot

    kk%x = 0.0d0
    kk%y = 0.0d0
    kk%z = 1.0d0

    TETA(1) = dasin(dot(DR(nt)*DR(1),kk)/(DS(nt)*DS(1)))

    if (dot(DR(nt),DR(1)).le.0.0d0) then
        TETA(1) = pi - TETA(1)
    end if

    if (TETA(1)>pi) then
        TETA(1) = TETA(1) - 2.0d0*pi
    end if

```

```

TETA(1) = -TETA(1)

do i = 2, nt
  TETA(i) = dasin(dot(DR(i-1)*DR(i),kk)/(DS(i-1)*DS(i)))
  if (dot(DR(i-1),DR(i)).le.0.0d0) then
    TETA(i) = pi - TETA(i)
  end if
  if (TETA(i)>pi) then
    TETA(i) = TETA(i) - 2.0d0*pi
  end if
  TETA(i) = -TETA(i)
end do

end subroutine

! this routine calculates curvatures and local line normal vectors
subroutine KAPPA_F

  use global_variables
  use vector_operator
  implicit none

  integer      :: i
  real(8)      :: alpha,beta,denom
  double precision, external :: absvec

  alpha = datan(dsin(TETA(1))/(DS(nt)/DS(1)+dcos(TETA(1))))
  KAPPA(1) = -2.0d0*dsin(alpha)/DS(1)
  beta = -0.5d0*pi+alpha
  call ccrot(beta)
  call dgemv('N',3,3,1.0d0,ANTI,3,DR(1),1,0.0d0,LLN(1),1)
  denom = absvec(LLN(1))
  LLN(1) = LLN(1)/denom

  do i = 2, nt
    alpha = datan(dsin(TETA(i))/(DS(i-1)/DS(i)+dcos(TETA(i))))
    KAPPA(i) = -2.0d0*dsin(alpha)/DS(i)
    beta = -0.5d0*pi+alpha
    call ccrot(beta)
    call dgemv('N',3,3,1.0d0,ANTI,3,DR(i),1,0.0d0,LLN(i),1)
    denom = absvec(LLN(i))
    LLN(i) = LLN(i)/denom
  end do

end subroutine

! auxiliary functions for surface energy anisotropy
double precision function gama(c,mmm,ww,xx)

  use global_variables
  implicit none

  double precision :: xx,c,ww,g_0
  integer          :: mmm
  g_0 = 1.0d0
  if (MODE.eq.1) then
    ! Ogurtani's smooth GFE function (Ogurtani, 2006a)
    gama = 1.0d0+c*(dsin(mmm*(xx-ww))**2)
  else if (MODE.eq.2) then
    ! Shenoy's GFE function having singularities (Ramasubramaniam & Shenoy, 2005)
    gama = g_0*(1.0d0-c+c*((dabs(dsin(mmm*0.5d0*(xx-ww)))+dabs(dcos(mmm*0.5d0*(xx-ww))))))
  else
    ! Curtate (Ogurtani, 2009a)
    gama = 1.0d0+c*dcos(ww)
  end if

```

```

end function

double precision function dgama (c,mmm,ww,xx)

    use global_variables
    implicit none

    double precision :: xx,c,ww,g_0
    integer          :: mmm
    g_0 = 1.0d0
    if (MODE.eq.1) then
        ! Derivative of Ogurtani's smooth GFE function
        dgama = mmm*c*dsin(2.0d0*mmm*(xx-ww))
    else if (MODE.eq.2) then
        ! Derivative of Shenoy's GFE function having sharp Dirac delta
        function singularities
        dgama = g_0*mmm*0.5d0*c*dsin(mmm*0.5d0*(xx-ww))*dcos(mmm*0.5d0*
        (xx-ww))*(1.0d0/dabs(dsin(mmm*0.5d0*(xx-ww)))-1.0d0/dabs(dcos(mmm*0.
        5d0*(xx-ww))))
    else
        ! Curtate
        dgama = -c*2.0d0*mmm*dsin(ww)/(1.0d0+xx*dcos(ww))
    end if

end function

double precision function SSf (c,mmm,ww,xx)

    use global_variables
    implicit none

    double precision :: xx,c,ww
    integer          :: mmm

    if (MODE.eq.1) then
        ! Ogurtani's smooth surface stiffness function
        SSf = (1.0d0+c*0.5d0)*(1.0d0+((-1.0d0)**mmm)*c*(1.0d0-4.0d0*mmm*
        *2)*dcos(2.0d0*mmm*(xx+ww)))/(c+2.0d0)
    else if (MODE.eq.2) then
        ! Shenoy's surface stiffness function
        SSf = 1.0d0-c+c*(1.0d0-0.25d0*mmm**2)*(dabs(dsin(0.5d0*mmm*(xx-
        ww)))+dabs(dcos(0.5d0*mmm*(xx-ww))))
    else
        ! Curtate
        SSf = 1.0d0+c*(dcos(ww)-((2.0d0*mmm)**2)*(xx+dcos(ww)))/(1.0d0+xx
        *dcos(ww)**3)
    end if

end function

double precision function zr (xx)

    use global_variables
    implicit none

    double precision :: xx

    zr = xx+alfa*dsin(xx)-2.0d0*mmR*(tet-phiR)-pi

end function

double precision function z1 (xx)

    use global_variables
    implicit none

    double precision :: xx

```

```

    z1 = xx+alfa*dsin(xx)-2.0d0*mmL*(tet-phiL)-pi
end function

double precision function rolling (z,znot)

    use global_variables
    implicit none

    interface
        double precision function z(x)
            double precision, intent(in) :: x
        end function z
    end interface

    double precision :: arrabs,znot

    arrabs = 1.0E-6
    call dzreal (z, arrabs, arrabs, 1.d-8, .01, 1, 100000, znot, znot,
info)
    rolling = znot

end function
! end. auxiliary functions for surface energy anisotropy

! this routine calculates triple junction fluxes and velocity plus the
! anisotropy coefficients
! DD stores the anisotropic diffusivities,
! SS stores the anisotropic surface stiffness
subroutine ANISOTROPY_F

    use global_variables
    use vector_operator
    implicit none

    integer      :: i
    type (vec)   :: kk,ei
    real(8)      :: gamL(2),gamR(2),TETL,TETR
    double precision, external :: dot,gama,dgama,SSf,rolling,zr,z1

    kk%x = 0.0d0
    kk%y = 0.0d0
    kk%z = 1.0d0

    ei%x = 1.0d0
    ei%y = 0.0d0
    ei%z = 0.0d0

    do i = 1, nt
        DTETA(i) = dasin(dot(ei*DR(i),kk)/(DS(i)))
        if (DR(i)%x.le.0.0d0) then
            DTETA(i) = pi - DTETA(i)
        end if
        if (DTETA(i)>pi) then
            DTETA(i) = DTETA(i) - 2.0d0*pi
        end if
        if ((i.lt.gb1).or((i.gt.gb2))) then
            if (MODE.eq.3) then
                tet = DTETA(i)
                zeta(i) = rolling (z1,zeta(i))
                SS(i) = SSf(BBL,mmL,zeta(i),alfa)
            else
                SS(i) = SSf(BBL,mmL,phiL,DTETA(i))
            end if
            DD(i) = 1.0d0+AAL*dcos(mmL*(DTETA(i)-phiL))**2
        else
            if (MODE.eq.3) then
                tet = DTETA(i)
            end if
        end if
    end do
end subroutine ANISOTROPY_F

```

```

        zeta(i) = rolling (zr,zeta(i))
        SS(i) = SSf(BBR,mmR,zeta(i),alfa)
    else
        SS(i) = SSf(BBR,mmR,phiR,DTETA(i))
    end if
    DD(i) = 1.0d0+AAR*dcos(mmR*(DTETA(i)-phiR))**2
end if
end do

TETL = DTETA(gb1-1)
TETR = DTETA(gb1)

gamL(1) = gama(BBL,mmL,phiL,TETL)
gamL(2) = dgama(BBL,mmL,phiL,TETL)
gamR(1) = gama(BBR,mmR,phiR,TETR)
gamR(2) = dgama(BBR,mmR,phiR,TETR)

Vu = 2.0d0*lamda-gamR(1)*dsin(TETR)+gamL(1)*dsin(TETL)-gamR(2)*dcos
(TETR)+gamL(2)*dcos(TETL)
JTd = gamR(1)*dcos(TETR)-gamL(1)*dcos(TETL)-gamR(2)*dsin(TETR)+gamL
(2)*dsin(TETL)
JLu = lamda+gamL(1)*dsin(TETL)+gamL(2)*dcos(TETL)
JRu = lamda-gamR(1)*dsin(TETR)-gamR(2)*dcos(TETR)

TETL = DTETA(gb2)
TETR = DTETA(gb2-1)

gamL(1) = gama(BBL,mmL,phiL,DTETA(gb2))
gamL(2) = dgama(BBL,mmL,phiL,DTETA(gb2))
gamR(1) = gama(BBR,mmR,phiR,DTETA(gb2-1))
gamR(2) = dgama(BBR,mmR,phiR,DTETA(gb2-1))

Vd = 2.0d0*lamda-gamR(1)*dsin(DTETA(gb2-1))+gamL(1)*dsin(DTETA
(gb2))-gamR(2)*dcos(DTETA(gb2-1))+gamL(2)*dcos(DTETA(gb2))
JTd = -gamL(1)*dcos(DTETA(gb2))+gamR(1)*dcos(DTETA(gb2-1))-gamR(2)*
dsin(DTETA(gb2-1))+gamL(2)*dsin(DTETA(gb2))
JRd = lamda-gamR(1)*dsin(DTETA(gb2-1))-gamR(2)*dcos(DTETA(gb2-1))

JLd = lamda+gamL(1)*dsin(DTETA(gb2))+gamL(2)*dcos(DTETA(gb2))

end subroutine ANISOTROPY_F

! this routine calculates the centroid position vectors and normal unit
vectors at the centroids
subroutine CENTROID_F

    use global_variables
    use vector_operator
    implicit none

    integer      :: i
    type (vec)   :: kk

    double precision, external  :: absvec,dot

    kk%x = 0.0d0
    kk%y = 0.0d0
    kk%z = -1.0d0

    do i = 1, nt-1
        NC(i) = kk*DR(i)/DS(i)
        RC(i) = 0.5d0*(RT(i)+RT(i+1))
    end do

    NC(nt) = kk*DR(nt)/DS(nt)
    RC(nt) = 0.5d0*(RT(nt)+RT(1))

end subroutine CENTROID_F

```

```

! this routine calculates the normal component of the electric field
! intensity vector at the centroid positions on the sidewalls (Neumann
! BC) and the electrostatic potential at the cathode and anode edges
! (Dirichlet BC) boundary due to uniformly distributed charge using
! IBEM
subroutine MU_F

  use global_variables
  use vector_operator

  implicit none

  integer :: i,j,kk
  type (vec) :: RCIJ
  real(8) :: tot
  double precision, external :: absvec,dot
  !
do i = 1, nu-1
  CC(i) = -NC(i)%x
  do j = 1, nt
    if (i.eq.j) then
      TT(i,j) = 0.5d0
    else
      do kk = 1,mint+1
        RC_MU(kk) = RT(j)-RC(i)+((kk-1)*DR(j))/mint
      end do
      RCIJ%x = 0.0d0
      RCIJ%y = 0.0d0
      RCIJ%z = 0.0d0
      do kk = 2, mint
        RCIJ = RCIJ+RC_MU(kk)/dot(RC_MU(kk),RC_MU(kk))
      end do
      RCIJ = RCIJ+0.5d0*((RC_MU(1)/dot(RC_MU(1),RC_MU(1))+
RC_MU(mint+1)/dot(RC_MU(mint+1),RC_MU(mint+1))))
      TT(i,j) = -0.5d0*DS(j)/(pi*mint)*dot(NC(i),RCIJ)
    end if
    if (j.eq.nt) then
      tot = 0.0d0
      do kk = 1, mint-1
        tot = tot + dlog(absvec(RT(j)+kk*DR(j)/mint-RC(i)))
      end do
      tot = tot + 0.5d0*(dlog(absvec(RT(j)-RC(i)))+dlog(absvec
(RT(1)-RC(i))))
      UU(i,j) = -0.5d0*dabs(DS(j))/(pi*mint)*tot
    else
      tot = 0.0d0
      do kk = 1, mint-1
        tot = tot + dlog(absvec(RT(j)+kk*DR(j)/mint-RC(i)))
      end do
      tot = tot + 0.5d0*(dlog(absvec(RT(j)-RC(i)))+dlog(absvec
(RT(j+1)-RC(i))))
      UU(i,j) = -0.5d0*dabs(DS(j))/(pi*mint)*tot
    end if
  end do
end do

do i = nu, nu+nr
  CC(i) = 0.0d0
  do j = 1, nt
    if (j.eq.nt) then
      tot = 0.0d0
      do kk = 1, mint-1
        tot = tot + dlog(absvec(RT(j)+kk*DR(j)/mint-RC(i)))
      end do
      tot = tot + 0.5d0*(dlog(absvec(RT(j)-RC(i)))+dlog(absvec
(RT(1)-RC(i))))
      TT(i,j) = -0.5d0*dabs(DS(j))/(pi*mint)*tot
    end if
  end do
end do

```

```

        UU(i,j) = TT(i,j)
    else
        tot = 0.0d0
        do kk = 1, mint-1
            tot = tot + dlog(absvec(RT(j)+kk*DR(j)/mint-RC(i)))
        end do
        tot = tot + 0.5d0*(dlog(absvec(RT(j)-RC(i)))+dlog(absvec
(RT(j+1)-RC(i))))
        TT(i,j) = -0.5d0*dabs(DS(j))/(pi*mint)*tot
        UU(i,j) = TT(i,j)
    end if
end do
end do

do i = nu+nr+1, nu+nr+nd-1
    CC(i) = -NC(i)%x
    do j = 1, nt
        if (i.eq.j) then
            TT(i,j) = 0.5d0
        else
            do kk = 1, mint+1
                RC_MU(kk) = RT(j)-RC(i)+((kk-1)*DR(j))/mint
            end do
            RCIJ%x = 0.0d0
            RCIJ%y = 0.0d0
            RCIJ%z = 0.0d0
            do kk = 2, mint
                RCIJ = RCIJ+RC_MU(kk)/dot(RC_MU(kk),RC_MU(kk))
            end do
            RCIJ = RCIJ+0.5d0*((RC_MU(1)/dot(RC_MU(1),RC_MU(1))+
RC_MU(mint+1)/dot(RC_MU(mint+1),RC_MU(mint+1))))
            TT(i,j) = -0.5d0*DS(j)/(pi*mint)*dot(NC(i),RCIJ)
        end if
        if (j.eq.nt) then
            tot = 0.0d0
            do kk = 1, mint-1
                tot = tot + dlog(absvec(RT(j)+kk*DR(j)/mint-RC(i)))
            end do
            tot = tot + 0.5d0*(dlog(absvec(RT(j)-RC(i)))+dlog(absvec
(RT(1)-RC(i))))
            UU(i,j) = -0.5d0*dabs(DS(j))/(pi*mint)*tot
        else
            tot = 0.0d0
            do kk = 1, mint-1
                tot = tot + dlog(absvec(RT(j)+kk*DR(j)/mint-RC(i)))
            end do
            tot = tot + 0.5d0*(dlog(absvec(RT(j)-RC(i)))+dlog(absvec
(RT(j+1)-RC(i))))
            UU(i,j) = -0.5d0*dabs(DS(j))/(pi*mint)*tot
        end if
    end do
end do

do i = nu+nr+nd, nt
    CC(i) = 0.0d0
    do j = 1, nt
        if (j.eq.nt) then
            tot = 0.0d0
            do kk = 1, mint-1
                tot = tot + dlog(absvec(RT(j)+kk*DR(j)/mint-RC(i)))
            end do
            tot = tot + 0.5d0*(dlog(absvec(RT(j)-RC(i)))+dlog
(absvec(RT(1)-RC(i))))
            TT(i,j) = -0.5d0*dabs(DS(j))/(pi*mint)*tot
            UU(i,j) = TT(i,j)
        else
            tot = 0.0d0
            do kk = 1, mint-1

```

```

        tot = tot + dlog(absvec(RT(j)+kk*DR(j)/mint-RC(i)))
    end do
    tot = tot + 0.5d0*(dlog(absvec(RT(j)-RC(i)))+dlog
(absvec(RT(j+1)-RC(i))))
    TT(i,j) = -0.5d0*dabs(DS(j))/(pi*mint)*tot
    UU(i,j) = TT(i,j)
end if
end do
end do

! compute the solution matrix of Ax=b, using LAPACK libraries on Intel
MKL 8.0
! dgetrf computes the LU factorization of a general m-by-n matrix.
call dgetrf(nt, nt, TT, nt, ipiv, info)
! dgetrs solves a system of linear equations with an LU-factored
square matrix
call dgetrs('N', nt, 1, TT, nt, ipiv, CC, nt, info)
! above statement sets CC = CC*TT**-1; now CC corresponds to
electrostatic charge density at the centroids of the segments

do i = 1, nt
    ! EF_1: potential due to applied electric field at the segment
midpoints
    EF_1(i) = -RC(i)%x
    ! EF_2: potential due to uniformly distributed charge along the
segments
    EF_2(i) = 0.0d0
    do j = 1, nt
        EF_2(i) = EF_2(i)+UU(i,j)*CC(j)
    end do
    ! total electrostatic potential at the upper and lower sidewalls
plus at the cathode and anode edges (segment midpoints)
    EF_TC(i) = EF_1(i) + EF_2(i)
end do

! extrapolation from centroids to nodes
do i = 1, nt
    if (i.eq.1) then
        EF_TN(1) = (EF_TC(nt)*DS(i)+EF_TC(i)*DS(nt))/(DS(i)+DS(nt))
    else
        EF_TN(i) = (EF_TC(i-1)*DS(i)+EF_TC(i)*DS(i-1))/(DS(i)+DS(i-
1))
    end if
end do

end subroutine

! this routine calculates the displacement matrix due to a unit force
which is r apart from the point of interest
type (arr) function US_S(r)

    use global_variables
    use vector_operator
    implicit none

    type (vec)  :: r,i,j
    type (arr)  :: tss
    double precision, external :: absvec, dot

    i%x = 1.0d0
    i%y = 0.0d0
    i%z = 0.0d0

    j%x = 0.0d0
    j%y = 1.0d0
    j%z = 0.0d0

    tss%x(1,1) = -(3.0d0-4.0d0*nu_s)*dlog(absvec(r))+dot(r,i)**2/dot(r,

```

```

r)
tss%x(1,2) = dot(r,i)*dot(r,j)/dot(r,r)
tss%x(2,1) = tss%x(1,2)
tss%x(2,2) = -(3.0d0-4.d0*nu_s)*dlog(absvec(r))+dot(r,j)**2/dot(r,r)

US_S = C0*tss

end function

! this routine calculates the traction function associated with a unit
! force situated at P and acting at point Q (r=QP vector), n is the
! unit outward normal at Q
type (arr) function TS_S(r,n)

    use global_variables
    use vector_operator
    implicit none

    type (vec)    :: n,r,i,j
    type (arr)    :: tss,tsk
    integer       :: ii,jj
    double precision, external :: dot

    i%x = 1.0d0
    i%y = 0.0d0
    i%z = 0.0d0

    j%x = 0.0d0
    j%y = 1.0d0
    j%z = 0.0d0

    tsk%x(1,1) = ((1.0d0-2.0d0*nu_s)+2.0d0*dot(r,i)**2/dot(r,r))*dot(r,
n)/dot(r,r)
    tsk%x(1,2) = 2.0d0*dot(r,i)*dot(r,j)*dot(r,n)/(dot(r,r)**2)
    tsk%x(2,1) = tsk%x(1,2)
    tsk%x(2,2) = ((1.0d0-2.0d0*nu_s)+2.0d0*dot(r,j)**2/dot(r,r))*dot(r,
n)/dot(r,r)

    tss%x(1,1) = 0.0d0
    tss%x(1,2) = (1.0d0-2.0d0*nu_s)*(dot(r,j)*dot(n,i)-dot(r,i)*dot(n,
j))/dot(r,r)
    tss%x(2,1) = -tss%x(1,2)
    tss%x(2,2) = 0.0d0

    do ii = 1,2
        do jj = 1,2
            TS_S%(jj,ii) = C2*(tsk%(ii,jj)+tss%(ii,jj))
        end do
    end do

end function

! this routine calculates the stress connection matrix (3by2) at a point
! Q for unit load situated at the point P for a given connection
! vector r (r=QP)
type (arr1) function SS_S(r)

    use global_variables
    use vector_operator
    implicit none

    type (vec)      :: r,i,j
    type (arr1)     :: sss
    real(8)         :: rxx, ryy, mag
    double precision, external :: absvec, dot

    mag = absvec(r)
    rxx = r%x/mag

```

```

ryy = r%y/mag

SS_S%x(1,1) = C2*(C3*rxx+2.0d0*rxx**3)/mag
SS_S%x(1,2) = C2*(-C3*ryy+2.0d0*ryy*rxx**2)/mag
SS_S%x(2,1) = C2*(-C3*rxx+2.0d0*rxx*ryy**2)/mag
SS_S%x(2,2) = C2*(C3*ryy+2.0d0*ryy**3)/mag
SS_S%x(3,1) = C2*(C3*ryy+2.0d0*ryy*rxx**2)/mag
SS_S%x(3,2) = C2*(C3*rxx+2.0d0*rxx*ryy**2)/mag

end function

! this routine computes stress grand matrix using IBEM
subroutine FS_S

use global_variables
use vector_operator
implicit none

integer :: i,j,kk
type (arr) :: tss,ttss,ttsk,uuss,uusk
type (arr),external :: TS_S,US_S
type (arr1) :: ssss,sssk
type (arr1),external :: SS_S
real(8),external :: dot

tss%x(1,1) = 0.5d0
tss%x(1,2) = 0.0d0
tss%x(2,1) = 0.0d0
tss%x(2,2) = 0.5d0

do i = 1, nt
! TR keeps elastostatic boundary conditions
if (i.le.nu-1) then
TR(i*2-1) = 0.0d0
TR(i*2) = r_s*sigx
else if (i.le.nu+nr) then
TR(i*2-1) = sigx
TR(i*2) = 0.0d0
else if (i.le.nu+nr+nd-1) then
TR(i*2-1) = 0.0d0
TR(i*2) = -1.0d0*r_s*sigx
else if (i.le.nt) then
TR(i*2-1) = -1.0d0*sigx
TR(i*2) = 0.0d0
end if
!
do j = 1, nt
if (i.eq.j) then
! FT is the traction connection grand matrix which
connects any two centroids for traction versus point force
interrelation
FT(2*i-1,2*j-1) = tss%x(1,1)
FT(2*i-1,2*j) = tss%x(1,2)
FT(2*i,2*j-1) = tss%x(2,1)
FT(2*i,2*j) = tss%x(2,2)
! GT is the stress connection grand matrix
GT(3*i-2,2*j-1) = 0.0d0
GT(3*i-1,2*j-1) = 0.0d0
GT(3*i,2*j-1) = 0.0d0
GT(3*i-2,2*j) = 0.0d0
GT(3*i-1,2*j) = 0.0d0
GT(3*i,2*j) = 0.0d0
else
do kk = 1,mint+1
RC_FS(kk) = RT(j)-RC(i)+((kk-1)*DR(j))/mint
end do
ttss = 0.5d0*(TS_S(RC_FS(1),(-1.0d0)*NC(i))+TS_S(RC_FS
(mint+1),(-1.0d0)*NC(i)))

```

```

        ssss = 0.5d0*(SS_S(RC_FS(1))+SS_S(RC_FS(mint+1)))
        do kk = 2, mint
            ttstk = TS_S(RC_FS(kk),(-1.0d0)*NC(i))
            ttss = ttss+ttstk
            sssk = SS_S(RC_FS(kk))
            ssss = ssss+sssk
        end do
        FT(2*i-1,2*j-1) = (DS(j)/mint)*ttss%x(1,1)
        FT(2*i-1,2*j) = (DS(j)/mint)*ttss%x(1,2)
        FT(2*i,2*j-1) = (DS(j)/mint)*ttss%x(2,1)
        FT(2*i,2*j) = (DS(j)/mint)*ttss%x(2,2)
        GT(3*i-2,2*j-1) = (DS(j)/mint)*ssss%x(1,1)
        GT(3*i-1,2*j-1) = (DS(j)/mint)*ssss%x(2,1)
        GT(3*i,2*j-1) = (DS(j)/mint)*ssss%x(3,1)
        GT(3*i-2,2*j) = (DS(j)/mint)*ssss%x(1,2)
        GT(3*i-1,2*j) = (DS(j)/mint)*ssss%x(2,2)
        GT(3*i,2*j) = (DS(j)/mint)*ssss%x(3,2)
    end if
end do
end do

! compute the solution matrix of Ax=b, using LAPACK libraries on Intel MKL 8.0
! dgetrf computes the LU factorization of a general m-by-n matrix.
call dgetrf(2*nt, 2*nt, FT, 2*nt, ipiv, info)
! dgetrs solves a system of linear equations with an LU-factored square matrix
call dgetrs('N', 2*nt, 1, FT, 2*nt, ipiv, TR, 2*nt, info)
! above statement sets TR = TR*FT**-1; now TR corresponds to force intensities situated at the centroids of the segments
! dgemv performs matrix-vector product; US = GT*TR is the stress grand matrix
call dgemv('N', 3*nt, 2*nt, 1.0d0, GT, 3*nt, TR, 1, 0.0d0, US, 1 )

end subroutine

! this routine computes stress components at the nodes
subroutine STRESS_S

    use global_variables
    use vector_operator
    implicit none

    integer      :: i
    type (vec)   :: ubvec(10000)
    real(8)      :: uxy(10000),hoop_TN(10000)
    real(8),external  :: dot

    do i = 1, nt
        ux(i) = US(3*i-2)
        uy(i) = US(3*i-1)
        uxy(i) = US(3*i)
        ubvec(i)%x = ux(i)*DR(i)%x + uxy(i)*DR(i)%y
        ubvec(i)%y = uxy(i)*DR(i)%x + uy(i)*DR(i)%y
        ubvec(i)%z = 0.0d0
        hoopstress(i) = dot(ubvec(i),DR(i))/(DS(i)**2)
    end do
    ! extrapolation from centroids to nodes
    do i = 2, nt
        hoop_TN(i) = (hoopstress(i-1)*DS(i)+hoopstress(i)*DS(i-1))/(DS(i)+DS(i-1))
    end do
    hoop_TN(1) = (hoopstress(nt)*DS(1)+hoopstress(1)*DS(nt))/(DS(1)+DS(nt))
    do i = 1, nt
        hoopstress(i) = hoop_TN(i)
    end do

```

```

end subroutine

!
subroutine CALC_F(nn)
  use global_variables
  use vector_operator
  implicit none

  integer      :: i,nn

  double precision, external  :: absvec,dot

  P = chi*EF_TN/ro + siglam*SE/ro**2 + xi*hoopstress/ro

  K = KAPPA*ro*SS+P

  do i = 1, nt
    RT(i) = RT(i)/ro
    DR(i) = DR(i)/ro
    DS(i) = DS(i)/ro
  end do

  ! compute node velocities
  do i = 1, nn
    if (i.eq.1) then
      if ((BC.eq.0).or.(BC.eq.2)) then
        V(i) = 0.5d0*MTA/omega*(lamda_A-dot(DR(i),(-1.0d0)*ta_o)
/DS(i))
      else
        V(i) = DD(i)*2.0d0*(K(i+1)-K(i))/(DS(i)**2)
      end if
    else if (i.eq.2) then
      if ((BC.eq.0).or.(BC.eq.2)) then
        V(i) = -0.5d0*MTA*delta/omega*(lamda_A-dot(DR(i-1),(-1.
0d0)*ta_o)/DS(i-1)) + DD(i)*(K(i+1)-K(i))/DS(i) - DD(i-1)*(P(i)-P(i-
1))/DS(i-1)
        V(i) = V(i)/(DS(i-1)+0.5d0*DS(i))
      else
        V(i) = DD(i)*(K(i+1)-K(i))/DS(i) - DD(i-1)*(K(i)-K(i-1))
/DS(i-1)
        V(i) = 2.0d0*V(i)/(DS(i)+DS(i-1))
      end if
    else if (i.eq.nu-1) then
      if (BC.eq.2) then
        V(i) = -0.5d0*MTC*delta/omega*(lamda_C-dot(DR(i),ta_o)/
DS(i)) - DD(i-1)*(K(i)-K(i-1))/DS(i-1) + DD(i)*(P(i+1)-P(i))/DS(i)
        V(i) = V(i)/(DS(i)+0.5d0*DS(i-1))
      else
        V(i) = DD(i)*(K(i+1)-K(i))/DS(i) - DD(i-1)*(K(i)-K(i-1))
/DS(i-1)
        V(i) = 2.0d0*V(i)/(DS(i)+DS(i-1))
      end if
    else if (i.eq.nu) then
      if (BC.eq.3) then
        V(i) = DD(i-1)*2.0d0*(K(i-1)-K(i))/(DS(i-1)**2)
      else if(BC.eq.2) then
        V(i) = 0.5d0*MTC/omega*(lamda_C-dot(DR(i-1),ta_o)/DS(i-
1))
      else
        V(i) = DD(i)*(K(i+1)-K(i))/DS(i) - DD(i-1)*(K(i)-K(i-1))
/DS(i-1)
        V(i) = 2.0d0*V(i)/(DS(i)+DS(i-1))
      end if
    else if (i.eq.nu+nr+1) then
      if (BC.eq.3) then
        V(i) = DD(i)*2.0d0*(K(i+1)-K(i))/(DS(i)**2)

```

```

else if(BC.eq.2) then
    V(i) = 0.5d0*MTC/omega*(lamda_C-dot(DR(i),ta_o)/DS(i))
else
    V(i) = DD(i)*(K(i+1)-K(i))/DS(i) - DD(i-1)*(K(i)-K(i-1))
/DS(i-1)
    V(i) = 2.0d0*V(i)/(DS(i)+DS(i-1))
end if
else if (i.eq.nu+nr+2) then
    if (BC.eq.2) then
        V(i) = -0.5d0*MTC*delta/omega*(lamda_C-dot(DR(i-1),ta_o)
/DS(i-1)) + DD(i)*(K(i+1)-K(i))/DS(i) - DD(i-1)*(P(i)-P(i-1))/DS(i-
1)
        V(i) = V(i)/(DS(i-1)+0.5d0*DS(i))
    else
        V(i) = DD(i)*(K(i+1)-K(i))/DS(i) - DD(i-1)*(K(i)-K(i-1))
/DS(i-1)
        V(i) = 2.0d0*V(i)/(DS(i)+DS(i-1))
    end if
else if (i.eq.nn-1) then
    if ((BC.eq.0).or.(BC.eq.2)) then
        V(i) = -0.5d0*MTA*delta/omega*(lamda_A-dot(DR(i),(-1.
0d0)*ta_o)/DS(i)) - DD(i-1)*(K(i)-K(i-1))/DS(i-1) + DD(i)*(P(i+1)-P
(i))/DS(i)
        V(i) = V(i)/(DS(i)+0.5d0*DS(i-1))
    else
        V(i) = DD(i)*(K(i+1)-K(i))/DS(i) - DD(i-1)*(K(i)-K(i-1))
/DS(i-1)
        V(i) = 2.0d0*V(i)/(DS(i)+DS(i-1))
    end if
else if (i.eq.nn) then
    if ((BC.eq.0).or.(BC.eq.2)) then
        V(i) = 0.5d0*MTA/omega*(lamda_A-dot(DR(i-1),(-1.0d0)*
ta_o)/DS(i-1))
    else
        V(i) = DD(i-1)*2.0d0*(K(i-1)-K(i))/(DS(i-1)**2)
    end if
else if ((i.gt.nu).and.(i.lt.nu+nr+1)) then
    if ((BC.eq.2).or.(BC.eq.3)) then
        V(i) = 0.0d0
    else
        V(i) = DD(i)*(K(i+1)-K(i))/DS(i) - DD(i-1)*(K(i)-K(i-1))
/DS(i-1)
        V(i) = 2.0d0*V(i)/(DS(i)+DS(i-1))
    end if
else if (i.eq.(gb1+1)) then
    V(i) = -0.5d0*MG*delta/omega*JRu + DD(i)*(K(i+1)-K(i))/DS(i)
- DD(i-1)*(P(i)-P(i-1))/DS(i-1)-0.5d0*Jgu
    V(i) = V(i) - MT*delta/omega*JTu
    V(i) = V(i)/(DS(i-1)+0.5d0*DS(i))
else if (i.eq.(gb1)) then
    V(i) = 0.5d0*MG/omega*Vu
else if (i.eq.(gb1-1)) then
    V(i) = -0.5d0*MG*delta/omega*JLu - DD(i-1)*(K(i)-K(i-1))/DS
(i-1) + DD(i)*(P(i+1)-P(i))/DS(i)-0.5d0*Jgu
    V(i) = V(i) + MT*delta/omega*JTu
    V(i) = V(i)/(DS(i)+0.5d0*DS(i-1))
else if (i.eq.(gb2+1)) then
    V(i) = -0.5d0*MG*delta/omega*JLd + DD(i)*(K(i+1)-K(i))/DS(i)
- DD(i-1)*(P(i)-P(i-1))/DS(i-1)-0.5d0*Jgd
    V(i) = V(i) - MT*delta/omega*JTd
    V(i) = V(i)/(DS(i-1)+0.5d0*DS(i))
else if (i.eq.(gb2)) then
    V(i) = 0.5d0*MG/omega*Vd
else if (i.eq.(gb2-1)) then
    V(i) = -0.5d0*MG*delta/omega*JRd - DD(i-1)*(K(i)-K(i-1))/DS
(i-1) + DD(i)*(P(i+1)-P(i))/DS(i)-0.5d0*Jgd
    V(i) = V(i) + MT*delta/omega*JTd

```

```

        V(i) = V(i)/(DS(i)+0.5d0*DS(i-1))
    else
        V(i) = DD(i)*(K(i+1)-K(i))/DS(i) - DD(i-1)*(K(i)-K(i-1))/DS
(i-1)
        V(i) = 2.0d0*V(i)/(DS(i)+DS(i-1))
    end if
end do

! determine the maximum node velocity
vmax = dabs(V(1))
do i = 1, nn
    if (dabs(V(i)).ge.vmax) then
        vmax = dabs(V(i))
    end if
end do

! compute new node positions
do i = 1, nn
    if (i.eq.1) then
        RT(i) = RT(i) + deltat*V(i)*ta_o
    else if (i.eq.nu) then
        if ((BC.eq.2).or.(BC.eq.3)) then
            RT(i) = RT(i) + deltat*V(i)*ta_o
        else
            RT(i) = RT(i) + deltat*V(i)*LLN(i)
        end if
    else if (i.eq.nu+nr+1) then
        if ((BC.eq.2).or.(BC.eq.3)) then
            RT(i) = RT(i) - deltat*V(i)*ta_o
        else
            RT(i) = RT(i) + deltat*V(i)*LLN(i)
        end if
    else if (i.eq.nn) then
        RT(i) = RT(i) - deltat*V(i)*ta_o
    else if (i.eq.gb1) then
        RT(i) = RT(i) + deltat*V(i)*ta
    else if (i.eq.gb2) then
        RT(i) = RT(i) + deltat*V(i)*td
    else
        RT(i) = RT(i) + deltat*V(i)*LLN(i)
    end if
end do
!
end subroutine

! this routine performs mesh refinement
subroutine MR_F

    use global_variables
    use vector_operator
    implicit none

    integer:: i
    double precision, external :: DCSVAL    !, absvec

    ! compute cubic spline interpolant
    call DELR_F    ! recall delr to compute sdata for new r set
    ! left side
    SDATA(1) = 0.0d0
    do i = gb1-1, 1, -1
        XDATA(gb1-i+1) = RT(i)%x
        YDATA(gb1-i+1) = RT(i)%y
        SDATA(gb1-i+1) = SDATA(gb1-i) + DS(i)
    end do
    SDATA(1) = 0.0d0
    XDATA(1) = RT(gb1)%x
    YDATA(1) = RT(gb1)%y
    ! routine DCSINT computes cubic spline interpolant

```

```

CALL DCSINT (NDATA, SDATA, XDATA, BREAK, CSCOEFX)
CALL DCSINT (NDATA, SDATA, YDATA, BREAK, CSCOEFY)
! RT(1) remains fixed here, but [RT(2)-RT(1)] grows
do i = 2, NDATA
! routine CSVAL evaluates a cubic spline at a given point
RT(gb1-i+2)%x = DCSVAL(dmean*(i-2),NDATA-1,BREAK,CSCOEFX)
RT(gb1-i+2)%y = DCSVAL(dmean*(i-2),NDATA-1,BREAK,CSCOEFY)
end do
!
! right side
SDATA(1) = 0.0d0
do i = gb1, nu-1
XDATA(i-gb1+1) = RT(i)%x
YDATA(i-gb1+1) = RT(i)%y
SDATA(i-gb1+2) = SDATA(i-gb1+1) + DS(i)
end do
XDATA(nu-gb1+1) = RT(nu)%x
YDATA(nu-gb1+1) = RT(nu)%y
! routine DCSINT computes cubic spline interpolant
CALL DCSINT (NDATA, SDATA, XDATA, BREAK, CSCOEFX)
CALL DCSINT (NDATA, SDATA, YDATA, BREAK, CSCOEFY)
do i = gb1, nu-1
! routine CSVAL evaluates a cubic spline at a given point
RT(i)%x = DCSVAL(dmean*(i-gb1),NDATA-1,BREAK,CSCOEFX)
RT(i)%y = DCSVAL(dmean*(i-gb1),NDATA-1,BREAK,CSCOEFY)
end do

end

! capillarity driven surface diffusion
subroutine CP

use global_variables
implicit none

hoopstress = 0.0d0
EF_TN = 0.0d0
CC = 0.0d0

do while ((t.le.nloop+1).and.((100.0d0-100.0d0/sw*RT(gb1)%y).lt.95.
0d0).and.((100.0d0+100.0d0/sw*RT(gb2)%y).lt.95.0d0))
call DELR_F
call PSIR_F
call KAPPA_F
call ANISOTROPY_F
call CALC_F(nt-nl)
call MR_F
if (t.eq.2**H) then
call output(H)
H = H+1
end if
deltat = eptime*dmean/vmax
timet = timet+deltat
t = t+1
end do

end subroutine

! electromigration and capillarity driven surface diffusion
subroutine EM

use global_variables
use vector_operator
implicit none

integer :: i

hoopstress = 0.0d0

```

```

ux = 0.0d0
uy = 0.0d0

do while ((t.le.nloop+1).and.((100.0d0-100.0d0/sw*RT(gb1)%y).lt.95.0d0).and.((100.0d0+100.0d0/sw*RT(gb2)%y).lt.95.0d0))
  call DELR_F
  call PSIR_F
  call KAPPA_F
  call ANISOTROPY_F
  call CENTROID_F
  call MU_F
  call CALC_F(nt-nl)
  call MR_F
  if (t.eq.2**H) then
    call output(H)
    H = H+1
  end if
  deltat = eptime*dmean/vmax
  timet = timet+deltat
  t = t+1
end do

end subroutine

! stress and capillarity driven surface diffusion
subroutine ES

  use global_variables
  use vector_operator
  implicit none

  integer :: i

  EF_TN = 0.0d0
  CC = 0.0d0

  do while ((t.le.nloop+1).and.((100.0d0-100.0d0/sw*RT(gb1)%y).lt.95.0d0).and.((100.0d0+100.0d0/sw*RT(gb2)%y).lt.95.0d0))
    call DELR_F
    call PSIR_F
    call KAPPA_F
    call ANISOTROPY_F
    call CENTROID_F
    call FS_S
    call STRESS_S
    call CALC_F(nt-nl)
    call MR_F
    if (t.eq.2**H) then
      call output(H)
      H = H+1
    end if
    deltat = eptime*dmean/vmax
    timet = timet+deltat
    t = t+1
  end do

end subroutine

! electromigration, stress and capillarity driven surface diffusion
subroutine EMS

  use global_variables
  use vector_operator
  implicit none

  integer :: i

  do while ((t.le.nloop+1).and.((100.0d0-100.0d0/sw*RT(gb1)%y).lt.95.0d0).and.((100.0d0+100.0d0/sw*RT(gb2)%y).lt.95.0d0))

```

```

        call DELR_F
        call PSIR_F
        call KAPPA_F
        call ANISOTROPY_F
        call CENTROID_F
        call MU_F
        call FS_S
        call STRESS_S
        call CALC_F(nt-nl)
        call MR_F
        if (t.eq.2**H) then
            call output(H)
            H = H+1
        end if
        deltat = eptime*dmean/vmax
        timet = timet+deltat
        t = t+1
    end do

end subroutine

! GROOVE
program GROOVE_v_1.8

    use dfport
    use vector_operator
    use global_variables
    implicit none

    integer :: i
    real(8) :: start,finish,dummy,itimet,elapsed_time
    double precision, external :: absvec

    elapsed_time = TIMEF( )

    call input

    if (cont.eq.0) then
        ! initialize
        call generate
        H = 0
        t = 0
        timet = 0.0d0
        Jgu = 0.0d0
        Jgd = 0.0d0
    else
        ! continue from the latest ooutput
        open(5,file='cont.txt')
        read(5,'(20(f30.16),5(i12),(f30.16),4(i10))') RT(1)%x,RT(1)%
        y,V(1),dummy,dummy,dummy,dummy,dummy,dummy,dummy,dummy,dummy,zeta(1)
        ,dummy,dummy,dummy,dummy,dummy,dummy,timet,H,t,nt,gb1,gb2,itimet,nu,
        nr,nd,nl
        RT(1)%z = 0.0d0
        do i = 2, nt
            read(5,'(13(f30.16))') RT(i)%x,RT(i)%y,V(i),dummy,dummy,
            dummy,dummy,dummy,dummy,dummy,dummy,dummy,zeta(i)
            RT(i)%z = 0.0d0
        end do
        close(5)

        write(*,*)
        print*, 'Experiment continues from H=', H
        write(*,*)

        deltat = timet - itimet
        H = H+1
        t = t+1
        Jgu = 0.0d0
    end if
end program

```

```

      Jgd = 0.0d0
      ta_o%x = 0.0d0
      ta_o%y = -1.0d0
      ta_o%z = 0.0d0
      ta = (RT(gb2)-RT(gb1))/absvec((RT(gb2)-RT(gb1)))
      td = (-1.0d0)*ta
end if
!
allocate(RC_MU(mint+1),RC_FS(mint+1))
allocate(FT(2*nt,2*nt),UT(2*nt,2*nt),TT(nt,nt),UU(nt,nt),CC(nt),TR_FS(
(nt),TR(2*nt),GT(3*nt,2*nt))
!
NDATA = gb1
allocate(XDATA(NDATA),YDATA(NDATA),SDATA(NDATA),BREAK(NDATA),CSCOEFX (
(4,NDATA),CSCOEFY(4,NDATA))
!
if (chi.eq.0.0d0) then
  if ((xi.eq.0.0d0).and.(siglam.eq.0.0d0)) then
    call CP
  else
    call ES
  end if
else
  if ((xi.eq.0.0d0).and.(siglam.eq.0.0d0)) then
    call EM
  else
    call EMS
  end if
end if
!
elapsed_time = TIMEF( )
!
write(*,*)
print '("Total Computation Time = ",f16.5," seconds.)',elapsed_time
read *

end program GROOVE_v_1.8

```

CURRICULUM VITAE

Name: Öncü AKYILDIZ

Date of Birth/Place: November 14, 1977/Çorum, TURKEY

Nationality: Turkish

E-mail: oncu_a@yahoo.com

EDUCATION

- Ph. D.** 05/2010 Metallurgical and Materials Engineering,
Middle East Technical University, Ankara, TURKEY
- M. Sc.** 10/2004 Metallurgical and Materials Engineering,
Middle East Technical University, Ankara, TURKEY
- B. Sc.** 06/2001 Metallurgical and Materials Engineering,
Middle East Technical University, Ankara, TURKEY

WORK EXPERIENCE

- Project Assistant** (2005-2010)
Metallurgical & Materials Engineering Department,
Middle East Technical University, Ankara, TURKEY
- Student Assistant** (2002-2005)
Metallurgical & Materials Engineering Department,
Middle East Technical University, Ankara, TURKEY

AWARDS

- ❖ *The Best Thesis Award, 2004. Graduate School of Natural and Applied Sciences, Middle East Technical University, Ankara, TURKEY.*
- ❖ *The Best Poster Award Nominee, 2006. Materials Research Society 2006 Spring Meeting, San Francisco, CA, USA.*

PUBLICATIONS

A. Thesis

1. Oncu AKYILDIZ, Ph. D. Thesis, METU, May 2010.
Computer simulation of grain boundary grooving by anisotropic surface drift diffusion due to capillary, electromigration and elastostatic forces
2. Oncu AKYILDIZ, M. Sc. Thesis, METU, September 2004.
Computer simulation of grain boundary grooving and cathode voiding in bamboo interconnects by surface diffusion under capillary and electromigration forces

B. Journal Articles

1. Oncu AKYILDIZ and Tarik O. OGURTANI
An irreversible thermodynamics of treatment of thermal grooving by surface drift diffusion: Effects of physicochemical properties and anisotropic diffusivity
Manuscript submitted for publication, May 2010.
2. Tarik O. OGURTANI and Oncu AKYILDIZ
Morphological evolution of voids by surface drift-diffusion driven by the capillary, electromigration and thermal-stress gradient induced by the steady state heat flow in passivated metallic thin films: Part-II (Applications)
Journal of Applied Physics, 104, 023522 (2008).
3. Tarik O. OGURTANI and Oncu AKYILDIZ
Morphological evolution of voids by surface drift-diffusion driven by the capillary, electromigration and thermal-stress gradient induced by the steady state heat flow in passivated metallic thin films: Part-I (Theory)
Journal of Applied Physics, 104, 023521 (2008).
4. Tarik O. OGURTANI, Oncu AKYILDIZ, and Ersin E. OREN
Morphological evolution of tilted grain-boundary thermal grooving by surface diffusion in bicrystal thin solid films having strong anisotropic surface Gibbs free energies
Journal of Applied Physics, 104, 013518 (2008).
5. Tarik O. OGURTANI and Oncu AKYILDIZ
Cathode edge displacement by voiding coupled with grain boundary grooving in bamboo like metallic interconnects by surface drift-diffusion under the capillary and electromigration forces
International Journal of Solids and Structures, 45 (3-4), 921-942 (2008)

6. Tarik O. OGURTANI and Oncu AKYILDIZ
Grain boundary grooving and cathode voiding in bamboo-like metallic interconnects by surface diffusion under capillary and electromigration forces
Journal of Applied Physics, 97, 093520 (2005).

C. Conference & Meeting Presentations

1. Tarik O. OGURTANI and Oncu AKYILDIZ*
Morphological evolution of intragranular voids under the thermal-stress gradient generated by the steady state heat flow in encapsulated metallic films: Special reference to flip chip solder joints
MRS 2007 Fall Meeting, "Symposium E: Theory, Modeling, and Numerical Simulation of Multiphysics Materials Behavior"
Poster Presentation, Boston, Massachusetts, USA, November 26-30, 2007.
2. Tarik O. OGURTANI and Oncu AKYILDIZ*
Computer simulations on grain boundary grooving and cathode edge displacement in bamboo-like metallic interconnects
MRS 2006 Spring Meeting, "Symposium F: Materials, Technology, and Reliability of Low-k Dielectrics and Copper Interconnects"
Poster Presentation, San Francisco, California, USA, April 17-21, 2006.

D. Articles in Conference Proceedings

1. Tarik O. OGURTANI and Oncu AKYILDIZ
Morphological evolution of intragranular voids under the thermal-stress gradient generated by the steady state heat flow in encapsulated metallic films: Special reference to flip chip solder joints
Selected, peer reviewed papers from the Symposium: Theory, Modeling and Numerical Simulation of Multi-Physics Materials Behavior organized within the MRS Fall Meeting 2007 held in Boston MA, USA, November 26-30, 2007. Editors: Veena Tikare, Graeme E. Murch, Frédéric Soisson and Jeung Ku Kang
Solid State Phenomena, 139, 151-156 (2008).
2. Tarik O. OGURTANI and Oncu AKYILDIZ
Computer simulations on grain boundary grooving and cathode edge displacement in bamboo-like metallic interconnects
Materials, Technology and Reliability of Low-k Dielectrics and Copper Interconnects.
Editors: T. Y. Tsui, Y-C. Joo, A. A. Volinsky, M. Lane, L. Michaelson.
Materials Research Society Symposium Proceedings 914, Warrendale, PA, 2006, 0914-F09-22.

* Presenting author